A New Crystal Plasticity-based Modeling of Damage Evolution in Advanced High Strength Steels under Varying Strain Rates, Temperatures, and Loading Conditions

by

Sandipkumar Himmatbhai Dayani

A thesis
presented to the University of Waterloo
in fulfillment of the
thesis requirement for the degree of
Doctor of Philosophy
in
Mechanical and Mechatronics Engineering

Waterloo, Ontario, Canada, 2026

© Sandipkumar Himmatbhai Dayani 2026

Examining Committee Membership

The following served on the Examining Committee for this thesis. The decision of the Examining Committee is by majority vote.

Supervisor	Kaan Inal, PhD Professor, Department of Mechanical and Mechatronics Engineering NSERC/General Motors Industrial Research Chair in "Integrated Computational Mechanics for Mass Efficient Automotive Structures" University of Waterloo
External Examiner	Marko Knezevic, PhD Professor, Department of Mechanical Engineering University of New Hampshire
Internal Examiner	Cliff Butcher, PhD Professor, Department of Mechanical and Mechatronics Engineering University of Waterloo
Internal Examiner	Adrian Gerlich, PhD Professor, Department of Mechanical and Mechatronics Engineering NSERC/TransCanada Industrial Research Chair in "Welding for Energy Infrastructure" University of Waterloo
Internal-external Examiner	Hassan Baaj, PhD, P. Eng. Professor, Department of Civil and Environmental Engineering Director of the Centre for Pavement and Transportation Technology Norman McLeod Chair in Sustainable Pavement Engineering University of Waterloo

Author's Declaration

This thesis consists of material all of which I authored or co-authored: see Statement of Contributions included in the thesis. This is a true copy of the thesis, including any required final revisions, as accepted by my examiners.

I understand that my thesis may be made electronically available to the public.

Statement of Contributions

The following co-authors have contributed to the current work as outlined below:

Professor Kaan Inal supervised this PhD thesis and provided guidance, conceptualization, discussion, project support, and editing throughout the work.

Dr. Waqas Muhammad provided mentorship, experimental support, EBSD measurements, microstructure characterization, mechanical testing data, and valuable discussions related to data interpretation.

Dr. Abhijit Brahme provided guidance, discussions, conceptualization, numerical modeling support, and editing of the work. He also provided support in converting EBSD measurements for use in the crystal plasticity simulations.

Fatemeh Hekmat, Trevor Sabiston, and Kathy Wang provided industrial support, project resources, and valuable discussions related to the application of the work to advanced automotive steels.

The balance of this work is my own.

Abstract

This thesis develops a crystal plasticity-based damage modeling framework for high-strength low-alloy (HSLA) steels and multiphase advanced high-strength steels (AHSS) to predict damage evolution, stress-strain softening, and failure over a range of strain rates, temperatures, and loading conditions. A thermodynamically consistent rate-dependent formulation is first developed for HSLA steels. In this baseline model, crystallographic slip, dislocation evolution, internal temperature rise, void nucleation, and void growth are coupled through thermodynamic driving forces and rate-dependent kinetic laws. Damage is introduced as an evolving internal variable that contributes to volumetric deformation, stiffness degradation, and the progressive loss of load-carrying capacity. The model is implemented in a Taylor-type crystal plasticity framework and calibrated using experimental characterization performed in this work on HR340 and HR550 steels, including tensile testing over quasi-static and intermediate strain rates, electron backscatter diffraction (EBSD) measurements for the initial texture, and high-speed infrared thermography for temperature evolution during deformation. Numerical predictions are compared against measured stress-strain curves, temperature histories, and texture evolution. The calibrated model captures the rate-dependent stress-strain response, temperature rise, damage accumulation, and post-necking softening behavior of the investigated HSLA steels.

The modeling strategy is then extended to multiphase AHSS with increasing microstructural complexity. For dual phase steels, the formulation incorporates phase specific ferrite and martensite plasticity, microstructure-sensitive void evolution, texture effects, and homogenized ferrite-martensite interface degradation. The model is evaluated for DP590 and DP780 steels under uniaxial tension, plane strain tension, and simple shear loading, allowing the influence of phase contrast, loading path, crystallographic texture, and interface-sensitive damage on failure response to be examined without explicitly meshing phase boundaries. For quenching and partitioning steels, the framework is adapted to account for evolving phase constitution by coupling crystallographic slip, retained-austenite transformation, thermomechanical effects, and phase-sensitive damage evolution. The Q&P model is applied to QP3Mn and QP980 steels to capture retained-austenite transformation, thermomechanical effects, damage-driven softening, and failure under different strain rate and temperature conditions. A transition strain analysis is introduced to distinguish the onset of macroscopic softening, rapid damage acceleration, and the shift from

retained-austenite-assisted stabilization to damage-dominated degradation. By treating HSLA, DP, and Q&P steels as nested levels of one state-variable framework, the thesis addresses whether the most enriched transformation- and damage-coupled law can reduce to the behavior of simpler alloys when inactive mechanisms are suppressed, rather than whether one empirical damage law can simply be recalibrated for every grade. The results demonstrate that predictive modeling of damage-driven softening requires a hierarchy of active mechanisms: void evolution for HSLA steels, phase/interface damage for DP steels, and retained-austenite transformation with phase-sensitive damage for Q&P steels. The proposed framework provides an efficient, microstructure-sensitive constitutive description linking crystallographic deformation, thermomechanical coupling, phase interaction, retained-austenite transformation, and damage evolution to the progressive failure response of high-strength automotive steels.

Acknowledgements

Completing this PhD has been one of the most challenging and meaningful journeys of my life, and I am deeply grateful to everyone who supported me along the way.

First and foremost, I would like to express my sincere gratitude to my supervisor, Professor Kaan Inal, for his guidance, patience, and encouragement throughout my doctoral studies. His technical expertise, thoughtful advice, and constant support have shaped the direction of this research and helped me grow as an independent researcher. I am especially grateful for the trust he placed in me and for giving me the opportunity to explore challenging research problems with confidence. Apart from his academic and technical support, I would like to thank him for his motivation, moral support, kindness and generosity throughout the entire process; without him this thesis would not have been completed.

I would like to extend my heartfelt thanks to Dr. Waqas Muhammad for his continuous support, mentorship, great friendship, and valuable discussions throughout this work. His help with experimental data, EBSD characterization, mechanical testing, and interpretation of material behavior has been extremely important to this thesis. I am also deeply thankful to Dr. Abhijit Brahme for his guidance, insight, and support in numerical modeling, crystal plasticity, microstructure analysis, and research discussions. His advice has helped me think more critically and improve the quality of my work.

I am grateful to Fatemeh Hekmat, Trevor Sabiston, Kathy Wang, and the collaborators at General Motors for their support, technical discussions, and industrial perspective. Their involvement helped connect this research to practical problems in advanced automotive steels and gave this work a broader engineering context.

I would also like to thank the members of the Computational Mechanics Research Group for creating a supportive and friendly research environment. I am especially grateful to Johann Scheepers, with whom I shared many technical discussions, research ideas, and life conversations. Those discussions helped me through many difficult moments during this journey. I am also

grateful to Dylan Budnick for his help in understanding AI and for many other helpful discussions. I would like to thank Jafar Ebadi Rajoli for the interesting discussions and thoughtful conversations. I would like to thank Chenglanqing Shu for being a wonderful lunch buddy and for making many long research days lighter and more enjoyable. I am also thankful to Advaith Narayanan, my EC4 neighbor, for his friendship, support, and encouragement throughout my PhD journey.

Most importantly, I would like to thank my beloved family. To my parents for all their support throughout my graduate studies and for sparking my initial interest in engineering. To my wife, Ruchita Khokhar, thank you for your love, patience, strength, and constant support. You stood beside me through the most stressful and uncertain moments of this PhD, and your belief in me gave me the strength to keep going. I am deeply grateful for every sacrifice you made and for the stability, warmth, and happiness you brought into my life during this journey. To my son, Marm Dayani, thank you for bringing joy, purpose, and motivation into my life. Your smile reminded me every day why perseverance matters.

I would also like to acknowledge the financial support provided by the Natural Sciences and Engineering Research Council of Canada Industrial – Research Chair program, General Motors of Canada, the International Student Doctoral Award, and the Dr. Gunhard A.E. Oravas Memorial Scholarship.

Table of Contents

List of Figures ..... **xiii**

List of Tables ..... **xviii**

1 Introduction **1**

2 Background **4**

2.1 Advanced High Strength Steels **4**

2.1.1 High Strength Low-Alloy Steel 5

2.1.2 Dual Phase Steel 6

2.1.3 Quenching and Partitioning Steel 8

2.2 Microstructural and Crystallographic Foundations **11**

2.2.1 Crystal Structure 11

2.2.2 Dislocations and Slip Systems 12

2.2.3 Crystallographic Orientation and Texture 14

2.2.4 Phase Fraction, Morphology, and Interface Characteristics 15

2.3 Ductile Damage in Metallic Alloys **16**

2.3.1 Void Nucleation 17

2.3.2 Void Growth 18

2.3.3 Void Shape Evolution 20

2.3.4 Stress State Dependence of Ductile Damage 22

2.3.5 Damage Mechanisms in AHSS 23

2.4 Experimental Techniques **25**

2.4.1 Electron Backscatter Diffraction 25

2.4.2 Digital Image Correlation 26

2.4.3 Infrared Thermography 27

2.5 Constitutive and Numerical Modeling Frameworks **28**

2.5.1 Constitutive Modeling 28

2.5.2 Crystal Plasticity 29

2.5.3 Polycrystal Homogenization 30

2.5.4 Thermomechanical Coupling 31

2.5.5 Transformation Coupled Modeling 32

3 Literature Review **34**

3.1 Constitutive Modeling of Ductile Damage in Metallic Alloys 34
3.2 Crystal Plasticity-based Damage Modeling 40
3.3 Interface Sensitive Damage Modeling in Multiphase Steels 45
3.4 Transformation-Coupled Damage Modeling in Q&P Steels 47
3.5 Summary of Literature Gaps 50
4 Research Scope and Objectives 52
4.1 Research Objectives 52
4.2 Summary of Contributions 53
5 Development of Thermodynamically Consistent Crystal Plasticity Damage Model for HSLA Steels 54
5.1 Introduction 56
5.2 Experimental Characterization 60
5.2.1 Mechanical Testing 60
5.2.2 Strain Measurements 61
5.2.3 High Speed Thermal Imaging 62
5.2.4 Microstructure Characterization 62
5.2.5 Experimental Results and Discussion 63
5.3 Model Development 66
5.3.1 Kinematics and Constitutive Framework 67
5.3.2 Thermodynamic Driving Forces 71
5.3.3 Dislocation Evolution 75
5.3.4 Kinetics Function for Damage Evolution 76
5.3.5 Temperature-Dependent Modeling 78
5.3.6 Numerical Approach 80
5.4 Result and Discussion 81
5.4.1 Model Calibration 81
5.4.2 Comparing Model Predictions with Experimental Data 83
5.4.3 Analysis of Microstructure 84
5.4.4 Effect of Temperature and Strain Rate on Dislocation Density 86
5.4.5 Damage Accumulation and Intermediate Strain Rate Predictions 87
5.5 Chapter Conclusion 88

6 Development of a Phase and Interface Driven Damage Model Coupled with Crystal Plasticity for Dual Phase Steels 90
6.1 Introduction 92
6.2 Modeling Approach 95
6.2.1 Kinematics and Constitutive Framework 96
6.2.2 Void Deformation Modes 99
6.2.3 Temperature-Dependent Modeling 104
6.3 Experimental Characterization 105
6.3.1 Microstructure Characterization 106
6.3.2 Mechanical Testing 107
6.4 Result and Discussion 112
6.4.1 Coupled Thermo-Mechanical Model and Boundary Conditions 112
6.4.2 Model Calibration and Validation 113
6.4.3 Strain-Path and Rate Dependence of Damage Evolution 116
6.4.4 Thermal Predictions 118
6.4.5 Strain Path-Dependent Texture Evolution 119
6.5 Texture Dependent Damage Evolution – Parametric Study 121
6.5.1 Quantification of Texture Components 121
6.5.2 Damage Evolution in Fiber Texture 122
6.6 Chapter Conclusion 125
7 Development of a Crystal Plasticity-Based Transformation Coupled Damage Evolution Model for Q&P Steels 127
7.1 Introduction 129
7.2 Modeling Approach 132
7.2.1 Deformation Kinematics 132
7.2.2 Governing Equations for Stress 135
7.2.3 Thermodynamic Equations with Damage 136
7.2.4 Kinetics Relations 142
7.3 Experimental Characterization 149
7.3.1 Experimental Procedure for QP980 149
7.3.2 Initial Microstructural Characterization 150

7.3.3 Tensile Response 153
7.3.4 Evolution of RA 154
7.4 Result and Discussion 155
7.4.1 Computational Framework and Thermomechanical Loading Conditions 155
7.4.2 Model Calibration and Validation 157
7.5 Chapter Conclusion 169
8 Conclusions and Future Work 171
8.1 Key Conclusions 171
8.1.1 Development of Thermodynamically Consistent Crystal Plasticity Damage Model for HSLA Steels 171
8.1.2 Development of a Phase and Interface Driven Damage Model Coupled with Crystal Plasticity for Dual Phase Steels 172
8.1.3 Development of a Crystal Plasticity-Based Transformation Coupled Damage Evolution Model for Q&P Steels 173
8.2 Limitations of the Proposed Work 174
8.3 Future Work 175
References 176
Appendices 199

List of Figures

Figure 2-1: Overview of tensile strength vs. uniform elongation for various classes of steel [27]. 5
Figure 2-2: Microstructure of HSLA (the white phase is ferrite, and the black phase is pearlite) [32]. 6
Figure 2-3: (a) Microstructure of DP steels quenched from 775 ℃ [37] and (b) Schematic schedule for the annealing process of DP steels [26]. 7
Figure 2-4: Example QP steel microstructure. The square in (a) is enlarged in (b) [44]. 9
Figure 2-5: Schematic illustration of the Q&P process along with schematic microstructure evolution during different intermediate steps [51]. 10
Figure 2-6: Schematic crystal lattice unit cells. 11
Figure 2-7: Illustration of different dislocation types in a crystal [55]. 12
Figure 2-8: BCC slip planes and directions [59]. 13
Figure 2-9: Representative BCC texture fibers and associated Euler-angle ranges [67]. 15
Figure 2-10: Representative microstructure of (a) SN – DP and (b) BM – DP steel showing the ferrite matrix (light grey) and martensite regions (dark grey) [69]. 16
Figure 2-11: SEM images of the nucleation mechanisms in DP steel (a) decohesion of ferrite/martensite interface and (b) fracture of martensite islands. 18
Figure 2-12: SEM micrographs of the DP steel during the in situ tensile test at strains equal to 0, 0.25, and 0.5 [73]. 20
Figure 2-13: Evolution of void morphology during tensile deformation of dual phase steel observed by in situ X-ray computed tomography [75]. 22
Figure 2-14: Schematic diagram of EBSD apparatus with Kikuchi pattern. 25
Figure 2-15: (a) EBSD image of HSLA with IPF map [89] and (b) Pole figure of HSLA in the RD-TD plane. 26
Figure 2-16: Schematic representation of a DIC process [95]. 27
Figure 2-17: Temperature evolution during tensile deformation [101]. 28
Figure 5-1: (a) MTS machine apparatus for 0.001 s^{-1} and 0.1 s^{-1} strain rates, (b) HISR machine setup for 1 s^{-1}, 10 s^{-1}, and 100 s^{-1} strain rates, and (c) The ASTM (E 8M-04) specimen geometry. 61

Figure 5-2: Inverse pole figure (IPF) map for (a) HR340 and (b) HR550, and grain size histogram for (c) HR340 and (d) HR550. 63
Figure 5-3: Pole figures for (a) HR340 and (b) HR550. 63
Figure 5-4: Eng. stress vs. Eng. strain (a-b) and change in temperature vs. Eng. strain (c-d) response for HR340 (a-c) and HR550 (b-d). [The legend indicates the strain rate in s^{-1} followed by the test number (e.g., 0.001_1 represent a strain rate of 0.001 s^{-1} for the first test)]. 64
Figure 5-5: Temperature increase at various strain rates, (a) 0.001 s^{-1}, (b) 0.1 s^{-1}, (c) 1 s^{-1}, (d) 10 s^{-1}, and (e) 100 s^{-1} for HR340. 66
Figure 5-6: Temperature increase at various strain rates, (a) 0.001 s^{-1}, (b) 0.1 s^{-1}, (c) 1 s^{-1}, (d) 10 s^{-1}, and (e) 100 s^{-1} for HR550. 66
Figure 5-7: Decomposition of the deformation gradient. 68
Figure 5-8: Comparison between the calibrated and measured stress–strain curves in the tension test at for (a) HR340 and (b) HR550. 82
Figure 5-9: Comparison between the calibrated and measured temperature-strain curves at 100 s^{-1} for (a) HR340 and (b) HR550. 83
Figure 5-10: Model prediction of (a) HR340 and (b) HR550 stress–strain response at various strain rates and compare with experiments. 84
Figure 5-11: Comparison between experiment and CP damage predicted temperature response at (a) 0.001 s^{-1}, (b) 0.1 s^{-1}, (c) 1 s^{-1}, and (d) 10 s^{-1} for HR340. 84
Figure 5-12: Comparison between experiment and CP damage predicted temperature response at (a) 0.001 s^{-1}, (b) 0.1 s^{-1}, (c) 1 s^{-1}, and (d) 10 s^{-1} for HR550. 84
Figure 5-13: Pole figures for HR340 at 0.001 s^{-1} and 100 s^{-1}, (a-c) experimental observations and (b-d) CPDM predictions. 85
Figure 5-14: Evolution of dislocation density and internal temperature rise at different strain rates for (a) HR340 and (b) HR550. 86
Figure 5-15: A comparison of (a) stress–strain response and (b) dislocation density evolution with and without considering internal temperature effect for HR340 and HR550. 87
Figure 5-16: Difference in damage levels at different strain rates in (a)HR340 and (b) HR550.. 88
Figure 5-17: Stress–strain prediction at intermediate strain rate for (a) HR340 and (b) HR550.. 88
Figure 6-1: Flowchart of constitutive model derivation. 95

Figure 6-2: Initial microstructure characterization of DP590 and DP780 steels on the RD–TD section: (a) DP590 inverse pole figure (IPF) map, (b) DP590 phase segmentation map, (c) DP590 phase-wise grain-size histogram, (d) DP780 IPF map, (e) DP780 phase segmentation map, and (f) DP780 phase-wise grain-size histogram. Ferrite is shown in blue and martensite in red in the phase maps. 107
Figure 6-3: Engineering stress–strain response for (a) DP590 and (b) DP780 steel tested in RD and TD under uniaxial tension across various strain rates. [The legend indicates the loading direction (RD or TD) followed by applied strain rate (e.g., RD_0.001 refers to testing in RD at a strain rate of 0.001 s^{-1})]. 108
Figure 6-4: Engineering stress–strain responses of DP590 and DP780 under multiaxial loading at 0.001 s^{-1} for specimens oriented along the RD and TD: (a) plane strain tension and (b) in-plane simple shear. 110
Figure 6-5: Infrared thermal fields showing the temperature increase during uniaxial tensile deformation in the RD: (a–e) DP590 and (f–j) DP780. In each column, the fields correspond to strain rates of 0.001, 0.1, 1, 10, and 100 s^{-1}, respectively. The color scale denotes the temperature rise above the initial test condition. 111
Figure 6-6: Measured temperature rise as a function of engineering strain during uniaxial tensile deformation of (a) DP590 and (b) DP780 at different strain rates. 111
Figure 6-7: Phase specific orientation maps. (a) DP590 ferrite, (b) DP590 martensite, (c) DP780 ferrite, and (d) DP780 martensite. 113
Figure 6-8: Experimental and CPDM-predicted responses for the calibration data set: (a) engineering stress–strain response in the RD for DP590 and DP780 at the selected strain rates, and (b) temperature evolution at 100 s^{-1} for DP590 and DP780. [The legend indicates the DP steel grade (590 or 780) for experimental and CPDM-predicted followed by applied strain rate (e.g., 590_Exp_0.001 refers to DP590 experimental at a strain rate of 0.001 s^{-1})]. 115
Figure 6-9: Experimental and CPDM-predicted engineering stress–strain responses of DP590 and DP780 under uniaxial tension in the RD at multiple strain rates. 117
Figure 6-10: Experimental and CPDM-predicted engineering stress–strain responses of DP590 and DP780 under uniaxial tension in the TD: (a) quasi-static strain rates and (b) intermediate strain rates. 117

Figure 6-11: Experimental and CPDM-predicted stress–strain responses of DP590 and DP780 at 0.001 s^{-1} in the RD and TD under (a) plane strain tension and (b) in-plane simple shear. 118
Figure 6-12: Experimental and CPDM-predicted temperature evolution under uniaxial tension for DP590 and DP780 steels at various strain rates in (a) RD and (b) TD. 119
Figure 6-13: Comparison of experimentally measured and CPDM-predicted bulk pole figures at the final deformed stage after uniaxial tension of DP590 and DP780 at different strain rates. The {100}, {110}, and {111} pole figures are arranged from left to right in each panel. Panels (a–d) show the experimentally measured pole figures, and panels (e–h) show the corresponding CPDM predictions. 120
Figure 6-14: Comparison of experimentally measured and CPDM-predicted bulk pole figures at the final deformed stage under multiaxial loading for DP590 and DP780. Panels (a–d) show the experimentally measured pole figures, and panels (e–h) show the corresponding CPDM predictions for the same loading conditions. 121
Figure 6-15: Relative fractions of the selected BCC texture components obtained from the bulk ODFs of DP590 and DP780. 122
Figure 6-16: Idealized {111} pole figures for the five selected crystallographic texture components used in the parametric study: (a) {112}<110> ; (b) {223}<110>; (c) {111}<110>; (d) {111}<112>; (e) {001}<110>. 123
Figure 6-17: Predicted influence of crystallographic orientation on the uniaxial tensile response of the idealized DP steel microstructure at 0.001 s^{-1}: (a) engineering stress–strain response and (b) damage evolution for the selected texture components. 124
Figure 6-18: Predicted influence of selected crystallographic texture components on tensile response and plastic anisotropy under uniaxial loading in the RD and TD: (a) engineering stress–strain response and (b) Lankford coefficient evaluated at 10% engineering strain. 125
Figure 7-1: Microstructure of QP3Mn from [292]. 151
Figure 7-2: Microstructure of QP980. 151
Figure 7-3: QP3Mn (a) RA and (b) tempered martensite texture. 152
Figure 7-4: QP980 (a) RA, (b) ferrite, and (c) tempered martensite texture. 153
Figure 7-5: Engineering stress–strain responses of QP3Mn and QP980 steels. 154
Figure 7-6: Evolution of retained austenite volume fraction during tensile deformation. 155

Figure 7-7: Comparison of experimental and CPDM predicted response for the calibration data set (a) Eng. stress–strain response at various strain rate for QP3Mn and QP980, (b) Eng. stress–strain response for at various temperature at 0.005 s^{-1} strain rate for QP3Mn, and (c) evolution of RAVF at various conditions. 161
Figure 7-8: Experimental and CPDM-predicted engineering stress–strain response at different strain rates for (a) QP3Mn and (b) QP980. 163
Figure 7-9: Thermomechanical response and internal variable evolution of QP980 at different strain rates: (a) experimental and CPDM predicted temperature rise, (b) predicted retained austenite volume fraction, and (c) predicted normalized damage variable. 164
Figure 7-10: (a) Experimental and CPDM predicted engineering stress–strain response (b) Predicted evolution of RAVF and damage variable for QP3Mn at 40 and 55 °C at a strain rate of 0.0005 s^{-1}. 166
Figure 7-11: Influence of initial RAVF on the tensile response: (a) engineering stress–strain behavior and (b) predicted evolution of RAVF and damage variable. 167

List of Tables

Table 2-1: The typical texture components in bcc materials [65]. 15
Table 2-2: Typical damage initiation sites and dominant damage mechanisms in advanced high-strength steels. 24
Table 5-1: Chemical composition of HSLA 340 and 550 (wt. %). 60
Table 5-2: Summary of DIC system and analysis parameters. 61
Table 5-3: Summary of IR camera system parameters. 62
Table 5-4: Averaged tensile properties of HR340 and HR550 steels across different repeats. 64
Table 5-5: Average of maximum temperature change during tensile testing within the necking region across different repeats. 66
Table 5-6: Material constant for the crystal plasticity model. 81
Table 5-7: List of parameters for HSLA steel. 81
Table 5-8: The calibrated parameters (curve fitting). 82
Table 5-9: Temperatures-dependent parameters. 82
Table 6-1: Chemical composition (wt. %) of as received DP590 and DP780 steels. 105
Table 6-2: Average tensile properties of DP590 and DP780 steels along RD. 109
Table 6-3: Average tensile properties of DP590 and DP780 steels along TD. 109
Table 6-4: Maximum temperature change during tensile testing. 112
Table 6-5: Model parameters for both grades of steel [77,248,257,264]. 113
Table 6-6: Calibrated coefficients for DP590 and DP780 steels. 114
Table 6-7: Relative fractions of selected BCC texture components (in %). 122
Table 7-1: Calibration and validation experimental data set. 157
Table 7-2: Literature coefficients. 159
Table 7-3: Calibrated plasticity and damage coefficients. 159
Table 7-4: Calibrated transformation coefficients. 161
Table 7-5: Characteristic strain measures extracted from the simulated response. 168

1 Introduction

The widespread adoption of electric vehicles has introduced new challenges to automotive structural design. Automakers are required to reduce vehicle mass and improve energy efficiency while simultaneously satisfying increasingly stringent crashworthiness and safety requirements. In electric vehicles, this challenge is intensified by the need to protect large battery systems from intrusion and excessive deformation during crash loading [1,2]. The use of lightweight structural materials remains a proven strategy for addressing these competing requirements. Advanced high-strength steels are particularly attractive for safety-critical automotive components because they provide high strength, useful ductility, manufacturability, and crash-energy absorption while allowing reductions in section thickness [3,4]. However, the complex microstructures that provide these properties also make their deformation and damage evolution difficult to predict under forming and crash-relevant loading conditions.

The mechanical performance of AHSS is governed by the deliberate design of microstructure. High strength low-alloy (HSLA) steels obtain their strength primarily through ferrite grain refinement, precipitation strengthening, and dislocation strengthening, while retaining a comparatively simple ferrite dominated microstructure [5]. Dual-phase (DP) steels achieve a higher strength–ductility balance through the mechanical contrast between a soft ferritic matrix and hard martensitic regions [6,7]. Quenching and partitioning (Q&P) steels introduce an additional level of complexity through the presence of metastable retained austenite, which can transform to martensite during deformation and contribute to transformation-induced plasticity [8,9]. These steels therefore represent a progression of increasing microstructural complexity, from ferrite dominated deformation in HSLA steels, to phase- and interface-controlled deformation in DP steels, to transformation-assisted deformation in Q&P steels.

Despite their advantages, the use of AHSS in forming and crashworthiness applications requires reliable prediction of damage evolution, stress–strain softening, and failure. In this thesis, failure refers to the progressive loss of load-carrying capacity associated with ductile damage evolution, rather than the explicit prediction of crack propagation or fracture surface formation. This distinction is important because the constitutive framework developed in this work is a material-point crystal plasticity damage model. The objective is therefore to represent the internal

degradation processes that govern softening in the stress–strain response, rather than to resolve a geometry dependent crack path.

Ductile damage in metallic materials has traditionally been described through void nucleation, void growth, and void interaction. Classical micromechanical studies established that void growth is strongly affected by stress triaxiality, while later porous plasticity and continuum damage models provided constitutive frameworks for representing damage accumulation and degradation [10–14]. However, AHSS present additional challenges because damage evolution is not controlled by stress state alone. It is also affected by crystallographic orientation, strain rate, temperature, phase contrast, phase-boundary incompatibility, retained-austenite stability, and loading path. As a result, models that reproduce a macroscopic stress–strain response without resolving these internal mechanisms may have limited transferability across steel grades, microstructures, and deformation conditions.

The need for predictive constitutive models has grown significantly as automotive design shifts toward virtual forming, crash simulation, and microstructure-sensitive material design. Phenomenological plasticity and damage models are computationally efficient and are commonly used in engineering simulations, but they often require extensive calibration and have limited ability to represent evolving anisotropy, phase specific deformation, or microstructure-dependent damage. Mechanistic constitutive models provide a more physically grounded alternative. In particular, crystal plasticity offers a suitable framework because it describes plastic deformation through crystallographic slip and can naturally incorporate texture, phase specific properties, dislocation evolution, and orientation-dependent deformation [15–17]. When coupled with damage evolution, crystal plasticity can connect local slip activity and microstructural state variables to the progressive softening observed at the macroscopic scale.

Several significant developments have already been made in crystal plasticity and micromechanical modeling of AHSS. Crystal plasticity finite element and representative volume element methods have clarified the role of ferrite–martensite morphology, strain partitioning, and local phase interactions in DP steels [18–21]. Thermomechanical crystal plasticity models have also improved the prediction of retained-austenite transformation in TRIP-assisted and Q&P steels over different strain rates and temperatures [22–25]. However, these developments often address individual aspects of the problem. Damage evolution, temperature rise, void kinetics, texture effects, interface-sensitive degradation, and retained-austenite transformation are frequently

treated separately or within computationally expensive full-field frameworks. A constitutive framework that can efficiently connect these effects within a crystal plasticity damage model is still lacking for prediction of damage driven softening and failure in AHSS.

This thesis develops a crystal plasticity-based damage modeling strategy for predicting damage evolution, post-necking softening, and failure in AHSS subjected to different strain rates, temperatures, and loading conditions. Rather than applying a single damage law across all steel grades, the work is organized around three material systems with progressively increasing microstructural and constitutive complexity. For HSLA steels, the formulation establishes the baseline coupling among crystallographic slip, dislocation evolution, internal temperature rise, void nucleation, void growth, and damage-induced degradation of the stress response. For DP steels, the constitutive description is reformulated to account for phase specific plasticity, ferrite–martensite mechanical interaction, stress state-sensitive void evolution, texture effects, and interface-driven damage. For Q&P steels, the framework further incorporates retained austenite transformation, thermomechanical loading, evolving phase contrast, and the transition from transformation-assisted hardening to damage-dominated softening. Through this progression, the thesis identifies the constitutive components required as AHSS microstructures become more complex and provides an efficient Taylor-type crystal plasticity route for linking microstructural deformation mechanisms to damage accumulation and failure.

This thesis is structured as follows. Chapter 2 presents the background required for the thesis, including advanced high-strength steels, crystallographic deformation, ductile damage mechanisms, and experimental characterization methods. Chapter 3 reviews constitutive and computational approaches for modeling ductile damage, crystal plasticity-based damage evolution, interface-sensitive damage in multiphase steels, and transformation-coupled damage in Q&P steels. Chapter 4 presents the research scope, objectives, and strategy of the proposed work. Chapters 5, 6, and 7 present the research contributions of this thesis through the HSLA, DP, and Q&P steel studies, respectively. Finally, Chapter 8 summarizes the main conclusions, limitations, and identifies future work required to extend the proposed modeling framework.

2 Background

This chapter presents the background information relevant to the topics investigated in this thesis. It begins with an overview of the advanced high strength steel grades considered in this work, namely high strength low-alloy, dual phase, and quenching and partitioning steels. The chapter then introduces the main microstructural and crystallographic concepts governing their mechanical response, followed by a discussion of ductile damage mechanisms in metallic alloys. An overview of the experimental techniques employed in this study is provided. Finally, the numerical modeling concepts are introduced.

2.1 Advanced High Strength Steels

Advanced high-strength steels (AHSS) have been developed to satisfy the increasing demand for structural materials that provide an improved balance of strength, ductility, crashworthiness, and manufacturability in automotive applications. Their development has been driven by the need to reduce vehicle mass while maintaining or improving occupant safety and structural integrity. Compared with conventional low-strength and high-strength steels, AHSS grades achieve superior combinations of tensile strength and elongation through deliberate control of phase constitution, phase stability, morphology, and crystallographic features [26]. As a result, AHSS grades now capture a central position in automotive body-in-white and safety-critical structural components.

AHSS are commonly classified into first-, second-, and third-generation families according to their microstructural features and the strength–ductility balance they provide. Figure 2-1 displays a schematic comparison of steel classes in terms of tensile strength and elongation, influenced by varying microstructure and phase composition [27]. First-generation AHSS include dual phase (DP), transformation induced plasticity (TRIP), complex-phase (CP), and martensitic steels. These grades rely mainly on multiphase microstructures produced through relatively lean alloying and controlled thermal processing. Second-generation AHSS, such as twinning-induced plasticity (TWIP) and certain austenitic stainless steels, achieve exceptional ductility but typically require high alloying additions and therefore higher cost. Third-generation AHSS are introduced to bridge the gap between these two families by delivering a more favorable compromise between cost, strength, and formability. Quenching and partitioning (Q&P) steels are one of the most representative examples of this third-generation concept [28]. Although high strength low-alloy steels are not always classified as AHSS in the strictest sense, they provide an important baseline

for understanding the evolution from ferrite-dominated steels toward increasingly heterogeneous and mechanically contrasted advanced steel microstructures. For this reason, the present thesis focuses on HSLA, DP, and Q&P steels as three material systems of increasing microstructural and constitutive complexity.

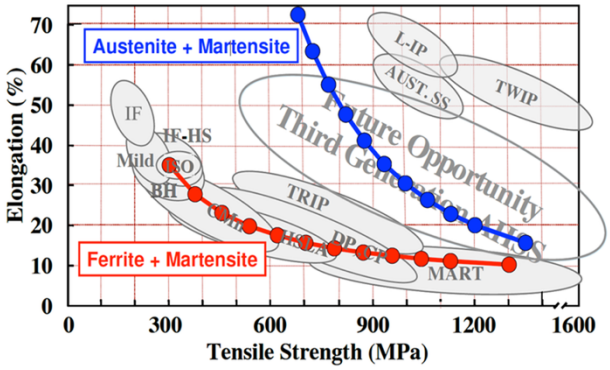


Figure 2-1: Overview of tensile strength vs. uniform elongation for various classes of steel [27].

2.1.1 High Strength Low-Alloy Steel

High-strength low-alloy (HSLA) steels are microalloyed steels developed to provide improved mechanical properties and enhanced atmospheric corrosion resistance compared with conventional carbon steels [29]. Fine ferrite grain size is the primary strengthening mechanism in HSLA steels. These steels typically contain 0.05–0.25 wt. % carbon, together with up to about 2.0 wt. % manganese and small additions of alloying elements such as copper, nickel, niobium, vanadium, titanium, chromium, molybdenum, calcium, rare-earth elements, or zirconium [30]. Elements such as niobium, vanadium, and titanium are particularly effective in improving strength through grain refinement and precipitation strengthening. This microstructural design makes HSLA steels attractive for structural and automotive applications where moderate-to-high strength is needed without the full complexity of multiphase AHSS microstructures [31].

The microstructure of HSLA steels is commonly ferrite-dominated, often with pearlite and a fine dispersion of alloy carbides or carbo-nitrides, as shown in Figure 2-2. This refined microstructure enables HSLA steels to achieve tensile strengths in the range of approximately 250–800 MPa while retaining useful ductility and weldability. Despite these advantages, the achievable strength–ductility combination in HSLA steels remains limited compared with more advanced multiphase steel grades. This limitation has motivated the development of steel families such as dual phase and quenching and partitioning steels, in which phase contrast, retained austenite stability, and

transformation-assisted deformation provide additional opportunities for improved strength and formability.



Figure 2-2: Microstructure of HSLA (the white phase is ferrite, and the black phase is pearlite) [32].

2.1.2 Dual Phase Steel

Dual phase (DP) steels are among the most widely used first-generation advanced high-strength steels for automotive applications because they provide a favorable balance of strength, ductility, and manufacturability at relatively low alloying cost. Their microstructure consists primarily of a soft ferrite matrix containing a harder martensitic phase, usually in the form of islands, clusters, or interconnected regions depending on composition and processing conditions. This ferrite–martensite phase contrast is the defining feature of DP steels and is responsible for their characteristic combination of continuous yielding, high initial work-hardening rate, and good ultimate tensile strength [26,33,34].

DP steels are generally produced by intercritical annealing of a ferrite–pearlite or cold-rolled precursor microstructure in the two-phase ferrite–austenite region, followed by rapid cooling to room temperature as illustrated in Figure 2-3b. During intercritical annealing, part of the microstructure transforms to austenite while ferrite remains stable. Subsequent quenching transforms the carbon-enriched austenite into martensite, thereby generating the final dual phase microstructure. The martensite fraction is mainly controlled by the intercritical annealing temperature, holding time, alloy chemistry, and cooling rate. This relatively simple processing route, together with lean alloying, is one of the reasons for the industrial success of DP steels.

The mechanical behavior of DP steels is governed not only by the presence of ferrite and martensite, but also by the details of their microstructure. The most influential microstructural descriptors are ferrite grain size, martensite volume fraction, martensite morphology, and the

spatial distribution and connectivity of the martensite phase. Reviews of ferritic–martensitic DP steels consistently identify these three primary factors as the dominant variables controlling strength and ductility. In practical terms, increasing martensite fraction generally raises strength, while finer ferrite grain size improves both strength and uniformity of deformation. Martensite morphology, however, plays a more complex role because it affects local strain partitioning, interface stresses, and damage initiation [34].

The crystallographic and micromechanical response of DP steels is also inherently heterogeneous. During deformation, the ferrite matrix accommodates most of the plastic strain at early stages, while martensite acts as a strong constraint. This mismatch in phase strength produces strain partitioning, geometrically necessary dislocation accumulation, back-stress hardening, and local stress concentration near ferrite–martensite interfaces. These effects are beneficial for work hardening, but they also make DP steels particularly sensitive to void nucleation through interface decohesion, martensite cracking, and highly localized plasticity in ferrite. For this reason, DP steels provide an especially useful material system for studying the coupling between microstructure, stress state, strain rate, and damage evolution [35].

Texture also influences the response of DP steels, although its role is often coupled with morphology and processing history. Ferrite typically retains body-centered cubic rolling and annealing textures, and the balance between α-fiber and γ-fiber components affects anisotropy, drawability, and local phase interaction. In more recent high-ductility DP grades, microalloying and processing refinements have been used not only to control grain size and precipitates, but also to improve phase homogeneity and texture development. These aspects become important when interpreting orientation-dependent deformation and the anisotropic progression of damage [36].

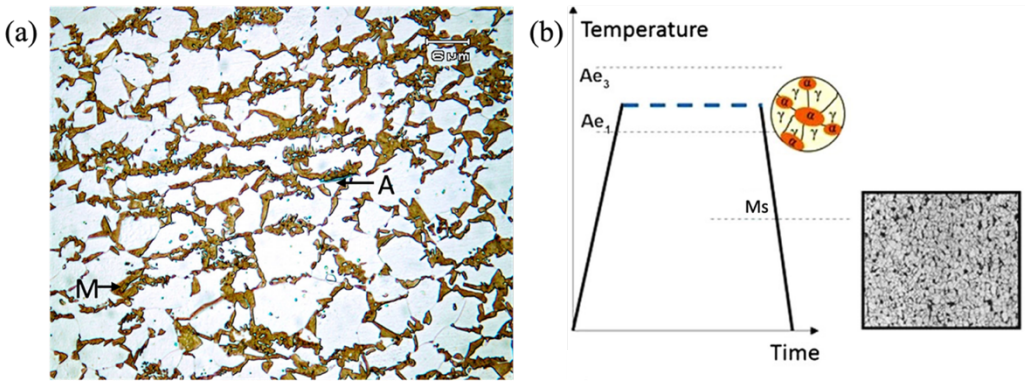


Figure 2-3: (a) Microstructure of DP steels quenched from 775 ℃ [37] and (b) Schematic schedule for the annealing process of DP steels [26].

Within the present thesis, DP steels occupy an intermediate position between HSLA and Q&P steels. Compared with HSLA steels, they introduce a much stronger phase contrast and a more heterogeneous local deformation field. Compared with Q&P steels, they do not involve retained-austenite transformation, which makes them well suited for isolating the role of phase morphology, strain partitioning, and stress-state effects on damage evolution. For this reason, DP steels provide a central platform for developing and evaluating crystal plasticity-based damage indicators under varying loading paths and strain rates.

2.1.3 Quenching and Partitioning Steel

Quenching and partitioning (Q&P) steels are widely regarded as representative third-generation advanced high-strength steels developed to achieve a strength–ductility balance intermediate between first- and second-generation AHSS at a comparatively moderate alloying cost [38,39]. The central concept of the Q&P process is to stabilize a controlled fraction of retained austenite in a predominantly martensitic microstructure so that the retained austenite can contribute to strain hardening during deformation through the transformation induced plasticity effect [8,40]. The combination of high strength, useful ductility, and enhanced strain-hardening capacity has made Q&P steels attractive for automotive structural applications [39,41].

The Q&P concept was first proposed by Speer and co-workers as a heat-treatment route in which steel is quenched to a temperature between the martensite-start temperature, M_s, and the martensite-finish temperature, M_f, so that only part of the austenite transforms to primary martensite [8]. The remaining untransformed austenite is then enriched in carbon during a subsequent partitioning step, during which carbon redistributes from the supersaturated martensite into the retained austenite [8,40]. After partitioning, the enriched austenite may remain stable to room temperature and be retained in the final microstructure [40,42]. Depending on the process design, partitioning may be performed at the quench temperature itself, often referred to as one-step Q&P, or at a higher partitioning temperature, referred to as two-step Q&P [28,40].

The final microstructure produced by Q&P processing commonly contains tempered or partitioned martensite together with retained austenite, and may also include ferrite or bainitic constituents depending on the alloy composition and thermal path. Figure 2-4 shows the typical microstructure of QP steels, which is composed of (F), tempered martensite (TM), and retained austenite (RA). The mechanical response of Q&P steels depends strongly on both the amount and the stability of retained austenite [41,43]. If the retained austenite is insufficiently stable, it transforms too early

during deformation and its contribution to sustained work hardening is reduced. If it is overly stable, the transformation-assisted contribution is delayed or diminished, and the benefit of the TRIP effect is not fully utilized. The optimum response is therefore obtained when the retained austenite exhibits an intermediate stability that allows progressive transformation over a broad strain range [41,43].

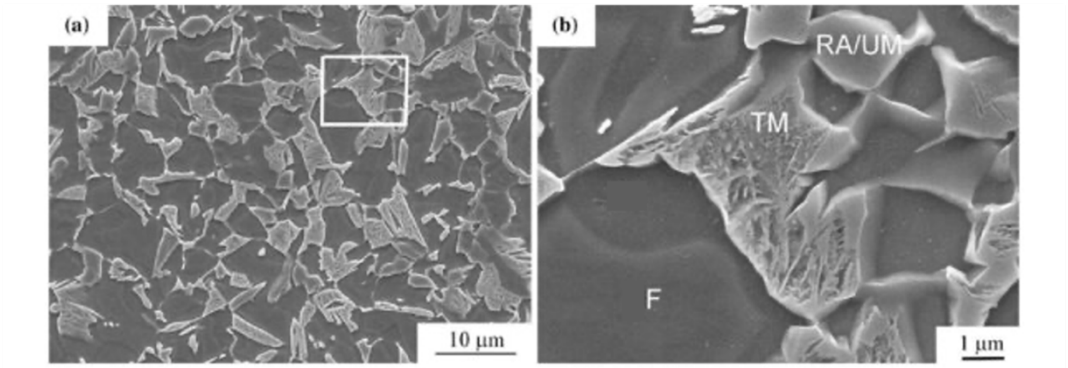


Figure 2-4: Example QP steel microstructure. The square in (a) is enlarged in (b) [44].

Austenite stabilization in Q&P steels is achieved primarily through carbon enrichment during the partitioning stage [40,45]. For this reason, the quench temperature plays a critical role because it determines the initial fraction of primary martensite and the amount of remaining austenite available for subsequent enrichment. The concept of an optimum quenching temperature was introduced to identify the quench temperature that maximizes the retained-austenite fraction after partitioning under the assumptions of the original constrained carbon equilibrium framework [45,46]. In practice, however, the optimum condition depends not only on thermodynamic considerations but also on the kinetics of competing reactions and the actual processing schedule [42,46].

One of the main complexities of the Q&P process is that carbon partitioning rarely occurs in isolation [42,47]. Competing reactions such as carbide precipitation, bainitic transformation, and partial decomposition of austenite can occur during partitioning and reduce the amount or stability of retained austenite at room temperature [48]. Experimental studies have shown that carbide precipitation may occur within martensite during partitioning, thereby consuming carbon that would otherwise stabilize austenite. Likewise, bainitic transformation can enrich the remaining austenite in carbon, but it also alters the final phase constitution and complicates the interpretation of partitioning behavior [47,49]. As a result, the final Q&P microstructure must be understood as

the product of interacting partitioning and transformation processes rather than as the consequence of carbon redistribution alone [42,47,49].

Alloying additions are therefore selected carefully in Q&P steels to promote austenite stabilization while suppressing undesirable competing reactions [40,47]. Silicon is commonly added because it delays or suppresses cementite formation and thereby preserves more carbon for enrichment of retained austenite [50]. Aluminum may also be used for a similar purpose, although its metallurgical and processing implications differ from those of silicon [50]. Manganese plays an additional role by increasing austenite stability and shifting transformation behavior, which is beneficial for retained-austenite retention in the final microstructure [40,41]. Through suitable alloy design and process selection, Q&P steels can therefore be tailored to achieve a desirable combination of martensite fraction, retained-austenite morphology, and retained-austenite stability. The Q&P thermal path and associated phase changes are summarized in Figure 2-5, showing how quenching, partitioning, carbon redistribution, and retained-austenite stabilization are linked during processing.

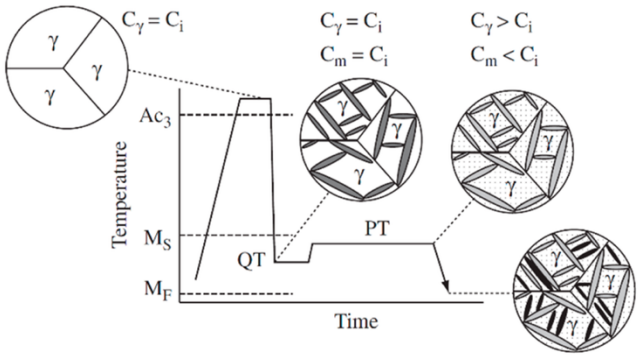


Figure 2-5: Schematic illustration of the Q&P process along with schematic microstructure evolution during different intermediate steps [51].

Within the present thesis, Q&P steels represent the most complex of the three steel systems considered because their deformation behavior depends not only on phase contrast and strain partitioning, but also on the stability and transformation of retained austenite. This introduces an additional coupling among microstructure, stress state, strain rate, temperature, and damage evolution that is not present in the same form in HSLA or DP steels. For this reason, Q&P steels provide the most demanding material system for extending the crystal-plasticity-based framework of this thesis toward transformation-assisted deformation and damage in advanced steels.

2.2 Microstructural and Crystallographic Foundations

Microstructure plays a central role in governing the deformation, damage evolution, and failure response of advanced high-strength steels. Even for similar chemical compositions, differences in phase constitution, grain size, crystallographic orientation, and phase morphology can lead to substantial changes in mechanical behavior. In steels such as HSLA, DP, and Q&P grades, these microstructural features determine not only the overall strength and ductility, but also the extent of strain partitioning, transformation behavior, and damage localization. This section therefore introduces the crystallographic and microstructural concepts most relevant to this dissertation, including crystal structure, dislocations and crystallographic slip, and crystallographic orientation and texture.

2.2.1 Crystal Structure

Metals are composed of aggregates of grains, each of which is an individual crystal. The smallest repeating arrangement of atoms that fully describes the atomic positions and symmetry of a crystal lattice is referred to as the unit cell. For a given type of unit cell, various arrangements of atoms are possible: body-centered cubic (BCC), face-centered cubic (FCC), hexagonal close-packed (HCP), or body-centered tetragonal (BCT). A schematic representation of these unit cells is shown in Figure 2-6. Ferrite possesses a BCC crystal structure, whereas austenite has an FCC crystal structure. Martensite forms from austenite through a transformation and is commonly described as a BCT phase because the interstitial carbon atoms distort the cubic lattice and introduce tetragonality [3].

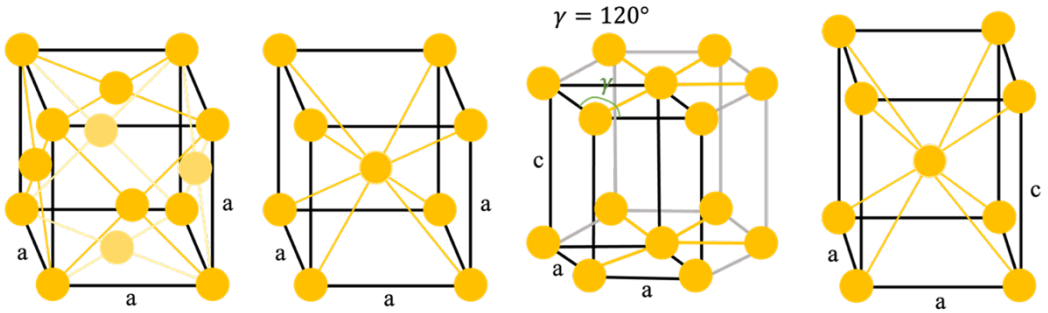


Figure 2-6: Schematic crystal lattice unit cells.

These crystal structures are directly relevant to the microstructures of advanced high-strength steels. Dual phase steels consist primarily of a BCC ferritic matrix together with carbon-enriched martensite, which is generally treated as BCT in the as-quenched condition [34]. Quenching and

partitioning steels typically contain ferrite, martensite, and retained austenite, where retained austenite is FCC and the martensitic constituent may be present as fresh martensite or as tempered/partitioned martensite depending on the thermal path [52]. In low-carbon steels and in tempered martensitic conditions, the tetragonality of martensite decreases and the structure is often approximated as BCC for practical analysis [53].

The crystal structure of each phase strongly influences deformation behavior because it governs atomic packing, slip-system activity, carbon solubility, and transformation characteristics. Consequently, the mechanical response of HSLA, DP, and Q&P steels depends not only on phase fraction, but also on the crystallographic nature of ferrite, martensite, and retained austenite.

2.2.2 Dislocations and Slip Systems

Plastic deformation in crystalline metals occurs primarily through the motion of dislocations, which are line defects in an otherwise ordered crystal lattice [54]. Dislocations are commonly classified as edge, screw, or mixed. This classification is based on the orientation of the dislocation line relative to the Burgers vector, $\boldsymbol{b}$, which defines the magnitude and direction of the lattice distortion. An edge dislocation may be visualized as the insertion of an extra half-plane of atoms into the lattice. In this case, the Burgers vector is perpendicular to the dislocation. A screw dislocation corresponds to a helical mismatch produced by relative shear of the crystal planes. Most dislocations in real materials exhibit mixed character, with both edge and screw components present along different segments of the line [54]. These different dislocation configurations are illustrated schematically in Figure 2-7.

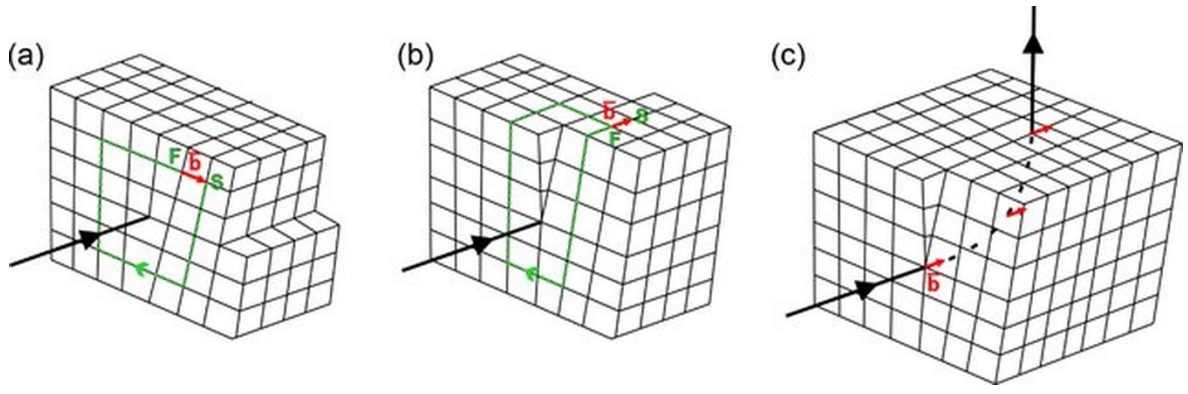


Figure 2-7: Illustration of different dislocation types in a crystal [55].

The collective motion of dislocations gives rise to crystallographic slip, which is the dominant plastic deformation mechanism in ferritic and austenitic steels under most loading conditions [56]. Slip occurs preferentially along specific crystallographic planes and directions that together define

the slip systems of the phase. In FCC phases such as austenite, the dominant slip family is {111}⟨110⟩, which provides 12 equivalent slip systems and contributes to the relatively high ductility of the phase [52,56]. In BCC phases such as ferrite, slip occurs predominantly along ⟨111⟩ directions on the {110}, {112}, and {123} plane families, although the relative activity of these families depends on crystal orientation, temperature, and loading conditions [57,58]. A schematic representation of the principal BCC slip planes and directions is shown in Figure 2-8. In practical constitutive descriptions of advanced high-strength steels, ferrite and low-carbon martensite are therefore often represented using BCC slip families, whereas retained austenite is described using FCC slip systems [52].

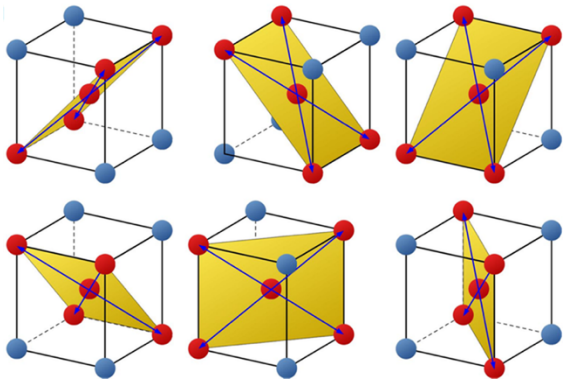


Figure 2-8: BCC slip planes and directions [59].

The onset of slip on a given system is commonly described using Schmid's law, which relates the applied stress state to the resolved shear stress acting on a slip plane and slip direction. Slip is activated when the resolved shear stress reaches a critical value, commonly referred to as the critical resolved shear stress (CRSS). For FCC metals, slip activation is generally well described by Schmid's law, whereas BCC metals often exhibit deviations because of the non-planar core structure and limited mobility of screw dislocations [56,58].

In ferritic steels, plastic flow is strongly influenced by the motion of 1/2⟨111⟩ screw dislocations, whose non-planar cores lead to temperature sensitivity, tension–compression asymmetry, and non-Schmid effects [57,58,60]. As a result, slip activity in ferritic steels cannot always be interpreted solely based on the maximum resolved shear stress [57]. In multiphase steels such as DP and Q&P grades, the different slip characteristics of ferrite, martensite, and retained austenite contribute directly to strain partitioning, local stress concentration, and the heterogeneous evolution of damage during deformation [61].

2.2.3 Crystallographic Orientation and Texture

The mechanical response of polycrystalline steels depends not only on phase constitution and grain size, but also on the crystallographic orientation of the grains. When the orientations are not random, the material is said to exhibit crystallographic texture. Texture influences yielding, plastic anisotropy, strain localization, and formability because grains deform more easily when their slip systems are favorably aligned with the applied stress [62,63]. In advanced high-strength steels, texture also affects strain partitioning between phases and therefore contributes indirectly to damage evolution.

Crystallographic orientation is commonly represented using Euler angles, pole figures (PFs), inverse pole figures (IPFs), and the orientation distribution function (ODF). A pole figure is a stereographic projection that shows the distribution of selected crystallographic plane normals with respect to the sample reference frame [64]. An inverse pole figure presents the orientation of a chosen sample direction, such as the rolling direction or normal direction, in the crystal reference frame [63,65]. The ODF provides a more complete description of texture because it represents the distribution of crystal orientations in Euler space. For cubic materials, textures are often visualized in reduced Euler space or by using selected sections of the ODF.

In body-centered cubic steels, texture is commonly described in terms of fiber textures. The most important are the α-fiber, defined by ⟨110⟩∥RD, and the γ-fiber, defined by {111}∥ND [62,66]. These fibers are especially relevant in ferritic steels because they influence plastic anisotropy and sheet formability. Typical BCC texture fibers and representative Euler-angle ranges are summarized in Table 2-1, while their locations on the $\phi_2 = 45°$ section are illustrated schematically in Figure 2-9. The γ-fiber is generally associated with improved deep drawability, whereas strong α-fiber components are often linked to reduced formability and stronger directional dependence of deformation [66].

Texture development in steels is strongly affected by thermomechanical processing. Rolling, annealing, and phase transformation modify the orientation distribution and may also introduce through-thickness texture gradients [65]. In dual phase steels, ferrite typically retains the dominant BCC texture, while the morphology and distribution of martensite further modify the anisotropic response [62,66]. In quenching and partitioning steels, the presence of retained austenite introduces an additional crystallographic contribution because the FCC austenite phase deforms and transforms differently from the surrounding martensitic matrix. For these reasons, texture must be

considered together with phase constitution and morphology when interpreting the deformation behavior of advanced steels.

Table 2-1: The typical texture components in bcc materials [65].

Texture fiber	Crystallographic definition	Euler angles
α-fiber	<110>//RD	0°,0°,45° - 0°,90°,45°
γ-fiber	<111>//ND	60°,54.7°,45° - 90°,54.7°,45°
η-fiber	<100>//RD	0°,0°,0° - 0°,45°,0°
ε-fiber	<110>//TD	90°,0°,45° - 90°,90°,45°

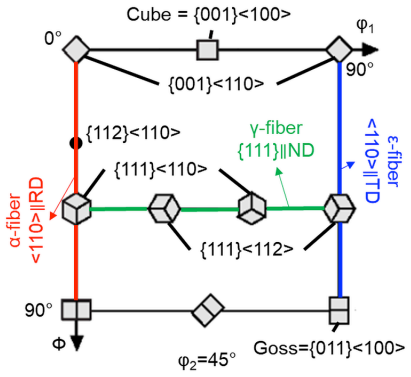


Figure 2-9: Representative BCC texture fibers and associated Euler-angle ranges [67].

2.2.4 Phase Fraction, Morphology, and Interface Characteristics

In AHSS, the mechanical response depends not only on crystal structure, slip activity, and texture, but also on the spatial arrangement of the phases [6,34]. In multiphase steels, deformation is inherently heterogeneous because the hard and soft phases do not carry load in the same manner. For this reason, phase fraction, phase morphology, and interface characteristics are important microstructural descriptors when interpreting deformation and damage in such materials [34,36].

The phase fraction strongly affects the balance between strength and ductility. In dual phase steels, increasing the martensite fraction generally increases the strength because a larger portion of the microstructure is occupied by the harder phase. At the same time, a higher martensite fraction promotes stronger local stress and strain partitioning, which increases deformation heterogeneity [35,36,68]. As a result, phase fraction influences not only the macroscopic flow behavior, but also the extent of localization that develops during deformation [35,36].

The morphology and topology of the hard phase are equally important. Martensite may appear as isolated islands, elongated regions, banded structures, or partially connected networks depending

on the processing route [34,36]. These different morphologies alter how the ferrite matrix is constrained during deformation. A microstructure containing isolated martensite islands does not deform in the same way as one containing connected or chain-like martensite regions [35,68]. Changes in martensite morphology and distribution have been shown to modify strain partitioning, strain hardening, and the preferred microscale failure mechanisms in dual phase steels [69]. A representative multiphase microstructure showing phase distribution and phase boundaries is presented in Figure 2-10.

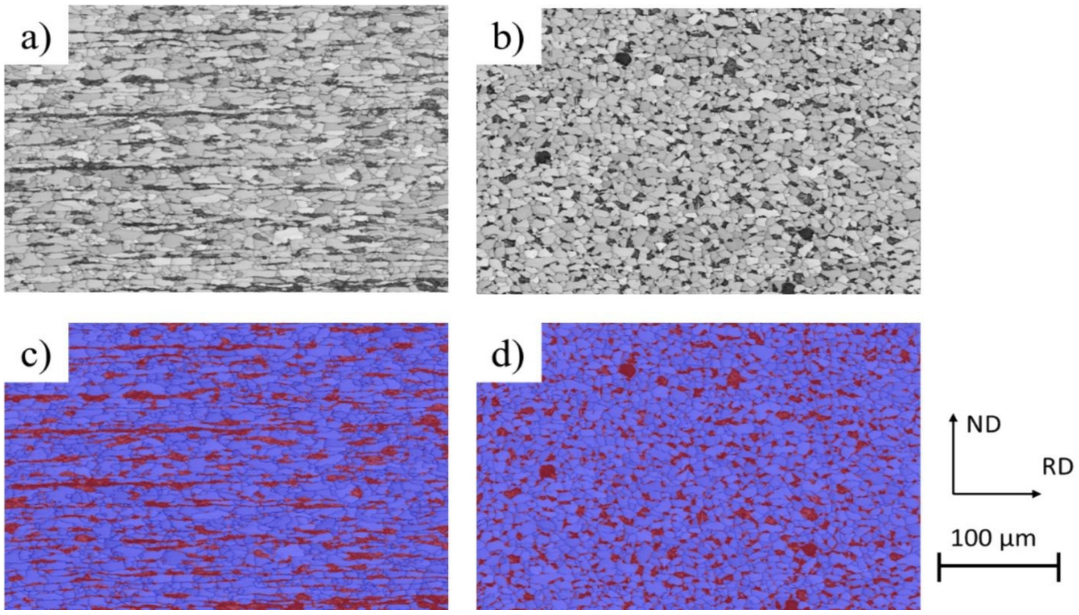


Figure 2-10: Representative microstructure of (a) SN – DP and (b) BM – DP steel showing the ferrite matrix (light grey) and martensite regions (dark grey) [69].

The interface characteristics between neighboring phases also plays a crucial role. In dual phase steels, ferrite–martensite interfaces are regions of mechanical mismatch because the adjacent phases differ strongly in strength and deformation mode [20]. These interfaces are natural sites of load transfer and strain incompatibility [20]. As deformation proceeds, local stress concentration can develop near the interfaces, and this contributes to highly non-uniform strain evolution in the surrounding microstructure [6]. For this reason, interface density and interface morphology are useful descriptors when describing the onset of localization and the early stages of damage development in multiphase steels [20].

2.3 Ductile Damage in Metallic Alloys

Ductile damage is a fundamental failure mechanism in metallic alloys. It is generally characterized by the nucleation, growth, and coalescence of microscopic voids. During the growth stage, voids

may also undergo shape evolution in response to the applied stress state and the plastic flow field. The evolution of these voids is governed by microstructural heterogeneity, including phase morphology, inclusion distribution, and the mechanical contrast between neighboring phases. At the microscale, plastic deformation leads to dislocation motion and accumulation, which generate local stress concentrations around inclusions, second-phase particles, and phase boundaries. These stress concentrations promote the initiation of microscopic cavities. As deformation proceeds, the voids enlarge under the combined action of plastic straining and hydrostatic stress, and eventually undergo shape change and coalescence. The progressive development of this internal damage reduces the load-carrying capacity of the material and ultimately leads to fracture. In advanced high-strength steels such as DP and Q&P grades, the heterogeneous multiphase microstructure makes the damage process more complex. The main mechanisms governing ductile damage are discussed in the following subsections.

2.3.1 Void Nucleation

Void nucleation is the first stage of ductile damage evolution. It plays a critical role in determining the onset of material degradation and the subsequent fracture response of advanced steels. In multiphase steels, void nucleation is highly heterogeneous because the microstructure contains phases with very different mechanical properties. In dual phase and transformation-assisted steels, the hard martensitic or bainitic regions are embedded in a softer ferritic matrix. This phase contrast promotes local stress concentration and strain incompatibility, which make void nucleation strongly dependent on the local microstructural arrangement and loading condition [11,34].

In classical ductile failure theories, void nucleation is commonly associated with the fracture of second-phase particles or with debonding at particle–matrix interfaces [70]. In advanced high-strength steels, however, the nucleation process is more complex. Several competing mechanisms may operate, including ferrite–martensite interface decohesion, cracking of brittle martensite, and debonding at inclusions or other heterogeneities [11,34]. The active mechanism depends on the local stress state, the morphology and distribution of the hard phase, and the strength of the surrounding interfaces.

In dual phase steels, the ferrite–martensite interface is widely recognized as a preferential site for damage initiation because it accommodates strong gradients in stress and plastic strain [6,34]. Experimental observations have shown that early voids may nucleate either by cracking of martensite or by decohesion of the ferrite–martensite interface. Martensite cracking is often

observed at relatively low strains in regions subjected to high tensile stress, where the hard phase cannot accommodate the imposed deformation [71]. As deformation proceeds, interfacial decohesion becomes increasingly important because the surrounding ferrite undergoes continued plastic flow, which intensifies strain incompatibility and promotes debonding along phase boundaries [20,71]. These two mechanisms are often found to coexist, although their relative importance varies with the microstructure and stress state.

The morphology of the martensitic phase also has a strong influence on the preferred nucleation path. Coarse or blocky martensite promotes early cracking because the local constraint is higher, and the phase is less able to distribute the deformation uniformly [72]. In contrast, finer and more uniformly dispersed martensite delays damage initiation and generally improves ductility [72]. In-situ observations further show that the dominant nucleation mode may vary with position relative to the fracture surface. Interface decohesion is often more prominent close to the fracture region, whereas martensite cracking and strain localization in ferrite may dominate farther away [20]. These findings indicate that void nucleation in advanced steels is not governed by a single mechanism, but by the competition between several microscale processes. Figure 2-11 shows representative micrographs of two common nucleation mechanisms in dual phase steel, namely ferrite–martensite interface decohesion and martensite cracking.

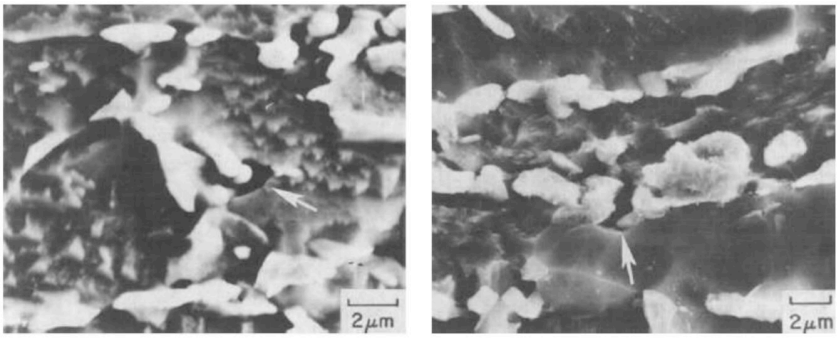


Figure 2-11: SEM images of the nucleation mechanisms in DP steel (a) decohesion of ferrite/martensite interface and (b) fracture of martensite islands.

2.3.2 Void Growth

Once voids are nucleated, their subsequent growth controls the progression of internal damage toward failure. Void growth occurs through continued plastic deformation of the surrounding matrix. As the material deforms, the matrix around the cavity flows plastically and the cavity expands. This process is strongly enhanced when plastic straining is accompanied by tensile

hydrostatic stress [10]. Under such conditions, the material surrounding the void is subjected not only to shear-driven plastic flow, but also to a dilatational tendency that promotes cavity enlargement [10].

The importance of hydrostatic stress in void growth has long been recognized in classical micromechanics. Rice and Tracey showed that void enlargement increases rapidly with increasing stress triaxiality, which explains why tensile loading paths are generally more damaging than shear-dominated ones [10]. In physical terms, a higher hydrostatic tensile stress lowers the resistance of the surrounding matrix to volumetric expansion. The void therefore grows more readily even when the equivalent plastic strain is similar [10]. Void growth is thus not controlled by plastic strain alone. It depends on the combined action of plastic flow and the local stress state.

In steels, void growth is further influenced by the surrounding microstructure. The matrix is not uniform, and the neighboring phases do not deform equally. In dual phase steels, for example, the ferrite matrix accommodates most of the plastic strain, while martensite acts as a local constraint. As a result, voids located in highly strained ferrite regions can grow more rapidly than voids embedded in more constrained regions [73,74]. The growth rate therefore varies from one cavity to another depending on the local phase arrangement, the distance to neighboring hard regions, and the stress concentration developed during deformation [73].

Tomography-based observations confirm that void growth in dual phase steels is highly heterogeneous. In situ X-ray microtomography studies have shown that some cavities begin to enlarge at relatively early stages of deformation, whereas others remain small until deformation becomes strongly localized [73]. These observations indicate that void growth is a local process governed by the microstructural environment of each cavity rather than by a single average material response [73,74]. This is particularly important in advanced high-strength steels, where the contrast in strength between neighboring phases amplifies strain partitioning and promotes non-uniform cavity evolution.

Another important feature of void growth is that it gradually increases the level of damage even before any final instability develops. The growing cavity reduces the effective load-bearing area of the material and intensifies the local plastic strain field in the surrounding matrix [10,73]. As deformation proceeds, neighboring cavities may begin to interact through their surrounding plastic zones. This interaction marks the transition toward more advanced stages of damage, which are discussed later in relation to void shape evolution and subsequent failure development. At the

growth stage itself, however, the main point is that cavity enlargement is driven by plastic flow, accelerated by hydrostatic tension, and strongly modulated by the local multiphase microstructure [10,73]. The strain-dependent progression of void growth is illustrated in Figure 2-12, where the in-situ SEM micrographs show that initially limited damage becomes more visible as tensile strain increases from 0 to 0.5.

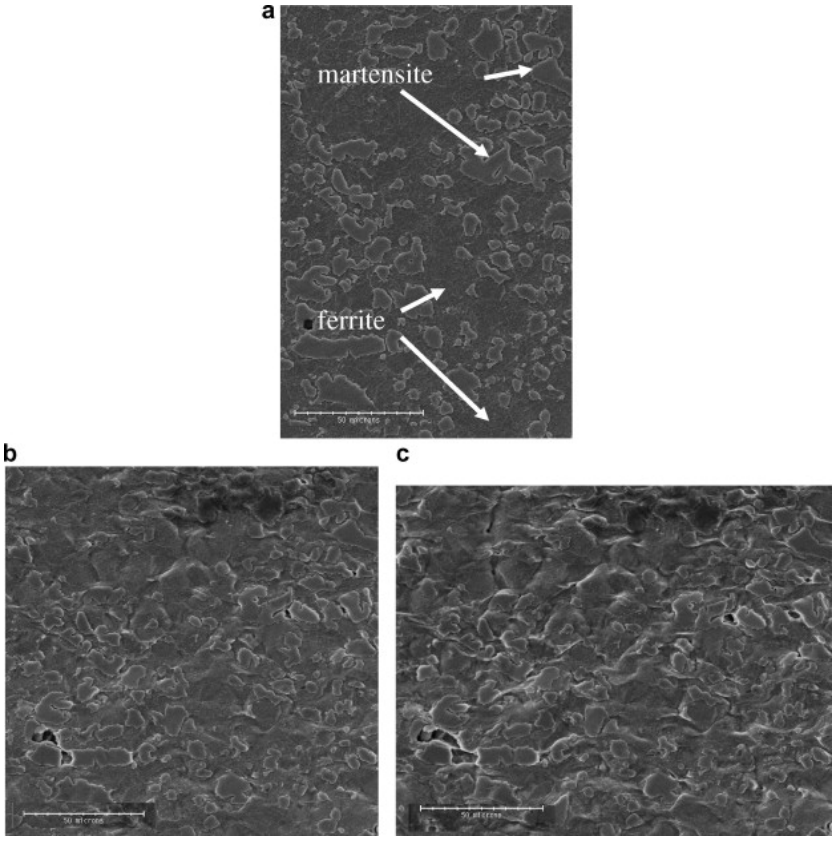


Figure 2-12: SEM micrographs of the DP steel during the in situ tensile test at strains equal to 0, 0.25, and 0.5 [73].

2.3.3 Void Shape Evolution

Void shape evolution is a distinct stage of damage development. Once a cavity has nucleated and begun to grow, its geometry no longer remains unchanged. Instead, the void evolves in response to the surrounding plastic flow and the local stress state [74,75]. This change in geometry is important because the shape of a void influences the local stress concentration around it and therefore affects the subsequent progression of damage [74,76].

Under uniaxial tensile loading, voids tend to elongate along the loading direction [75,77]. This occurs because plastic flow in the surrounding matrix is directionally biased, so the cavity expands more rapidly along the principal tensile axis than in the transverse directions [75,77]. In dual phase

steels, this tendency is further influenced by the local arrangement of ferrite and martensite. Cavities embedded in highly strained ferrite regions can develop pronounced elongation, whereas those near hard martensitic regions may evolve differently because the neighboring phase constrains the surrounding plastic deformation [76,78].

The shape evolution of a void is commonly described using quantities such as aspect ratio and orientation [77,78]. The aspect ratio represents the ratio of the major to the minor void dimensions and provides a simple measure of how far the cavity departs from an equiaxed shape [77]. Experimental observations on advanced steels have shown that the aspect ratio of individual voids often increases during tensile straining because the cavities extend in the loading direction [75,77]. At the same time, the orientation of the major axis may evolve as the local deformation field changes, especially when the void is influenced by nearby phase boundaries, shear flow lines, or neighboring cavities [77,78].

Void shape evolution is not controlled by plastic strain alone. It is also sensitive to the stress state. At relatively low stress triaxiality, cavities tend to develop a more elongated geometry because directional plastic flow dominates [10]. As triaxiality increases, the cavity expansion becomes more dilatational, and the void may evolve toward a more equiaxed or isotropic shape [75]. In other words, the same void can exhibit different shape-evolution paths depending on whether the deformation is dominated by directional stretching or by nearly volumetric tensile expansion [10]. This transition is particularly relevant in tensile tests where necking gradually raises the local triaxiality [75].

In advanced high-strength steels, void shape evolution is also influenced by the nucleation mechanism. Cavities formed by ferrite–martensite interface decohesion do not necessarily evolve in the same manner as cavities originating from martensite cracking [78]. Recent tomography studies on dual phase steels have shown that microvoids associated with martensitic cracking can exhibit a more shear-dominated shape development, whereas other voids follow a more classical tension-driven evolution [75]. This highlights that void shape evolution is not a purely geometric consequence of loading but also retains a strong memory of the local microstructural origin of the cavity [75]. The corresponding change in cavity geometry is shown in Figure 2-13, highlighting how voids evolve from relatively compact features toward elongated morphologies during tensile deformation.

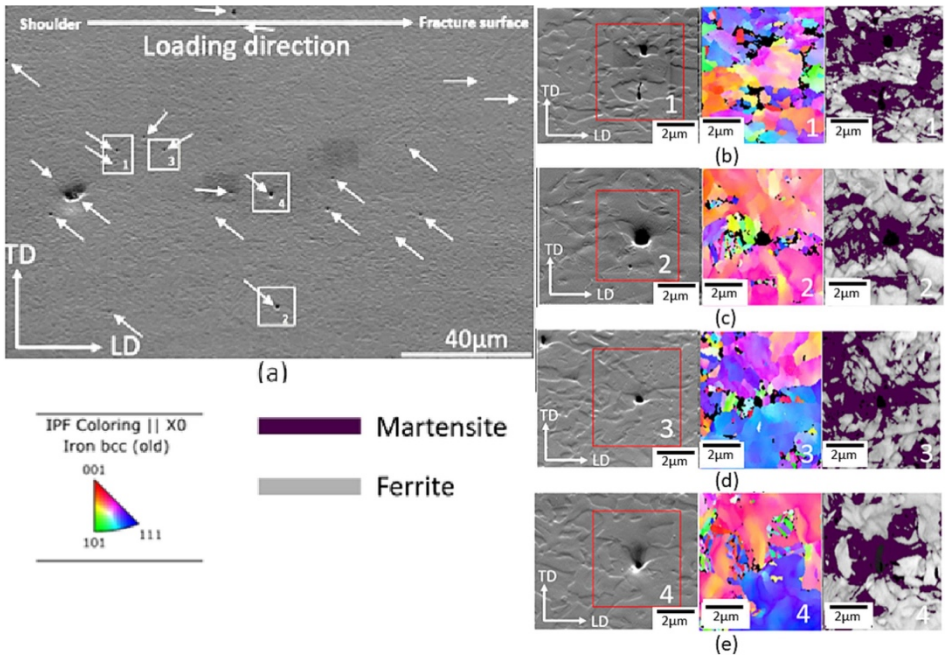


Figure 2-13: Evolution of void morphology during tensile deformation of dual phase steel observed by in situ X-ray computed tomography [75].

2.3.4 Stress State Dependence of Ductile Damage

Ductile damage is strongly dependent on the local stress state. In metallic materials, the stress state is commonly described using stress triaxiality and a parameter related to the third invariant of the deviatoric stress, often expressed through the Lode angle or Lode parameter [14,79,80]. Stress triaxiality represents the ratio of the mean stress to the equivalent stress. It quantifies the relative contribution of hydrostatic tension to the local deformation state [79]. The Lode parameter distinguishes between different deviatoric loading modes, even when the stress triaxiality is similar [14,80]. These two quantities together provide a more complete description of the mechanical conditions governing damage evolution.

The influence of stress triaxiality on ductile damage has been established through both experiments and micromechanical analyses. Higher triaxiality promotes void enlargement because the surrounding matrix is subjected to stronger hydrostatic tension [10,79]. Under such conditions, damage develops mainly through void growth and interaction. At lower triaxiality, the hydrostatic contribution is reduced, and the material can sustain larger plastic deformation before failure [79]. When the stress state approaches shear-dominated conditions, the damage process changes character and may no longer be governed primarily by classical tension-driven void growth [79,80].

Stress triaxiality alone is not sufficient to describe the full stress-state dependence of ductile damage. The Lode parameter also affects the deformation mode and the path by which damage develops, especially at low and moderate triaxialities [80]. The Lode parameter affects the mode of plastic localization, the rate of void growth, and the subsequent path toward failure [14]. At high triaxiality, the influence of the Lode parameter becomes less pronounced because the damage process is dominated by hydrostatic tension [80]. At low and intermediate triaxiality, however, different Lode states may lead to very different damage responses even when the triaxiality is similar [14,80].

This distinction is especially important for sheet metals subjected to different loading paths. Uniaxial tension, plane-strain tension, biaxial stretching, and simple shear do not produce the same combination of triaxiality and Lode parameter. As a result, they do not activate damage in the same way [14,79,80]. Uniaxial and plane-strain tension usually promote tensile damage development, whereas shear-dominated loading may favor intense local plastic flow and a different mode of failure initiation [80]. In advanced high-strength steels, this effect becomes more pronounced because the heterogeneous microstructure introduces additional local stress and strain gradients [81]. This is one of the main reasons why damage modeling for AHSS must account explicitly for stress-state effects. It is not sufficient to describe damage evolution only as a function of accumulated plastic strain.

2.3.5 Damage Mechanisms in AHSS

The damage mechanisms operating in advanced high-strength steels depend strongly on phase constitution, phase morphology, and interface characteristics. Although void nucleation, growth, and shape evolution remain the fundamental stages of ductile damage, the dominant local mechanism varies from one steel class to another. This variation arises because HSLA, DP, and Q&P steels differ in phase contrast, spatial phase distribution, and deformation compatibility between neighboring constituents [34,82,83]. Table 2-2 summarizes the typical damage initiation sites and dominant damage mechanisms in these three steel families.

In HSLA steels, damage is usually associated with inclusions, second-phase particles, and particle–matrix interfaces. Since the matrix is comparatively more uniform than in multiphase AHSS, damage development often follows the classical sequence of particle cracking or debonding, followed by void growth in the surrounding ferritic matrix [84]. The details still depend on

microstructural features such as inclusion population and pearlite morphology, but the governing mechanisms are generally less complex than in steels with strong phase contrast [84].

In DP steels, the damage process is more heterogeneous because the soft ferrite matrix deforms together with a much harder martensitic phase. Two mechanisms are repeatedly reported as dominant: ferrite–martensite interface decohesion and martensite cracking [82,85]. Their relative importance depends strongly on martensite volume fraction, martensite morphology, and local stress state. At lower martensite fractions, interface decohesion is often dominant, whereas at higher martensite fractions or in highly constrained regions, cracking of martensite becomes more prominent [82].

In Q&P steels, the damage process is further complicated by the presence of retained austenite and by the evolving mechanical contrast between phases during deformation. When the microstructural architecture is favorable, metastable retained austenite can improve damage tolerance by delaying localization and enhancing crack-growth resistance through transformation-assisted plasticity [86,87]. However, damage resistance remains sensitive to the local microstructure. Fresh martensite, hard segregated regions, boundary carbides, and unfavorable phase arrangements can promote early cracking and reduce deformation compatibility [86,88]. The governing mechanisms in Q&P steels therefore depend not only on phase contrast, but also on retained-austenite morphology, phase stability, and the matrix condition surrounding the retained austenite [86–88].

Table 2-2: Typical damage initiation sites and dominant damage mechanisms in advanced high-strength steels.

Steel class	**Typical microstructural features**	**Common damage initiation sites**	**Dominant damage mechanisms**
HSLA	Ferrite-dominated microstructure with inclusions, pearlite, and second-phase particles	Inclusions, particles, particle–matrix interfaces	Particle cracking, interface debonding, classical void growth in ferritic matrix
DP	Ferrite matrix with martensite islands or networks	Ferrite–martensite interfaces, martensite regions, highly strained ferrite	Interface decohesion, martensite cracking, localized ferrite damage
Q&P	Martensitic matrix with retained austenite and possible ferrite/bainitic constituents	Phase boundaries, hard martensitic regions, segregated or carbide-rich regions	Interface-related damage, cracking in hard regions, transformation-affected damage development

2.4 Experimental Techniques

In this section, a brief overview of the experimental characterization techniques is presented. These techniques are either directly employed in the study or play a crucial role in developing and validating numerical models. The techniques include electron backscatter diffraction, digital image correlation, and infrared thermography.

2.4.1 Electron Backscatter Diffraction

Electron backscatter diffraction (EBSD) is a powerful microstructure characterization technique commonly employed to investigate the crystallographic texture, grain morphology, and orientation of a metallic sample. The process involves directing a focused electron beam from a scanning electron microscope (SEM) onto a tilted specimen surface. The diffraction of electrons from the crystal lattice generates Kikuchi patterns, which are captured by a detector and analyzed to determine the local crystallographic orientation. The electron beam scans the specimen, capturing the crystallographic texture across a representative section. Figure 2-14 illustrates a schematic of the EBSD apparatus. In the context of HSLA, DP, and QP steels, EBSD provides critical insights into the microstructure, including phase identification, grain size, grain morphology, texture, and grain boundaries. This is essential for understanding how microstructural features influence the damage mechanisms. Figure 2-15 displays the EBSD image alongside the rolling direction inverse pole figure (RD-IPF) for HSLA steel and a sample (111) pole figure for hot rolled HSLA alloy, respectively. The crystallographic data collected from EBSD is visualized as orientation maps, where each color represents a unique grain orientation based on the inverse pole figure (IPF) color key. Additionally, pole figures or orientation distribution function (ODF) plots can be used to assess the dominant texture components, which play a critical role in determining mechanical anisotropy.

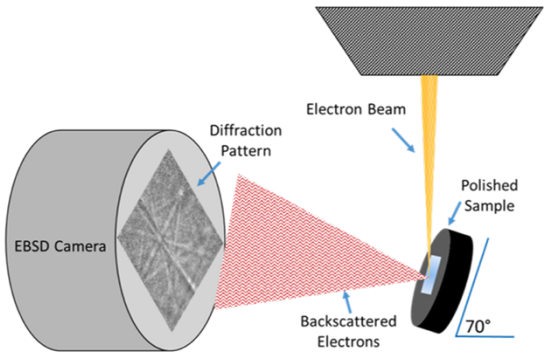


Figure 2-14: Schematic diagram of EBSD apparatus with Kikuchi pattern.

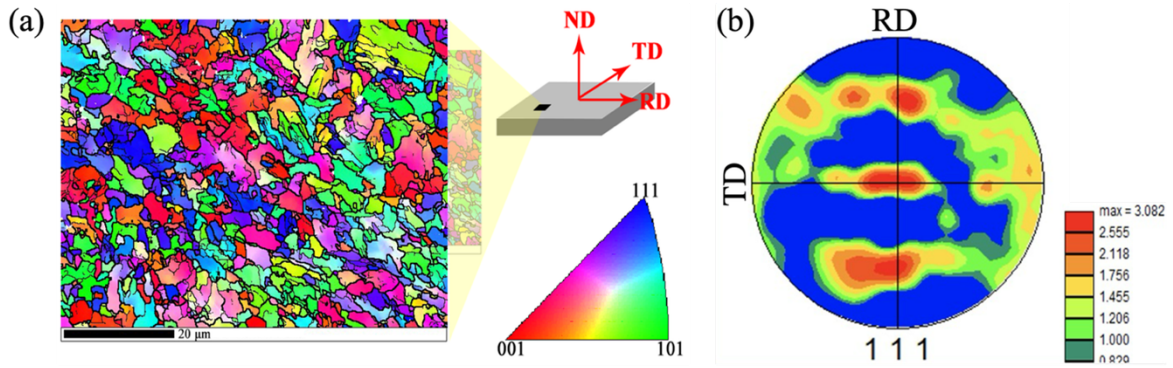


Figure 2-15: (a) EBSD image of HSLA with IPF map [89] and (b) Pole figure of HSLA in the RD-TD plane.

2.4.2 Digital Image Correlation

Digital image correlation (DIC) is an image-based non-contact technique for strain measurements during the deformation [90], initially developed in the 1980s [91]. The DIC technique acquires digital images of a specimen under different applied loads and then uses correlation algorithms to track the displacement of local regions. This process results in quantitative full-field data for the displacement and strain development between the imaged stages. In the DIC method, the specimen surface is typically spray painted with a random black-and-white speckle pattern prior to testing. A series of images acquired at a predetermined frame rate throughout the deformation process is used to determine the DIC measurements. This helps to obtain the complete strain history across the speckled region. The DIC software is then used to analyze the captured images and generate full-field strain maps for every load step. Moreover, this technique aids in measuring local strains near the location of failure, which are difficult to obtain with conventional strain gauges or extensometers [92]. A speckle pattern serves as the marker for deformation information and is highly influential in achieving accurate results [93]. The speckle pattern consists of high contrast features with varying greyscale intensity, which are of an appropriate size based on the pixel resolution of the camera, diameter of 3–5 pixels are typical [94]. The basic DIC workflow is summarized in Figure 2-16, showing how sequential speckle-pattern images are correlated to obtain displacement and strain fields during deformation.

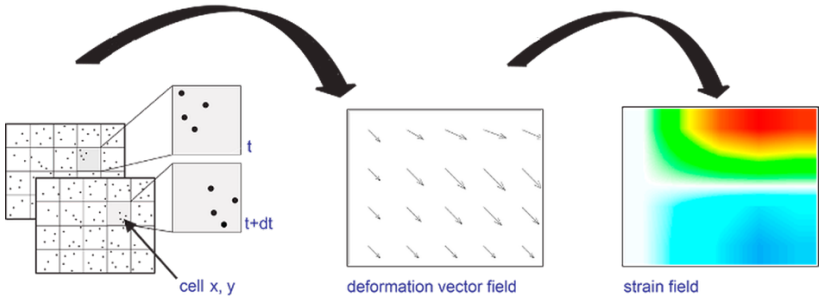


Figure 2-16: Schematic representation of a DIC process [95].

2.4.3 Infrared Thermography

Infrared thermography is a non-contact experimental technique used to measure the surface temperature field of a specimen during mechanical deformation. The method detects infrared radiation emitted from the specimen surface, which depends on the local temperature and surface emissivity. The recorded signal is converted into a quantitative temperature map after camera calibration and emissivity correction [96]. During elastic loading, temperature changes are small and are associated primarily with thermoelastic effects. Once plastic deformation begins, a significant fraction of the plastic work is dissipated as heat, characterized by the Taylor–Quinney coefficient [97–99]. The remaining fraction is stored in the material through dislocation accumulation and substructure formation. At low strain rates, heat dissipates to the surroundings and deformation remains near isothermal. At higher strain rates, heat dissipation is insufficient, and deformation approaches adiabatic conditions, producing a measurable local temperature rise [99,100].

Infrared thermography is particularly useful for sheet-metal deformation because it provides full-field temperature information without surface contact. Since localized plastic deformation generates local heat, temperature maps can identify regions where deformation becomes concentrated during necking [96]. When synchronized with mechanical data and digital image correlation measurements, the technique provides a direct experimental link between the stress–strain response, strain localization, and deformation induced heating [96]. For advanced high-strength steels, this is especially important because thermal softening influences strain hardening, damage accumulation, and the onset of softening at intermediate and high strain rates.

The accuracy of infrared thermography depends on controlling surface emissivity, camera frame rate, spatial resolution, and integration time according to the strain rate and specimen geometry. For high-rate tests, a sufficiently high frame rate is required to capture rapid temperature evolution

during the short deformation time [100]. Since the technique measures surface temperature only, the recorded field does not represent the full through-thickness distribution. In the present context, infrared thermography is used to evaluate temperature evolution during uniaxial tensile deformation and to support thermomechanical interpretation of the stress–strain response. Figure 2-17 shows an example of temperature evolution measured during tensile deformation.

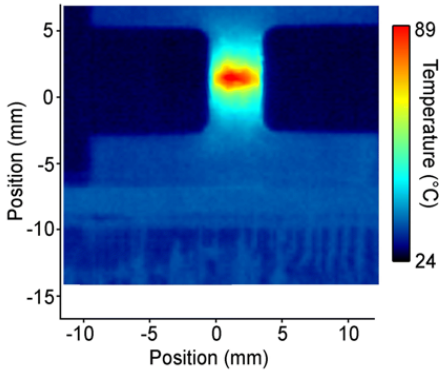


Figure 2-17: Temperature evolution during tensile deformation [101].

2.5 Constitutive and Numerical Modeling Frameworks

Numerical modeling provides a useful framework for interpreting deformation mechanisms and predicting material response under loading conditions that may not be easily accessible through experiments alone. For AHSS steels, numerical modeling is particularly important because the macroscopic response is strongly affected by microstructural heterogeneity. Grain orientation, phase fraction, phase morphology, strain partitioning, stress state, strain rate, and temperature can all influence the onset of localization and damage development. Constitutive models used for these materials must therefore balance physical fidelity and computational efficiency. A model with detailed microstructural resolution may provide local field information but may become impractical for repeated simulations over many loading paths, strain rates, or material states. Conversely, a simplified macroscopic model may be efficient but may not capture the internal mechanisms responsible for damage-driven softening.

2.5.1 Constitutive Modeling

Constitutive models are mathematical formulations that relate the stress state of a material to its deformation history, internal microstructural state, and applied thermal and mechanical boundary conditions. In the field of solid mechanics and plasticity, constitutive models are broadly classified into two categories: phenomenological models and physics-based mechanistic models [15,16]. Phenomenological models capture macroscopic stress–strain behavior through empirical functions

calibrated to experimental data. These models are computationally efficient and can be incorporated into large-scale finite element simulations without significant computational overhead. The Johnson-Cook model [101] is a widely used example that expresses the flow stress as a function of plastic strain, strain rate, and temperature through multiplicative factors. However, phenomenological models generally do not consider the underlying mechanisms of deformation. They represent the material response at the macroscopic level without explicitly incorporating grain-level slip activity, crystallographic orientation, dislocation evolution, or phase specific deformation characteristics. As a result, their calibration may not transfer reliably across different loading conditions, microstructures, or steel grades without modification.

Physics-based mechanistic models are founded on the physical mechanisms that govern deformation at the microstructural level [15,16,49]. These models introduce material state variables such as dislocation density, crystallographic texture, phase volume fraction, or void content that evolve during deformation and directly influence the constitutive response. The principal advantage of mechanistic models is their ability to connect macroscopic deformation behavior to the underlying microstructural state. This connection makes them more physically meaningful and, in principle, more transferable across different loading conditions, strain rates, temperatures, and microstructures without requiring complete recalibration. Mechanistic models also allow the evolution of internal state variables to be compared with experimentally measurable quantities such as dislocation density measured by EBSD kernel average misorientation or temperature rise captured by infrared thermography which provides a more rigorous basis for model validation. The primary limitation of mechanistic models is their higher computational cost, because the constitutive update must be resolved at the grain level for each orientation in the aggregate.

2.5.2 Crystal Plasticity

Crystal plasticity is a continuum constitutive framework in which plastic deformation is described through crystallographic slip on discrete slip systems. Unlike isotropic plasticity models, crystal plasticity explicitly accounts for the orientation of each crystal lattice [15,102,103]. This makes it suitable for modeling textured polycrystalline metals, where the mechanical response depends strongly on the alignment of slip systems with the applied stress state.

In a single crystal, plastic deformation occurs when the resolved shear stress on a slip system reaches the resistance to slip. The resolved shear stress on slip system α is commonly written as

$$\boldsymbol{\tau^{\alpha}} = \boldsymbol{\sigma}\colon(\boldsymbol{s}^{\alpha}\otimes\boldsymbol{m}^{\alpha}) \quad 2\text{-}1$$

where $\boldsymbol{\sigma}$ is the Cauchy stress, $\boldsymbol{s}^{\alpha}$ is the slip direction, and $\boldsymbol{m}^{\alpha}$ is the slip-plane normal. A rate-dependent slip law is often used to describe the shear rate on each slip system

$$\dot{\gamma}^{(\alpha)} = \dot{\gamma}_0 \left|\frac{\tau^{\alpha}}{g^{\alpha}}\right|^{\frac{1}{m}} sgn(\tau^{\alpha}) \quad 2\text{-}2$$

where $\dot{\gamma}_0$ is the reference shear rate, g^{α} is the slip resistance, and m is the rate-sensitivity exponent. The slip resistance evolves during deformation through hardening laws that may depend on accumulated slip, dislocation density, temperature, and phase specific properties.

Crystal plasticity is particularly useful for AHSS steels because ferrite, martensite, and retained austenite do not deform in the same manner. Ferrite and low-carbon martensite are commonly represented using BCC slip systems, while retained austenite is represented using FCC slip systems. This allows phase specific plasticity, texture effects, dislocation-based hardening, and orientation dependent deformation to be introduced directly into the constitutive response.

2.5.3 Polycrystal Homogenization

Engineering metals are polycrystalline aggregates composed of many grains with different crystallographic orientations. Each grain responds differently to the same macroscopic loading condition because the orientation of its slip systems differs from neighboring grains. A homogenization scheme is therefore required to connect the single crystal response to the macroscopic stress–strain response of the polycrystal.

The earliest homogenization assumptions are introduced by Sachs and Taylor. In the Sachs model, all grains are assumed to experience the same stress state [104]. This assumption satisfies stress equilibrium in an average sense but does not enforce strain compatibility between grains. In the Taylor model, all grains are assumed to experience the same macroscopic deformation [105]. This assumption enforces compatibility but does not resolve stress equilibrium between neighboring grains. Taylor-type models are computationally efficient and are widely used for texture sensitive constitutive modeling, but they may overestimate the macroscopic flow stress because each grain is constrained to deform according to the imposed aggregate deformation.

More advanced mean field schemes are developed to overcome some of these limitations. Self-consistent approaches treat each grain as an inclusion embedded in an effective medium, allowing stress and strain to vary from grain to grain while satisfying compatibility and equilibrium in an approximate average sense [106–108]. Viscoplastic self-consistent and elastic-viscoplastic self-

consistent models further extend this idea to rate-dependent and elastic-viscoplastic polycrystals [109–111]. These methods generally provide a more relaxed estimate of grain interaction than Taylor-type models, but they are more complex to implement when additional internal variables such as damage, temperature, interface degradation, and transformation are coupled to the crystal response.

Full-field approaches, including crystal plasticity finite element methods and spectral or fast Fourier transform-based methods, provide a more spatially resolved description of polycrystal deformation [16,112]. These methods assign orientations and phase properties to elements or voxels in a representative microstructure and solve the local mechanical equilibrium problem. They can capture local strain gradients, grain-neighborhood effects, phase-boundary stress concentration, and localization patterns more directly than mean-field methods. For multiphase steels, full-field crystal plasticity is especially useful for investigating strain partitioning between ferrite and martensite and for identifying damage-prone regions near phase boundaries. However, the computational cost becomes significant when many microstructures, strain rates, temperatures, textures, and loading paths must be simulated.

The present thesis uses a Taylor-type crystal plasticity framework. This choice is made because the objective is to develop an efficient material point constitutive model capable of predicting stress–strain response, texture deformation, temperature evolution, damage accumulation, and post-necking behavior over a broad range of deformation conditions. The framework is not intended to resolve the local morphology of strain localization, individual grain boundary damage, or explicit phase-boundary separation. Instead, the effects of phase contrast and interface-sensitive damage are introduced through homogenized internal variables and phase interaction terms. This provides a balance between microstructure sensitivity and computational efficiency for the HSLA, DP, and Q&P steel applications considered in this thesis.

2.5.4 Thermomechanical Coupling

During plastic deformation, a significant fraction of the mechanical energy dissipated by crystallographic slip is converted into heat within the deforming material. At low strain rates, heat generated by plastic work can dissipate to the surroundings during deformation, and the internal temperature rise within the gauge section remains relatively small. At intermediate and high strain rates, the time available for heat transfer decreases, and the deformation becomes closer to

adiabatic. Under these conditions, internal temperature rise can influence flow stress, dislocation evolution, localization, and damage accumulation.

The fraction of plastic work dissipated as heat is characterized by the Taylor-Quinney coefficient, χ, which represents the ratio of heat generated by plastic deformation to the total plastic work expended [97]. The volumetric heat generation rate associated with plastic slip is written as,

$$\dot{Q}_{gen} = \chi \, W_p \tag{2-3}$$

where $\dot{Q}_{gen}$ is the plastic heat generation rate and W_p is the plastic power density, computed as the sum of the resolved shear stress and shear rate products over all active slip systems. Under adiabatic conditions, the Taylor-Quinney coefficient can be estimated directly from experimental temperature measurements as,

$$\chi = \rho c_p \Delta\theta / W_p \tag{2-4}$$

where ρ is the material density, c_p is the specific heat capacity at constant pressure, and $\Delta\theta$ is the measured temperature rise during deformation. Reported values of χ for steels and other metallic alloys generally fall in the range of 0.85 to 1.0, reflecting that most but not all of the plastic work is converted to heat [113,114]. The remainder is stored in the microstructure in the form of dislocation line energy and other lattice defects. In the present thesis, the Taylor-Quinney coefficient is treated as a material parameter and is calibrated using high-speed infrared thermography measurements acquired during tensile testing at different strain rates.

Thermomechanical coupling is important in rate-dependent deformation because strain rate hardening and thermal softening may occur simultaneously. Increasing strain rate can raise the flow stress due to the rate sensitivity of dislocation motion. At the same time, deformation induced heating can reduce the flow resistance by enhancing thermally activated recovery and softening. In Q&P steels, temperature can also modify the stability of retained austenite and influence martensitic transformation kinetics. Therefore, temperature evolution may affect not only the flow response but also the balance between hardening, transformation, localization, and damage.

2.5.5 Transformation Coupled Modeling

Transformation coupled modeling is required for steels in which the phase constitution evolves during deformation. In transformation-assisted and Q&P steels, retained austenite may progressively transform into martensite during mechanical loading through the TRIP effect [8,22,40]. This transformation alters the phase fraction, local deformation resistance, strain partitioning, and hardening response of the material during deformation. As a result, the

constitutive response cannot be described solely through crystallographic slip and conventional hardening laws. The transformation process must be represented as an evolving internal mechanism that contributes to the macroscopic deformation and modifies the mechanical response of the aggregate as the phase balance changes.

In Q&P steels, the TRIP effect provides additional ductility and work-hardening capacity because the progressive formation of martensite can sustain the strain-hardening rate and delay the onset of plastic instability [8,40,41]. However, the same transformation progressively increases the local mechanical contrast between phases as deformation proceeds. The stability of retained austenite is influenced by several factors, including carbon enrichment, morphology, surrounding phase arrangement, crystallographic orientation, stress state, strain rate, and temperature [8,40,41]. Retained austenite that is insufficiently stable transforms too early and its contribution to sustained work hardening is diminished. Conversely, overly stable retained austenite does not transform effectively over the deformation range of interest, and the benefit of the TRIP effect is not fully realized. As a result, transformation-coupled models must account not only for the initial retained-austenite fraction, but also for how its mechanical stability evolves during deformation.

From a constitutive perspective, transformation is introduced through an internal variable representing either the transformed martensite fraction or the remaining retained austenite volume fraction. In simpler formulations, transformation is described as a function of accumulated plastic strain through semi-empirical kinetic relations [22]. More physically motivated models introduce a transformation driving force that depends on stress state, temperature, crystallographic orientation, and phase stability [23,52]. In crystal plasticity formulations, this approach is particularly useful because transformation can be coupled with crystallographic slip, lattice orientation, and phase specific mechanical response [23–25]. The total deformation then includes both slip-induced plastic deformation and transformation-induced deformation, while the constitutive update accounts for the evolving phase constitution at each increment of loading.

3 Literature Review

This chapter reviews the constitutive and computational approaches used to model ductile damage in advanced high-strength steels, with emphasis on crystal plasticity-based damage formulations. The discussion covers classical damage models, rate-dependent and thermomechanically coupled deformation, microstructure-sensitive damage in multiphase steels, and transformation-coupled damage in Q&P steels. The chapter concludes by identifying the key limitations in the existing literature and positioning the present thesis within these gaps.

3.1 Constitutive Modeling of Ductile Damage in Metallic Alloys

Constitutive modeling of ductile damage in metallic alloys has evolved from empirical failure indicators to micromechanically motivated porous plasticity, continuum damage mechanics, and more recent coupled computational frameworks. The main objective of these models is to represent how plastic deformation progressively degrades the stress-carrying capacity of a material and eventually leads to failure. Early micromechanical studies established the foundation for modern ductile damage modeling by showing that void evolution depends strongly on the local stress state. McClintock [115] analyzed the enlargement of cylindrical voids, while Rice and Tracey [10] examined the growth of spherical voids in a triaxial stress field. Their work demonstrated that ductile damage cannot be described using equivalent plastic strain alone because hydrostatic stress strongly accelerates cavity growth. The Rice–Tracey relation is commonly expressed in incremental form as

$$\frac{dR}{R} = C_{RT} exp\left(\frac{3}{2}\eta\right) d\varepsilon_p \qquad 3\text{-}1$$

where R is the void radius, ε_p is the equivalent plastic strain, $\eta = \sigma_m/\sigma_{eq}$ is the stress triaxiality, $\sigma_m$is the mean stress, σ_{eq} is the von Mises equivalent stress, and C_{RT} is a material or model constant. This expression illustrates a key principle of ductile damage modeling: two material points may accumulate similar plastic strain but develop very different damage if their local hydrostatic stress states are different. This idea is particularly important for sheet metals because uniaxial tension, plane strain tension, biaxial stretching, and simple shear produce different combinations of equivalent plastic strain, hydrostatic stress, and deviatoric stress state.

A first class of constitutive approaches is based on uncoupled phenomenological fracture criteria. These models introduce a scalar fracture indicator that accumulates during plastic deformation and reaches a critical value at failure. One common form is

$$D = \int_0^{\bar{\varepsilon}_p} \frac{d\bar{\varepsilon}_p}{\bar{\varepsilon}_f(\eta, L, \dot{\varepsilon}, \theta)} \quad 3\text{-}2$$

where D is the accumulated damage indicator and $\bar{\varepsilon}_f$ is the fracture strain, which may depend on stress triaxiality η, Lode parameter L, strain rate $\dot{\varepsilon}$, and temperature θ. Failure is usually assumed to occur when $D = 1$. These models are attractive because they are simple to implement in finite element simulations and can be calibrated using different specimen geometries. However, they are often uncoupled from the constitutive response. In other words, the material may continue to follow the same plasticity law while damage is accumulated separately as a failure indicator. This limits their ability to represent gradual stress softening before failure.

The Johnson–Cook failure model is one of the most widely used phenomenological formulations for high-rate deformation problems [116]. In this model, the failure strain is expressed as a function of stress triaxiality, strain rate, and temperature:

$$\varepsilon_f = [D_1 + D_2 exp(D_3\eta)]\left[1 + D_4 ln\left(\frac{\dot{\varepsilon}}{\dot{\varepsilon}_0}\right)\right][1 + D_5\theta^*] \quad 3\text{-}3$$

here D_1-D_5 are material parameters, $\dot{\varepsilon}_0$ is a reference strain rate, and θ^* is the normalized temperature. The importance of this model lies in its practical inclusion of strain rate and temperature effects, particularly for impact and high-rate deformation problems. Nevertheless, the Johnson-Cook fracture law remains phenomenological. It does not explicitly represent void nucleation, void growth, void coalescence, crystallographic slip, phase-level deformation, or the local microstructural origin of damage.

Subsequent phenomenological failure models improved stress state sensitivity by incorporating the Lode parameter. This development was motivated by the limitation that stress triaxiality alone cannot distinguish all relevant deviatoric stress states. Bao and Wierzbicki [79] demonstrated that the failure strain varies significantly across different triaxiality regimes, while Bai and Wierzbicki [14] introduced pressure and Lode-angle dependence into plasticity and failure modeling. These models are important for sheet metals because uniaxial tension, plane strain tension, biaxial stretching, and simple shear involve different combinations of hydrostatic and deviatoric stress state. A general stress-state-dependent failure strain may be expressed as

$$\bar{\varepsilon}_f = F(\eta, L) \tag{3-4}$$

where F defines a failure surface in the space of stress triaxiality and Lode parameter. Lou et al. [117] and Lou and Huh [118] further developed shear-sensitive criteria to improve failure prediction under low triaxiality conditions. These formulations are useful for constructing failure loci for sheet metals, but they still require extensive calibration and generally do not identify the underlying microstructural origin of damage. For advanced high-strength steels, this is a major limitation because the same macroscopic stress state may activate different damage mechanisms depending on phase fraction, phase morphology, texture, and local strain partitioning.

A second major group of models is continuum damage mechanics. In this approach, damage is introduced as an internal state variable that modifies the effective stress or stiffness of the material. For an isotropic scalar damage variable, the effective stress is written as

$$\tilde{\sigma} = \frac{\sigma}{1 - D} \tag{3-5}$$

where $\tilde{\sigma}$ is the effective stress, σ is the nominal stress, and D is a scalar damage variable. The corresponding elastic stiffness degradation can be expressed as

$$\mathbb{C}_{eff} = (1 - D)\mathbb{C}_0 \tag{3-6}$$

where $\mathbb{C}_0$ is the undamaged stiffness tensor. This approach allows damage to reduce the stress-carrying capacity of the material during deformation, making it more suitable for describing progressive softening than uncoupled failure indicators. Lemaitre [119] developed a thermodynamic framework for ductile damage in which damage evolution is linked to the energy release rate. The damage driving force is commonly defined from the Helmholtz free energy Ψ as

$$Y = -\frac{\partial \Psi}{\partial D} \tag{3-7}$$

where Y is the thermodynamic force conjugate to damage. A general damage evolution equation may then be expressed as

$$\dot{D} = \dot{\lambda}_d \left(\frac{Y}{Y_0}\right)^s \tag{3-8}$$

where $\dot{\lambda}_d$ is a damage multiplier, Y_0 is a reference damage resistance, and s is a material exponent. The advantage of this structure is that damage evolution is linked to thermodynamic dissipation rather than introduced only as an empirical failure condition. However, the scalar damage variable in many continuum damage models remains phenomenological. It represents an averaged degradation of the material, but it is not always directly connected to measurable microstructural

quantities such as void volume fraction, void number density, interface degradation, or phase specific damage.

A third and highly influential class of constitutive models is porous plasticity. Porous plasticity models provide a stronger micromechanical basis by representing damage through the void volume fraction. Gurson [11] introduced a yield function for porous ductile materials in which porosity directly affects yielding. The model was later modified by Tvergaard [120] and Tvergaard and Needleman [121] to improve agreement with numerical cell calculations and experimental observations. The resulting Gurson–Tvergaard–Needleman (GTN) model is commonly written as

$$\Phi = \left(\frac{\sigma_{eq}}{\sigma_y}\right)^2 + 2q_1 f^* cosh\left(\frac{3q_2\sigma_m}{2\sigma_y}\right) - \left(1 + q_3 f^{*2}\right) = 0 \tag{3-9}$$

where σ_{eq} is the von Mises equivalent stress, σ_y is the matrix flow stress, σ_m is the mean stress, f^* is the effective void volume fraction, and q_1, q_2, and q_3 are Tvergaard parameters. This model is important because the damage variable directly enters the yield function. As porosity increases, the material yield surface changes and the stress-carrying capacity decreases. Therefore, unlike uncoupled failure indicators, porous plasticity naturally couples damage evolution to the constitutive response.

In GTN-type models, porosity evolution is usually decomposed into void growth and void nucleation contributions:

$$\dot{f} = \dot{f}_{growth} + \dot{f}_{nucleation} \tag{3-10}$$

The growth term follows from plastic incompressibility of the matrix and is often written as

$$\dot{f}_{growth} = (1 - f)\mathrm{tr}(\boldsymbol{D}^p) \tag{3-11}$$

where f is porosity and $\boldsymbol{D}^p$ is the plastic rate of deformation. Void nucleation is commonly described using a normal distribution in plastic strain, following Chu and Needleman [122]:

$$\dot{f}_{nucleation} = \frac{f_N}{s_N\sqrt{2\pi}} \exp\left[-\frac{1}{2}\left(\frac{\bar{\varepsilon}_p - \varepsilon_N}{s_N}\right)^2\right]\dot{\varepsilon}_p \tag{3-12}$$

where f_N is the volume fraction of nucleating particles, ε_N is the mean nucleation strain, and s_N is the standard deviation. This formulation is useful because void nucleation is not assumed to occur at a single strain value. Instead, nucleation is distributed over a range of plastic strains. This idea remains influential in many later damage models, including models for steels containing inclusions, second-phase particles, and phase boundaries.

Although GTN-type models provide a strong foundation for ductile damage modeling, the classical formulation has important limitations. It was primarily developed for damage processes dominated by hydrostatic tension and void volume growth. Under shear dominated or low triaxiality conditions, the mean stress is small, and the classical porosity growth term may not increase sufficiently, even though experiments show that failure can still occur through void distortion, shear localization, or inter-void linking. This limitation is important for sheet metals because simple shear and plane strain loading are common in forming and crash related deformation. Nahshon and Hutchinson [123] modified the Gurson model by introducing a shear damage contribution associated with the third invariant of the deviatoric stress. A generalized shear-modified porosity evolution equation can be written as

$$\dot{f} = (1 - f)\mathrm{tr}(\boldsymbol{D}^p) + \dot{f}_{nucleation} + \dot{f}_{shear} \quad 3\text{-}13$$

where $\dot{f}_{shear}$ shear introduces additional damage growth under shear-dominated loading. A common form is

$$\dot{f}_{shear} = k_w f \omega(\sigma) \frac{\boldsymbol{s}:\boldsymbol{D}^p}{\sigma_{eq}} \quad 3\text{-}14$$

where $k_w$is a shear damage parameter, $\omega(\sigma)$ is a stress state function based on third invariant, and $\boldsymbol{s}$ is the deviatoric stress tensor. This extension improves the ability of porous plasticity models to capture low triaxiality failure prediction, but it also introduces additional calibration parameters. As a result, the model becomes more flexible but less directly transferable across material grades and loading conditions.

Porous plasticity models have also been extended to include void shape, void orientation, anisotropy, and coalescence. The Gologanu-Leblond-Devaux model generalized Gurson-type porous plasticity to non-spherical voids, especially spheroidal cavities [124]. Pardoen and Hutchinson [125] later incorporated void shape effects and coalescence criteria based on inter-void ligament localization. These developments improved the micromechanical description of ductile failure by recognizing that voids do not only grow in volume; they also distort, rotate, and interact with neighboring voids. Reviews by Benzerga and Leblond [76] and by Pineau et. Al [126] further showed that the transition from void growth to coalescence is influenced by void morphology, matrix hardening, anisotropy, and stress state. A simplified representation may define the porosity and void aspect ratio as

$$f = \frac{V_{void}}{V}, \qquad \lambda_v = \frac{a}{b} \tag{3-15}$$

where V_{void} is the void volume, V is the material volume, and λ_v is the aspect ratio between major and minor void axes. A generic void-shape evolution law may be written as

$$\dot{\lambda}_v = \mathcal{F}(\eta, L, \boldsymbol{D}^p, \lambda_v) \tag{3-16}$$

where void shape evolves as a function of stress triaxiality, Lode parameter, plastic flow direction, and current void geometry. These formulations are physically meaningful because voids in sheet metals may elongate, rotate, or distort depending on loading path. However, the additional internal variables increase the complexity of parameter identification. This is especially challenging for advanced steels, where the observed void shape evolution may depend on the local phase arrangement and the nucleation site.

Another important computational approach is cohesive zone modeling for representing damage and failure, particularly at interfaces. In these models, separation is governed by a traction–separation law. A simple cohesive relation may be written as

$$T = (1 - d)K\delta \tag{3-17}$$

where T is the cohesive traction, K is the penalty stiffness, δ is the separation, and d is a cohesive damage variable. These models are particularly useful for simulating interface decohesion, which is relevant for multiphase steels where ferrite-martensite boundaries or austenite-martensite interfaces may act as damage initiation sites. However, they require the interface geometry or potential failure path to be explicitly represented. Their predictions are also sensitive to cohesive strength, fracture energy, mesh size, interface geometry, and the assumed traction-separation law. Therefore, they are powerful for local interface studies but less convenient for broad constitutive simulations across many strain rates, textures, and microstructures.

Phase-field damage models have also gained attention because they represent cracks or highly degraded zones through a continuous scalar field. A typical energy functional may be written as

$$\Pi = \int g(c)\psi_e(\boldsymbol{\varepsilon})\, dV + \int G_c \left(\frac{c^2}{2l} + \frac{l}{2} |\nabla c|^2 \right) dV \tag{3-18}$$

where c is the phase-field damage variable, $g(c)$ is the degradation function, ψ_e is the elastic or elastic-plastic strain energy density, G_c is the fracture toughness, and l is the regularization length scale. Phase-field models are attractive because they allow complex crack paths to emerge without prescribing the crack geometry. Recent ductile phase-field models have been coupled with

plasticity, crystal plasticity, and fatigue formulations. However, their use in large parametric studies remains limited by computational cost and by the need to calibrate fracture energy, length scale, degradation functions, and plastic-damage coupling assumptions.

For advanced high-strength steels, the limitations of conventional damage models become more significant because deformation and failure are controlled by coupled microstructural mechanisms. HSLA steels require constitutive descriptions that can account for strain rate-dependent plasticity, dislocation evolution, temperature rise, and damage-induced softening. DP steels require models that include ferrite-martensite phase contrast, strain partitioning, interface-driven damage, and loading-path dependence. Q&P steels introduce further complexity because retained-austenite transformation changes the phase constitution, local strength contrast, and damage susceptibility during deformation. Therefore, a constitutive model that is calibrated only through macroscopic failure strain may not be sufficiently transferable across these material systems.

The literature therefore shows a clear progression in ductile damage modeling. Phenomenological criteria are efficient but often uncoupled from constitutive softening. Continuum damage mechanics introduces progressive degradation, but its damage variables are often phenomenological. Porous plasticity provides a micromechanical basis through void volume fraction, but classical forms require extensions for shear-dominated loading, void shape evolution, anisotropy, and microstructural heterogeneity. Cohesive zone and phase-field models can represent interface separation and crack development more explicitly, but they require spatially resolved geometry and higher computational cost. These limitations motivate crystal plasticity-based damage modeling, where the evolution of damage can be linked more directly to crystallographic slip, texture, phase specific deformation, stress state, strain rate, temperature, and transformation effects.

3.2 Crystal Plasticity-based Damage Modeling

Crystal plasticity-based damage modeling provides a microstructure-sensitive route for describing the progressive degradation of metallic materials. Unlike macroscopic damage models, which usually consider the material as a homogeneous continuum, crystal plasticity introduces the effects of crystallographic orientation, slip system activity, texture evolution, and phase specific plasticity directly into the constitutive response. This is particularly important for advanced high-strength steels because the onset of damage-driven softening is controlled not only by the macroscopic stress state, but also by the local slip activity, phase contrast, and strain partitioning among grains

and phases. Therefore, crystal plasticity-based damage models are well suited for linking microstructural deformation mechanisms to the gradual loss of load carrying capacity observed in stress–strain curves.

The foundation of most crystal plasticity formulations is the decomposition of deformation into elastic lattice distortion and plastic slip. In finite deformation form, the deformation gradient is commonly written as

$$\boldsymbol{F} = \boldsymbol{F}_e \boldsymbol{F}_p \tag{3-19}$$

where $\boldsymbol{F}_e$ represents elastic stretching and lattice rotation, and $\boldsymbol{F}_p$ represents crystallographic plastic deformation. Plastic flow is described as the sum of shear rates on active slip systems,

$$\boldsymbol{L}_p = \dot{\boldsymbol{F}}_p \boldsymbol{F}_p^{-1} = \sum_{\alpha=1}^{N_s} \dot{\gamma}^{\alpha} \boldsymbol{s}^{\alpha} \otimes \boldsymbol{m}^{\alpha} \tag{3-20}$$

where $\dot{\gamma}^{\alpha}$ is the shear rate on slip system α, $\boldsymbol{s}^{\alpha}$ is the slip direction, $\boldsymbol{m}^{\alpha}$ is the slip-plane normal, and N_s is the number of slip systems. The resolved shear stress is obtained from the projection of the stress state onto each slip system,

$$\boldsymbol{\tau}^{\boldsymbol{\alpha}} = \boldsymbol{\sigma} : (\boldsymbol{s}^{\alpha} \otimes \boldsymbol{m}^{\alpha}) \tag{3-21}$$

A rate-dependent power law is then often used to describe slip kinetics

$$\dot{\gamma}^{(\alpha)} = \dot{\gamma}_0 \left| \frac{\tau^{\alpha}}{g^{\alpha}} \right|^{\frac{1}{m}} sgn(\tau^{\alpha}) \tag{3-22}$$

where $\dot{\gamma}_0$ is the reference shear rate, g^{α} is the slip resistance, and m is the rate-sensitivity exponent. This structure allows crystal plasticity to capture the directional dependence of plastic flow arising from crystal orientation and evolving slip resistance. As a result, local differences in slip activity can be connected to strain localization and damage accumulation, rather than being hidden inside a macroscopic plastic strain measure.

Early efforts to couple damage with crystal plasticity introduced damage as an internal variable associated with void evolution, stiffness degradation, or volumetric expansion. Bammann and Aifantis [127] provided an early internal-state-variable framework for ductile metals in which damage was linked to inelastic deformation and microstructural evolution. Potirniche et al. [17] later developed a crystal plasticity damage formulation in which the deformation gradient was multiplicatively decomposed into elastic, plastic, and volumetric damage-related contributions.

Their work was important because it introduced damage within the same kinematic structure used to describe crystallographic slip, rather than treating damage only as a final failure indicator.

A common kinematic extension for crystal plasticity damage models is therefore

$$\boldsymbol{F} = \boldsymbol{F}_e \boldsymbol{F}_v \boldsymbol{F}_p \tag{3-23}$$

where $\boldsymbol{F}_v$ represents the volumetric contribution associated with damage. If damage is represented by a scalar void volume fraction or porosity-like variable ϕ, the damage-induced volumetric deformation gradient may be expressed as

$$\boldsymbol{F}_v = \frac{1}{(1-\phi)^{1/3}} \boldsymbol{I} \tag{3-24}$$

The corresponding damage-induced rate of deformation is

$$\boldsymbol{D}_v = \frac{\dot{\phi}}{3(1-\phi)} \boldsymbol{I} \tag{3-25}$$

This form is useful because it connects damage evolution to volumetric expansion at the material point, while the deviatoric plastic response remains governed by crystallographic slip. It also provides a natural route for coupling the damage variable to the stress update, since an increase in ϕ reduces the effective resistance of the material and contributes to stress relaxation. This type of formulation is directly relevant to material-point damage modeling, where the goal is to reproduce damage-driven softening rather than simulate an explicit crack path.

Damage can also be coupled to the crystal stress response through stiffness degradation. A common representation is

$$\mathbb{C}_{eff} = (1-\phi)\mathbb{C}_e \tag{3-26}$$

where $\mathbb{C}_{eff}$ is the effective elastic stiffness and $\mathbb{C}_e$ is the undamaged crystal stiffness. In rate form, the stress update may be written schematically as

$$\hat{\boldsymbol{\sigma}} = \mathbb{C}_{eff} : \boldsymbol{D} - \sum_{\alpha=1}^{N} \dot{\gamma}^{(\alpha)} \boldsymbol{R}^{(\alpha)} - \frac{\dot{\phi}}{3(1-\phi)} \left(\mathbb{C}_{eff} : \boldsymbol{I} \right) \tag{3-27}$$

where $\hat{\boldsymbol{\sigma}}$ is an objective stress rate, $\boldsymbol{D}$ is the total rate of deformation, and $\boldsymbol{R}^{(\alpha)}$ contains the elastic projection and lattice-rotation terms associated with slip system α. This form illustrates the main advantage of a crystal plasticity damage model: slip activity, lattice orientation, and damage-induced softening enter the constitutive update simultaneously. Damage is therefore not only a post-processing failure indicator, but an evolving state variable that contributes to the stress–strain response.

A major contribution of crystal plasticity-based damage modeling is the ability to capture orientation-dependent void growth and damage evolution. Potirniche et al. [128] showed that lattice orientation affects void growth and coalescence in single crystals, demonstrating that void evolution is not controlled only by stress triaxiality and equivalent plastic strain. Yerra et al. [129] further examined void growth and coalescence in single crystals using three-dimensional crystal plasticity finite element calculations and showed that the influence of orientation becomes particularly important at low stress triaxiality. Ha and Kim [130] similarly investigated void behavior in FCC single crystals and showed that void growth depends on stress triaxiality, crystallographic orientation, and initial void volume fraction. These studies are important because they show why isotropic porous plasticity is not sufficient when the local deformation field is governed by crystallographic slip. Crystal plasticity-based void-cell simulations explicitly resolve the slip activity around voids and therefore provide a more mechanistic description of damage evolution.

Several strategies have been used to introduce damage evolution into crystal plasticity. One strategy is to use a porosity-like variable, where void nucleation and growth are embedded into the crystal plasticity update. In this case, the damage rate may be written as

$$\dot{\phi} = \dot{\phi}_n + \dot{\phi}_g \tag{3-28}$$

where $\dot{\phi}_n$ represents nucleation and $\dot{\phi}_g$ represents growth of existing voids. The growth contribution can be linked to stress triaxiality through a Rice–Tracey model, while nucleation may be introduced using a statistical distribution in plastic strain or a microstructure-dependent criterion. A second strategy is to degrade the slip resistance or elastic stiffness as a function of accumulated damage. A third strategy is to couple crystal plasticity with cohesive zone or phase-field descriptions so that local separation or highly degraded zones can develop along grain boundaries, phase boundaries, or predefined interfaces. Each approach provides a different balance between physical interpretation, numerical cost, and calibration complexity.

At the polycrystal scale, crystal plasticity damage models are commonly implemented using either full-field or mean-field homogenization strategies. In full-field crystal plasticity finite element or spectral methods, each grain, element, or voxel is assigned a crystallographic orientation and constitutive response, allowing local stress and strain heterogeneity to be resolved explicitly. This approach is useful for investigating local strain localization, void growth, and damage-sensitive fields near grain boundaries or phase boundaries. However, it becomes computationally expensive

when many orientations, microstructures, strain rates, temperatures, and loading paths must be evaluated. Mean-field and Taylor-type formulations are less spatially resolved, but they provide an efficient route for linking texture, phase specific plasticity, macroscopic stress–strain response, and damage-driven softening. Therefore, the choice between full-field and mean-field crystal plasticity depends on whether the objective is local microstructural resolution or efficient constitutive prediction.

For advanced high-strength steels, this distinction is especially important. Full-field crystal plasticity simulations have shown that strain localization and damage-sensitive fields are strongly affected by local phase arrangement, phase contrast, and crystallographic orientation [6,16,18]. These studies demonstrate the mechanistic value of spatially resolved crystal plasticity for interpreting local degradation processes. However, a fully resolved representation is not always necessary or practical when the aim is to develop a constitutive model capable of predicting the stress–strain response, texture-sensitive deformation, and damage-driven softening across multiple strain rates and loading paths. In this case, a Taylor-type or mean-field crystal plasticity framework can retain the essential orientation and phase sensitivity while remaining computationally efficient.

Crystal plasticity has also become an important modeling basis for multiphase and transformation-assisted steels. In dual phase steels, it provides a way to distinguish ferrite and martensite plasticity, quantify strain partitioning, and assess how texture and phase contrast influence damage-sensitive deformation. In Q&P steels, crystal plasticity additionally provides a framework for coupling crystallographic slip with retained-austenite transformation and phase-sensitive degradation. These applications require further model extensions beyond the general CP damage structure described here. In particular, strain rate and temperature effects, ferrite–martensite interface degradation, and transformation-coupled damage introduce distinct modeling challenges. These topics are therefore reviewed separately in the following sections to avoid conflating the general crystal plasticity damage framework with material-specific extensions.

The literature therefore shows that crystal plasticity-based damage modeling has developed as a bridge between microstructural deformation mechanisms and macroscopic stress–strain softening. Porosity-based crystal plasticity models introduce void-induced degradation into slip-based constitutive updates, while full-field implementations provide detailed insight into local strain localization and damage-sensitive fields. Mean-field and Taylor-type formulations offer a more efficient alternative when the objective is to predict material-point response across multiple

thermomechanical conditions. These observations motivate the modeling direction adopted in this thesis: an efficient crystal plasticity-based damage framework that preserves the key orientation, texture, and phase-sensitive features needed for HSLA, DP, and Q&P steels, while remaining practical for simulations over different strain rates, temperatures, and loading paths.

3.3 Interface Sensitive Damage Modeling in Multiphase Steels

In multiphase steels, an additional modeling difficulty arises because damage-sensitive deformation is strongly influenced by phase boundaries. In ferrite–martensite steels, the soft ferritic phase and hard martensitic phase deform differently, producing local strain partitioning and stress concentration near interfaces. Therefore, interface-sensitive damage modeling requires a framework that can represent phase-level deformation, local incompatibility, and interfacial degradation while retaining the crystallographic character of plastic flow.

Dual phase steels have been widely used as model materials for this class of problem because their ferrite–martensite microstructure provides a clear example of mechanical heterogeneity. In crystal plasticity-based simulations, the microstructure is commonly represented using a representative volume element in which ferrite and martensite are assigned distinct constitutive descriptions. The local equilibrium problem is solved over the microstructure, and the macroscopic stress is obtained by volume averaging,

$$\langle \sigma \rangle = \frac{1}{V} \int \sigma(x) dV = \sum_{p=1}^{N_p} v_p \langle \sigma^{(p)} \rangle \qquad 3\text{-}29$$

where V is the RVE volume, v_p is the volume fraction of phase p, and $\langle \sigma^{(p)} \rangle$ is the phase-averaged stress. This approach allows local stress and strain fields to be examined near ferrite–martensite interfaces, where damage-sensitive deformation often develops. Kadkhodapour et al. [18] used a single crystal plasticity model to study damage initiation in DP steels and showed that the morphology and distribution of martensite strongly influence local stress and strain heterogeneity. Tasan et al. [6] combined in-situ deformation experiments with crystal plasticity simulations and showed that strain localization in DP steels is spatially heterogeneous and closely related to the ferrite–martensite microstructure. These studies established the value of CP-based micromechanics for identifying damage-prone regions in multiphase steels.

In many early CP-based simulations of DP steels, ferrite–martensite interfaces were modeled as perfectly bonded. In this case, displacement compatibility is enforced across the interface and the

boundary itself does not possess a separate degradation law. Such models are useful for identifying regions of high local plastic strain, hydrostatic stress, or phase-boundary stress concentration, but they cannot directly represent interface decohesion. The interface is therefore considered indirectly: it influences the local mechanical fields through phase contrast and morphology, but it does not evolve as a separate damage-bearing entity. This limitation motivated later approaches in which interfaces were assigned their own constitutive response.

One common method for explicit interface modeling is to couple crystal plasticity in the bulk phases with cohesive-zone laws along phase boundaries. In this approach, ferrite and martensite deform according to their assigned phase specific constitutive models, while the interface follows a traction–separation relation. A simplified mixed-mode cohesive law may be written as

$$T_n = (1 - d_{int})K_n\delta_n, \qquad T_s = (1 - d_{int})K_s\delta_s \tag{3-30}$$

where T_n and T_s are the normal and shear tractions, K_n and K_s are the interface stiffnesses, δ_n and δ_s are the corresponding separations, and d_{int} is an interface damage variable. Interface damage initiation is often defined using a mixed-mode stress or separation criterion, for example,

$$\left(\frac{\langle T_n \rangle}{T_{n,c}}\right)^2 + \left(\frac{T_s}{T_{s,c}}\right)^2 = 1 \tag{3-31}$$

where $T_{n,c}$ and $T_{s,c}$ are the critical normal and shear interface strengths, and $\langle T_n \rangle$ denotes the tensile part of the normal traction. After initiation, the cohesive stiffness is progressively degraded through d_{int}. This type of model is physically attractive because it treats the interface as a constitutive entity rather than only as a geometric boundary.

The CP–cohesive strategy has been used to separate the roles of matrix plasticity, martensite behavior, and phase-boundary degradation. Qin et al. [19] investigated the influence of phase and interface properties on stress-state-dependent failure initiation in DP steels using computational modeling. Their study used a GTN-type description for ductile ferrite degradation and a cohesive-zone description for ferrite–martensite interface decohesion, showing that phase and interface properties can significantly affect the predicted failure response under different stress states. This type of framework is important because it demonstrates that interface strength cannot be treated as a secondary detail; it can change the predicted location and strain level of damage initiation.

More recent models have combined crystal plasticity with cohesive-zone descriptions in three-dimensional microstructures. Aydiner et al. [21] used a crystal plasticity and cohesive-zone framework to investigate competing damage mechanisms in DP steels, including ferrite–

martensite interface decohesion, ferrite–ferrite boundary decohesion, and martensite-related degradation. Such models are useful because they allow different degradation paths to be represented within one microstructure-sensitive simulation. They also show that the dominant damage mechanism may change with martensite morphology, martensite connectivity, interface strength, and applied stress state. However, these simulations require explicit interface geometry, interface meshing, cohesive parameters, and substantial computational cost. As a result, they are highly informative for mechanism identification, but less convenient for repeated material-point simulations over many loading paths, strain rates, or texture states.

The role of microstructure morphology has also been examined through high-fidelity CP simulations and sensitivity analysis. Fehlemann et al. [131] developed a three-dimensional statistically representative volume element framework for DP800 steel using crystal plasticity, damage indicators, surrogate modeling, and variance-based global sensitivity analysis. Their study introduced a phase-boundary decohesion indicator and showed that the martensite-to-ferrite phase ratio, martensite strength, phase grain size, and martensite morphology influence damage tolerance. This type of work reflects a recent shift in interface-sensitive modeling: rather than analyzing only one microstructure, high-fidelity simulations are increasingly used to identify which microstructural descriptors most strongly affect damage resistance.

3.4 Transformation-Coupled Damage Modeling in Q&P Steels

In Q&P steels, interface driven damage problem becomes more complex because one of the phases evolves during deformation. The retained austenite can progressively transform into martensite, changing the phase fraction, local strength contrast, strain partitioning, and internal stress state. Therefore, transformation-coupled damage modeling must account not only for phase specific plasticity, but also for the evolving mechanical stability of retained austenite and its effect on damage-driven softening.

Early constitutive descriptions of transformation-induced plasticity were often based on empirical or semi-empirical transformation kinetics. A widely used foundation is the Olson–Cohen type relation, in which the martensite volume fraction evolves with plastic strain as

$$f_{\alpha'} = 1 - \exp\left[-\beta\left(1 - \exp\left(-\alpha\bar{\varepsilon}_p\right)\right)^n\right] \quad 3\text{-}32$$

where $f_{\alpha'}$ is the transformed martensite fraction, $\bar{\varepsilon}_p$ is the equivalent plastic strain, and α, β, and n are material parameters associated with shear-band formation and martensitic nucleation. This

class of model is useful because it relates deformation induced transformation to accumulated plastic strain. However, it does not explicitly account for crystallographic orientation, stress state, variant selection, phase neighborhood, or the local stability of individual retained-austenite regions. These limitations become important for Q&P steels because retained austenite stability depends strongly on morphology, carbon enrichment, surrounding phases, temperature, and loading path.

Later micromechanical and thermodynamic models introduced the transformation driving force more explicitly. In these approaches, martensitic transformation is activated when the mechanical and chemical driving forces overcome a transformation resistance. A generic transformation driving force for variant β\betaβ may be written as

$$f_{tr}^{\beta} = \boldsymbol{\sigma}: \boldsymbol{P}_{tr}^{\beta} - \Delta G_{chem}(\theta) - R_{tr}^{\beta} \qquad 3\text{-}33$$

where $\boldsymbol{\sigma}: \boldsymbol{P}_{tr}^{\beta}$ represents the mechanical work associated with transformation, $\Delta G_{chem}(\theta)$ is the temperature-dependent chemical free-energy contribution, and R_{tr}^{β} is the resistance to transformation. This type of formulation provides a more physical basis than a purely strain-controlled transformation law because it allows stress state, temperature, and variant orientation to influence transformation. Turteltaub and Suiker [22] developed a thermomechanical formulation for transformation-induced plasticity in ferrous alloys and established a basis for coupling martensitic transformation with the mechanical response of multiphase steels. Their framework showed that retained-austenite transformation can be treated as a thermodynamically driven internal process rather than only as an empirical function of plastic strain.

Crystal plasticity extended this idea by embedding transformation within a slip-based constitutive framework. In such models, the total deformation is governed by crystallographic slip and by transformation-induced deformation. A common representation introduces a transformation contribution to the velocity gradient,

$$\boldsymbol{L}_{tr} = \sum_{\beta=1}^{N_v} \dot{\xi}^{\beta} \gamma_{tr} \boldsymbol{b}^{\beta} \otimes \boldsymbol{d}^{\beta} \qquad 3\text{-}34$$

where $\dot{\xi}^{\beta}$ is the transformation rate of martensite variant β, N_v is the number of possible martensitic variants, γ_{tr} is the transformation shear magnitude, $\boldsymbol{b}^{\beta}$ is the transformation direction, and $\boldsymbol{d}^{\beta}$ is the habit-plane normal. A corresponding rate law may be expressed as

$$\dot{\xi}^{\beta} = \dot{\xi}_0 \left| \frac{f_{tr}^{\beta}}{f_{cr}} - 1 \right|^{m_{tr}} \left(1 - \sum_{\beta=1}^{N_v} \xi^{\beta} \right) \quad 3\text{-}35$$

where f_{cr} is a critical transformation resistance and m_{tr} is a transformation-rate exponent. This form captures two important features: transformation occurs only when the driving force exceeds a resistance, and the available retained austenite decreases as transformation progresses.

Several crystal plasticity models have used this type of transformation kinematics to describe TRIP and Q&P steels. Ma and Hartmaier [132] proposed a deformation–phase transformation coupling framework for TRIP-assisted steels that considered the elastic–plastic deformation of ferrite and austenite, the transformation of austenite to martensite, and the elastic response of martensite. Park et al. [52] developed a crystal plasticity model for third-generation multiphase AHSS with martensitic transformation, using phase specific constitutive behavior and transformation kinetics to reproduce the quasi-static mechanical response of Q&P-type steels. Yang et al. [24] studied QP1180 steel under different strain paths using experiments and crystal plasticity simulation and showed that retained-austenite transformation depends on both strain path and crystal orientation. Their model incorporated multiple-variant transformation kinetics driven by transformation potential, which allowed strain-path-dependent retained-austenite evolution to be represented more accurately than simple strain-based transformation laws. Park et al. [25] later developed a crystal plasticity model with stress-state-dependent martensitic transformation for QP980 steel, showing that the interaction between transformation and plasticity is essential for predicting the mechanical behavior of Q&P steels.

Another important modeling development concerns phase-resolved parameter identification. Q&P steels contain mechanically distinct phases whose properties cannot always be measured directly by conventional macroscopic tests. Hu et al. [133] used synchrotron X-ray diffraction combined with crystal plasticity to determine individual phase constitutive properties of a TRIP-assisted QP980 steel. This type of method is important because transformation-coupled models require phase specific constitutive parameters for ferrite, martensite, and retained austenite. Without reliable phase-level parameters, transformation kinetics may compensate artificially for errors in phase strength, hardening, or strain partitioning. Phase-resolved calibration therefore improves the physical meaning of transformation-coupled simulations.

Thermomechanical coupling further complicates retained-austenite transformation. The stability of retained austenite depends on temperature, and deformation induced heating can change the

apparent transformation rate during mechanical loading. Connolly et al. [23] developed a thermomechanically coupled crystal plasticity model incorporating transformation-induced plasticity over a wide range of strain rates and temperatures. Their work showed that transformation modeling in TRIP-assisted steels must account for both strain rate dependence and temperature evolution. This is particularly relevant to Q&P steels because strain rate can influence the balance between transformation-assisted hardening and thermal stabilization of retained austenite. A transformation law that is calibrated only under isothermal quasi-static conditions may therefore be insufficient for predicting the response across broader thermomechanical conditions.

More recent mesoscale and full-field models have attempted to resolve the microstructural environment of retained austenite more explicitly. Cheng et al. [134] developed a mesoscale crystal plasticity model for QP steels that incorporated detailed microstructures into high-resolution finite element simulations to predict deformation and martensitic transformation kinetics. Their work emphasized that retained-austenite stability and transformation rate depend strongly on local strain path and initial microstructure, which are difficult to capture using analytical transformation rules alone. Such high-resolution models are useful for identifying local transformation hotspots and phase-neighborhood effects. However, they require detailed microstructural input and are computationally more demanding than mean-field constitutive models.

The coupling between transformation and damage is not straightforward because retained austenite can have competing effects. At lower strain levels, transformation can enhance work hardening and delay localization by redistributing deformation and increasing the strain-hardening capacity. At larger strain levels, continued transformation may increase the amount of hard martensitic phase, intensify phase contrast, and promote local incompatibility near phase boundaries. A transformation-coupled damage model must therefore be able to represent both stabilization and degradation tendencies within the same framework. This requirement distinguishes Q&P steel modeling from conventional DP steel modeling, where the hard phase fraction is usually fixed during deformation.

3.5 Summary of Literature Gaps

While substantial research exists on constitutive modeling of ductile damage in metallic alloys, several deficiencies remain for advanced high-strength steels subjected to different strain rates, temperatures, and loading conditions. First, much of the ductile damage literature is still dominated by macroscopic failure criteria, continuum damage mechanics, and porous plasticity formulations

[10–14,76,79,116–119,122–126,135]. These approaches provide important descriptions of stress-state-dependent damage evolution, but they generally do not account for crystallographic orientation, texture evolution, phase specific plasticity, or local deformation heterogeneity. Second, although crystal plasticity-based damage models have improved the connection between slip activity, orientation dependence, and damage evolution [6,16–18,127,128], many of these works focus on single-phase materials, idealized void-cell calculations, or computationally intensive full-field simulations. As a result, relatively few efficient crystal plasticity-based formulations are available for predicting damage-driven softening and loss of load-carrying capacity across multiple steel grades, strain rates, temperatures, and loading paths. Third, for multiphase steels, existing CP and RVE-based studies have shown that phase contrast, martensite morphology, phase-boundary incompatibility, and interface degradation strongly influence damage-sensitive deformation [6,18–21,131,136]. However, many interface-sensitive models require explicitly resolved ferrite–martensite boundaries, cohesive-zone parameters, and high spatial resolution. These models are valuable for identifying local degradation mechanisms, but they are less suitable for broad constitutive studies involving many textures, microstructures, and loading conditions. Finally, although significant progress has been made in modeling retained-austenite transformation, variant selection, strain-path dependence, and thermomechanical effects in Q&P steels [22–24,52,132–134], most transformation-coupled crystal plasticity models focus primarily on transformation-assisted hardening and retained-austenite evolution. The coupling between retained-austenite transformation, evolving phase contrast, damage accumulation, and the transition from hardening to damage-driven softening remains comparatively less developed. These deficiencies motivate the need for a crystal plasticity-based damage framework capable of linking crystallographic slip, stress-state-dependent void evolution, thermomechanical effects, interface-sensitive degradation, and transformation-coupled phase evolution to the progressive loss of load-carrying capacity in advanced high-strength steels.

4 Research Scope and Objectives

This research aims to develop an advanced constitutive modeling framework for predicting damage evolution, post-necking behavior, and failure in advanced high-strength steels. The materials considered in this thesis include high strength low-alloy steels, dual-phase steels, and quenching and partitioning steels. These material systems are selected because they represent increasing levels of microstructural and constitutive complexity: void driven damage in HSLA steels, phase- and interface-sensitive damage in DP steels, and transformation-coupled damage in Q&P steels.

As such, the research hypothesis is:

"A Taylor-type crystal plasticity damage framework incorporating thermodynamically consistent driving forces for void evolution, phase specific plasticity, and retained-austenite transformation can predict the experimentally measured stress–strain response, temperature evolution, damage-driven softening, and failure strain of HSLA, DP, and Q&P steels for various strain rates, temperatures, and loading paths"

The proposed constitutive models must capture the dominant deformation and damage mechanisms associated with each steel class. For HSLA steels, the model must account for crystallographic slip, dislocation evolution, internal temperature rise, void nucleation, void growth, and damage-induced degradation of the stress response. For dual-phase steels, the model must account for phase specific plasticity, ferrite–martensite mechanical interaction, stress-state-sensitive void evolution, texture effects, and interface-driven damage. For Q&P steels, the model must account for retained-austenite transformation, thermomechanical loading, evolving phase contrast, and the transition from transformation-assisted deformation to damage-dominated softening. A Taylor-type crystal plasticity framework is used throughout this work because it retains microstructure sensitivity while remaining efficient for material-point simulations over a broad range of deformation conditions.

4.1 Research Objectives

The objectives of this research are to:

1. Develop a thermodynamically consistent baseline crystal plasticity damage model for rate-dependent void-driven damage evolution in HSLA steels.

2. Develop a microstructure- and interface-sensitive damage evolution model for dual-phase steels for various loading conditions.
3. Develop a transformation-coupled crystal plasticity damage model for retained austenite containing Q&P steels.

4.2 Summary of Contributions

The work completed to achieve the research objectives is presented in the next three chapters. Research objective (1) is completed in Chapter 5. Research objective (2) is completed in Chapter 6. Research objective (3) is completed in Chapter 7. These chapters are based on the following published, submitted, or prepared manuscripts:

Chapter 5: **S. Dayani**, W. Muhammad, A. Brahme, F. Hekmat, T. Sabiston, K. Inal, *Thermodynamically consistent damage evolution model coupled with rate-dependent crystal plasticity: Application to high-strength low alloy steel at various strain rates*, International Journal of Plasticity 186 (2025), 104255.

Chapter 6: **S. Dayani**, W. Muhammad, A. Brahme, F. Hekmat, T. Sabiston, K. Wang, K. Inal, *Microstructure-informed thermomechanical crystal plasticity damage modeling of dual-phase steels*, manuscript is submitted to Journal of Materials Research and Technology, JMRT-D-26-07085.

Chapter 7: **S. Dayani**, W. Muhammad, A. Brahme, F. Hekmat, T. Sabiston, K. Wang, K. Inal, *A thermomechanically coupled crystal plasticity damage model for quenching and partitioning steels: Effects of retained austenite stability, strain rates, and temperatures*, manuscript is submitted to International Journal of Plasticity, INTPLA-D-26-00833.

5 Development of Thermodynamically Consistent Crystal Plasticity Damage Model for HSLA Steels

In this chapter, a thermodynamically consistent rate-dependent crystal plasticity damage model is developed for high strength low-alloy steels. The model incorporates crystallographic slip, dislocation density evolution, internal temperature rise, void nucleation, and void growth within a unified constitutive framework. Damage is introduced as an evolving internal variable that contributes to volumetric deformation and degradation of the stress response, allowing the model to capture damage-driven post-necking behavior and failure. Detailed experimental characterization is performed for HR340 and HR550 steels using electron backscatter diffraction, uniaxial tensile testing over quasi-static and intermediate strain rates, digital image correlation, and high-speed infrared thermography. The proposed model is calibrated and validated against experimentally measured stress–strain responses, temperature evolution, and texture evolution. The chapter also investigates the coupled influence of strain rate and internal temperature rise on dislocation evolution, damage accumulation, and post-necking softening behavior.

The chapter presents an accepted manuscript of an article published in International Journal of Plasticity.

International Journal of Plasticity 2025;186:104255. Doi: 10.1016/j.ijplas.2025.104255

Thermodynamically Consistent Damage Evolution Model Coupled with Rate-dependent Crystal Plasticity: Application to High Strength Low-alloy Steel at Various Strain Rates

Sandipkumar Dayani[a], Waqas Muhammad[a], Abhijit Brahme[a], Fatemeh Hekmat[b], Trevor Sabiston[c], Kaan Inal[a]

[a] Department of Mechanical and Mechatronics Engineering, University of Waterloo, Waterloo, Ontario, N2L 3G1, Canada

[b] General Motors Technical Centre, General Motors, Warren, MI, 48092, United States

[c] Canadian Technical Centre, General Motors of Canada Limited, Oshawa, Ontario, L1J 0C5, Canada

Overview

High-strength low-alloy (HSLA) steels demonstrate superior strength and load-bearing capacity compared to traditional plain carbon steel. However, these steels are susceptible to microstructural damage even at intermediate strain rates, which can compromise their performance in automotive application. This research aims to investigate the stress–strain response, internal temperature rise, and damage evolution in HSLA steels under quasi-static and intermediate strain rates. The initial microstructure of two different grades of HSLA steels, HR340 and HR550, are characterized using Electron Backscatter Diffraction (EBSD) data. During uniaxial tensile tests at various strain rates, a high-speed infrared thermal camera is utilized to capture the rise of the instantaneous surface temperature within the gauge section of the specimens. A new, thermodynamically consistent rate-dependent crystal plasticity formulation is developed. The damage evolution is governed by a thermodynamic driving force that accounts for various effects (i.e., temperature, void nucleation, and void growth). A power-law based damage formulation is proposed to account for the effects of strain rates and internal temperature rise on the damage evolution. The constitutive model is implemented into a crystal plasticity (CP) formulation to study the effects of damage, temperature and texture evolution on localized deformation in HSLA steel. The constitutive model is calibrated using experimental stress–strain data and temperature evolution measurements at different strain rates. The new model not only accurately predicts the softening/post-necking behavior and failure of HR340 and HR550 but also accurately captures temperature variations in the material, aligning well with experimental results. The texture evolution prediction by the developed model also demonstrated good agreement with experimentally observed texture evolution at different strain

rates. This study highlights the significant influence of strain rate and internal temperature rise on the damage, dislocation density evolution and microstructural behavior of HSLA steels. The model serves as a robust physics-based foundation for future investigative studies.

Keywords: High-strength low alloy (HSLA) steel; Crystal plasticity; Damage evolution; Internal temperature change; Void nucleation; Thermodynamic framework; Texture evolution

5.1 Introduction

Over the past decade, significant progress has been made in the development of high-strength low alloy (HSLA) structural steels, showcasing an exceptional combination of high strength and ductility. HSLA steels became a good choice for applications where structural integrity, weight reduction, and sustainability are key considerations. They offer the advantage of reduced weight without compromising passenger safety and while meeting stringent environmental standards [5]. Understanding and accurately representing the evolution of damage in HSLA steels is important since this directly impacts their reliability and performance in scenarios involving dynamic forces, such as crashworthiness.

It is well-known that plastic deformation leads to a process of damage accumulation involving void nucleation, growth, and coalescence, ultimately leading to fracture in structural alloys [126]. Numerous research has focused on developing micromechanics-based models for the ductile fracture process. Early pioneering work by McClintock [12] and Rice and Tracey [10] delved into ductile failure, employing micromechanical modeling strategies and examining void growth in infinite elastic-plastic materials containing single voids. McClintock [12] considered cylindrical voids, while Rice and Tracey [10] explored the response of spherical voids. Needleman [137] pioneered the use of unit cell analyses to study void growth in elastic-plastic materials containing a periodic array of voids. Furthermore, various constitutive models have been proposed to describe the processes of nucleation [137–140], growth [10–12,141], and coalescence of voids [142]. These models have been developed to simulate the initiation and progression of damage, ultimately leading to failure under monotonic loads in macroscale formulations.

In ductile fracture mechanics, void nucleation and growth are considered critical drivers of material damage, particularly in high-strength alloys subjected to complex loading conditions. Void nucleation typically initiates at microstructural imperfections, such as precipitates and inclusions, and is strongly influenced by stress triaxiality and strain rate. High triaxiality conditions, such as those near geometric notches, promote nucleation by increasing hydrostatic

stress, while lower triaxiality conditions, dominated by deviatoric stresses, influence void growth rather than coalescence [143,144]. Additionally, strain rate sensitivity has been shown to favor nucleation over void growth, with higher strain rates accelerating the initiation of voids, as observed in studies on BCC and FCC metals [145,146]. These findings indicate that void nucleation and growth rather than coalescence are essential mechanisms in ductile failure. This study, therefore, focuses on nucleation and growth to model damage evolution, omitting coalescence for a more targeted and physically justified approach to fracture analysis.

Due to their mechanism-based formulation to represent grain-level behavior, crystal plasticity (CP) models are extensively used to understand and predict mechanical behavior, texture evolution, and strain localization in polycrystal materials [103]. Guery et al. [147] investigated the slip activities of austenitic stainless-steel employing in-situ microscopic digital image correlation and the crystal plasticity finite element method (CPFEM). Yalçinkaya et al. [148] investigated the effects of the martensite phase and the grain size of the ferrite phase on the plasticity and localized deformation of dual phase steel with a crystal plasticity model. Connolly et al. [23,149] later introduced thermodynamically consistent rate-dependent crystal plasticity models for quenched and partitioned steel to capture plastic slip and martensitic phase transformation for various strain rates and temperatures. The microscopic evolution of local strain partitioning for DP steels under various loading conditions was simulated using a CPFEM approach by Misirlioglu et al. [150]. Given the complexity of material behavior, integrating damage evolution with crystal plasticity offers a robust approach to thoroughly investigate damage progression and failure in materials.

Bammann and Aifantis [127] pioneered a deformation gradient to model void growth within a multiplicatively decomposed kinematics map, although in a non-crystal plasticity framework. Potirniche et al. [17] investigated the impact of lattice rotation on void behavior and reported that the void growth rate varies with orientations under uniaxial tension by utilizing CP theory. Abed et al. [151] examined damage in steel at different plastic strain levels under low and intermediate strain rates, developing an isotropic damage model to capture damage evolution during the deformation process. Hu et al. [152] developed an integrated CP and continuum damage mechanics model to simulate the entire deformation history of 5052 aluminum alloy under elevated temperatures. Shang et al. [153] introduced an extended model for void growth that considers the influence of grain size, demonstrating a threshold grain size for inducing macroscopic deformation localization. An analysis of the microstructure and damage evolution in martensitic steel, by

utilizing a multiscale finite element model in combination with the GTN (Gurson-Tvergaard-Needleman) model was presented by Meade et al. [154]. Similarly, Frodal et al. [155] utilized a CP framework that was coupled with damage to simulate the ductile fracture in polycrystalline specimens with varying initial textures. The impact of crystallographic orientation on the growth of voids in polycrystalline materials has been explored by Liu et al. [156] and later by Zhu et al. [157]. Salvini et al. [158] developed a coupled crystal plasticity and phase field damage model to examine the effects of grain boundary misorientation and carbide precipitation on damage initiation in stainless steel. However, all the above studies examined the effect of crystallographic orientation based on a distribution of random grain orientations.

Understanding the damage behavior of HSLA steel under different strain rates is crucial for its use in automotive applications. Even at intermediate strain rates, most of the energy involved in deforming the material is dissipated as heat, with only a minor fraction being retained within the material. Thus, the generated heat leads to work softening in the material [159]. Extensive literature exists on deformation induced heating and thermal phenomena during mechanical straining. It is well-established that a significant portion of the plastic work is transformed into heat [114,160–165]. Various physical processes occurring during deformation involve the generation or absorption of heat simultaneously. At a macroscopic level, this is experienced as deformation induced heating, where a fraction of the plastic work dissipates as heat. This continuous temperature change during deformation significantly influences the stress–strain response and the damage behavior of a material. For instance, heating can reduce the yield stress and ductility of the material during a tensile test. Numerous investigations have been carried out to address this issue [96,166,167]. Lin and Wagoner [160] conducted an experimental investigation of deformation induced heating during tensile testing, demonstrated the influence of temperature rise on ductility. Galiev et al. [168] focused on both experimental and numerical investigations of local temperature changes in the fracture zone during high-strain tensile testing, highlighting the impact of adiabatic heating on flow stress.

Dislocation density is a pivotal aspect in modeling microstructural-based damage evolution models for HSLA steel, especially under varying strain rates and temperatures. Traditionally, numerous approaches have focused on establishing phenomenological relationships that link material flow stress to temperature and strain rate [169,170]. Dislocations within the material profoundly influence its mechanical properties by dictating the movement, interaction, and accumulation of

dislocations during deformation [171]. As deformation progresses, the evolution of dislocation density serves as a crucial indicator of the microstructural changes occurring under different loading conditions, reflecting both strain hardening and softening phenomena [172]. This evolution is intrinsically linked to the interplay between strain rate and temperature. Higher temperatures enhance dislocation mobility, promoting dynamic recovery processes and recrystallization that can reduce dislocation density [173,174]. Conversely, at lower temperatures or high strain rates, dislocation multiplication dominates, leading to increased density and localized hardening effects. For instance, in stainless steel, thermally activated recovery at elevated temperatures leads to decreased dislocation densities, thereby mitigating strain hardening [173].

Many damage models primarily focus on predicting the final fracture condition and often make the simplifying assumption of linear damage accumulation, starting from the initiation of plasticity up to fracture at a given strain rate [14,116]. Only a limited number of models incorporate non-linear damage accumulation laws that can be adjusted to accommodate the aforementioned damage measurements [175], it is worth mentioning that previous iterations of these non-linear laws did not fully consider the influence of strain rates on damage mechanisms at the microstructural level. However, recent advancements in crystal plasticity modeling address these limitations by incorporating strain rate effects, heat generation, and void formation mechanisms [158,176–179]. Despite these advancements, many existing models still do not fully account for the effects of strain rates and internal temperature rise on the initiation and propagation of localized deformation.

In this paper, a micromechanics-based temperature-dependent damage evolution model is proposed and coupled with a crystal plasticity constitutive framework to comprehensively model the stress–strain response (including softening/post-necking) and failure in HSLA steels. The proposed crystal plasticity damage model (CPDM) is among the initial, if not the first, constitutive models suitable for both quasi-static ($0.001 – 0.1\ s^{-1}$) and intermediate strain rates ($1 – 500\ s^{-1}$) while also integrating the coupling between damage and temperature evolution within the material. The predictive capabilities of the CPDM are demonstrated by using commercially available HR340 and HR550 sheet materials. Electron Back Scatter Diffraction (EBSD) is employed to characterize the initial microstructure of both sheets. Additionally, a state-of-the-art, ultra-high frame-rate infrared thermal camera is used to capture the temperature evolution in HSLA steels during the deformation process at room temperature. A new damage model is developed, incorporating a strain rate-dependent formulation to accurately capture the softening/post-necking

behavior and failure at various strain rates in HSLA steels. In addition, a novel thermodynamic-based framework is developed, considering isothermal, adiabatic, and general thermal boundary conditions to capture the temperature evolution in the material effectively. The successful implementation of the CPDM represents a significant advancement towards establishing a framework capable of accounting for temperature-dependent damage evolution at varying strain rates, ultimately aiding in the precise prediction of local temperature rise and failure in HSLA steels.

5.2 Experimental Characterization

In the present work, two different grades of HSLA steel, HR340 and HR550 where "HR" signifies "Hot Rolled" processing and the numerical values denote the minimum yield strength in MPa, with a nominal sheet thickness of 1.30 mm, are used. The chemical composition of each HSLA steel is provided in Table 5-1.

Table 5-1: Chemical composition of HSLA 340 and 550 (wt. %).

	Fe	C	Si	Mn	Al	S	Ti	Nb
HR340	Bal	0.08	0.014	0.41	0.041	0.01	0.001	0.04
HR550	Bal	0.05	0.225	0.547	0.026	0.002	0.055	0.014

5.2.1 Mechanical Testing

Uniaxial tensile tests at strain rates of 0.001 s^{-1} and 0.1 s^{-1} are conducted at room temperature using an MTS servo-hydraulic tensile machine equipped with a 10 kN load cell. In addition, tensile tests at strain rates of 1 s^{-1}, 10 s^{-1}, and 100 s^{-1} are performed using a Hydraulic Intermediate Strain Rate (HISR) apparatus. The HISR apparatus employs a slack-type engagement assembly to pull the specimen in tension at a constant strain rate and is equipped with a 13.3 kN hydraulic actuator featuring a 101.6 mm stroke [180]. To avoid any geometrical effect from one test to another, the same sample geometry is used for test at all strain rates. The geometry of the specimen used for these tests is presented in Figure 5-1(c), featuring a gauge length of 12.5 mm and a width of 1.75 mm. This geometry is sufficiently compact to minimize signal rise time and achieve dynamic equilibrium during high-rate experiments, extending up to a strain rate of 1000 s^{-1} [181]. To ensure the consistency of the results, a minimum of three repetitions are performed for each test condition. Figure 5-1(a) and Figure 5-1(b) provide schematic representations of the experimental setup for the MTS and HISR apparatuses, respectively.

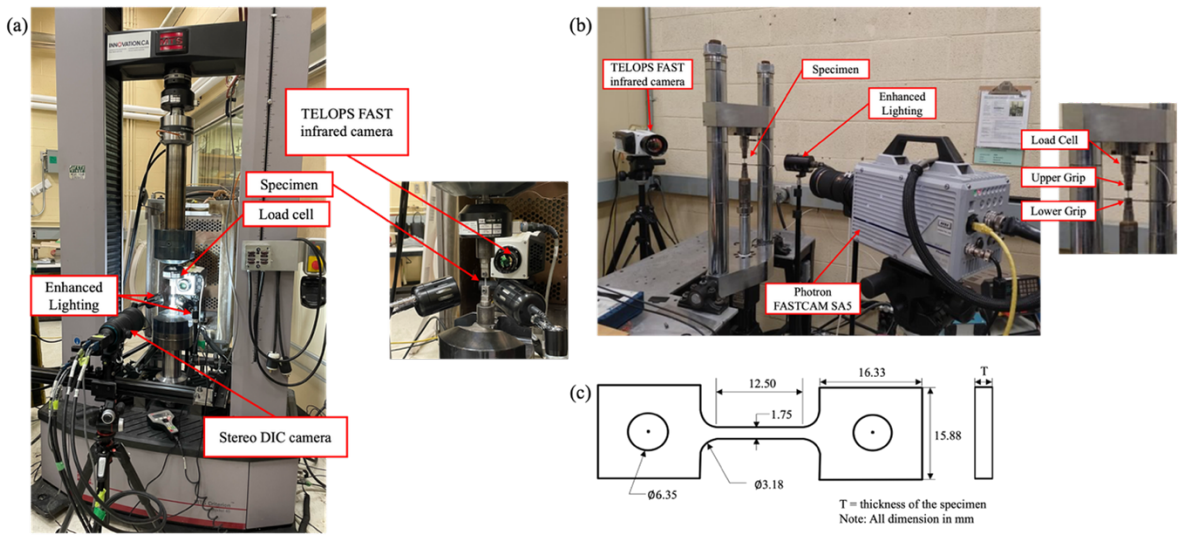


Figure 5-1: (a) MTS machine apparatus for 0.001 s^{-1} and 0.1 s^{-1} strain rates, (b) HISR machine setup for 1 s^{-1}, 10 s^{-1}, and 100 s^{-1} strain rates, and (c) The ASTM (E 8M-04) specimen geometry.

5.2.2 Strain Measurements

A digital image correlation (DIC) system is employed to capture speckled deformed images of the gage section of the tensile specimen during testing. A high-resolution Point Grey Research GRAS-50S5M-C cameras are employed for 0.001 s^{-1} and 1 s^{-1}, while Photron FASTCAM SA5 high-speed cameras are utilized for strain rates of 1 s^{-1}, 10 s^{-1} and 100 s^{-1}. The speckle pattern is applied using Rust-Oleum spray paint in a random manner, following the recommendations provided by Correlated Solutions. The DIC data is subsequently analyzed using VIC-3D, a commercial software, to extract local strain evolution during tensile deformation. The hardware and analysis parameters for DIC corresponding to each strain rate are provided in Table 5-2.

Table 5-2: Summary of DIC system and analysis parameters.

Strain rate (s^{-1})		**0.001**	**0.1**	**1**	**10**	**100**
DIC hardware parameter	Camera manufacturer & model	Point Grey Research GRAS-50S5M-C		Photron FASTCAM SA5		
	Lens manufacturer, model, focal length	Tamron, SP F/3.5 Di, 180 mm		Sigma, f/2.8 EX DG OS HSM, 180 mm		
	Frame rate (Hz)	2	20	2000	15000	84000
	Speckling technique	Paint spray				
DIC analysis parameter	DIC software name and manufacturer	Vic-3D 7, Correlated Solutions				

Subset size (px)	11
Step size (px)	3
Strain filter	5
Subset weight	Gaussian – center weight
Strain filer weights	Gaussian– 90% center-weight

5.2.3 High Speed Thermal Imaging

The surface temperature of the specimen is measured using a high-speed infrared radiation (IR) camera with a mid-wavelength range (λ = 3-5 μm) from the Telops IRC-TS series. The Telops FAST camera can achieve up to 3100 frames per second (fps) in full frame mode and 120,000 fps in sub-window mode. The camera setting for each strain rate are detailed in Table 5-3.

Table 5-3: Summary of IR camera system parameters.

Strain rate (s^{-1})	**0.001**	**0.1**	**1**	**10**	**100**
Camera manufacturer and model	Telops IRC TS-IR-2K				
IR software name and manufacturer	HypIR, Telops				
Lens manufacturer, model, focal length	Telops bayonet mounted lens, f/2.5, 50 mm		Telops bayonet mounted lens, f/2.5, 100 mm		
Frame rate (Hz)	2	100	2000	15000	21000
Image size (px)	320x256	320x256	64x112	64x96	64x80

5.2.4 Microstructure Characterization

Microstructure and texture characterization are conducted using a field-emission ThermoScientific Quattro Environmental SEM, which is equipped with a Lumis EBSD detector. A step size of 0.5 μm is consistently applied for all EBSD measurements, and the resulting data underwent further processing using the TSL OIM^{TM} software. To ensure data accuracy, a neighbor CI correlation index of 0.2 is employed during post-processing to remove mis-index points in the dataset.

The EBSD images presented in Figure 5-2(a-b) are captured on the plane on the rolling direction (RD)- transverse direction (TD) planes. The measured grain sizes for HR340 and HR550 are 12.71 μm and 7.21 μm, respectively. The grain size histograms, Figure 5-2(c-d), illustrate the grain size distributions for both materials, revealing a broader distribution for HR340 and a narrower distribution for HR550. In Figure 5-3(a-b), pole figures for HR340 and HR550 are presented,

respectively. Notably, the intensity of pole figures for HR340 and HR550 present weak textures, with maximum intensities of 3.055 and 2.641, respectively.

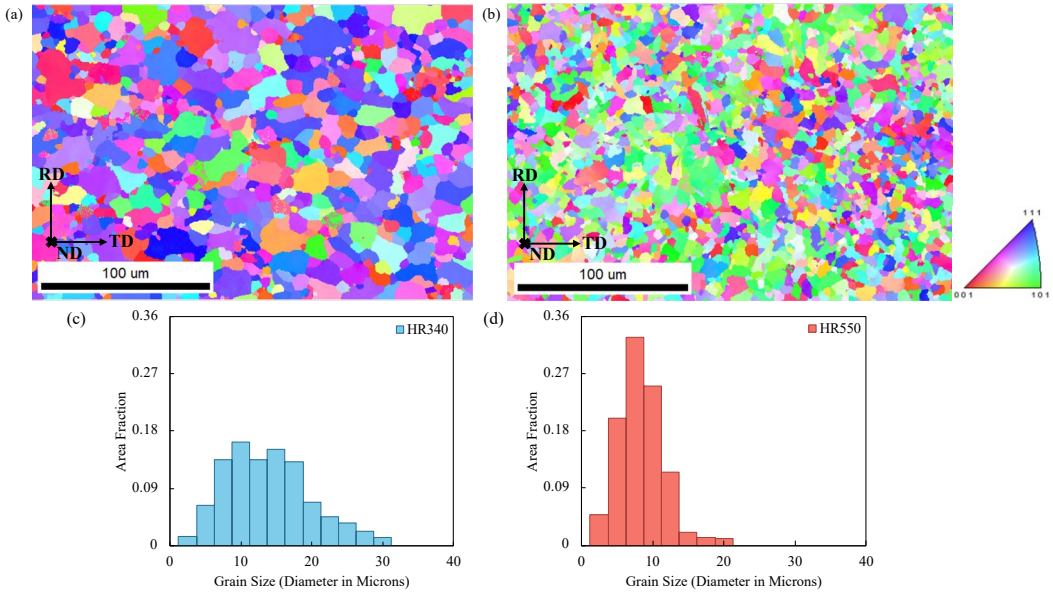


Figure 5-2: Inverse pole figure (IPF) map for (a) HR340 and (b) HR550, and grain size histogram for (c) HR340 and (d) HR550.

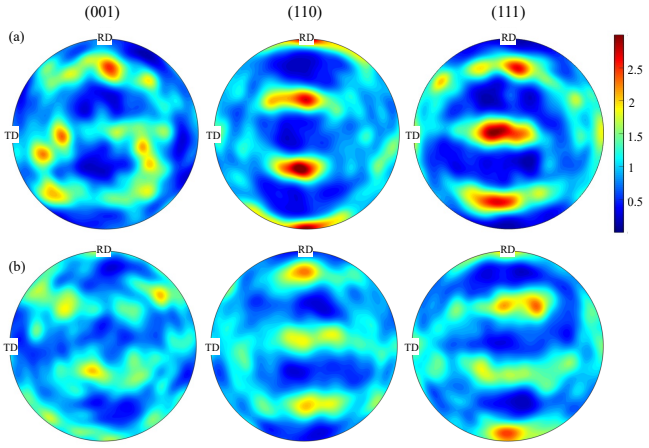


Figure 5-3: Pole figures for (a) HR340 and (b) HR550.

5.2.5 Experimental Results and Discussion

The engineering stress–strain curves, obtained from the uniaxial tensile tests conducted at different strain rates with the specimens oriented along the RD, are presented in Figure 5-4(a-b) for HR340 and HR550, respectively. For HR340, the strain at failure is nearly the same at lower strain rates (0.001, 0.1, and 1 s^{-1}). However, the elongation to failure increases as increases strain rate (10 s^{-1} and 100 s^{-1}), which indicates improved ductility; a similar phenomenon is also observed for

HR550. Notably, HR340 outperforms HR550 in terms of elongation to failure, which can be attributed to differences in material composition and microstructure. HR550 contains higher silicon content (shown in Table 5-1) than HR340 which contributes to an increase in the strength of the material. This is attributed to the role of silicon in enhancing the hardenability of steel by inhibiting grain growth [182]. Also, the lower silicon content contributes to increased elongation to failure. The yield stress, ultimate tensile strength (UTS), elongation to failure and the corresponding standard deviations across different repeats at different strain rates are summarized in Table 5-4 for both grades of HSLA steels. The yield stress for HR340 and HR550 specimens at 0.001 s^{-1} is 394.6 MPa and 602.5 MPa respectively, and the UTS for these specimens is 587.3 MPa and 764.3 MPa (see Table 5-4). It is shown that yield stress increased by approx. 36% and 15% as strain rate increased from 0.001 s^{-1} to 100 s^{-1} for HR340 and HR550 respectively.

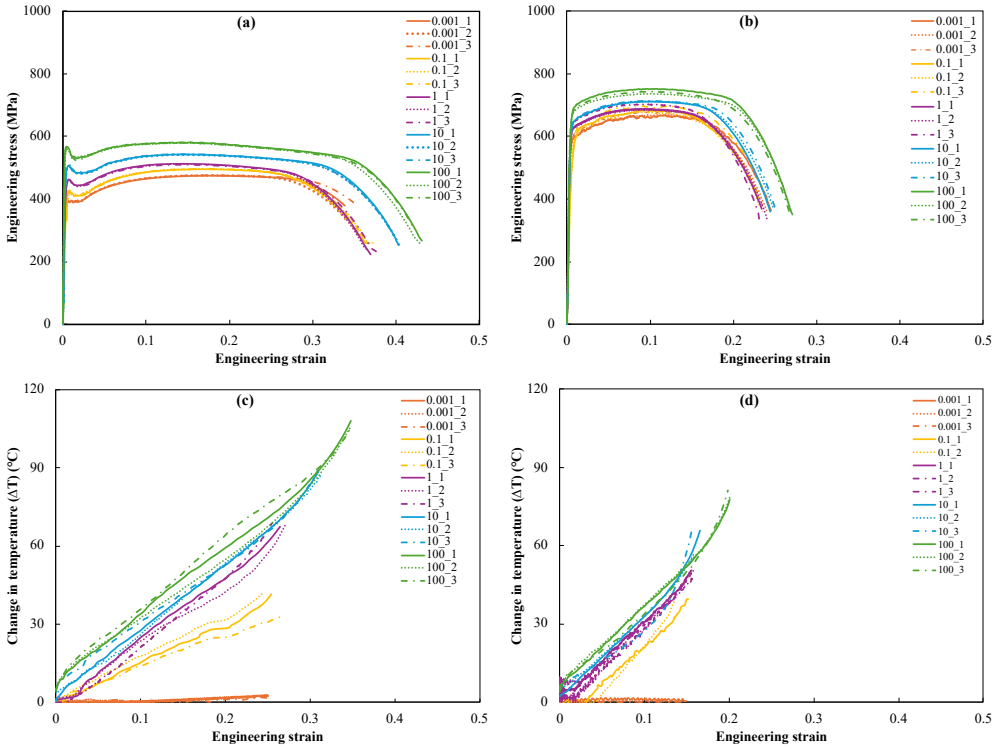


Figure 5-4: Eng. stress vs. Eng. strain (a-b) and change in temperature vs. Eng. strain (c-d) response for HR340 (a-c) and HR550 (b-d). [The legend indicates the strain rate in s^{-1} followed by the test number (e.g., 0.001_1 represent a strain rate of 0.001 s^{-1} for the first test)].

Table 5-4: Averaged tensile properties of HR340 and HR550 steels across different repeats.

HR340	HR550

Strain rate (s^{-1})	Yield stress (MPa)	UTS (MPa)	Elongation (%)	Yield stress (MPa)	UTS (MPa)	Elongation (%)
0.001	394.6±0.2	587.3±0.0	29.21±0.0	602.5±0.8	764.3±0.2	21.94±2.1
0.1	418.5±0.1	606.1±0.0	31.47±3.3	606.3±2.1	771.3±1.9	20.69±4.0
1	458.3±0.0	617.9±0.0	30.43±0.0	636.2±3.3	773.13±1.9	20.98±1.7
10	503.4±0.1	666.6±0.1	33.89±0.1	659.8±0.1	808.9±0.6	22.22±0.4
100	539.5±1.8	710.8±0.2	35.53±0.1	691.5±1.7	844.6±0.1	23.84±0.1

In this study, the changes in temperature within the localized region are carefully tracked during the tensile tests performed on both types of steel. Figure 5-4(c-d) demonstrate the change in temperature near the neck region as a function of engineering strain. The data collected from the neck region is a collection of many data points over time. These data points are then averaged to give a single value that represents the general behavior in the necking region during the test. The graphs show a significant temperature change as the strain rate increases. This phenomenon can be attributed to several contributing factors, including strain rate sensitivity, adiabatic heating resulting from plastic deformation, and the dissipation of mechanical energy [183]. Consequently, the higher strain rate induces a global temperature increase, primarily due to the reduced time available for dissipating the heat generated by plastic deformation [184]. At quasi-static strain rates, the lower heat generation due to slower deformation processes results in negligible temperature rise in the material. Although heat dissipation can occur, the primary reason for the lack of temperature increase is the low amount of heat generated initially. Conversely, at higher strain rates, temperature increases rapidly due to the adiabatic heating effect caused by the rapid deformation. Furthermore, the generated heat has the potential to influence the underlying damage mechanisms. Table 5-5 summarizes the average maximum temperature change and the corresponding standard deviations within the neck region across different repeats.

The temperature distributions over a gauge length of the specimens during the tensile test are measured. The temperature hotspots (shown in Figure 5-5 and Figure 5-6) observed in the thermal images correspond to the strain concentrations identified in the DIC measurements. This correlation is ensured by synchronizing the thermal and mechanical data acquisition systems, allowing for an accurate spatial and temporal alignment of the data. These images were captured \ prior to failure, highlighting the regions of localized deformation. The strain hotspots, which

indicate regions of localized deformation, are directly associated with areas of increased temperature, reflecting the local accumulation of plastic work and its conversion to heat.

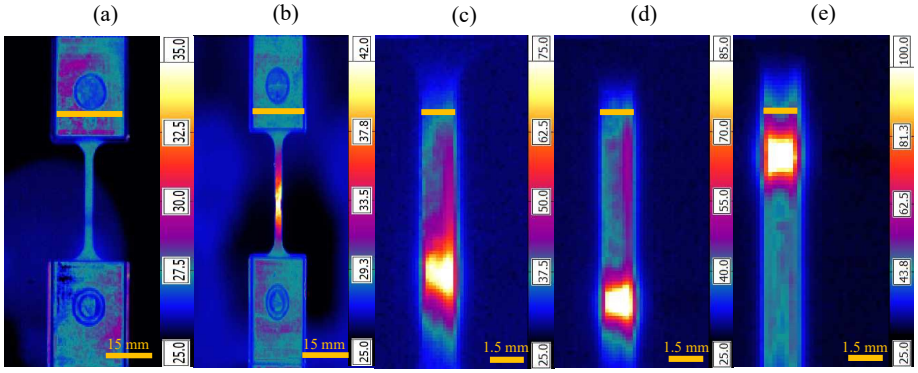


Figure 5-5: Temperature increase at various strain rates, (a) 0.001 s^{-1}, (b) 0.1 s^{-1}, (c) 1 s^{-1}, (d) 10 s^{-1}, and (e) 100 s^{-1} for HR340.

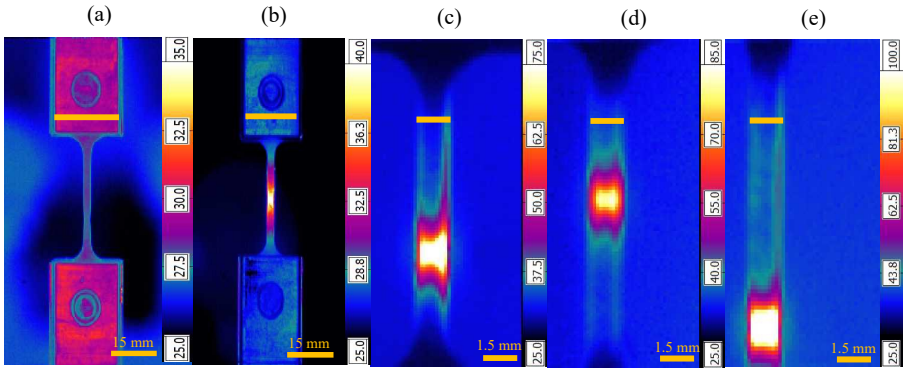


Figure 5-6: Temperature increase at various strain rates, (a) 0.001 s^{-1}, (b) 0.1 s^{-1}, (c) 1 s^{-1}, (d) 10 s^{-1}, and (e) 100 s^{-1} for HR550.

Table 5-5: Average of maximum temperature change during tensile testing within the necking region across different repeats.

Strain rate (s^{-1})	**0.001**	**0.1**	**1**	**10**	**100**
Max. Temp. (HR340) (°C)	2.5±1.7	41.8±0.5	67.4±1.1	83.7±0.3	118.1±1.3
Max. Temp. (HR550) (°C)	2.1±0.6	39.3±1.1	43.7±1.9	65.8±2.1	83.1±1.5

5.3 Model Development

This section outlines the formulation of a constitutive model designed to simulate damage evolution, incorporating void nucleation and growth. The new CPDM can account for the large strain behavior and damage evolution in HSLA steels at various temperatures and strain rates. Damage in metals is typically associated with the interplay of elastic and plastic components and

damage components of deformation. Elastic deformation preserves the crystalline lattice within each grain, while plastic deformation involves irreversible processes, such as slip system activity on crystallographic planes. These plastic processes can result in both deviatoric effects and volumetric changes due to the initiation and expansion of voids stemming from microscale defects [185]. Moreover, the focus is placed on the volume fraction of voids rather than their geometric shape. This approach enables a more comprehensive representation of the void effects on the overall stress–strain behavior of the material. Additionally, the Tylor-type polycrystal plasticity model is employed to simulate the deformation behavior of HSLA alloys. This model assumes that all grains within the polycrystal undergo the same deformation as the macroscopic deformation of the continuum, thereby simplifying the complex microstructural interactions that occur during deformation.

5.3.1 Kinematics and Constitutive Framework

The overall deformation of a crystallite arises from three distinct physical mechanisms: crystallographic slip involving the motion of dislocations on active slip systems, volumetric expansion due to damage initiation, and elastic lattice distortion. In the case of BCC crystals, plastic deformation occurs through crystallographic slip on 12 {110} <111> and 12 {112} <111> slip systems. This plastic deformation can be visualized as a series of plastic simple shears along various slip systems, with the lattice and slip system vectors ($\mathbf{s}^{(\alpha)}$, $\mathbf{m}^{(\alpha)}$) remaining essentially undistorted and unrotated (note that "α" is not a tensor index and ranges from one to the number of slip systems). Subsequently, the material undergoes volumetric expansion as damage initiates and progresses. Finally, the material and lattice are considered to undergo elastic deformation and rigid rotation from the state of volumetric expansion to the current configuration, taking the material from the undeformed state, $\mathbf{R_0}$, to the final deformed state, $\mathbf{R}$ (as demonstrated Figure 5-7). The intermediate configuration ($\overline{\mathbf{R}}$) is mapped by plastic deformation gradient and following volumetric deformation gradient new intermediate configuration ($\widetilde{\mathbf{R}}$) is mapped.

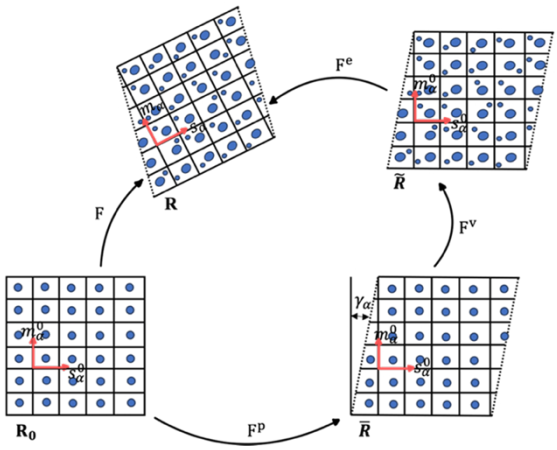


Figure 5-7: Decomposition of the deformation gradient.

Following this multiplicative decomposition of the deformation gradient, the total deformation gradient **F** can be expressed as:

$$\mathbf{F} = \mathbf{F}^{e}\mathbf{F}^{v}\mathbf{F}^{p} \tag{5-1}$$

Under the specified conditions for each of the defined deformation gradients,

$$\det(\mathbf{F}^{e}) = J^{e},\ \det(\mathbf{F}^{p}) = 1,\ \det(\mathbf{F}^{v}) > 1 \tag{5-2}$$

where, $\mathbf{F}^{p}$ is solely associated with crystallographic slipping along the specific slip systems, $\mathbf{F}^{v}$ represents the continuous distribution of voids contributing to permanent volume change, and $\mathbf{F}^{e}$ accounts for the elastic deformation and any rigid body rotation.

Following the Eq. 5-1, the spatial gradient of velocity **L** can be expressed as:

$$\mathbf{L} = \dot{\mathbf{F}}\mathbf{F}^{-1} \tag{5-3}$$

$$\mathbf{L} = \dot{\mathbf{F}}^{e}\mathbf{F}^{e-1} + \mathbf{F}^{e}\dot{\mathbf{F}}^{v}\mathbf{F}^{v-1}\mathbf{F}^{e-1} + \mathbf{F}^{e}\mathbf{F}^{v}\dot{\mathbf{F}}^{p}\mathbf{F}^{p-1}\mathbf{F}^{v-1}\mathbf{F}^{e-1} \tag{5-4}$$

Hence, the velocity gradients associated with elastic, volumetric, and plastic deformations in the current configuration are derived from Eq. 5-4

$$\mathbf{L}^{e} = \dot{\mathbf{F}}^{e}\mathbf{F}^{e-1} \tag{5-5}$$

$$\mathbf{L}^{v} = \mathbf{F}^{e}\dot{\mathbf{F}}^{v}\mathbf{F}^{v-1}\mathbf{F}^{e-1} \tag{5-6}$$

$$\mathbf{L}^{p} = \mathbf{F}^{e}\mathbf{F}^{v}\dot{\mathbf{F}}^{p}\mathbf{F}^{p-1}\mathbf{F}^{v-1}\mathbf{F}^{e-1} \tag{5-7}$$

Decomposing the provided relations into their symmetric and antisymmetric components yields the elastic, volumetric, and plastic strain rates, represented as $\mathbf{D}^{e}$, $\mathbf{D}^{v}$ and $\mathbf{D}^{P}$, respectively. Furthermore, there exists a relationship between the plastic spin $\boldsymbol{\Omega}^{p}$ and the spin $\boldsymbol{\Omega}^{e}$, which is associated with rigid lattice rotation.

$$\mathbf{D} = \frac{1}{2}[\mathbf{L} + \mathbf{L}^{T}] = \mathbf{D}^{e} + \mathbf{D}^{v} + \mathbf{D}^{P} \quad 5\text{-}8$$

$$\mathbf{\Omega} = \frac{1}{2}[\mathbf{L} - \mathbf{L}^{T}] = \mathbf{\Omega}^{e} + \mathbf{\Omega}^{p} \quad 5\text{-}9$$

As mentioned earlier, it is assumed that slip plasticity occurs solely due to plastic shearing along slip systems [15]. This results in the distortion of each shear plane normal and direction, such that

$$\mathbf{s}_{\alpha}^{e} = \mathbf{F}^{e}\mathbf{s}_{\alpha} \quad 5\text{-}10$$

$$\mathbf{m}_{\alpha}^{e} = \mathbf{m}_{\alpha}\mathbf{F}^{e-1} \quad 5\text{-}11$$

where $\mathbf{s}_{\alpha}^{e}$ and $\mathbf{m}_{\alpha}^{e}$ represent the fully deformed configuration of the shear plane direction and normal, respectively. The introduction of the following symmetric and skew-symmetric tensors for each slip system α can be made.

$$\mathbf{P}_{\alpha} = \frac{1}{2}[\mathbf{s}_{\alpha}^{e} \otimes \mathbf{m}_{\alpha}^{e} + \mathbf{m}_{\alpha}^{e} \otimes \mathbf{s}_{\alpha}^{e}] \quad 5\text{-}12$$

$$\mathbf{W}_{\alpha} = \frac{1}{2}[\mathbf{s}_{\alpha}^{e} \otimes \mathbf{m}_{\alpha}^{e} - \mathbf{m}_{\alpha}^{e} \otimes \mathbf{s}_{\alpha}^{e}] \quad 5\text{-}13$$

To derive an equation that represents the volumetric deformation gradient $\mathbf{F}^{v}$ as a function of the accumulated damage in the material, we utilize the approach developed by Horstemeyer et al. [186]. Let ϕ represent the volume of porosity (cracks/voids) per unit volume of material. The increase in material volume (V_v) from configuration $\overline{R}$ to $\widetilde{R}$ is related to the total volumes for each of the two configurations, $\widetilde{V}$ and V_0, respectively. ($\widetilde{V}$ is volume of material in $\widetilde{R}$ configuration and V_0 is material volume in $\overline{R}$ configuration). This establishes the following relation between these material volumes:

$$\widetilde{V} = V_0 + V_v \quad 5\text{-}14$$

The definition of porosity is expressed as:

$$\phi = \frac{V_v}{\widetilde{V}} \quad 5\text{-}15$$

Based on the deformation gradient, it follows that

$$J = \det(\mathbf{F}^{v}) = \frac{\widetilde{V}}{V_0} = \frac{1}{1 - \phi} \quad 5\text{-}16$$

It is assumed that the change in porosity causes only an isotropic volumetric change in the material (any plastic anisotropy comes from the deviatoric plasticity including crystal reorientation and from an anisotropic hardening in the kinetics), the volumetric deformation gradient is written as

$$\mathbf{F}^{\mathrm{v}} = \frac{1}{(1-\phi)^{1/3}}\,\mathbf{I} \tag{5-17}$$

The plastic strain -rate and spin for the crystal can be expressed as follows:

$$\mathbf{D}^{\mathrm{p}} = \sum_{\alpha} \mathbf{P}_{\alpha}\dot{\gamma}_{\alpha} \tag{5-18}$$

$$\mathbf{\Omega}^{\mathrm{p}} = \sum_{\alpha} \mathbf{W}_{\alpha}\dot{\gamma}_{\alpha} \tag{5-19}$$

where $\dot{\gamma}_{\alpha}$ is the shear rate on the slip system α.

As mentioned earlier, the damage is isotropic which mean spin becomes zero. The volumetric strain rate and spin rate can be written as,

$$\mathbf{D}^{\mathrm{v}} = \frac{\dot{\phi}}{3(1-\phi)}\mathbf{I} \tag{5-20}$$

$$\mathbf{\Omega}^{\mathrm{v}} = 0 \tag{5-21}$$

The kinetic equations for the plastic shear rate on a slip system, $\dot{\gamma}_{\alpha}$, and the damage rate, $\dot{\phi}$, are expressed as functions of the thermodynamic driving force and a corresponding critical driving force, as follows:

$$\dot{\gamma}_{\alpha} = \dot{\gamma}_{\alpha}\left(f_p^{\alpha}, g_p^{\alpha}\right) \tag{5-22}$$

$$\dot{\phi} = \dot{\phi}(f_d, g_d) \tag{5-23}$$

where f_p^{α} and g_p^{α} are the thermodynamic driving force and critical driving force for plastic slip and f_d and g_d is the thermodynamic driving force and critical driving force for damage. The thermodynamic driving forces are presented in section 3.2.

The stress is assumed to follow a hyper-elastic constitutive law

$$\boldsymbol{S}^{e} = \mathbb{C} : \boldsymbol{E}^{e} \tag{5-24}$$

where $\mathbf{S}^{\mathrm{e}}$ is the second Piola-Kirchhoff stress, $\mathbf{E}^{\mathrm{e}}$ is the elastic Green-Lagrange strain given by $\mathbf{E}^{\mathrm{e}} = \left(\mathbf{F}^{\mathrm{e}}\mathbf{F}^{\mathrm{e}T} - \mathbf{I}\right)/2$, and $\mathbb{C}$ is the 4th order elastic moduli tensor.

Next, the total time derivative of Eq. 5-24 is rearranged giving the elastic Jaumann derivative of Kirchhoff stress

$$\hat{\boldsymbol{\tau}}^{\mathrm{e}} = \dot{\boldsymbol{\tau}} - \mathbf{\Omega}^{\mathrm{e}}\boldsymbol{\tau} + \boldsymbol{\tau}\mathbf{\Omega}^{\mathrm{e}} = \boldsymbol{\mathcal{L}}\mathbf{D}^{\mathrm{e}} \tag{5-25}$$

where, $\hat{\boldsymbol{\tau}}^{\mathrm{e}}$ is the Jaumann rate of the Kirchhoff stress tensor $\boldsymbol{\tau}$ based on the lattice rotation, and $\boldsymbol{\mathcal{L}}$ is the elastic moduli tensor in the fully deformed configuration defined by,

$$\boldsymbol{\mathcal{L}} = \mathbf{F}^{\mathrm{e}}\mathbf{F}^{\mathrm{e}}\mathbb{C}\mathbf{F}^{\mathrm{e}\mathrm{T}}\mathbf{F}^{\mathrm{e}\mathrm{T}} \quad 5\text{-}26$$

It is assumed that $\boldsymbol{\tau}:\mathbf{D}$ and $\mathbf{D}:\boldsymbol{\tau}$ are small relative to $\dot{\boldsymbol{\tau}}$. The total Jaumann rate of the Kirchhoff stress is:

$$\hat{\boldsymbol{\tau}} = \dot{\boldsymbol{\tau}} - \boldsymbol{\Omega\tau} + \boldsymbol{\tau\Omega} = \hat{\boldsymbol{\tau}}^{e} - \sum_{\alpha=1}^{N} \boldsymbol{B}_{\alpha}\dot{\gamma}_{\alpha} \quad 5\text{-}27$$

where N is number of slip system and $\boldsymbol{B}_{\alpha}$ is

$$\boldsymbol{B}_{\alpha} = \boldsymbol{W}_{\alpha}\boldsymbol{\tau} - \boldsymbol{\tau}\boldsymbol{W}_{\alpha} \quad 5\text{-}28$$

To reformulate constitutive Eq. 5-27 in terms of the Jaumann rate $\hat{\sigma}$ of the Cauchy stress, where $\sigma = \det(\mathbf{F})^{-1}\boldsymbol{\tau}$, the constitutive update for a single crystal is ultimately expressed through the following relationship.

$$\hat{\boldsymbol{\sigma}} = \boldsymbol{\mathcal{L}}:\mathbf{D} - \sum_{\alpha} \dot{\gamma}_{\alpha}\,\mathbf{R}_{\alpha} - \frac{\dot{\phi}}{3(1-\phi)}(\boldsymbol{\mathcal{L}}:\mathbf{I}) - \sigma\mathrm{tr}(\mathbf{D}) \quad 5\text{-}29$$

where a second-order tensor $\mathbf{R}_{\alpha}$ is introduced for each slip system as follows:

$$\mathbf{R}_{\alpha} = \boldsymbol{\mathcal{L}}\mathbf{P}_{\alpha} + \mathbf{B}_{\alpha} \quad 5\text{-}30$$

The three terms in Eq. 5-29 represent elastic trial stress, plastic slip, and damage evolution terms.

5.3.2 Thermodynamic Driving Forces

As outlined in the previous section, the evolution of plastic slip rate and the damage variable is governed by thermodynamic driving forces derived from an energy balance law. This energy balance law, expressed in the undeformed configuration, is given by

$$\rho_0\dot{e} + \nabla\cdot\boldsymbol{q} - \rho_0 r - \boldsymbol{S}:\dot{\boldsymbol{E}} = 0 \quad 5\text{-}31$$

where ρ_0 denotes the material density in its undeformed configuration, $\dot{e}$ represents the rate of change of internal energy density, $\nabla\cdot\boldsymbol{q}$ indicates the divergence of the heat flux, and r accounts for any applied volumetric heating, such as electromagnetic heating. The terms $\boldsymbol{S}$ and $\dot{\boldsymbol{E}}$ correspond to the second Piola-Kirchhoff stress and the Green-Lagrange strain rate, respectively. Compliance with the second law of thermodynamics is achieved by ensuring that the energy dissipation rate $\mathcal{D}$ remains non-negative throughout the process [187] so that

$$\mathcal{D} = -\rho_0\dot{e} + \rho_0\theta\dot{\eta} + \boldsymbol{S}:\dot{\boldsymbol{E}} - \frac{\nabla\theta\cdot\boldsymbol{q}}{\theta} \geq 0 \quad 5\text{-}32$$

where $\dot{\eta}$ is the rate of change of entropy density and θ is the temperature. The dissipation rate can be decomposed into three components

$$\mathcal{D} = \mathcal{D}_p + \mathcal{D}_v + \mathcal{D}_\theta \geq 0 \quad (5\text{-}33)$$

with $\mathcal{D}_\mathrm{p}$, $\mathcal{D}_\mathrm{v}$ and $\mathcal{D}_\theta$ being the dissipations associated with dislocation motion, damage evolution, and heat conduction, respectively, and can defined as

$$\mathcal{D}_p = \sum_{\alpha=1}^{N} \boldsymbol{f}_p^{(\alpha)} \dot{\gamma}_\alpha \quad (5\text{-}34)$$

$$\mathcal{D}_v = f_v \dot{\phi} \quad (5\text{-}35)$$

$$\mathcal{D}_\theta = -\frac{\nabla\theta \cdot \boldsymbol{q}}{\theta} \quad (5\text{-}36)$$

The entropy density can be separated into five components

$$\eta = \eta_e + \eta_v + \eta_p + \eta_m \quad (5\text{-}37)$$

where η_e is the thermal component of the reversible entropy density, η_v is the entropy density related to void mechanisms, η_p represents the entropy density associated with dislocation motion, and η_m is the thermomechanical coupling component of the reversible entropy density.

The thermal component of the reversible entropy density is defined by Turteltaub and Suiker [22],

$$\eta_e = h_A ln\left(\frac{\theta}{\theta_T}\right) \quad (5\text{-}38)$$

where h_A is the specific heat capacity of the grain, and θ_T is the reference temperature. The rate of the entropy density dislocation motion component can be expressed as

$$\dot{\eta}_p = \dot{\gamma}_\alpha \varphi_\alpha \quad (5\text{-}39)$$

where φ_α is the entropy change per unit slip on the slip system α and is assumed to be constant. Next, the rate of the entropy density associated with void mechanism is assumed to be,

$$\dot{\eta}_v = \dot{\phi}\, S_\phi \quad (5\text{-}40)$$

where S_ϕ is the entropy change during damage evolution and is also assumed to be constant.

Using the decomposition of entropy and the Legendre transformation between internal energy and the Helmholtz free energy, defined by $\Psi = \mathrm{e} - \theta\eta_\mathrm{e}$, the dissipation rate can be reformulated as

$$\mathcal{D} = -\rho_0 \dot{\Psi} - \rho_0 \dot{\theta}\eta_e + \rho_0 \theta \dot{\eta}_m + \rho_0 \theta \dot{\eta}_p + \rho_0 \theta \dot{\eta}_v + \boldsymbol{S} : \dot{\boldsymbol{E}} - \frac{\nabla\theta \cdot \boldsymbol{q}}{\theta} \geq 0 \quad (5\text{-}41)$$

The Helmholtz free energy is assumed to follow the form $\Psi(\mathbf{E}^\mathrm{e}, \theta, \rho_d, \phi)$ where ρ_d is the dislocation density of grain. The rate of change of Helmholtz free energy can then be written as

$$\dot{\Psi} = \frac{\partial \Psi}{\partial \boldsymbol{E}^e} : \dot{\boldsymbol{E}}^e + \frac{\partial \Psi}{\partial \theta}\dot{\theta} + \frac{\partial \Psi}{\partial \rho_d}\dot{\rho_d} + \frac{\partial \Psi}{\partial \phi}\dot{\phi} \quad (5\text{-}42)$$

For simplicity, the rate of change of dislocation density is represented as

$$\dot{\rho}_d = w_p^\alpha |\dot{\gamma}^\alpha| \tag{5-43}$$

where w_p^α is the dependence of dislocation density on the plastic slip rates, as outlined by Connolly et al. [23],

$$w_p^\alpha = \left[\frac{1}{bk_1}\sqrt{\rho_d} - k_2\rho_d exp\left(\frac{Q}{\theta}\right)\right] sign(\dot{\gamma}^\alpha) \tag{5-44}$$

In Eq. 5-44, b is the Burgers vector magnitude, k_1 and k_2 are calibration coefficient, θ is the temperature and Q is a temperature-related constant.

The Helmholtz free energy and its total time derivative can be partitioned into four distinct contributions,

$$\Psi = \Psi_m + \Psi_{th} + \Psi_d + \Psi_v \tag{5-45}$$

where Ψ_m represents the contribution of bulk elastic strain energy, Ψ_{th} denotes thermal energy, Ψ_d indicates the dislocation energy and Ψ_v is the volumetric energy coupled with void evolution (nucleation and growth).

Substituting the total time derivatives of the Helmholtz free energy Ψ and rewriting $\mathbf{S} : \dot{\mathbf{E}}$ in terms of $\boldsymbol{\tau}$ and $\boldsymbol{D}$, (using $\dot{\mathbf{E}} = \mathbf{F}^{\mathrm{e}T}\mathbf{D}^{\mathrm{e}}\mathbf{F}^{\mathrm{e}}$) leads to,

$$\begin{aligned}\mathcal{D} = -\rho_0 \left[\mathbf{F}^{\mathrm{e}} \frac{\partial \Psi}{\partial \mathbf{E}^{\mathrm{e}}} \mathbf{F}^{\mathrm{e}T} : \mathbf{D}^{\mathrm{e}} + \frac{\partial \Psi}{\partial \theta}\dot{\theta} + \frac{\partial \Psi}{\partial \rho_d}\dot{\rho_d} + \frac{\partial \Psi}{\partial \phi}\dot{\phi}\right] \\ + \rho_0\theta\left[\mathbf{F}^{\mathrm{e}} \frac{\partial \eta_m}{\partial \mathbf{E}^{\mathrm{e}}} \mathbf{F}^{\mathrm{e}T} : \mathbf{D}^{\mathrm{e}} + \frac{\partial \eta_m}{\partial \eta_e}\frac{\partial \eta_e}{\partial \theta}\,\dot{\theta}\right] + \rho_0\theta\sum_{\alpha=1}^{N}\dot{\gamma}_\alpha\,\varphi_\alpha + \rho_0\theta\dot{\phi}\,S_\phi \\ - \rho_0\dot{\theta}\left[h_A\, ln\left(\frac{\theta}{\theta_T}\right)\right] + \boldsymbol{\tau}: [\boldsymbol{D}^e + \boldsymbol{D}^p + \boldsymbol{D}^v] - \frac{\nabla\theta \cdot \boldsymbol{q}}{\theta}\end{aligned} \tag{5-46}$$

Substituting Eqs. 5-18 and 5-20 into Eq. 5-46 and isolating $\mathbf{D}^{\mathrm{e}}$, θ, γ and ϕ produces

$$\mathcal{D} = \left[\boldsymbol{\tau} - \rho_0 \mathbf{F}^{\mathrm{e}} \frac{\partial \Psi}{\partial \mathbf{E}^{\mathrm{e}}} \mathbf{F}^{\mathrm{e}T} + \rho_0 \theta \mathbf{F}^{\mathrm{e}} \frac{\partial \eta_m}{\partial \mathbf{E}^{\mathrm{e}}} \mathbf{F}^{\mathrm{e}T}\right] : \mathbf{D}^{\mathrm{e}} + \left[-\rho_0 \frac{\partial \Psi}{\partial \theta} - \rho_0 \left[h_A \, ln\left(\frac{\theta}{\theta_T}\right)\right] + \rho_0 \theta \frac{\partial \eta_m}{\partial \eta_e} \frac{\partial \eta_e}{\partial \theta}\right] \dot{\theta} + \sum_{\alpha=1}^{N} \left[\boldsymbol{\tau} : \boldsymbol{P}_\alpha - \rho_0 w_p^\alpha \frac{\partial \Psi}{\partial \rho_d} + \rho_0 \theta \varphi_\alpha\right] \dot{\gamma}_\alpha + \left[\frac{1}{3(1-\phi)} (\boldsymbol{\tau} : \mathbf{I}) - \rho_0 \frac{\partial \Psi}{\partial \phi} + \rho_0 \theta S_\phi\right] \dot{\phi} - \frac{\nabla \theta \cdot \boldsymbol{q}}{\theta} \quad 5\text{-}47$$

The five terms contained in Eq. 5-47 represent the elastic, thermal rate, plastic slip, damage evolution, and heat transfer dissipation rates. An exact dissipation rate requires exact forms of the Helmholtz free energy and thermomechanical coupling entropy are required to determine the plastic slip and damage driving forces. Following the Coleman and Noll [188] procedure, the terms multiplied by $\mathbf{D}^{\mathrm{e}}$ and $\dot{\theta}$ must vanish, resulting in the following additional constraints:

$$\rho_0 \frac{\partial \Psi}{\partial \boldsymbol{E}^e} = \boldsymbol{S}^e + \rho_0 \theta \frac{\partial \eta_m}{\partial \boldsymbol{E}^e} \quad 5\text{-}48$$

$$\rho_0 \frac{\partial \Psi}{\partial \theta} = \rho_0 \theta \frac{\partial \eta_m}{\partial \eta_e} \frac{\partial \eta_e}{\partial \theta} - \rho_0 \left[h_A \, ln\left(\frac{\theta}{\theta_T}\right)\right] \quad 5\text{-}49$$

Integrating Eq. 5-48 with respect to the elastic Green-Lagrange strain $\mathbf{E}^{\mathrm{e}}$ gives,

$$\Psi = \frac{\mathbb{C} :: (\boldsymbol{E}^e \otimes \boldsymbol{E}^e)}{2\rho_0} + \Psi_{th} + \Psi_v + \Psi_d \quad 5\text{-}50$$

where the remaining terms are dependent only on temperature, dislocation density, and damage. Connolly et al. [23] derived Ψ_{th} as,

$$\Psi_{th} = -\eta_e \theta + h_A \theta \quad 5\text{-}51$$

It should be noted that Connolly et al.[23] demonstrated that under certain assumptions, Ψ_d is given by,

$$\Psi_d = \frac{\omega \mu}{2\rho_0} b^2 \rho_d \quad 5\text{-}52$$

where ω is the coefficient representing the impact of dislocation density on energy for grain and μ is the elastic shear modulus of the grain. In this work, it is assumed that $\mu = \mathrm{C}_{44}$.

Lemaitre [189] showed that Ψ_v can be expressed as,

$$\Psi_v = \frac{1}{2\rho_0} \kappa \phi^2 \quad 5\text{-}53$$

where κ is a scalar relating to isotropic damage hardening. Therefore, the total free energy can be defined as

$$\Psi = \frac{\mathbb{C} :: (E_e \otimes E_e)}{2\rho_0} - \eta_e\theta + h_A\theta + \frac{\omega\mu}{2\rho_0} b^2\rho_d + \frac{1}{2\rho_0}\kappa\phi^2 \quad 5\text{-}54$$

The driving forces for plastic slip ($f_p^{(\alpha)}$) and damage evolution (f_d) can be defined as

$$f_p^{(\alpha)} = \boldsymbol{\tau}: \boldsymbol{P}_\alpha + \frac{1}{2}\omega\mu b^2 k_2 \rho_d - \frac{\omega\mu b}{2}\sqrt{\rho_d} + \rho_0\theta\varphi_\alpha \quad 5\text{-}55$$

$$f_d = \frac{1}{3(1-\phi)}(\boldsymbol{\tau}: \boldsymbol{I}) - \kappa\phi + \rho_0\theta S_\phi \quad 5\text{-}56$$

Lastly, the temperature evolution is obtained by substituting Eq. 5-54 into Eq. 5-31, using the Legendre transformation and rearranging to produce

$$2\rho_0 h_A\dot{\theta} = \rho_0 r - \nabla\cdot\boldsymbol{q} + \boldsymbol{M}_e: \boldsymbol{D}_e + \sum_{\alpha=1}^{N} M_p^\alpha \dot{\gamma}^\alpha + \frac{1}{3(1-\phi)} M_v\dot{\phi} \quad 5\text{-}57$$

where

$$\boldsymbol{M}_e = \boldsymbol{\tau} - \rho_0 \boldsymbol{F}_e[\boldsymbol{I}: \mathbb{C}]\boldsymbol{F}_e^T \quad 5\text{-}58$$

$$M_p^\alpha = \boldsymbol{\tau}: \boldsymbol{P}_\alpha - \frac{1}{2}\omega\mu b^2 w_p^\alpha \quad 5\text{-}59$$

$$M_v = \frac{1}{3(1-\phi)}(\boldsymbol{\tau}: \boldsymbol{I}) - \kappa\phi \quad 5\text{-}60$$

5.3.3 Dislocation Evolution

Both the ambient temperature and the internal temperature rise during deformation play a significant role in the material response. In this work, a dislocation density-based hardening is used to better capture the effect of temperature. The temperature affects the evolution of dislocations, as it influences the accumulation of dislocations within a material. During loading, dislocations can multiply and interact, leading to strain hardening and determining the response of the material to the applied loading as well as the microstructure of the material. Temperature affects this process by altering the mobility and storage of dislocations. As the temperatures increase, the dislocation velocity increases, potentially leading to a higher likelihood of dynamic annihilation of dislocations. This, in turn, affects the storage of dislocations and hence the hardening kinetics. Thus, the dislocation accumulation on active slip systems evolves during plastic deformation and is described by a Kocks-Mecking (KM) type evolution law, as presented in Kitayama et al. [190],

$$\dot{\rho}_d = \left[\frac{1}{bk_1}\sqrt{\rho_d} - k_2\rho_d exp\left(\frac{Q}{\theta}\right)\right]|\dot{\gamma}^{\alpha}| \quad 5\text{-}61$$

where θ is the temperature and Q is a temperature-related constant. In this equation, the first term represents the dislocation generation, and the second term represents the dynamic recovery of dislocations.

The dislocation plasticity kinetics function is assumed to be governed by the following power-law expression:

$$\dot{\gamma}_{\alpha} = \dot{\gamma}_0 \,\mathrm{sgn}\left(f_p^{(\alpha)}\right)\left|\frac{f_p^{(\alpha)}}{g_p^{(\alpha)}}\right|^{1/m_p} \quad 5\text{-}62$$

where $\dot{\gamma}_0$ represents a reference shear rate assumed to be uniform for all slip systems, $g_p^{(\alpha)}$ is the critical driving force for dislocation plasticity on slip system α, and m_p is the plasticity strain rate exponent.

The critical driving force for plasticity is defined using as initial value g_p^0 for all slip systems and related to the dislocation density as follows,

$$g_p^{(\alpha)} = g_p^0 + c_i\mu b\sqrt{\rho_d}\exp\left(\frac{\mathrm{Q}}{\theta}\right) \quad 5\text{-}63$$

where c_i is the interaction coefficient between dislocation in grain. The internal temperature effect proposed in this study aligns with the approach outlined by Potirniche et al. [17].

5.3.4 Kinetics Function for Damage Evolution

The new damage evolution model that can capture the rate-sensitivity is given by:

$$\dot{\phi} = \dot{\phi}_0 \left|\frac{f_d}{g_d}\right|^{1/m_d} \quad 5\text{-}64$$

where $\dot{\phi}_0$ is the reference damage rate (considering initial porosity in the material), g_d is the critical driving force for damage evolution, and m_d is the damage rate exponent. The introduction of a strain rate-sensitive parameter into the damage model is motivated by the need to account for the influence of strain rate on damage evolution in materials. It is assumed that materials subjected to relatively higher strain rates may exhibit increased damage evolution due to the rapid deformation processes, and thus, potentially leading to reduced material ductility.

The critical driving force for damage evolution is defined using as initial value g_d^0 and governed by a rate of change law so that

$$g_d = h_d \phi_{part} \tag{5-65}$$

where h_d captures the dependency of the critical driving force on damage evolution and ϕ_{part} is the volume fraction of voids nucleated from inclusion particles and is defined as the ratio of the volume of an element in its current state to its volume in the initial reference state,

$$\phi_{part} = \frac{V_v}{\tilde{V}} = \frac{V_v}{N}\frac{N}{\tilde{V}} = v\lambda \tag{5-66}$$

where λ is the void nucleation, and v is void growth.

In this work, it is assumed that voids are nucleated from particles and the state of damage in a material can be characterized based on the occurrence of void nucleation and void growth. In the undeformed configuration, the number of voids per unit volume is assumed to be λ_0, which can be expressed as $\lambda_0 = {}^{N}/_{V_0}$

where N is the total number of voids distributed within the material volume V_0. The average void volume then becomes

$$v_{vol} = {}^{1}/_{N}\sum_{i=1}^{N} v_i \tag{5-67}$$

where v_i is the void volume from each particle that has nucleated a void. Accordingly, the total volume of voids becomes

$$V_v = \lambda_0 V_0 v_{vol} \tag{5-68}$$

These parameters are further described briefly in the next sections.

5.3.4.1 Void Nucleation

The evolution equation for void nucleation depends on various factors, which include a length scale parameter (chosen to be the mean size of inclusions for this study), volume fraction of second phase materials, stress state (invariants of stress), strain rate, and fracture toughness. Past research has proposed nucleation models attempting to address some of these characteristics, as demonstrated by [11,140,191–193] among others. However, Horstemeyer and Gokhale [138] included all the features mentioned above that have been observed to influence the damage state and developed a void nucleation rate model given by

$$\dot{\lambda} = \frac{\|\dot{\bar{\varepsilon}}\|\sqrt{d}}{K_{IC} f^{\frac{1}{3}}}\lambda\left(a\left[\frac{4}{27} - \frac{J_3^2}{J_2^3}\right] + b\frac{J_3}{J_2^{3/2}} + c\left\|\frac{I_1}{\sqrt{J_2}}\right\|\right)\exp\left(\frac{Q}{\theta}\right) \tag{5-69}$$

where $\dot{\varepsilon}$ is an equivalent strain rate, K_{IC} is the fracture toughness of the material, f is volume fraction of second phase particles, and d is a length scale parameter. Furthermore, a, b, and c are the material constants and used to address the void nucleation contribution from torsional, compressive, and tensile loads; I_1, J_2 and J_3 are stress invariants defined as, $I_1 = \sigma_{ii}, J_2 = \frac{1}{2}S_{ij}S_{ij}$ and $J_3 = \det(S_{ij})$, with S_{ij} being the deviatoric stress $S_{ij} = \sigma_{ij} - \frac{1}{3}\sigma_{kk}\delta_{ij}$. θ is the temperature and Q is a temperature-related constant described in 5.3.5.

It should be mentioned that the stress state at void nucleation is highly triaxial. Both $\frac{4}{27} - \frac{J_3^2}{J_2^3}$ and $\frac{J_3}{J_2^{3/2}}$ are negligible, compared to $\frac{I_1}{\sqrt{J_2}}$ [194]. The triaxiality factor, c, in Eq. 5-69 in tension is dominant and has been shown to relate to tensile stress state and damage nucleation by Dighe et al. [195]. Hence, the void nucleation model can be simplified to the following expression

$$\dot{\lambda} = \frac{\sqrt{d}}{K_{IC} f^{\frac{1}{3}}} \|\dot{\varepsilon}\| c\lambda \left\| \frac{I_1}{\sqrt{J_2}} \right\| \exp\left(\frac{Q}{\theta}\right) \qquad 5\text{-}70$$

5.3.4.2 Void Growth

In addition to the nucleation of voids, void growth is also a critical aspect that influences the damage state. For the evolution of the void growth factor v for voids nucleated from second-phase particles, McClintock [12] growth rule of a void with radius R is used in this research.

$$\dot{v} = v\dot{\varepsilon} \frac{3\sqrt{3}}{2(1-n)} \sinh\left(\sqrt{3}\,(1-n)\frac{\sqrt{2}}{3}\,\frac{I_1}{\sqrt{J_2}}\right) \qquad 5\text{-}71$$

where *n* is material constant and is related to the strain hardening exponent and is determined from the tension tests. The above equation the void volume grows as the strain and/or stress triaxiality increases.

5.3.5 Temperature-Dependent Modeling

In this work, a novel temperature-dependent framework is introduced, with the assumption that the temperature within the control volume remains approximately spatially invariant. This allows to establish the governing thermal boundary conditions so that:

$$\Delta Q = Q_{gen} - Q_{bound} \qquad 5\text{-}72$$

where, Q_{gen} is the total volumetric heat generation and Q_{bound} is the heat lost to the thermal boundary.

The current thermal model primarily focuses on the energy stored due to plastic deformation and the energy transferred to the environment through heat dissipation. This approach aims to capture the overall temperature rise during deformation under the assumption of uniform deformation conditions. In the context of HSLA steel, studies have indicated that the energy expended for surface generation, including void formation and growth, is generally minimal compared to the total energy involved in deformation processes. Dolzhenko et al. [172] suggest that the primary contributors to mechanical behavior in HSLA steels are related to mechanisms such as grain refinement, precipitation strengthening, and dislocation interactions, rather than significant energy expenditures on surface generation.

The dissipation resulting from strain leads to the generation of internal heat. However, not all the mechanical energy is perfectly converted into thermal energy, as some of it is stored in microstructural transformations at the dislocation level [113]. To account for this, a comprehensive framework requires the determination of the fraction of energy transformed into heat through an experimentally obtained coefficient, which may vary between different cases. Taylor and Quinney proposed a coefficient to express the efficiency of this transformation given by,

$$Q_{gen} = \chi \, W_p \tag{5-73}$$

here, W_p denotes the plastic power, and χ is the Taylor-Quinney parameter, typically falling within the range of 0.85 to 1.0.

In case of adiabatic conditions, the Taylor-Quinney coefficient can be calculated by,

$$\chi = \frac{\rho \, c_p \, \Delta\theta}{W_p} \tag{5-74}$$

where, ρ, c_p, and $\Delta\theta$ stands for density of material, heat capacity and change in temperature respectively.

The thermal boundary heat loss is further divided into three components: conduction Q_{cond}, convection Q_{conv}, and radiation Q_{rad}. Conduction takes place at the two faces that are connected to the rest of the uniaxial tension specimen, while convection occurs on all the surfaces exposed to the air (i.e., all other surfaces). These heat flux components are defined as follows,

$$Q_{bound} = \int \nabla \, q \, dV = Q_{cond} + Q_{conv} + Q_{rad} \tag{5-75}$$

$$Q_{cond} = 2h_{cond}(\theta_{ext} - \theta) \tag{5-76}$$

$$Q_{conv} = 2R_{conv}(\theta_{\infty} - \theta) \tag{5-77}$$

$$Q_{rad} = 2\sigma\,\alpha(\theta^4 - \theta_\infty^4) \quad 5\text{-}78$$

where h_{cond} is the convection coefficient between the air and control volume, θ_{ext} is the temperature of an exterior boundary, R_{conv} is a coefficient governing conduction from the control volume into the rest of sample, σ is the Stefan-Boltzmann constant (5.67 e^{-08} W/ (m^2 K^4)), α is the emissivity and θ_∞ is the temperature of the thermal boundaries (i.e., the air and the gripping mechanism for the sample).

5.3.6 Numerical Approach

The numerical implementation employs a semi-implicit, forward-gradient time-integration procedure based on the methodology developed by Peirce et al. [196,197]. This work uses the tangent modulus for rate-dependent solids, known as the rate-tangent modulus method, established by Peirce et al. [196] for single crystal plasticity. This algorithm provides a higher-order estimate of the plastic slip vector and damage variable increment, $\Delta\gamma$ and $\Delta\phi$.

The increment in damage is obtained by differentiating Eq. 5-66

$$\dot{\phi}_{part} = \dot{\lambda} v + \lambda \dot{v} \quad 5\text{-}79$$

Assuming all the variables are known at time t, the update of damage and temperature is performed for a time interval from t to t+Δt. The void nucleation components are updated explicitly from the integral forms of their rate equations,

$$\Delta\lambda_t = C_{coef}\, exp\left\{\frac{\dot{\bar{\varepsilon}}\,\Delta t_{t+1}\sqrt{d}}{K_{IC} f^{\frac{1}{3}}}\left(c\left\|\frac{I_1}{\sqrt{J_2}}\right\|\right) exp\left(\frac{Q}{\theta}\right)\right\} \quad 5\text{-}80$$

where, C_{coef} is a constant that comes from integration. If C_{coef} has larger values, it will lead to a higher rate of nucleation, which in turn will increase the total count of nucleated voids in a given volume. The growth of voids is updated as,

$$\Delta v_t = \frac{4}{3}\left\{R_0 exp\left[\dot{\bar{\varepsilon}}\,\Delta t_{t+1}\frac{\sqrt{3}}{2(1-n)} sinh\left(\sqrt{3}(1-n)\frac{\sqrt{2}I_1}{3\sqrt{J_2}}\right)\right]\right\}^3 \quad 5\text{-}81$$

The heat generated through the plastic work is given by,

$$\Delta T_{gen} = \chi\frac{\Delta W_p}{\rho\, c_p} \quad 5\text{-}82$$

The heat loss due to conduction, convection, and radiation is calculated as,

$$\Delta T_{cond} = h_{cond}(\theta_{ext} - \theta)\Delta t_{t+1} \quad 5\text{-}83$$

$$\Delta T_{conv} = R_{conv}(\theta_\infty - \theta)\Delta t_{t+1} \quad 5\text{-}84$$

$$\Delta T_{rad} = \sigma\alpha(\theta^4{}_{\infty} - \theta^4)\Delta t_{t+1} \quad 5\text{-}85$$

$$\Delta T_{bound} = \frac{2\,(\Delta T_{cond} + \Delta T_{conv} + \Delta T_{rad})}{\rho c_p t e^{\varepsilon}} \quad 5\text{-}86$$

The final change in temperature at the end of the time step is,

$$\Delta T_t = \Delta T_{gen} - \Delta T_{bound} \quad 5\text{-}87$$

5.4 Result and Discussion

The experimental data has been segregated into two sets for the purpose of CPDM calibration and validation. Simulations are conducted using a Taylor-type polycrystal plasticity model with initial grain orientations derived from experimental observations. Microstructures are created for HR340 and HR550, each comprising approximately 500 grains. The plasticity parameters for HSLA steels are presented in Table 5-6.

Table 5-6: Material constant for the crystal plasticity model.

Alloy	C_{11}(GPa)	C_{12}(GPa)	C_{44}(GPa)	$\dot{\gamma}^0$ (s^{-1})	$\dot{\phi}^0$
HSLA steel	262.07	101.92	80.078	0.001	0.001

5.4.1 Model Calibration

This section outlines the calibration parameters for the stress–strain response for the material under various loading rates. The mechanical behavior of the material is a pivotal aspect of this work, and precise calibration serves as the foundation for subsequent predictions using damage modeling based on crystal plasticity. Table 5-7 and Table 5-8 present the damage constant parameters and the calibrated parameters obtained through curve fitting at various strain rates for both steels respectively. The values of crystal plasticity damage parameters are determined by fitting experimental stress strain data in uniaxial tension tests (Figure 5-8), following a similar approach to Horstemeyer and Gokhale [138]. The parameters for the HR340 and HR550 alloys demonstrate notable differences which can be attributed to variations in their microstructural characteristics and mechanical properties. Specifically, HR550, with its finer grain size and distinct chemical composition, exhibits a higher resolved shear stress and a different hardening behavior compared to HR340. These microstructural distinctions contribute to the observed variations in work hardening parameters and fracture toughness, thereby reflecting the distinct characteristics (stress–strain response, strain rate sensitivity, etc.) of each alloy.

Table 5-7: List of parameters for HSLA steel.

Dislocation parameters	k_1=44, k_2=5, b=0.28e-9 m,ρ_0=10 1/m^2
Damage parameters	d = 6 μm, R$_0$=10 μm, n=0.1, C_{coef}=1, f=0.003, K_{Ic}=175 MPa$\sqrt{\text{m}}$, Q=100, h_d =250 MPa
Thermodynamic parameters	φ_α=0.1, S_ϕ=0.1, m_p=0.001, m_d=0.78e-3, ω=20, c_a=0.5, h_A=450 mJ/g · K, κ=500

Table 5-8: The calibrated parameters (curve fitting).

Material	**Strain rate (s^{-1})**	**Resolved shear stress (τ_0) (MPa)**	**Interaction coefficient (c_i)**	**Triaxiality factor (c)**
HR340	0.001	132	0.29	1.2E5
	1	142	0.22	6.2E5
	100	149	0.25	4.3E5
HR550	0.001	235	0.30	3.1E5
	1	241	0.23	7.1E5
	100	244	0.25	6.3E5

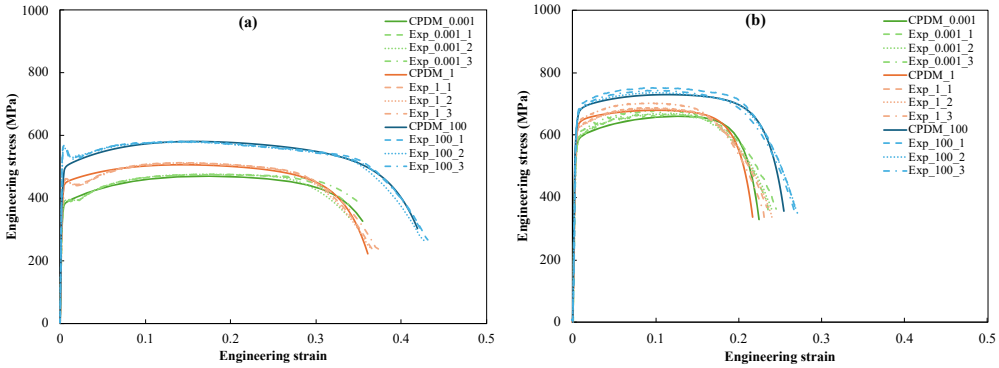


Figure 5-8: Comparison between the calibrated and measured stress–strain curves in the tension test at for (a) HR340 and (b) HR550.

Table 5-9: Temperatures-dependent parameters.

Alloy	**ρ (kg/m^3)**	**C_p (J/kg-°C)**	**R_{conv} (m^2/W)**	**h_{cond} (W/m^2-K)**	**α**	**χ**	**θ (K)**	**θ_{ext} (K)**	**θ_∞ (K)**
HSLA steel	7800	280	18	15	0.8	0.9	328	300	298

The temperature-dependent parameters are calibrated with the experiments performed at 100 s^{-1} (Figure 5-9), and the calibrated parameters are presented in Table 5-9.

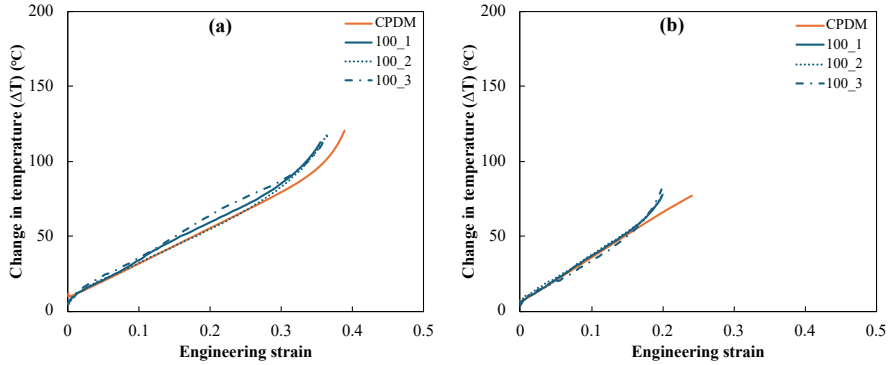


Figure 5-9: Comparison between the calibrated and measured temperature-strain curves at 100 s^{-1} for (a) HR340 and (b) HR550.

5.4.2 Comparing Model Predictions with Experimental Data

In this subsection, the calibrated CPDM is employed to predict the uniaxial tension behavior of the HR340 and HR550 steels at strain rates of 0.1 s^{-1} and 10 s^{-1}. Figure 5-10 display the comparisons between the predicted engineering stress–strain responses by the CPDM and the experimental data for HR340 and HR550 steel. As can be seen from the figures, the predictions with the CPDM demonstrate good agreement with the experimental results.

A minor variation is observed when simulating the behavior of HR340 at a strain rate of 0.1 s^{-1}. A minor disparity emerges in the neck region on the stress–strain curve, demonstrating a slight misalignment between the developed CPDM and the experimental data. Conversely, for HR550 at a strain rate of 0.1 s^{-1}, the CPDM predicts slightly higher yield stress and reduced elongation to failure compared to the experimental results. These variations underscore the sensitivity of the CPDM to specific parameters such as resolved shear stress, hardening parameter, and fracture toughness of each steel grade when predicting their responses under different strain rates.

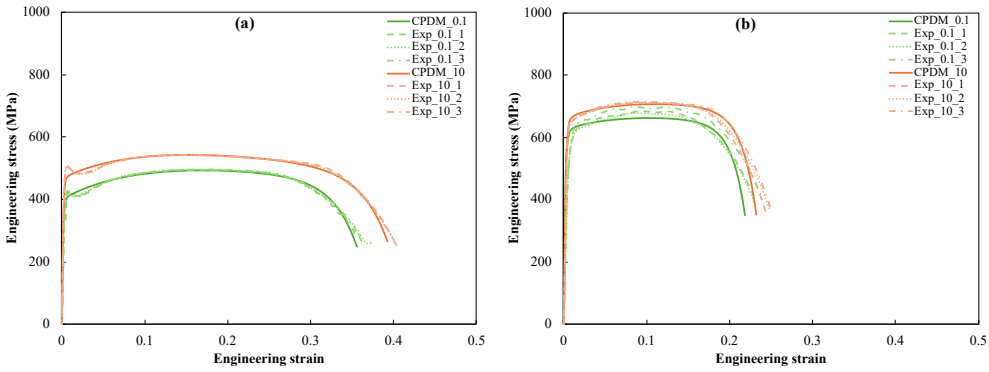


Figure 5-10: Model prediction of (a) HR340 and (b) HR550 stress–strain response at various strain rates and compare with experiments.

The CPDM is also used to predict the change in temperature rise at 0.001 s^{-1}, 0.1 s^{-1}, 1 s^{-1}, and 10 s^{-1}. Figure 5-11 illustrates the temperature evolution as a function of the engineering strain for HR340 across different strain rates. The predictions with the model show excellent agreement with the experimental data for all strain rates. However, a minor deviation in the predicted curve at the 10 s^{-1} strain rate indicated a lower value than the experimental data at higher strains. The proposed CPDM effectively reproduces the temperature evolution for the remaining strain rates, exhibiting excellent agreement with the corresponding experimental data. Figure 5-12 compares the CPDM predictions and the experiments for the temperature vs. engineering strain relationship of HR550 at various strain rates. The predicted curve displays a lower value than the experimental results at a strain rate of 0.1 s^{-1}, while it agrees well with the experiment results for other strain rates. It should be noted that the experimental repeats show variation for HR550 at strain rate 0.1 s^{-1}.

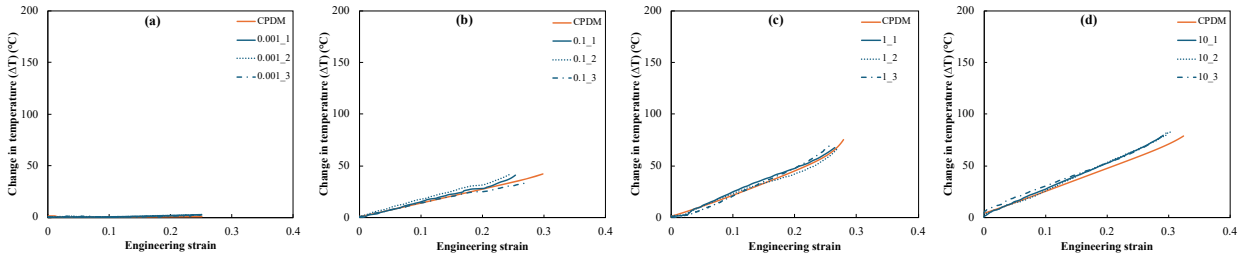


Figure 5-11: Comparison between experiment and CP damage predicted temperature response at (a) 0.001 s^{-1}, (b) 0.1 s^{-1}, (c) 1 s^{-1}, and (d) 10 s^{-1} for HR340.

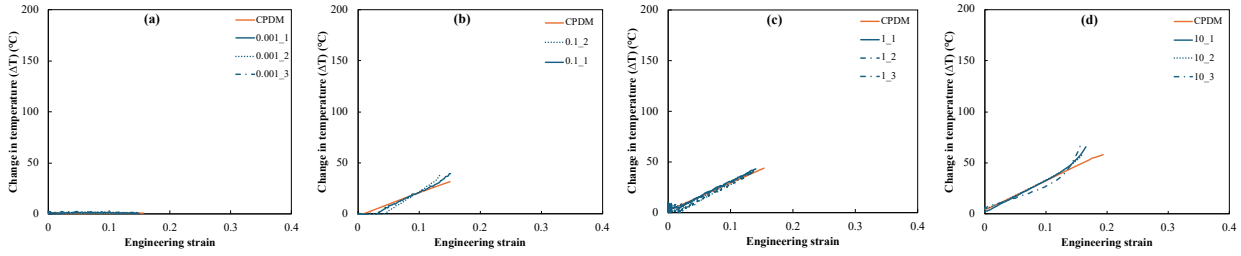


Figure 5-12: Comparison between experiment and CP damage predicted temperature response at (a) 0.001 s^{-1}, (b) 0.1 s^{-1}, (c) 1 s^{-1}, and (d) 10 s^{-1} for HR550.

5.4.3 Analysis of Microstructure

The following section compares the predicted texture evolution with those measured for the HR340. Figure 5-13 presents a comparison of pole figures in the (001), (110), and (111) orientations, plotted at 30% strain for HR340 steel at strain rates of 0.001 s^{-1} and 100 s^{-1}. Figure

5-13(a-c) present the experimental observations, while Figure 5-13(b-d) illustrate the CPDM predictions. This approach allows for an examination of the texture changes at the material failure, offering insights into the deformation mechanisms under varying strain rates. The results indicate that the pattern of texture evolution remains consistent across the different strain rates for HSLA steels. However, the intensity of the texture becomes more pronounced as the strain rate increases. The simulated data shows a lower maximum intensity percentage increase compared to the measured data; however, the trend of increasing intensity from lower to higher strain rates is accurately captured. Additionally, both the measured data and the simulated data show a strengthening of the texture as highlighted in Figure 5-13. This underscores the accuracy and robustness of the developed model in predicting the crystallographic texture evolution under different deformation conditions.

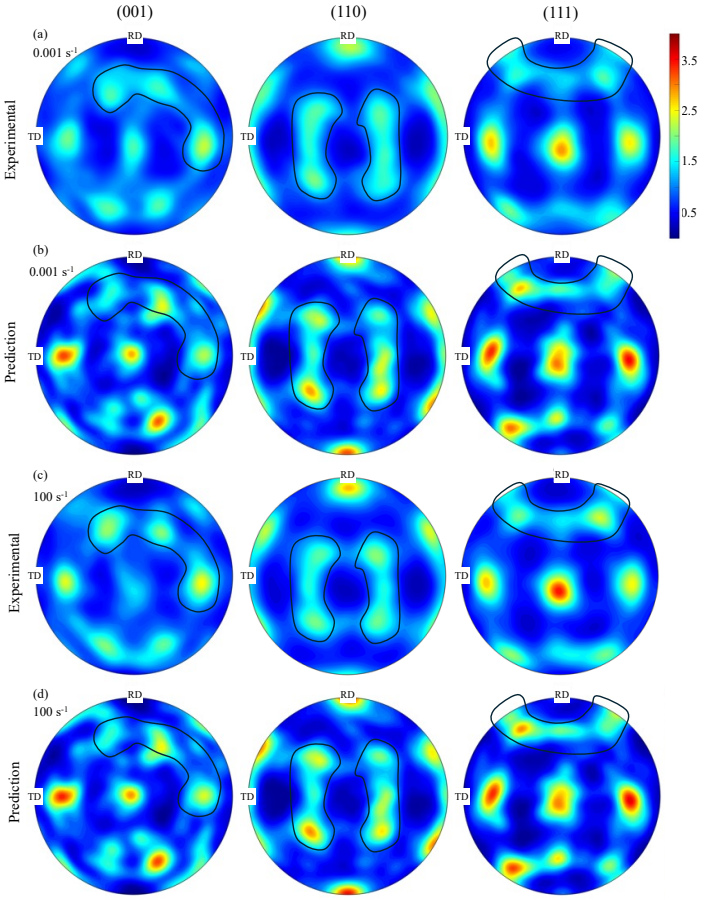


Figure 5-13: Pole figures for HR340 at 0.001 s^{-1} and 100 s^{-1}, (a-c) experimental observations and (b-d) CPDM predictions.

5.4.4 Effect of Temperature and Strain Rate on Dislocation Density

Figure 5-14 illustrates the influence of temperature and strain rate on dislocation density during plastic deformation. At lower and intermediate strains, the dislocation density increases significantly for both HR340 and HR550 steels, primarily due to enhanced dislocation mobility and interaction frequency. During this phase, dislocations accumulate as they interact and form tangles, contributing to work hardening. The strain rate plays a critical role in this region, with higher strain rates leading to greater dislocation densities [198]. This behavior can be attributed to the limited time available for recovery mechanisms, such as dislocation annihilation, climb, or cross-slip, at elevated strain rates [199]. Consequently, the dislocation multiplication dominates over recovery, resulting in a net increase in dislocation accumulation.

As the strain progresses, the internal temperature begins to rise due to the conversion of plastic work into heat, with the temperature reaching above 60°C at high strains. This temperature increase activates dynamic recovery processes, such as dislocation climb and annihilation, which mitigate the further accumulation of dislocations. Consequently, the rate of dislocation density growth slows down and eventually saturates at high strains, as observed in both materials. While the influence of strain rate persists in this regime, it becomes less pronounced at elevated temperatures, where thermally activated recovery processes dominate over strain rate-dependent dislocation multiplication. HR550 exhibits a slightly higher rate of dislocation density accumulation compared to HR340, suggesting material-specific differences in dislocation storage and recovery behavior.

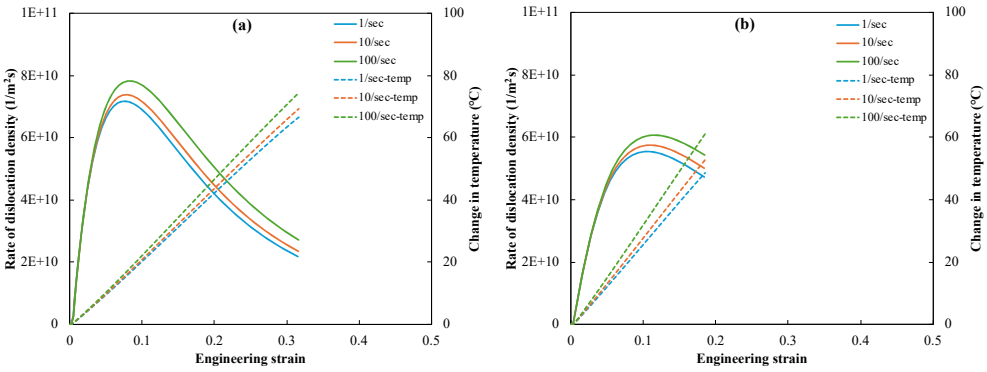


Figure 5-14: Evolution of dislocation density and internal temperature rise at different strain rates for (a) HR340 and (b) HR550.

To better understand the effect of internal temperature rise, a comparison is presented for HSLA steel with and without considering internal temperature effects. Figure 5-15 depicts the stress–

strain behavior and dislocation density evolution for HSLA steel under a strain rate of 100/sec. The stress–strain graph shows that, without considering internal temperature effects, the material achieves a higher peak stress and maintains greater strength throughout deformation. In contrast, incorporating internal temperature effects reduces the peak stress and accelerates strain softening, likely due to thermally activated recovery [200]. The dislocation density curve reveals that dislocation accumulates more significantly without internal temperature effects, while internal temperature promotes dislocation annihilation and recovery, leading to a lower overall dislocation density. These results underscore the critical role of internal temperature in influencing the mechanical behavior and microstructural evolution of HSLA steel during deformation.

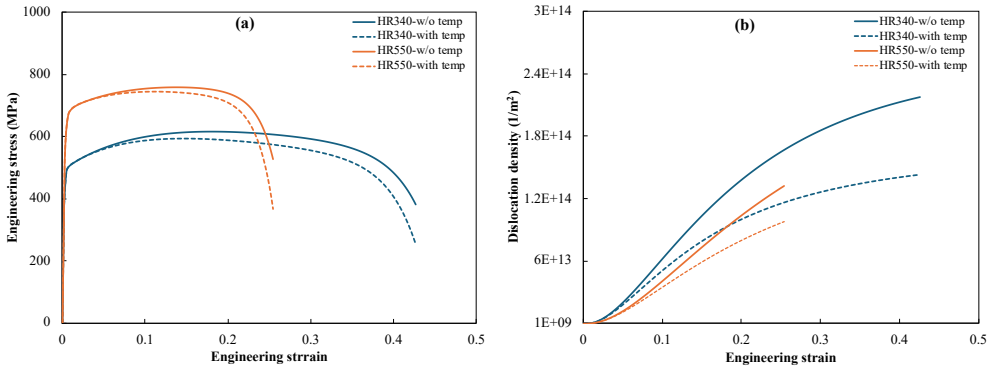


Figure 5-15: A comparison of (a) stress–strain response and (b) dislocation density evolution with and without considering internal temperature effect for HR340 and HR550.

5.4.5 Damage Accumulation and Intermediate Strain Rate Predictions

In this section, the total damage accumulation leading to the softening in the stress–strain response is examined. Figure 5-16 illustrates the damage evolution throughout the deformation process at different strain rates for both grades of HSLA steels. Predictions with the CPDM show that the strain rate is a sensitive parameter influencing damage accumulation. A higher strain rate delays the onset of damage evolution because the strain rate significantly impacts the void nucleation model. At lower strain rates, void nucleation may occur more readily, leading to an earlier onset of damage evolution. In contrast, higher strain rates delay the onset of localized deformation processes, contributing to damage.

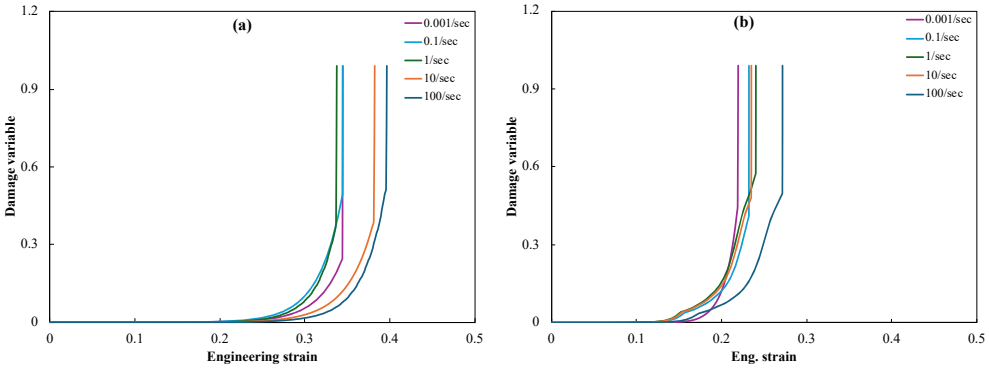


Figure 5-16: Difference in damage levels at different strain rates in (a)HR340 and (b) HR550.

Finally, the CPMD is employed to predict the large strain behavior of both HSLA steels under relatively higher strain rates, including 200 s^{-1}, 300 s^{-1}, and 500 s^{-1}. Figure 5-17 shows prediction by the CPDM model at intermediate strain rates. Temperature plays a significant role because temperature and strain rate exhibit an equivalent effect on thermally activated deformation mechanisms. However, material properties of HSLA steel do not undergo significant changes until temperature exceeds approximately 200 ^{o}C [201]. Therefore, the predictions presented in Figure 5-17 align well with the experimental observations. The predictions show similar tendencies; as the strain rate increases, the damage (nucleation and growth) evolution slows down, thus providing more ductility at higher strain rates.

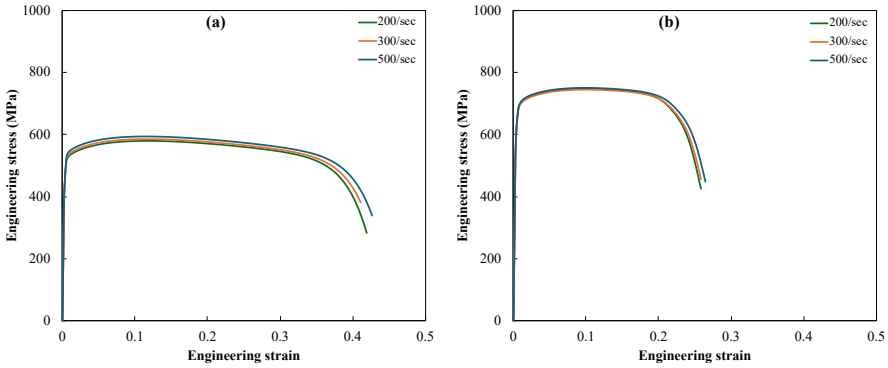


Figure 5-17: Stress–strain prediction at intermediate strain rate for (a) HR340 and (b) HR550.

5.5 Chapter Conclusion

In this paper, a new crystal plasticity constitutive model that incorporates damage evolution and internal temperature distribution in the HSLA steel is developed. The traditional kinematics approach is modified by introducing a volumetric component within the multiplicative decomposition of the total deformation gradient to account for damage evolution at the grain level.

Damage is characterized by considering void nucleation and growth originating from second-phase particles and initial material porosity. Furthermore, the thermodynamic framework introduced in this work allow temperature changes in the material to be tracked during the tensile tests.

To characterize the initial microstructure and damage behavior of commercially available HR340 and HR550 steels, EBSD and uniaxial tension experiments are conducted. A high-speed infrared camera enabled the real-time monitoring of the temperature distribution within the material. Plasticity and damage parameters are calibrated at different strain rates using experimental stress–strain data, while temperature parameters are calibrated at 100 s^{-1}. Several key findings and conclusions emerged from these analyses:

- The CPDM effectively predicted the stress–strain response at 0.1 s^{-1} and 10 s^{-1}, demonstrating excellent agreement with experimental results; the CPDM accurately captured the softening/post-necking behavior and failure of HSLA steel. Additionally, the local temperature evolution predicted by the proposed model at strain rates 0.001 s^{-1}, 0.1 s^{-1}, 1 s^{-1}, and 10 s^{-1} demonstrated very good agreement with experimental data. Predictions also show that the onset of damage is delayed as the strain rate increases.
- The CPDM accurately predicted texture evolution across different strain rates. While the pole locations are not affected by strain rates, the intensity of texture strength increases as the strain rate increases.
- Higher strain rates lead to increased dislocation accumulation due to insufficient recovery time for mechanisms like annihilation and climb. At elevated temperatures, thermally activated recovery processes dominate, balancing dislocation generation and accumulation.

Finally, the presented work shows a significant advancement in understanding damage evolution in HSLA steels by developing a strain rate-sensitive damage evolution model that also incorporates internal temperature rise effects. By capturing the interplay between strain rate and thermal changes, the model enhances the predictive capability of damage progression and material behavior under various strain rates.

6 Development of a Phase and Interface Driven Damage Model Coupled with Crystal Plasticity for Dual Phase Steels

In this chapter, a crystal plasticity damage model is developed to describe deformation and damage evolution in dual phase steels. The formulation combines rate-dependent crystal plasticity, thermomechanical coupling, stress state sensitive void nucleation and growth, void shape evolution, and homogenized interface-driven void nucleation to describe damage-driven softening and failure in DP steels. Ferrite and martensite are treated using phase specific constitutive descriptions, while the interface contribution is introduced without explicitly resolving ferrite–martensite boundary. The framework is applied to DP590 and DP780 sheets. The initial microstructure and crystallographic texture are characterized using electron backscatter diffraction, while uniaxial tension, simple shear, and plane-strain tension responses are used to calibrate and evaluate the model under different strain rates and loading paths. Temperature rise during deformation is measured using infrared thermography to support the thermomechanical response. The chapter also investigates the role of preferred BCC texture components in controlling anisotropic hardening, local triaxiality, damage growth, and post-necking deformation.

This chapter presents a manuscript submitted to the Journal of Materials Research and Technology.

Journal of Materials Research and Technology, JMRT-D-26-07085

Microstructure-Informed Thermomechanical Crystal Plasticity Damage Modeling of Dual-Phase Steels

Sandipkumar Dayani[a], Waqas Muhammad[a], Abhijit Brahme[a], Fatemeh Hekmat[b], Trevor Sabiston[c], Kathy Wang[b], Kaan Inal[a]

[a] Department of Mechanical and Mechatronics Engineering, University of Waterloo, Waterloo, Ontario, N2L 3G1, Canada

[b] General Motors Technical Centre, General Motors, Warren, MI, 48092, United States

[c] Canadian Technical Centre, General Motors of Canada Limited, Oshawa, Ontario, L1J 0C5, Canada

Overview

Dual-phase (DP) steels offer a useful strength-formability balance, but their damage response depends on phase contrast, crystallographic texture, strain rate, stress state, temperature rise and void evolution. This study develops a thermomechanically coupled, rate-dependent crystal plasticity damage framework for DP590 and DP780 sheets. Phase-classified electron backscatter diffraction data are used to define ferrite and martensite orientation distribution within a Taylor-type homogenization scheme. Damage is represented through statistically distributed void nucleation, Rice-Tracey-type growth, ellipsoidal shape evolution and a homogenized ferrite-martensite interface contribution driven by phase-level plastic strain mismatch. The model is calibrated using selected uniaxial stress–strain and temperature data and assessed against additional strain rates, rolling/transverse directions, plane strain tension and in-plane shear. The simulations capture the measured trends in rate-dependent strengthening, direction-dependent ductility, temperature rise and stronger damage accumulation under higher triaxiality loading. Idealized texture simulations indicate that strength, Lankford coefficient and damage resistance are not optimized by the same texture components. The results provide a compact structure property modeling route for interpreting deformation and damage in DP steels under automotive forming and crash relevant loading.

Keywords: Dual-phase steel; Crystal plasticity; Damage evolution; Void nucleation; Thermomechanical coupling; Strain path; Texture

6.1 Introduction

Advanced high-strength steels (AHSS) are widely used in lightweight automotive structures because they can reduce structural mass while meeting strength and formability requirements. Among AHSS grades, dual-phase (DP) steels are attractive as their ferritic matrix and martensitic islands provide a useful strength-ductility balance [7,202]. During plastic deformation, mechanical contrast between ferrite and martensite promotes strain partitioning, enhanced work hardening and delayed macroscopic necking [6,20,203,204]. The same heterogeneity, however, also promotes anisotropic plastic flow and damage processes such as ferrite-martensite interface decohesion and martensite cracking [7,205,206]. Predictive modeling of DP-steel failure therefore requires a constitutive description that links microstructure-sensitive deformation with strain rate- and loading path-dependent damage evolution.

Damage initiation in DP steels involves several competing mechanisms. Experimental and numerical studies have identified ferrite-martensite (F/M) interface decohesion, ferrite-ferrite (F/F) boundary separation and martensite cracking as common nucleation events [21,68,207]. Their relative importance depends on martensite volume fraction, morphology, size and spatial distribution, which control local strain partitioning, strain hardening capacity and ductility [208–211]. Strain mapping studies show that plastic deformation localizes preferentially in ferrite, especially in large ferrite grains constrained by adjacent martensite islands [69,212]. Void nucleation may therefore occur through martensite cracking, along F/M interfaces or at F/F boundaries adjacent to martensite, depending on local phase arrangement and stress state [68,78,213,214]. These observations motivate models that treat damage evolution as a microstructure and stress state sensitive process rather than as a purely macroscopic failure criterion.

In-situ experiments, crystal plasticity calculations and full-field micromechanical simulations have clarified how microstructural heterogeneity controls deformation partitioning and damage initiation in DP steels [6,21,131,215–220]. These studies show that local stress and strain concentrations near phase boundaries, martensite substructures and banded or elongated features can shift both the onset and preferred location of damage, even under macroscopically simple loading [21,220–222]. Recent dual-scale studies of temperature-dependent plasticity and damage, together with sensitivity analyses of microstructure-property relations, further show that local phase interactions influence the progression toward failure [131,219]. Full-field approaches are

therefore valuable for mechanistic interpretation, but their computational cost remains high when broad ranges of strain rate, loading path and texture must be examined systematically. This motivates efficient constitutive frameworks that retain the dominant microstructure-sensitive mechanisms without resolving every interface explicitly.

Representative volume element (RVE) models based on synthetic or experimentally informed microstructures have been widely used to assess how phase fraction, martensite morphology and spatial arrangement influence strain concentrations and damage initiation [18,136,223]. Within continuum damage mechanics, Gurson-Tvergaard-Needleman (GTN)-type porous plasticity models are frequently used to describe void nucleation and growth. Classical GTN formulations, however, are less reliable under shear-dominated or low-triaxiality conditions unless additional stress state terms are introduced, and they do not naturally represent void shape evolution [13,76,123,224,225]. Cohesive zone models and extended finite element methods can represent interface decohesion and crack growth more directly [226–230], but they require fine spatial resolution, local fracture calibration and substantially greater numerical complexity [231–233]. The remaining challenge is to retain mechanistic fidelity across loading path, strain rate and microstructural variation without making the model impractical for broader parametric or structure property studies.

Crystal plasticity (CP)-based formulations provide a suitable path for this purpose because they link crystallographic orientation, phase contrast and slip activity to anisotropic deformation and damage-sensitive local fields [102,149,234–236]. CP and crystal plasticity finite element studies of DP steels have shown that ferrite orientation affects shear localization, phase specific constitutive contrast controls strain partitioning and texture evolution depends on loading path and local slip activity [21,150,237–241]. Ductile-damage studies have also shown that void evolution is sensitive to loading path and stress state, including plane-strain tension and simple shear [242,243]. Recent CP-based virtual-laboratory strategies and sensitivity studies have strengthened the connection between phase properties, microstructure descriptors and macroscopic response [131,136,241]. Nevertheless, stress state sensitive void kinetics with void shape evolution, thermomechanical coupling and grade-to-grade assessment remain only partly integrated in CP descriptions of DP steels.

Thermomechanical coupling is important for DP steels at intermediate and high strain rates. Plastic work converted into heat can produce measurable temperature rises in AHSS and DP steels,

influencing flow stress, localization and damage accumulation [219,244–246]. For example, the flow stress of DP600 at 10% strain has been reported to decrease by about 195 MPa when temperature increases from 21 to 300 °C [247]. These observations indicate that thermal softening can modify the competition between strain rate hardening and damage development during post-uniform deformation. Models that neglect thermomechanical coupling may therefore represent the apparent rate dependence of the flow response while still misrepresenting localization and damage evolution.

Crystallographic texture is another source of anisotropy in rolled DP steel sheets that is not captured by texture-agnostic damage models. Prior thermomechanical processing produces texture that affects elastic-plastic response, Lankford coefficient and direction-dependent formability [248,249]. In body-centered cubic (BCC) sheets, alpha-fiber (<110>||RD) and gamma-fiber ({111}||ND) components are particularly influential [250,251]. Texture-dependent variations in the Lankford coefficient affect thickness strain, work hardening and localization resistance [252,253], while CP studies show that different fiber textures produce distinct strength, hardening and anisotropy along rolling, transverse and diagonal directions [254,255]. A direct constitutive link between selected texture components, post-necking damage evolution and strain-path-dependent failure remains limited for DP steels, particularly when thermomechanical and stress state effects are considered together.

Taken together, the literature shows that deformation and damage in DP steels cannot be interpreted from microstructure, stress state, thermomechanical effects or texture in isolation. The macroscopic response emerges from their coupled interaction, especially after localization and damage accumulation begin. Existing models have advanced individual parts of this problem, including phase-sensitive deformation, interface damage, thermal softening and anisotropic flow, but these effects are often treated separately or within computationally expensive full-field frameworks [136,219,241,256]. This motivates a modeling framework that efficiently connects measured microstructure and texture to rate- and path-dependent damage evolution, while remaining suitable for comparative analysis across DP steel grades.

This work addresses that need by developing a thermomechanically coupled, rate-dependent crystal plasticity damage model for DP steels. The formulation combines stress state sensitive void nucleation, Rice-Tracey-type growth, ellipsoidal void shape evolution and a homogenized interface-driven nucleation term based on phase level ferrite-martensite plastic strain mismatch.

The framework is assessed using commercially available DP590 and DP780 sheets. Initial microstructure and texture are characterized by electron backscatter diffraction (EBSD), and uniaxial tension, simple shear and plane strain tension tests are used for calibration and validation across several strain rates and loading directions. Infrared thermography provides temperature histories for evaluating the thermomechanical component. Finally, EBSD-measured and idealized BCC texture inputs are used to examine how crystallographic orientation influences damage evolution and plastic anisotropy. The objective is not to replace full-field interface-resolved modeling, but to provide an efficient microstructure-informed constitutive route for interpreting structure-property trends in DP steels.

6.2 Modeling Approach

The constitutive framework used in this work is presented in five parts as shown in Figure 6-1. Section 6.2.1 introduces the thermomechanically coupled crystal plasticity formulation for ferrite and martensite within a common kinematic and stress update framework, with phase contrast introduced through phase specific strength and hardening laws. Section 6.2.2 describes ferrite phase void kinetics, including void nucleation, Rice–Tracey-type growth and ellipsoidal shape evolution. Section 6.2.2.4 introduces a homogenized ferrite–martensite interface nucleation term driven by phase-level plastic strain mismatch and phase interaction. Finally, Section 6.2.3 presents the thermal balance that couples plastic dissipation, heat exchange and temperature-dependent softening.

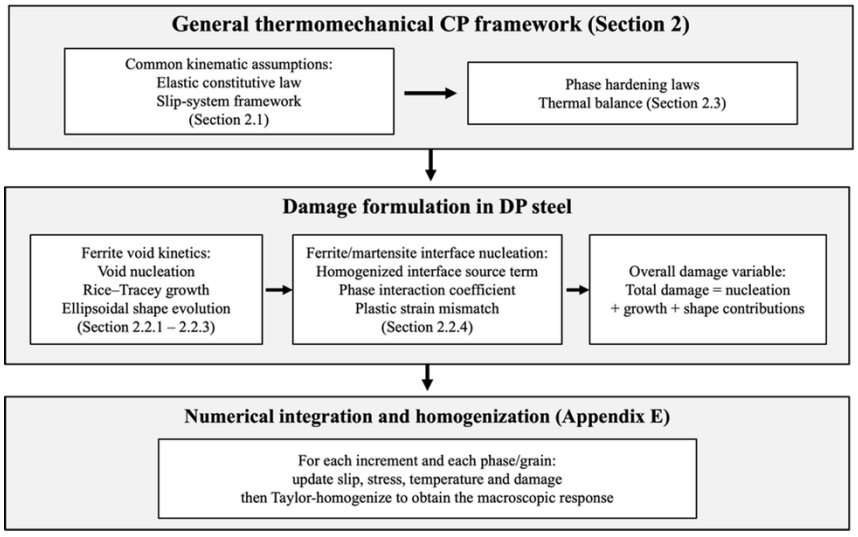


Figure 6-1: Flowchart of constitutive model derivation.

6.2.1 Kinematics and Constitutive Framework

Ferrite and martensite are described within a common thermomechanically coupled crystal plasticity structure. The same kinematics, slip system projection, stress update and Taylor homogenization are used for both phases, while phase contrast is introduced through phase specific strength and hardening parameters. Martensite is assigned a dislocation density-based hardening expression. This avoids treating martensite as rigid while retaining its higher slip resistance and different hardening response.

The present formulation extends the rate-dependent crystal plasticity damage model previously reported by Dayani et al. [257] for HSLA steel. That earlier study was developed for a predominantly ferritic microstructure and focused on void-driven damage evolution under strain rate-dependent loading. It was not intended to represent the additional heterogeneity introduced by dual phase steels, particularly the role of ferrite–martensite interfaces, phase morphology, and phase-dependent strain partitioning in damage initiation and evolution. The current work therefore adapts and extends that formulation to DP590 and DP780 by incorporating a homogenized interface-driven nucleation contribution together with microstructure-sensitive descriptions appropriate for DP steel under multiple loading paths and strain rate conditions.

Following Potirniche et al. [17], the deformation gradient, $\boldsymbol{F}$, is multiplicatively decomposed as

$$\boldsymbol{F} = \boldsymbol{F}_e \boldsymbol{F}_v \boldsymbol{F}_p \tag{6-1}$$

where $\boldsymbol{F}_e$, $\boldsymbol{F}_v$, and $\boldsymbol{F}_p$ represent the kinematics of elastic, void-induced, and plastic components, respectively. This decomposition allows for accurate treatment of large lattice rotations, damage-induced anisotropy, and microstructural degradation through void evolution.

The velocity gradient, $\boldsymbol{L}$, follows from the deformation gradient and is decomposed into elastic, $\boldsymbol{L}_e$, void volumetric, $\boldsymbol{L}_v$, and plastic, $\boldsymbol{L}_p$, contribution as

$$\boldsymbol{L} = \dot{\boldsymbol{F}}\boldsymbol{F}^{-1} = \boldsymbol{L}_e + \boldsymbol{L}_v + \boldsymbol{L}_p \tag{6-2}$$

$$\boldsymbol{L}_e = \dot{\boldsymbol{F}}_e {\boldsymbol{F}_e}^{-1} \tag{6-3}$$

$$\boldsymbol{L}_v = \boldsymbol{F}_e \dot{\boldsymbol{F}}_v {\boldsymbol{F}_v}^{-1} {\boldsymbol{F}_e}^{-1} \tag{6-4}$$

$$\boldsymbol{L}_p = \boldsymbol{F}_e \boldsymbol{F}_v \dot{\boldsymbol{F}}_p {\boldsymbol{F}_p}^{-1} {\boldsymbol{F}_v}^{-1} {\boldsymbol{F}_e}^{-1} \tag{6-5}$$

The velocity gradient is further decomposed into its symmetric and skew-symmetric parts, $\boldsymbol{D}$ and $\boldsymbol{\Omega}$, which in turn are separated into elastic, volumetric, and crystallographic plastic contributions as

$$\boldsymbol{D} = \frac{1}{2}(\boldsymbol{L} + \boldsymbol{L}^T) = \boldsymbol{D}_e + \boldsymbol{D}_v + \boldsymbol{D}_p \quad 6\text{-}6$$

$$\boldsymbol{\Omega} = \frac{1}{2}(\boldsymbol{L} - \boldsymbol{L}^T) = \boldsymbol{\Omega}_e + \boldsymbol{\Omega}_v + \boldsymbol{\Omega}_p \quad 6\text{-}7$$

Plastic deformation is assumed to occur by crystallographic slip on discrete systems. The deformed slip direction and slip plane normal in the current configuration are given by

$$\boldsymbol{s}_e^{(\alpha)} = \boldsymbol{F}_e \boldsymbol{F}_v \boldsymbol{s}^{(\alpha)} \quad 6\text{-}8$$

$$\boldsymbol{m}_e^{(\alpha)} = \boldsymbol{m}^{(\alpha)} {\boldsymbol{F}_v}^{-1} {\boldsymbol{F}_e}^{-1} \quad 6\text{-}9$$

where $\boldsymbol{s}_e^{(\alpha)}$ and $\boldsymbol{m}_e^{(\alpha)}$are the fully deformed slip direction and normal, respectively. The plastic strain rate and plastic spin due to slip are written as

$$\boldsymbol{D}_p = \sum_{\alpha=1}^{N} \dot{\gamma}^{(\alpha)} \boldsymbol{P}^{(\alpha)} \quad 6\text{-}10$$

$$\boldsymbol{\Omega}_p = \sum_{\alpha=1}^{N} \dot{\gamma}^{(\alpha)} \boldsymbol{W}^{(\alpha)} \quad 6\text{-}11$$

where $\dot{\gamma}^{(\alpha)}$ is the plastic shear rate on slip system α, N is the number of slip systems, and $\boldsymbol{P}^{(\alpha)}$ and $\boldsymbol{W}^{(\alpha)}$ are the symmetric and skew-symmetric slip-system tensors, defined as

$$\boldsymbol{P}^{(\alpha)} = \frac{\boldsymbol{s}_e^{(\alpha)} \otimes \boldsymbol{m}_e^{(\alpha)} + \boldsymbol{m}_e^{(\alpha)} \otimes \boldsymbol{s}_e^{(\alpha)}}{2} \quad 6\text{-}12$$

$$\boldsymbol{W}^{(\alpha)} = \frac{\boldsymbol{s}_e^{(\alpha)} \otimes \boldsymbol{m}_e^{(\alpha)} - \boldsymbol{m}_e^{(\alpha)} \otimes \boldsymbol{s}_e^{(\alpha)}}{2} \quad 6\text{-}13$$

The void-induced volumetric strain rate is expressed as

$$\boldsymbol{D}_v = \frac{\dot{\phi}}{3(1-\phi)} \boldsymbol{I} \quad 6\text{-}14$$

$$\boldsymbol{\Omega}_v = 0 \quad 6\text{-}15$$

where ϕ is the scalar damage variable and $\boldsymbol{I}$ is 2nd order identity tensor.

The rate-dependent constitutive update for a single crystal is written as

$$\hat{\boldsymbol{\sigma}} = \boldsymbol{\mathcal{L}} : \boldsymbol{D} - \sum_{\alpha=1}^{N} \dot{\gamma}^{(\alpha)} \boldsymbol{R}^{(\alpha)} - \frac{\dot{\phi}}{3(1-\phi)} (\boldsymbol{\mathcal{L}} : \boldsymbol{I}) - \sigma tr(\boldsymbol{D}) \quad 6\text{-}16$$

where $\hat{\boldsymbol{\sigma}}$ is the Jaumann rate of Cauchy stress, $\boldsymbol{\mathcal{L}}$ is the elastic moduli, and $\boldsymbol{R}^{(\alpha)} = \boldsymbol{\mathcal{L}} \boldsymbol{P}^{(\alpha)} + \boldsymbol{W}^{(\alpha)} \boldsymbol{\tau} - \boldsymbol{\tau} \boldsymbol{W}^{(\alpha)}$. $\boldsymbol{\tau}$ is the Kirchhoff stress tensor. Additional details of the constitutive formulation are given in Dayani et al. [257].

The shear rate on each slip system follows the rate-dependent power law

$$\dot{\gamma}^{(\alpha)} = \dot{\gamma}_0 sgn\left(\tau^{(\alpha)}\right) \left|\frac{\tau^{(\alpha)}}{g^{(\alpha)}}\right|^{\frac{1}{m}-1} \quad 6\text{-}17$$

where $\dot{\gamma}_0$ is a reference shear rate, m is the rate sensitive exponent, $\tau^{(\alpha)}$ is the resolved shear stress and $g^{(\alpha)}$ represent the slip system resistance. Slip resistance evolves via a hardening law, and is defined according to

$$\dot{g}^{(\alpha)} = \sum_{\alpha} \boldsymbol{h}^{\alpha\beta} \left|\dot{\gamma}^{\beta}\right| \quad 6\text{-}18$$

where ${g_0}^{(\alpha)}$ is the initial hardness, and $\boldsymbol{h}^{\alpha\beta}$ are the hardening moduli, typically dependent on cumulative slip $\gamma^{(\alpha)}$, defined as

$$g^{(\alpha)} = {g_0}^{(\alpha)} + \sum_{\beta} \boldsymbol{h}^{\alpha\beta}\ \gamma^{(\beta)}\ , \gamma^{(\alpha)} = \int_0^t \left|\dot{\gamma}^{(\alpha)}\right| dt \quad 6\text{-}19$$

The hardening moduli evolve as

$$h^{\beta} = h_0 \left(\frac{h_0 \gamma_{\alpha}}{\tau_0 n} + 1\right)^{n-1} \exp\left(\frac{Q}{\theta}\right) \quad 6\text{-}20$$

where h_0 is a hardening constant, n is the hardening exponent, τ_0 is the critical resolved shear stress, θ is the temperature, and Q is a temperature-related constant. Eq. 6-20 is used to for modeling ferrite phase.

Although martensite is traditionally modeled as a rigid or brittle phase, experimental evidence has shown that it can undergo plastic deformation, particularly at elevated stress levels [210]. In the present work, martensitic plasticity is described using a dislocation-based hardening law,

$$g^{(\alpha)} = {g_0}^{(\alpha)} + c_i \mu b \sqrt{\rho_d} \exp\left(\frac{\mathrm{Q}}{\theta}\right) \quad 6\text{-}21$$

where c_i is the interaction coefficient between dislocation in grain, μ is shear modulus, and b is burger vector.

The evolution of dislocation density is given by

$$\dot{\rho}_d = \left[\frac{1}{b k_1}\sqrt{\rho_d} - k_2 \rho_d \exp\left(\frac{Q}{\theta}\right)\right] |\dot{\gamma}^{\alpha}| \quad 6\text{-}22$$

where $k_1$and k_2 are material-specific parameters. This allows martensitic grains to lattice rotation and slip activation.

In this paper, phase specific constitutive response means that ferrite and martensite follow the same CP kinematic framework but use different internal strength and hardening evolution laws. This

distinction keeps deformation partitioning interpretable: differences in macroscopic response can be traced to phase strength contrast, martensite fraction, texture and damage parameters rather than to unrelated constitutive assumptions.

6.2.2 Void Deformation Modes

Ductile damage in the present framework is described through the evolution of microscopic voids. The formulation accounts for changes in void volume and ellipsoidal shape under the local stress and strain state. Voids are assumed to nucleate initially as spherical cavities and then evolve according to the deformation history.

6.2.2.1 Void Kinetics and Damage Variable

Voids are initially spherical and evolve into ellipsoids in response to local stress and strain fields. Representative void family per phase $p \in \{f, m\}$ and orientation g: number density $n^{(p)}$ and principal radii $R_k^{(p)}$ with $k = 1,2,3$. The corresponding damage variable, defined as the void volume fraction in each phase, is written as

$$\phi^{(p)} = n^{(p)} V_{void}^{(p)} \tag{6-23}$$

where V_{void} is the volume of a single ellipsoidal void and is defined by

$$V_{void}^{(p)} = \frac{4}{3}\pi R_1^{(p)} R_2^{(p)} R_3^{(p)} \tag{6-24}$$

This definition eliminates the need for an explicit representation volume, allowing direct implementation within a Taylor homogenization-based CP framework. Each crystal is treated as a statistical ensemble of microvoids, so that and capture the micromechanical trend without explicit tracking of individual cavities. This assumption preserves the physical basis of void evolution while maintaining computational efficiency.

The total damage rate is given by

$$\dot{\phi}^{(p)} = \dot{n}^{(p)} V_{void}^{(p)} + n^{(p)} \dot{V}_{void}^{(p)} \tag{6-25}$$

where the first term corresponds to new void formation and the second to the growth and distortion of existing voids.

6.2.2.2 Void Growth and Shape Evolution

Void growth is driven by plastic deformation and is influenced by the triaxiality of the principal stress. In the present framework, the spherical-growth contribution follows the classical Rice–Tracey form [10] ,

$$\frac{dR^{(p)}}{R^{(p)}} = \alpha_{RT}\exp\left(\frac{3}{2}T^{(p)}\right)d\varepsilon_p^{(p)} \tag{6-26}$$

where $R^{(p)}$ denotes the spherical void radius, $\varepsilon_p^{(p)}$ represents the equivalent plastic strain, and $T^{(p)}$ defines the stress triaxiality ratio (see Appendix B). Although α_{RT} is often taken as a constant, Huang [258] showed that it should depend on triaxiality, which leads to the modified form

$$\frac{dR^{(p)}}{R^{(p)}} = \alpha_{growth}\exp\left(\frac{3}{2}T^{(p)}\right)d\varepsilon_p^{(p)},\ \alpha_{growth} = \begin{cases} 0.427\cdot T^{1/4} & \frac{1}{3} \le T \le 1 \\ 0.427 & T \ge 1 \end{cases} \tag{6-27}$$

In addition to volumetric expansion, voids undergo shape evolution, typically deforming into ellipsoidal geometries. Following Landron et al. [74], he evolution of the ellipsoidal radii along the principal directions is written as

$$\frac{dR_k^{(p)}}{R_k^{(p)}} = \frac{dR^{(p)}}{R^{(p)}} + f\cdot d\varepsilon_k^{(p)} \tag{6-28}$$

where $dR_k^{(p)}/R_k^{(p)}$ represent the growth rate of the void radius in the direction k, $d\varepsilon_k$ is the incremental principal strain in the k^{th} direction, and f is a constant parameter controlling the void shape change magnitude, commonly assigned as $5/3$ based on existing experimental validations. While this approach effectively captures shape evolution under quasi-static conditions, it does not account for strain rate effects. At high strain rates, void growth is affected by both strain rate sensitivity and adiabatic heating. To extend Eq. (6-28) to dynamic conditions, a rate- and temperature-dependent form is introduced.

$$\frac{dR^{(p)}}{R^{(p)}} = \alpha_{growth}{T^{(p)}}^{1/4} exp\left(\frac{3}{2}(T^{(p)} + L^{(p)})\right)\ {d\varepsilon_p^{(p)}}^{1/c_1} \tag{6-29}$$

$$\frac{dR_k^{(p)}}{R_k^{(p)}} = \frac{dR^{(p)}}{R^{(p)}} + f\cdot d\varepsilon_k^{(p)} - \frac{Q}{\theta^2}d\theta \tag{6-30}$$

where $L^{(p)}$ is the Lode angle, c_1 is the strain rate sensitivity coefficient, Q is a thermal activation constant with units of temperature (K), θ is the instantaneous material temperature, and $d\theta$ is its increment. Shape evolution modifies the ratios of the ellipsoidal axes but does not contribute an additional volumetric source to the single void volume, porosity increases through nucleation and the spherical-growth kernel. Microstructure influences shape indirectly via the local partitioning of plastic flow (orientation class and phase contrast), and strain rate/temperature affect it through the same growth kernel and thermal softening already present in the model. The last term introduces thermal softening, ensuring the right-hand side remains dimensionless. Eqs. (6-29) –

(6-30) are evaluated per grain or crystal within CP framework using the local stress tensor and plastic strain increments. Thus, triaxiality, Lode parameters, and temperature are orientation- and phase-dependent, providing microstructure sensitivity absent in classical macroscopic models.

The corresponding single void volume rate becomes

$$\frac{dV_{void}^{(p)}}{V_{void}^{(p)}} = \sum_k \frac{dR_k^{(p)}}{R_k^{(p)}} = \frac{dR^{(p)}}{R^{(p)}} + f\sum_k d\varepsilon_k^{(p)} - \frac{Q}{\theta^2}d\theta \quad 6\text{-}31$$

The extended formulation is used as a compact phenomenological representation of how stress triaxiality, strain rate and temperature modify void growth and shape evolution. The associated parameters should therefore be interpreted as effective damage parameters calibrated at the homogenized crystal scale, not as directly measured void dimensions.

6.2.2.3 Stress State Dependent Void Nucleation Model

Void nucleation is modeled using a Gaussian distribution, which is commonly used to represent statistically distributed nucleation in heterogeneous materials [122]. The nucleation rate is written as

$$\dot{n}_{bulk}^{(p)} = \frac{N}{s_N\sqrt{2\pi}} exp\left[-\frac{1}{2}\left(\frac{\varepsilon_p - \varepsilon_N}{s_N}\right)^2\right]\dot{\varepsilon}_p^{(p)} \quad 6\text{-}32$$

where N is the total number of nucleation sites, ε_N, s_N represent the mean and standard deviation of the nucleation strain, respectively. Since nucleation occurs at random locations along the interfaces or within the individual phases, the maximum number of void nucleation sites in the DP steels is difficult to measure, making the determination of N from metallurgical analysis. Chu and Needleman [122] and Søvik [259] assumed ε_N and s_N, to be material-specific parameters that are constant for all stress state. However, Pathak et al. [143] studied that nucleation rates differ dramatically between stress states; therefore, the adoption of a simple strain-controlled nucleation model with ε_N, as a material parameter cannot predict the nucleation behavior for such a wide range of stress states.

To incorporate such dependencies, the mean nucleation strain is redefined as a function of strain rate and stress triaxiality,

$$\varepsilon_N = (A + B\, log_{10}(\dot{\varepsilon})\,) * \big(1 + 2 * (T_{tension} - T)\big) \quad 6\text{-}33$$

where A and B are calibration parameters across range of strain rate and $T_{tension}$ is the triaxiality under uniaxial tension. The expression ensures that nucleation delayed under lower-triaxiality shear state and accelerated under high triaxiality tension.

6.2.2.4 Interface Driven Void Nucleation Model

In DP steel, void nucleation is also triggered by stress concentration at the ferrite–martensite interfaces. The mechanical contrast between the soft ferrite matrix and the hard martensitic phase leads to high local stress and strain gradients, especially under complex loading conditions. The formation of interfacial voids near phase boundaries is induced by these gradients. Following Saeidi et al. [83] the interface-driven nucleation contribution is expressed as

$$\dot{n}_{int} = CN_i\left(1 - exp\left(-\frac{\sigma_{i,0}}{\sigma_c}\cdot\frac{\varepsilon_p^2}{2T\varepsilon_{p,0}}\right)\right) \quad 6\text{-}34$$

where n_{int} is the number of nucleated voids, C is an empirical constant, σ_c is the interface strength, $\sigma_{i,0}$ is the interface stress at initial yielding, which is equal to σ_{ys} and $\varepsilon_{p,0}$ is a characteristic plastic strain value, N_i is the initial potential nucleation sites, and equal to the number of initial triple junctions in the microstructure.

To improve the physical fidelity and generality of this model, the present study introduces two key modifications. Instead of explicitly tracking the ferrite–martensite interface geometry, a phase interaction coefficient, I, is defined from ferrite, v_f, and martensite, v_m, volume fraction as

$$I = v_f^{2/3}\cdot v_m \quad 6\text{-}35$$

The exponent $2/3$ s not intended as a universal scaling law, but as a geometrically motivated approximation based on the observation that interfacial area scales with the two-dimensional measure of a three-dimensional phase domain. Martensite is treated as a dispersed phase, for which the interfacial area scales linearly with its volume fraction. Under this assumption, the maximum of I occurs at $v_f \approx 0.4$, which is consistent with the expected morphology in DP steels. The non-dimensionalities follow the standard scaling of surface area with volume fraction, with additional assumptions on phase morphology as described above. If microstructural measurements are available, the exponent may be treated as a fit parameter to account for deviations from the isotropic grain assumption.

In the Taylor-type homogenization framework, the ferrite and martensite phases deform under the same macroscopic strain rate but accumulate distinct internal plastic strains due to their different strength. It is recognized that the uniform deformation assumption inherent to the Taylor framework does not explicitly resolve local stress concentrations at individual ferrite–martensite interfaces, as would be possible in a full-field micromechanical model. The present formulation is

therefore intended to capture the macroscopic consequences of phase interactions in a homogenized manner, with interface effects entering through the interface-driven nucleation term rather than through direct spatial resolution of the local interface stress field. The original total plastic strain term is replaced by the strain mismatch $\Delta\varepsilon_p$ between phases, defined as

$$\Delta\varepsilon_p = \left|D_p^M - D_p^F\right| \tag{6-36}$$

where D_p^M and D_p^F are the plastic strains in martensite and ferrite, respectively. This resulting phase-level plastic strain mismatch serves as a homogenized measure of interfacial plastic incompatibility. Although the physical interface is not explicitly resolved, this scalar quantity represents the average shear and normal strain discontinuity that develops across ferrite-martensite boundaries. Prior crystal plasticity simulations and experimental strain mapping [209–211] confirm that the magnitude of this mismatch correlates strongly with interface stress localization and void initiation. Consequently, $\Delta\varepsilon_p$ is adopted here as the mechanistic driving term for interfacial nucleation in Eq. (6-34).

The resulting modified expression for interface-driven void nucleation becomes

$$\dot{n}_{int} = I \cdot CN_i \left(1 - \exp\left(-\frac{\sigma_{i,0}}{\sigma_c} \cdot \frac{\Delta\varepsilon_p^2}{2T\varepsilon_{p,0}}\right)\right) \tag{6-37}$$

Here, the source term, C, is interpreted as an effective interfacial-area contribution rather than a resolved interface density. At each increment, the phase-level plastic strain mismatch is evaluated and accumulated into the current nucleation state. The formulation therefore captures the tendency for ferrite-martensite incompatibility to promote nucleation, while acknowledging that the actual interface morphology is homogenized.

The total void nucleation evolution, combining bulk and interface contributions, is given by

$$\dot{n}^{(p)} = \dot{n}_{bulk}^{(p)} + \dot{n}_{int} \tag{6-38}$$

Substituting this result into Eq. 6-25 gives the complete damage-rate form,

$$\dot{\phi}^{(p)} = \dot{n}^{(p)} V_{void}^{(p)} + \phi\left[\frac{\dot{R}^{(p)}}{R^{(p)}} + f\sum_k \dot{\varepsilon}_k^{(p)} - \frac{Q}{\theta}\dot{\theta}\right] \tag{6-39}$$

Eq. 6-39 is decomposed into the following physical contributions:

$$\dot{\phi}^{(p)} = \dot{\phi}_n^{(p)} + \dot{\phi}_g^{(p)} + \dot{\phi}_s^{(p)} \tag{6-40}$$

The nucleation-induced ($\dot{\phi}_n^{(p)}$) damage rate is expressed as

$$\dot{\phi}_n^{(p)} = \pi R^{(p)^3} \exp\left(3\left(f\varepsilon_1 + f\varepsilon_2 + f\varepsilon_3 + \frac{Q}{\theta}\right)\right)\dot{n}^{(p)} \quad 6\text{-}41$$

Void growth ($\dot{\phi}_g^{(p)}$) contribution is given by

$$\dot{\phi}_g^{(p)} = \phi\frac{\dot{R}^{(p)}}{R^{(p)}} = \begin{cases} \phi \cdot 0.427 \cdot T^{1/4} \exp\left(\frac{3}{2}(T^{(p)} + L^{(p)})\right)\dot{\varepsilon}_p & \frac{1}{3} \le T \le 1 \\ \phi \cdot 0.427 \exp\left(\frac{3}{2}(T^{(p)} + L^{(p)})\right)\dot{\varepsilon}_p & T \ge 1 \end{cases} \quad 6\text{-}42$$

Shape evolution ($\dot{\phi}_s^{(p)}$) contribution is written as

$$\dot{\phi}_s^{(p)} = \phi^{(p)} \cdot f(\dot{\varepsilon}_1 + \dot{\varepsilon}_2 + \dot{\varepsilon}_3 - \frac{Q}{\theta^2}\dot{\theta}) \quad 6\text{-}43$$

Eqs. (6-41) – (6-43) decompose the total damage rate into statistically driven nucleation, volumetric growth and anisotropic shape evolution. Each contribution depends on stress state, temperature and strain rate obtained from the CP field variables. The evolving void volume fraction then reduces the effective stress carrying capacity of each grain within the Taylor homogenization scheme.

6.2.3 Temperature-Dependent Modeling

As intermediate and high strain rate deformation in DP steels involves non-negligible heat generation, the constitutive model is coupled with a simplified thermal balance. This subsection introduces the thermal model used to represent conversion of plastic work into heat and heat exchange with the surroundings, allowing the interaction among strain rate hardening, thermal softening and damage evolution to be assessed.

A temperature-dependent framework is integrated into the crystal-plasticity damage model to account for thermomechanical coupling during plastic deformation. The formulation builds on the approach used for HSLA steels by Dayani et al. [257] and is adapted here for DP steels. The thermal source term is associated with plastic dissipation; elastic deformation is not treated as a significant source of temperature rise.

A spatially uniform temperature is assumed within each control volume, which allows the thermal response to be described through a simplified energy balance. Under this assumption, the first law of thermodynamics is written as

$$\Delta Q = Q_{gen} - Q_{bound} \quad 6\text{-}44$$

where Q_{gen} represents the volumetric heat generated due to plastic deformation and Q_{bound} denotes the heat dissipation through thermal boundaries.

The heat generation term is taken as a fraction of the plastic work,

$$Q_{gen} = \chi W_p, W_p = \int_0^{\varepsilon_p} \sigma(\varepsilon_p) d\varepsilon_p \quad 6\text{-}45$$

here, χ is the Taylor-Quinney coefficient, which characterizes the fraction of plastic deformation energy converted into heat. Under adiabatic conditions, χ is estimated from

$$\chi = \frac{\rho\, c_p\, \Delta\theta}{W_p} \quad 6\text{-}46$$

where ρ is the material density, c_p is the specific heat capacity, and $\Delta\theta$ is the observed temperature increase during deformation. Experimental measurements for various metals report χ values in the range of 0.85 – 1.0, depending on microstructure and strain rate sensitivity.

Heat dissipation to the surroundings is represented through conduction, convection, and radiation as

$$Q_{bound} = Q_{cond} + Q_{conv} + Q_{rad} \quad 6\text{-}47$$

The individual contributions are defined as

$$Q_{cond} = 2h_{cond}(\theta_{ext} - \theta) \quad 6\text{-}48$$

$$Q_{conv} = 2R_{conv}(\theta_\infty - \theta) \quad 6\text{-}49$$

$$Q_{rad} = 2\sigma\, \alpha(\theta^4 - \theta_\infty^4) \quad 6\text{-}50$$

where h_{cond} denotes the conduction coefficient, R_{conv} represents the convection heat transfer coefficient, σ is the Stefan-Boltzmann constant (5.67 e^{-08} W/ (m^2 K^4)), and α is emissivity. The variables θ_{ext} and θ_∞ represent the external and ambient temperatures, respectively.

Heat generation during plastic deformation is treated as dominated by slip-related plastic dissipation, including dislocation accumulation and dynamic recovery processes [113,172]. The contribution of void formation and interface-driven damage to the thermal budget is assumed to be secondary compared with bulk plastic work. This assumption justifies using plastic dissipation as the principal heat source while still allowing temperature rise to influence strain localization and damage evolution under dynamic and crash-relevant loading conditions.

6.3 Experimental Characterization

Commercial DP590 and DP780 sheet steels with a nominal thickness of 1.3 mm are characterized to provide the experimental data used for model calibration and validation. The chemical compositions of the as-received materials are listed in Table 6-1.

Table 6-1: Chemical composition (wt. %) of as received DP590 and DP780 steels.

	C	Mn	Si	Al	Cr	Ni	Mo	P	N	S	Fe
DP590	0.06	2.14	0.01	0.022	0.06	0.02	0.008	0.018	0.006	0.004	Bal.
DP780	0.10	2.28	0.10	0.046	0.04	0.01	0.093	0.018	0.008	0.002	Bal.

6.3.1 Microstructure Characterization

Microstructure and crystallographic texture characterization are performed using a field-emission ThermoScientific Quattro Environmental SEM equipped with a Lumis EBSD detector. EBSD scans are conducted on the sheet rolling direction-transverse direction (RD-TD) plane with a step size of 0.4 μm. This section is selected to quantify the in-plane microstructural and crystallographic features relevant to the RD and TD loading directions investigated experimentally and numerically. A single RD-TD section does not explicitly resolve through-thickness banding or other out-of-plane heterogeneities. Accordingly, the martensite fraction measured from the EBSD map is interpreted as a two-dimensional area-fraction estimate rather than an exact three-dimensional volume fraction. No stereological correction is applied because three-dimensional characterization, such as serial sectioning or tomography, is beyond the scope of this study.

The EBSD data are first cleaned using TSL OIM™ software, while grain reconstruction, phase classification, texture analysis and orientation extraction for the CPDM input are performed in MTEX. A confidence-index (CI) threshold of 0.2 is used during cleaning. Post-processing then uses a phase-classification workflow based on kernel average misorientation (KAM), CI and grain size. Grains are reconstructed using a 10° misorientation threshold, and KAM is evaluated using a 5° threshold. Point-wise phase classification is first obtained from the KAM-based criterion and then refined at the grain level using average KAM, average CI and grain size for each reconstructed grain. Final ferrite and martensite labels are assigned using a majority-rule criterion within each grain. The grain sizes reported here are obtained from the reconstructed grains using the same grain-size metric adopted in the post-processing workflow.

The initial microstructures of DP590 and DP780 are summarized in Figure 6-2 using IPF maps, phase segmentation maps and phase-wise grain size histograms. DP590 contains a ferritic matrix with dispersed martensite islands, whereas DP780 shows a higher martensite content and a more connected martensitic network. EBSD analysis gives martensite area fractions of 21.95% for DP590 and 48.34% for DP780. These values are two-dimensional area-fraction estimates and should not be interpreted as exact three-dimensional volume fractions. The DP590 value is consistent with reported values for comparable DP590 grades [260,261], while the higher

martensite fraction in DP780 is consistent with the expected strengthening role of martensite in DP780-type steels [262]. The average ferrite and martensite grain sizes are 6.82 μm and 3.67 μm for DP590, and 4.64 μm and 4.50 μm for DP780. Thus, DP780 is finer and more homogeneous overall, while DP590 retains a more evident rolling texture tendency.

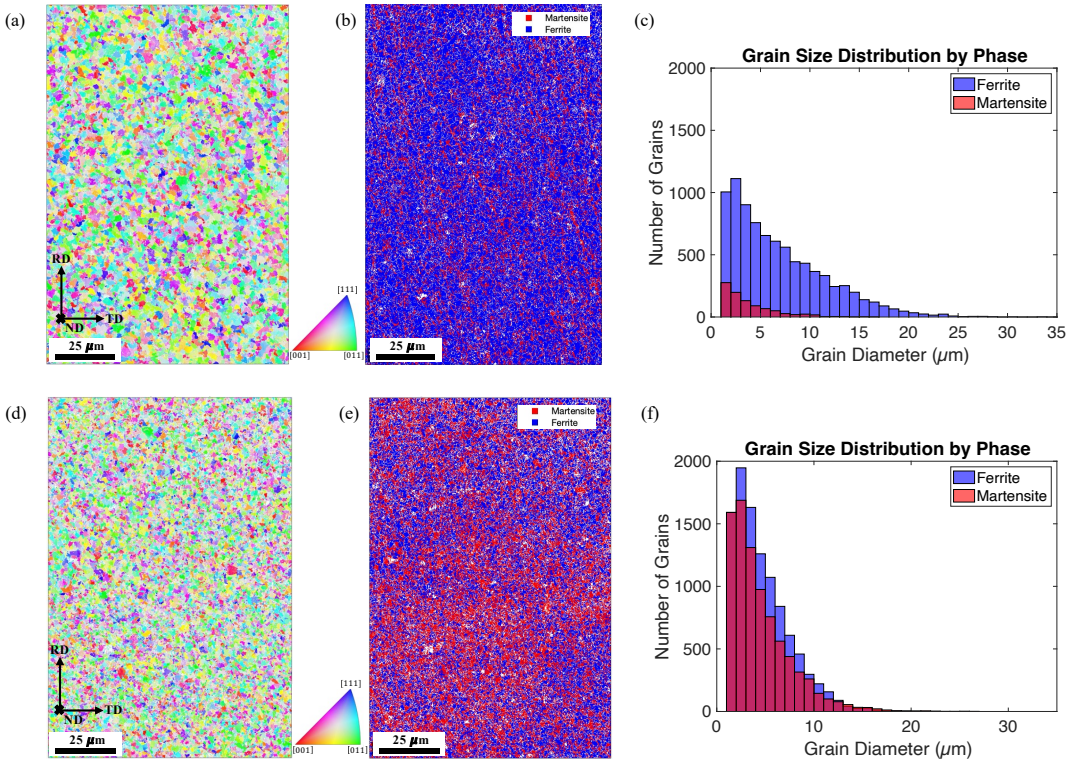


Figure 6-2: Initial microstructure characterization of DP590 and DP780 steels on the RD–TD section: (a) DP590 inverse pole figure (IPF) map, (b) DP590 phase segmentation map, (c) DP590 phase-wise grain-size histogram, (d) DP780 IPF map, (e) DP780 phase segmentation map, and (f) DP780 phase-wise grain-size histogram. Ferrite is shown in blue and martensite in red in the phase maps.

6.3.2 Mechanical Testing

Uniaxial tensile tests are conducted in the rolling direction (RD) and transverse direction (TD) at strain rates of 0.001, 0.1, 1, 10 and 100 s^{-1} using an MTS servo-hydraulic tensile machine and a hydraulic intermediate strain rate apparatus. Additional simple shear and plane strain tension tests are performed to characterize damage behavior under multiaxial loading. For both loading cases, specimens are machined with the principal axis aligned with either RD or TD. In the simple shear tests, deformation occurs in the sheet plane, and the reported RD and TD responses correspond to specimens in which the in-plane shearing direction is aligned with RD and TD, respectively. These

tests are performed under quasi-static loading at room temperature using an MTS Criterion 45 servo-hydraulic tensile machine with a 100 kN load cell. Specimen geometries are provided in Appendix A. High-resolution strain fields are captured using a stereoscopic GRAS-50S5M-C camera system with Tamron AF Micro 180 mm lenses. A random speckle pattern is applied using Rust-Oleum spray paint following Correlated Solutions recommendations. The data are analyzed using VIC-2D to extract local strain evolution. Surface temperature evolution is measured using a high-speed mid-wavelength infrared camera from the Telops IRC-TS series; camera settings are summarized in Appendix A.

Figure 6-3 compares the engineering stress–strain responses of DP590 and DP780 under uniaxial loading in RD and TD over the investigated strain rate range. TD specimens generally show slightly higher yield and tensile strength than RD specimens. Average flow stress, ultimate tensile strength (UTS), elongation to failure and standard deviations are summarized in Table 6-2 and Table 6-3. Both steels exhibit positive strain rate sensitivity. In DP590, the flow stress increases from approximately 440 MPa at 0.001 s^{-1} to 500 MPa at 100 s^{-1}, while UTS increases from about 625 MPa to 700 MPa. DP780 shows higher strength at all strain rates, with flow stress increasing from about 550 MPa to 600 MPa and UTS from about 750 MPa to 825 MPa. The higher strength of DP780 is attributed mainly to its higher martensite fraction and finer microstructure, which increase constraint on ferrite, reduce the effective ferrite slip length and increase resistance to plastic flow.

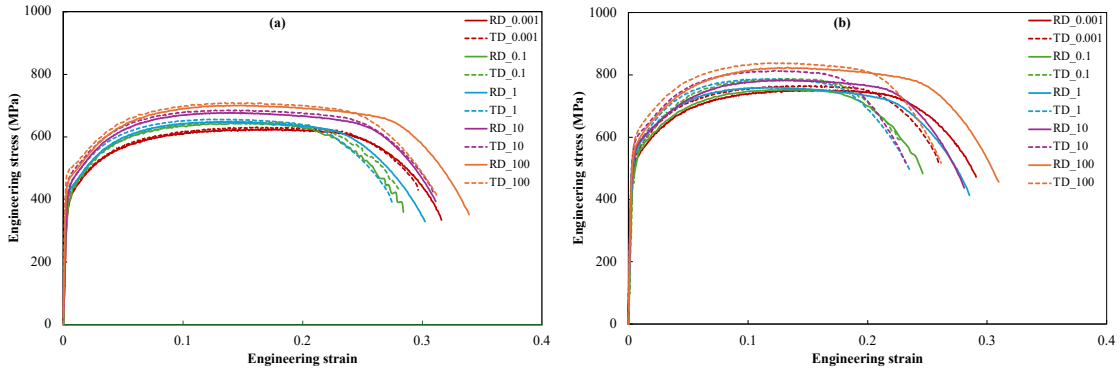


Figure 6-3: Engineering stress–strain response for (a) DP590 and (b) DP780 steel tested in RD and TD under uniaxial tension across various strain rates. [The legend indicates the loading direction (RD or TD) followed by applied strain rate (e.g., RD_0.001 refers to testing in RD at a strain rate of 0.001 s^{-1})].

The tensile tests also show direction- and rate-dependent elongation to failure. TD specimens generally exhibit lower elongation than RD specimens for both steels. The relatively larger scatter in DP780 elongation at 10 s^{-1} is attributed to the higher sensitivity of post-uniform deformation and terminal softening to small variations in specimen condition and damage evolution at this rate. Elongation decreases gradually between 0.001 and 1 s^{-1}, most likely because of increased damage accumulation and reduced strain-hardening capacity. A partial recovery in ductility is observed at 100 s^{-1}, with elongations of approximately 34% for DP590 and 31% for DP780, close to their respective quasi-static values of about 32% and 30%. This recovery is attributed to adiabatic heating and thermal softening, which can moderate localization at high loading rates [263]. The trend reinforces the need to treat strain rate, microstructure and local temperature rise together.

Table 6-2: Average tensile properties of DP590 and DP780 steels along RD.

	DP590			DP780		
Strain rate (s^{-1})	Yield stress (MPa)	UTS (MPa)	Elongation (%)	Yield stress (MPa)	UTS (MPa)	Elongation (%)
0.001	439.5±2.3	624.8±1.7	31.6±2.3	553.9±1.6	751.9±1.7	29.0±1.5
0.1	450.7±3.2	644.5±1.2	28.6±1.2	569.3±2.1	753.7±1.4	24.8±2.5
1	457.8±1.1	648.4±1.5	30.2±1.8	585.2±1.1	760.0±1.1	28.8±1.8
10	476.4±2.2	677.6±0.5	31.1±2.4	590.8±2.2	797.1±0.3	28.1±4.5
100	492.8±1.6	701.3±2.5	33.9±2.2	602.6±1.9	823.9±1.0	30.9±1.1

Table 6-3: Average tensile properties of DP590 and DP780 steels along TD.

	DP590			DP780		
Strain rate (s^{-1})	Yield stress (MPa)	UTS (MPa)	Elongation (%)	Yield stress (MPa)	UTS (MPa)	Elongation (%)
0.001	446.4±2.6	632.3±1.2	29.6±2.2	564.5±1.9	765.4±1.0	25.9±2.1
0.1	455.6±2.5	649.8±2.6	27.9±3.5	574.6±2.8	778.7±0.3	22.8±1.1
1	475.1±1.4	656.2±1.5	27.5±1.7	589.4±2.2	786.6±1.1	23.6±0.6
10	498.5±1.7	685.8±2.2	30.9±2.3	615.5±1.5	814.4±1.4	23.2±2.6
100	514.3±2.5	709.2±2.9	31.2±1.9	633.6±1.4	838.3±1.7	26.1±1.2

Figure 6-4 shows the stress–strain responses under plane-strain tension and in-plane simple shear at 0.001 s^{-1} for RD- and TD-oriented specimens. Under plane-strain tension, DP780 shows a sharper post-peak stress decline, consistent with earlier localization under triaxial constraint. Its

higher martensite fraction and finer microstructure increase flow stress while reducing uniform elongation under this loading path. In simple shear, both steels show extended hardening and high ductility, with failure strains exceeding 100%. DP780 sustains higher stress and stronger hardening than DP590; however, this should be interpreted as a response under the present shear geometry and measurement method rather than as a universal ranking of shear damage resistance.

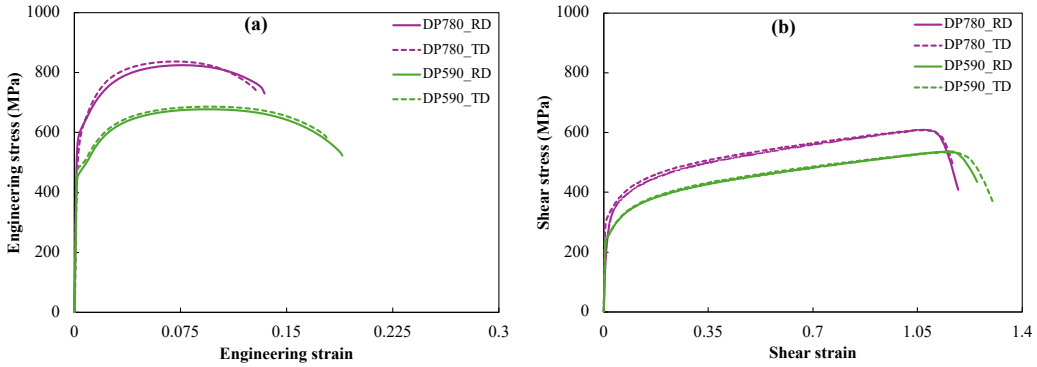


Figure 6-4: Engineering stress–strain responses of DP590 and DP780 under multiaxial loading at 0.001 s^{-1} for specimens oriented along the RD and TD: (a) plane strain tension and (b) in-plane simple shear.

Temperature evolution during uniaxial tensile testing is monitored using infrared thermography. Temperature hotspots in the thermal images coincide with DIC-identified strain concentrations, indicating that the measured temperature rise is associated mainly with localized plastic deformation. For each test, the temperature history is extracted from a region centered on the eventual necking zone and spatially averaged to obtain a representative local response. Representative thermal fields are shown in Figure 6-5, and the corresponding temperature histories are presented in Figure 6-6.

The temperature histories in Figure 6-6 should not be interpreted as significant heating during a purely elastic regime. The thermal signal is extracted from a region centered on the eventual localization zone and synchronized with the mechanical strain record. In the synchronized dataset, the point plotted at zero strain reflects a post-synchronization strain offset of approximately 0.2%, rather than an exactly undeformed state. Therefore, especially at intermediate and high strain rates, the first plotted points may already include the onset of local inelastic deformation in that region, making the temperature rise appear sharp at small nominal strain. Differences between DP590 and DP780 do not scale with macroscopic stress level alone; they reflect local deformation heterogeneity, phase-wise strain partitioning and the degree of adiabaticity during deformation.

A minimal temperature rise is recorded under quasi-static loading, whereas a clear increase is observed at higher strain rates, indicating a transition toward increasingly adiabatic deformation. The temperature rise above the initial condition increases from approximately 2 K at 0.001 s^{-1} to about 100 K at 100 s^{-1} for both grades. The apparent discontinuity between 0.001 and 0.1 s^{-1} reflects the transition from near isothermal to partially adiabatic conditions: heat exchange remains effective at very low strain rates but becomes insufficient as deformation time decreases. The resulting thermal softening is consistent with the observed partial ductility recovery at high loading rates.

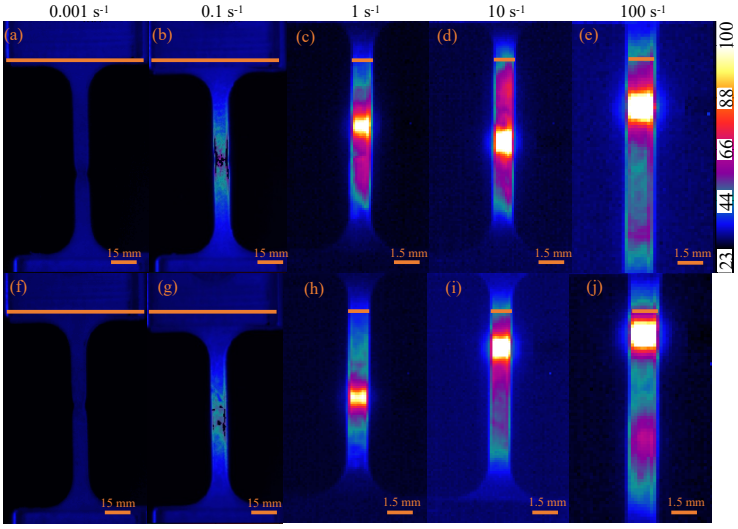


Figure 6-5: Infrared thermal fields showing the temperature increase during uniaxial tensile deformation in the RD: (a–e) DP590 and (f–j) DP780. In each column, the fields correspond to strain rates of 0.001, 0.1, 1, 10, and 100 s^{-1}, respectively. The color scale denotes the temperature rise above the initial test condition.

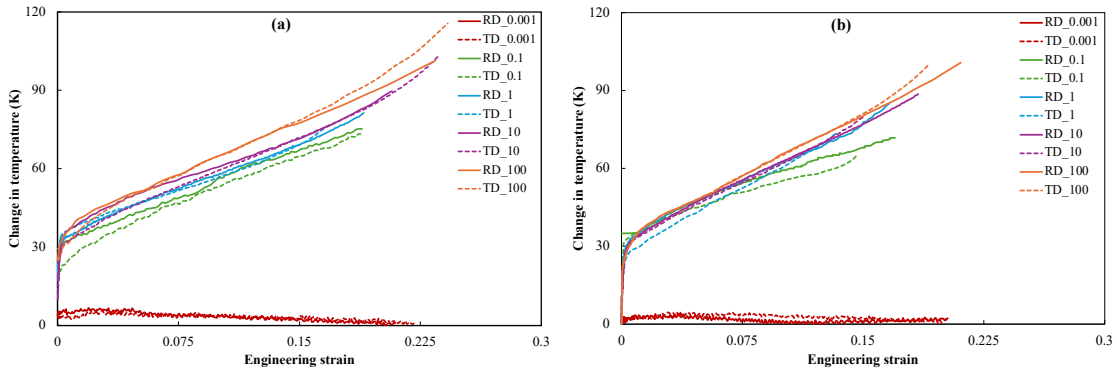


Figure 6-6: Measured temperature rise as a function of engineering strain during uniaxial tensile deformation of (a) DP590 and (b) DP780 at different strain rates.

Table 6-4 summarizes the direction-dependent thermal response. For DP590, TD shows a higher maximum temperature rise than RD across the investigated rates, reaching about 115 K at 100 s^{-1} compared with about 101 K in RD. DP780 shows the opposite trend, with RD reaching about 100 K and TD about 96 K at 100 s^{-1}. These differences indicate that temperature evolution is affected by strain rate, loading direction, microstructural morphology, martensite distribution and plastic-work dissipation. Because DP780 has higher flow stress but lower uniform strain, whereas DP590 has lower flow stress but higher uniform strain, their maximum temperature rises are similar in magnitude. This supports the inclusion of both directional anisotropy and thermomechanical coupling in the DP-steel constitutive model.

Table 6-4: Maximum temperature change during tensile testing.

Strain rate (s^{-1})	0.001	0.1	1	10	100
DP590 – RD	2.1±0.4	70.9±1.2	79.1±0.9	89.6±1.5	101.3±1.3
DP590 – TD	2.5±0.7	73.4±2.2	82.1±1.5	95.2±4.1	115.1±1.4
DP780 – RD	2.4±0.6	73.4±1.1	82.2±1.4	86.8±1.1	100.9±1.6
DP780 – TD	2.2±0.2	65.2±2.5	73.8±1.7	80.6±1.4	96.3±1.1

6.4 Result and Discussion

The proposed framework is first calibrated against uniaxial tensile data for DP590 in RD at selected strain rates of 0.001, 1 and 100 s^{-1}. It is then assessed against intermediate strain rates not used in calibration, TD responses, plane strain tension and simple shear. DP780 is calibrated with limited additional grade specific parameters and then assessed under the same strain rate and loading path conditions. Thermal parameters are calibrated using the 100 s^{-1} response and then compared with lower rate temperature histories. Ferrite and martensite are denoted by subscripts F and M, respectively.

6.4.1 Coupled Thermo-Mechanical Model and Boundary Conditions

The constitutive model is implemented within a homogenized thermomechanical crystal plasticity damage model. Ferrite and martensite orientations are extracted separately from the phase-classified EBSD dataset. After phase labeling, the measured ferrite and martensite orientations are treated as independent orientation pools, from which phase specific orientation sets are sampled for the simulations. The input therefore retains the measured phase fraction and phase specific orientation distributions within the present homogenized framework. A total of 1000 grains, 500

ferrite and 500 martensite orientations, is used in each simulation, as shown in Figure 6-7. The model does not include geometric grain boundaries or grain-level free surfaces. Loading paths are imposed through prescribed macroscopic deformation gradients consistent with the intended stress states; the boundary-condition expressions are summarized in Appendix C. Plastic slip within each phase is integrated using a rate-tangent scheme [196].

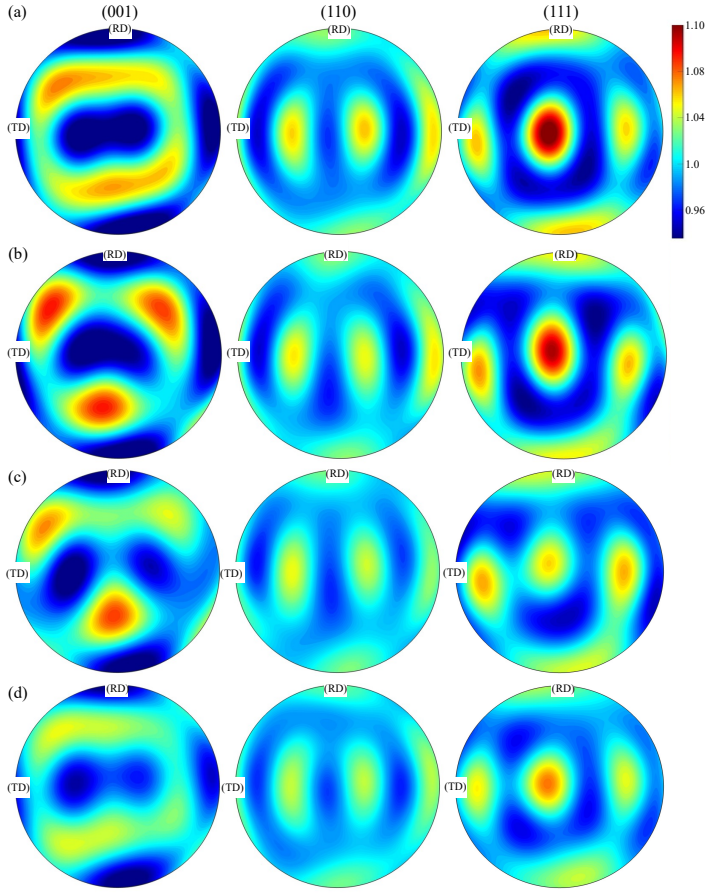


Figure 6-7: Phase specific orientation maps. (a) DP590 ferrite, (b) DP590 martensite, (c) DP780 ferrite, and (d) DP780 martensite.

6.4.2 Model Calibration and Validation

This subsection presents the parameter identification strategy and the first stage of model assessment. The framework is calibrated against selected uniaxial tensile data and then assessed against additional mechanical and thermal responses to examine strain rate dependence, microstructure sensitivity and grade to grade transferability. The material parameters used in the formulation are summarized in Table 6-5.

Table 6-5: Model parameters for both grades of steel [77,248,257,264].

Parameter type	Values
Elastic moduli (GPa)	$C_{11}^F = 233.3$, $C_{12}^F = 135.5$, $C_{44}^F = 118.0$, $C_{11}^M = 372.4$, $C_{12}^M = 345.0$, $C_{44}^M = 191.0$
Thermal parameters	$\rho_0 = 7800\ {}^{kg}/_{m^3}$, $R_{conv} = 18\ {}^{m^2}/_{W}$, $\alpha = 0.8$, $\chi = 0.9$, $h_{cond} = 15\ {}^{W}/_{m^2 - K}$,
Interface damage and evolution	$N_i = 0.41$, $\sigma_c = 2400\ MPa$, $\sigma_{i,0} = 550\ MPa$, $C = 10$

The model coefficients are determined through a staged manual calibration process using the mean squared error (MSE) metric

$$MSE = \sum_{i=1}^{N_\sigma} \left(\frac{\sigma_i^{Sim} - \sigma_i^{Exp}}{\sigma_i^{Exp}} \right)^2 + \sum_{i=1}^{N_\theta} \left(\frac{\theta_i^{Sim} - \theta_i^{Exp}}{\theta_i^{Exp}} \right)^2 \quad 6\text{-}51$$

Calibration is performed sequentially rather than by adjusting all coefficients simultaneously. First, elastic constants and initial strengths set the early elastic-plastic transition. Second, hardening and rate sensitivity parameters are adjusted to match pre-necking flow stress over the selected RD strain rates as shown in Table 6-6. Third, thermal parameters are checked against measured temperature histories. Finally, damage parameters are tuned to post-peak softening and terminal strain while keeping the same damage model for both grades. The assessment cases are then run without further adjustment unless explicitly stated.

Table 6-6: Calibrated coefficients for DP590 and DP780 steels.

Initial strength and Specific heat capacity	DP590	$g_0^F = 125.0$ MPa, $g_0^M = 240.0$ MPa, $c_p = 300\ J/kg$-℃
	DP780	$g_0^F = 130.0$ MPa, $g_0^M = 245.0$ MPa, $c_p = 310\ J/kg$-℃
Dislocation parameters	Both grades	$k_1 = 45$, $k_2 = 15$, $b = 0.28e^{-9}\ m$, $c_i = 0.95$, $\rho_d = 10\ m^{-2}$
Hardening parameters	Both grades	$h_0 = 2.58 \cdot g_0^F$, $n = 0.15$, $m = 0.01$, $\dot{\gamma}_0 = 0.001\ s^{-1}$
Temperature parameters	Both grades	$Q = 50\ K$, $\theta = 300\ K$, $\theta_{ext} = 298\ K$, $\theta_\infty = 293\ K$
Damage parameters	Both grades	$A = 1.4$, $B = 0.1$, $c_1 = 2.1$, $s_N = 0.26$
length scale and defect density	DP590	$d^F = 1\ \mu m$, ${N_0}^F = 35000$
	DP780	$d^F = 5\ \mu m$, ${N_0}^F = 48000$

Although Table 6-5 and Table 6-6 contains many entries, not all of them are independent fitting variables. Elastic constants, density, heat-capacity values and thermal boundary parameters are fixed or taken from material data; orientation sets, and phase fractions are measured from EBSD; and the remaining fitted parameters are constrained by stress–strain response, temperature rise and

terminal strain. The length scale and defect density should be interpreted as effective homogenized descriptors of the initial damage, not as direct measurements of a single physical void size.

Figure 6-8(a) compares measured and predicted engineering stress–strain responses for the calibration data set: DP590 over selected strain rates of 0.001, 1 and 100 s^{-1}, together with DP780 at 0.001 s^{-1}. The model captures the main features of the elastic response, strain hardening, peak stress, post-necking softening and final failure. The DP590 results indicate that rate-dependent plastic flow and damage evolution can be represented with calibrated parameter set over the tested range. The DP780 response, obtained with limited additional calibration, suggests that the grade difference can be represented mainly through microstructural descriptors and phase specific constitutive parameters rather than by changing the damage evolution laws. Figure 6-8(b) compares measured and predicted temperature evolution at 100 s^{-1} for both grades. The predicted temperature rise follows the measured trend associated with plastic dissipation, supporting the thermomechanical coupling used in the model.

The larger effective length scale and defect density assigned to DP780 should not be interpreted as measured void radii or directly measured void counts. They represent homogenized descriptors of the initial damage, accounting for the higher martensite fraction and denser ferrite-martensite incompatibility sites in DP780. This interpretation is less direct than a fully resolved interface model; future validation against independent void statistics from SEM, TEM or tomography is therefore needed.

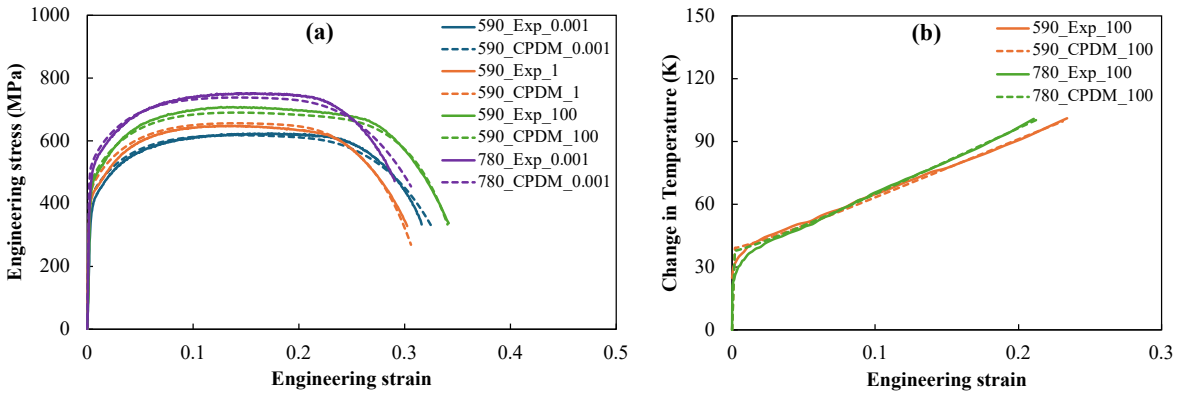


Figure 6-8: Experimental and CPDM-predicted responses for the calibration data set: (a) engineering stress–strain response in the RD for DP590 and DP780 at the selected strain rates, and (b) temperature evolution at 100 s^{-1} for DP590 and DP780. [The legend indicates the DP steel

grade (590 or 780) for experimental and CPDM-predicted followed by applied strain rate (e.g., 590_Exp_0.001 refers to DP590 experimental at a strain rate of 0.001 s^{-1})].

6.4.3 Strain-Path and Rate Dependence of Damage Evolution

Figure 6-9 compares experimentally measured and CPDM-predicted engineering stress–strain responses for DP590 and DP780 steels over a broad range of strain rates. All simulations are performed outside the strain rate regime used for calibration, thereby assessing the predictive capability of the proposed framework. This is particularly relevant when compared with GTN type porous plasticity models, for which damage parameters are commonly recalibrated to maintain accuracy across different strain rate regimes [11,13,265].

For DP780, the model captures the measured increase in flow stress and peak strength with increasing strain rate, together with the associated ductility reduction. These trends arise from coupled rate-dependent slip kinetics, thermal softening and stress state-dependent void nucleation and growth, without introducing separate strain rate specific damage parameters. Similar agreement is obtained for DP590, although deviations near terminal softening remain. These deviations are expected because the Taylor-type homogenized framework does not include nonlocal regularization or explicit localization band formation. Unlike classical GTN formulations, where softening is governed mainly by void volume fraction, the present CPDM links damage evolution to crystallographic slip activity, local stress triaxiality and temperature rise.

A key advantage of the present framework is that the same damage model structure is used for both DP590 and DP780. Differences in response are represented through measured phase fraction, phase specific orientation distributions, phase strength and effective initial damage descriptors. This does not prove universal transferability, but it shows that the model can compare two DP grades without introducing an entirely new damage formulation for each grade.

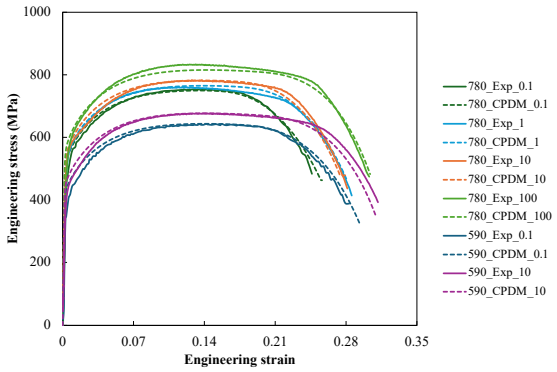


Figure 6-9: Experimental and CPDM-predicted engineering stress–strain responses of DP590 and DP780 under uniaxial tension in the RD at multiple strain rates.

Figure 6-10 extends the assessment to the TD for DP590 and DP780. Using the same parameter set, the CPDM captures the overall TD stress–strain response, including the onset of necking and post-peak softening trends, with deviations mainly in the final stage of deformation where localization is strongest. The agreement indicates that directional differences are represented through crystallographic slip activity and stress state-dependent void evolution rather than through direction specific parameter tuning.

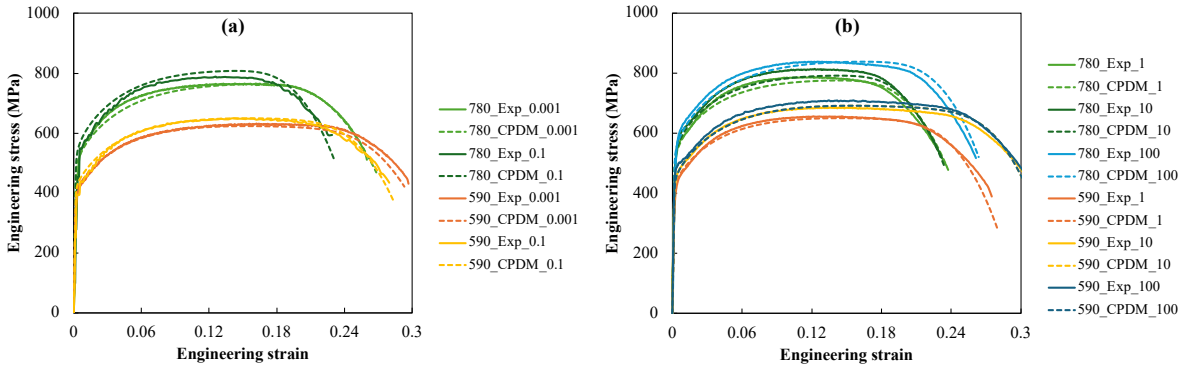


Figure 6-10: Experimental and CPDM-predicted engineering stress–strain responses of DP590 and DP780 under uniaxial tension in the TD: (a) quasi-static strain rates and (b) intermediate strain rates.

Figure 6-11 compares measured and predicted responses under plane strain tension and in-plane simple shear at 0.001 s^{-1} for DP590 and DP780 in RD and TD. Under plane strain tension, the model captures the overall stress–strain response and the onset of post-peak softening for both materials and orientations, although discrepancies increase near terminal localization. Directional differences are reproduced without orientation specific damage parameter adjustment. Under simple shear, the predicted response is also consistent with the experiments over much of the deformation range, with larger deviations at high shear strains. This behavior reflects the different damage mechanisms active at low triaxiality, where shear-dominated void distortion and slip-mediated damage accumulation are more important than purely volumetric void growth. Compared with classical GTN-type models, which often require shear specific modifications or recalibration, the present formulation provides a unified stress state sensitive description for the loading paths considered here.

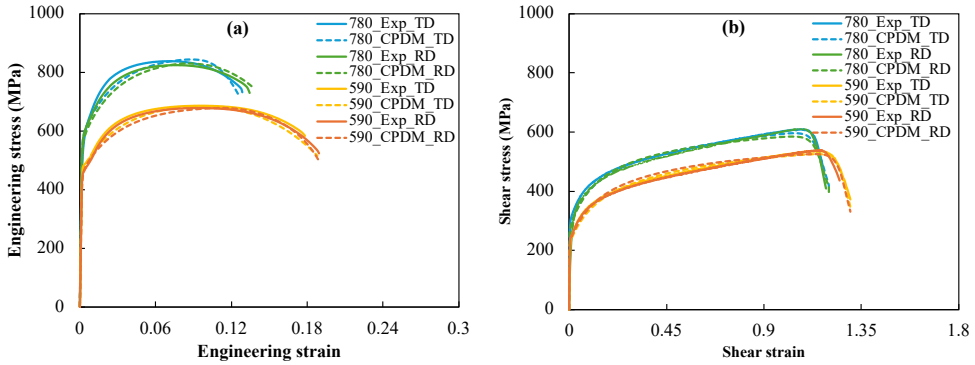


Figure 6-11: Experimental and CPDM-predicted stress–strain responses of DP590 and DP780 at 0.001 s^{-1} in the RD and TD under (a) plane strain tension and (b) in-plane simple shear.

These comparisons support, but do not prove, transferability of the damage formulation across loading path and stress state. The model separates high triaxiality plane strain tension from low triaxiality shear because void growth, nucleation and shape evolution depend on stress triaxiality, Lode parameter and strain rate. A stricter validation would require local damage measurements for each loading path.

6.4.4 Thermal Predictions

The thermomechanically coupled response is evaluated by comparing predicted and measured temperature evolution during uniaxial tension from 0.001 to 100 s^{-1} for both DP590 and DP780 in RD and TD. Figure 6-12 shows temperature rise as a function of engineering strain. At 0.001 s^{-1}, the model predicts negligible temperature increase, consistent with near isothermal deformation. With increasing strain rate, it captures the progressive temperature rise associated with larger plastic dissipation and reduced time for heat diffusion. The predicted trends are generally consistent with the measurements, particularly before strong localization. At 100 s^{-1}, the model tends to underestimate the measured temperature rise at large strains. This may result from the homogeneous temperature assumption and the use of a constant Taylor-Quinney coefficient, whereas the fraction of plastic work converted into heat may evolve during deformation. A strain-dependent Taylor-Quinney coefficient and spatially resolved thermal field may improve the final stage prediction. Despite this limitation, the model reproduces the overall strain rate and orientation dependence of the thermal response without introducing rate specific thermal fitting parameters.

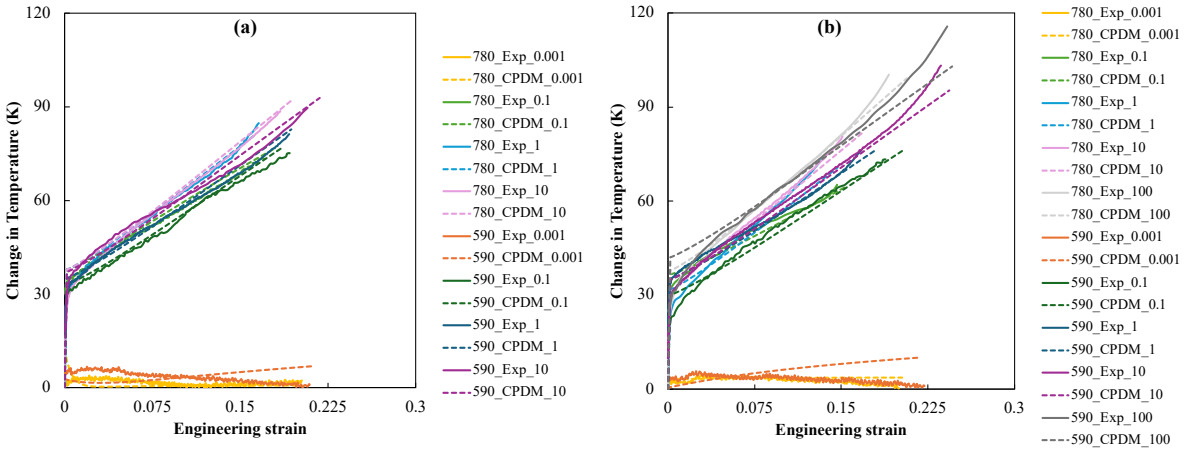


Figure 6-12: Experimental and CPDM-predicted temperature evolution under uniaxial tension for DP590 and DP780 steels at various strain rates in (a) RD and (b) TD.

6.4.5 Strain Path-Dependent Texture Evolution

Texture evolution under different strain paths is important because texture controls slip system activation, anisotropic hardening and localization in sheet metals. In DP steels, deformation induced texture changes also reflect load sharing, phase interaction and orientation-dependent slip activity. Comparing measured and predicted pole figures therefore provides an additional check on whether the model captures broad orientation redistribution, beyond matching macroscopic stress–strain curves alone.

This subsection separates measured texture evolution from model sensitivity to texture. Pole figure comparisons are used to assess whether the CPDM captures broad orientation redistribution, whereas the subsequent idealized texture study isolates selected BCC components. Figure 6-13 compares measured and predicted {100}, {110} and {111} pole figures after uniaxial tension at 0.001 and 100 s^{-1}. Because the initial textures are weak, the comparison is interpreted in terms of relative symmetry, lobe movement and intensity changes rather than exact component by component agreement.

Figure 6-14 extends the comparison to simple shear and plane strain loading at the final deformed stage for DP590 and DP780. Deformation produces texture reorganizations relative to the initial state, with sharper features in DP590 and more diffuse features in DP780. Under simple shear, textures sharpen and rotate away from the RD-TD symmetry axes, consistent with the imposed shear geometry. Under plane strain, textures evolve toward stronger banding along RD-TD symmetry lines. The CPDM captures the main qualitative features of the measured pole figures,

including dominant lobe symmetry, relative strengthening of {111} and {110} features and weak evolution of {100}. This agreement supports the orientation update and slip activity trends, but it should not be interpreted as complete validation of phase specific texture evolution.

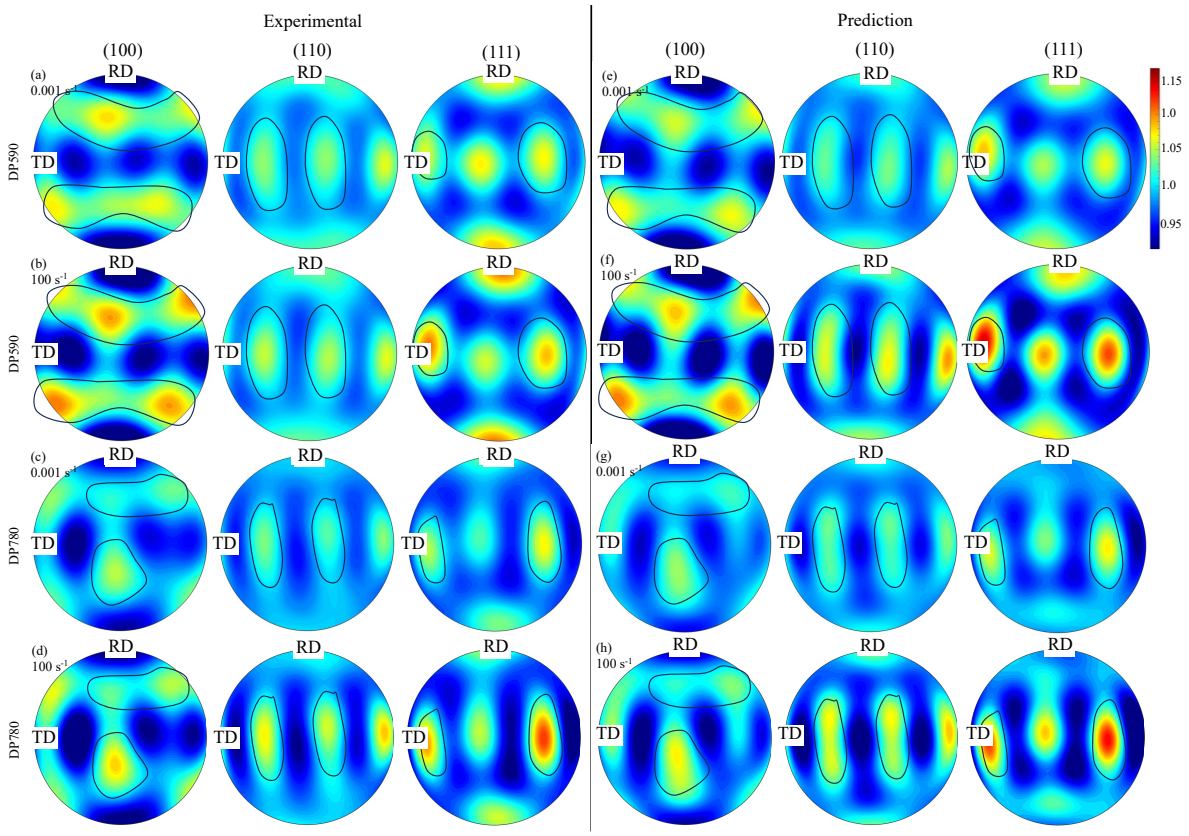


Figure 6-13: Comparison of experimentally measured and CPDM-predicted bulk pole figures at the final deformed stage after uniaxial tension of DP590 and DP780 at different strain rates. The {100}, {110}, and {111} pole figures are arranged from left to right in each panel. Panels (a–d) show the experimentally measured pole figures, and panels (e–h) show the corresponding CPDM predictions.

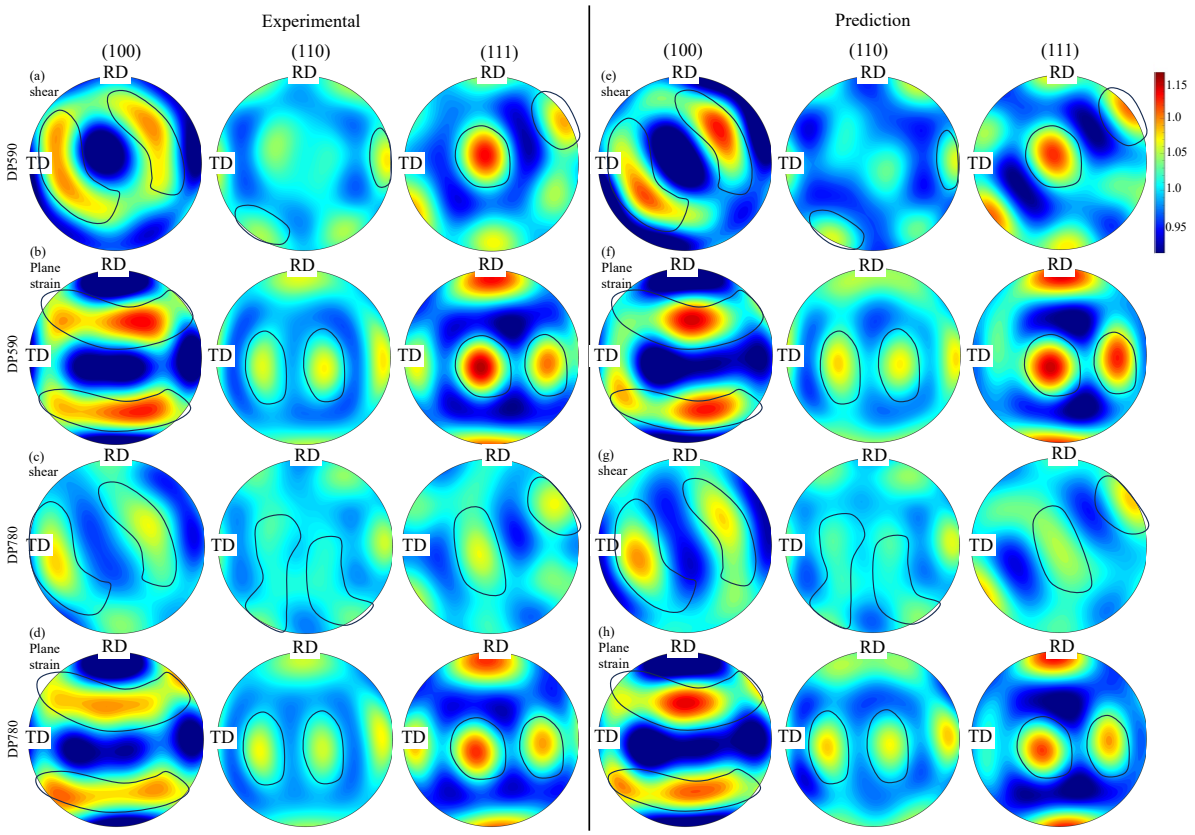


Figure 6-14: Comparison of experimentally measured and CPDM-predicted bulk pole figures at the final deformed stage under multiaxial loading for DP590 and DP780. Panels (a–d) show the experimentally measured pole figures, and panels (e–h) show the corresponding CPDM predictions for the same loading conditions.

6.5 Texture Dependent Damage Evolution – Parametric Study

The preceding validation shows that the framework captures the dominant strain rate, loading path and directional trends observed experimentally. A parametric study using idealized texture components is then performed to isolate the role of crystallographic orientation in damage evolution while holding other microstructural variables fixed. These simulations are not intended to reproduce the complete measured sheet texture; they provide a controlled orientation sensitivity analysis.

6.5.1 Quantification of Texture Components

Crystallographic orientation is important for connecting microstructural design to macroscopic formability in DP steels. Bulk texture analysis can correlate anisotropy with forming response, but the contribution of individual texture components to damage initiation, growth and localization is

more difficult to isolate experimentally. This is especially important for DP steels because phase contrast and ferrite-martensite incompatibility make the stress–strain response sensitive to the crystallographic configuration of the constituent grains.

Relative fractions of selected BCC texture components are estimated from the orientation distribution function (ODF) derived from the EBSD data. Table 6-7 and Figure 6-15 summarize the component fractions for DP590 and DP780. The values are obtained from the bulk ODF using a 20° misorientation tolerance around the ideal BCC component centers and are used only as comparative indicators between the two grades.

Table 6-7: Relative fractions of selected BCC texture components (in %).

Material	{112}<110>	{223}<110>	{111}<110>	{111}<112>	{001}<110>
DP590	7.87	12.09	10.84	8.96	5.65
DP780	11.03	8.56	6.49	9.93	8.56

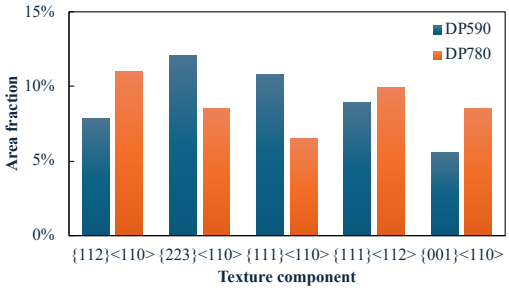


Figure 6-15: Relative fractions of the selected BCC texture components obtained from the bulk ODFs of DP590 and DP780.

6.5.2 Damage Evolution in Fiber Texture

Uniaxial tensile simulations are performed at 0.001 s^{-1} to examine the effect of crystallographic orientation on damage response. Five representative BCC rolling-texture components are selected: α-fibers, γ-fibers, and rotated cube orientations. For this idealized study, the same nominal crystallographic orientation is assigned to ferrite and martensite to isolate the effect of the selected texture component. This assumption is not intended to reproduce the actual ferrite-martensite orientation relationship in DP steels. Ferrite and martensite retain their different constitutive parameters from the reference DP590 model. Each simulation uses 1000 grains with orientations distributed within a 15° misorientation tolerance around the selected component center. A sensitivity check using narrower and broader tolerances showed that the spread affects the

quantitative onset and level of damage acceleration but preserves the overall texture-dependent trend. The corresponding {111} pole figures are shown in Figure 6-16.

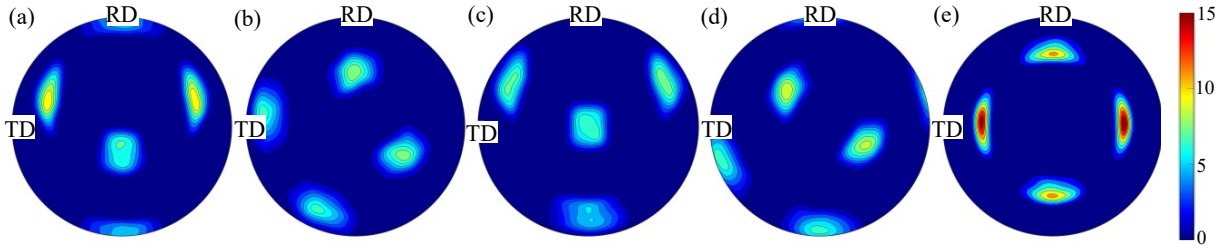


Figure 6-16: Idealized {111} pole figures for the five selected crystallographic texture components used in the parametric study: (a) {112}<110> ; (b) {223}<110>; (c) {111}<110>; (d) {111}<112>; (e) {001}<110>.

The present framework does not use a single critical damage threshold to define failure. The damage variable evolves continuously and progressively degrades the constitutive response. Texture components are therefore compared using the strain range over which damage accelerates, and post-peak softening becomes pronounced. Figure 6-17 shows the predicted engineering stress–strain response and damage evolution for selected texture components under uniaxial tension at 0.001 s^{-1}. Orientation significantly affects strength, elongation and post-peak response. The rotated cube {001}<110> component shows the lowest strength and earliest softening, indicating less favorable slip activity and faster localization in the idealized aggregate. The α-fiber {112}<110> component develops the highest flow stress and strong hardening, but damage rises sharply after initiation. The {223}<110> component shows larger elongation and more gradual damage accumulation. The γ-fiber related {111}<112> and {111}<110> components fall between these limits, combining intermediate strength with delayed and more gradual damage growth. This trend is consistent with texture-based formability analyses of BCC sheets, where γ-fiber character generally improves drawability and {001}<110> type orientations are less favorable [253,266]..

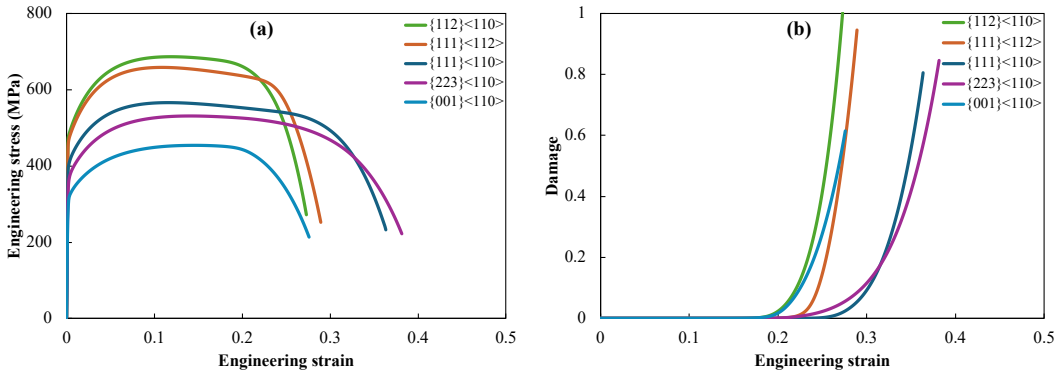


Figure 6-17: Predicted influence of crystallographic orientation on the uniaxial tensile response of the idealized DP steel microstructure at 0.001 s^{-1}: (a) engineering stress–strain response and (b) damage evolution for the selected texture components.

These simulations suggest a mechanistic link between crystallographic orientation, local stress triaxiality and damage kinetics. The result should not be generalized from a single ideal component to a full rolling texture. In real sheets, neighboring orientations along a fiber, phase distribution and strain path history can dilute or change the response of an isolated component.

Figure 6-18 compares the predicted engineering stress–strain response and Lankford coefficient for selected idealized texture components under RD and TD uniaxial loading. The anisotropy in Figure 6-18(b) is evaluated at 10% engineering strain to provide a stable comparison among components. In the uniaxial implementation, the loading, in-plane transverse and thickness directions correspond to the 1-, 2- and 3-directions, respectively, and the Lankford coefficient is evaluated as the ratio of transverse to thickness strain increments. For the idealized study, RD and TD responses are generated by rotating the same component centered orientation map about the sheet normal. The reported anisotropy therefore reflects the transformed response of the same crystallographic texture state rather than two independently generated textures.

The predicted r-values are orientation sensitive but should be interpreted carefully. The γ-fiber orientations are generally associated with favorable normal anisotropy in BCC sheet steels and can show weak in-plane anisotropy when the fiber is well distributed. The differences predicted here arise because each component is isolated as an idealized texture state; they do not imply that a complete γ-fiber is intrinsically more anisotropic than other measured texture families. Thus, flow stress, r-value and damage accumulation are related but not interchangeable measures of orientation sensitivity. In the present model, {223}<110> delays damage most effectively, whereas γ-fiber components primarily influence plastic anisotropy. This distinction is important for DP-

steel design because a texture favorable for deep drawing does not necessarily minimize local damage once ferrite-martensite incompatibility and stress triaxiality are included.

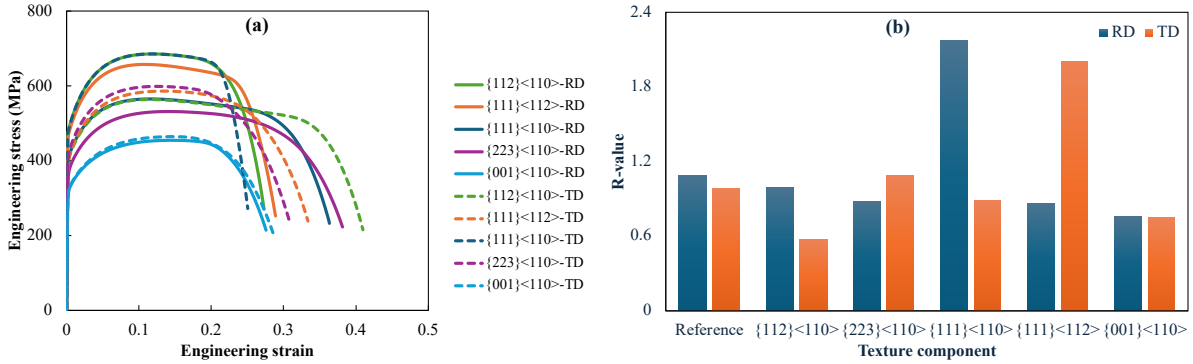


Figure 6-18: Predicted influence of selected crystallographic texture components on tensile response and plastic anisotropy under uniaxial loading in the RD and TD: (a) engineering stress–strain response and (b) Lankford coefficient evaluated at 10% engineering strain.

6.6 Chapter Conclusion

This study developed a thermomechanically coupled, rate-dependent crystal plasticity damage framework for DP590 and DP780 steels. The model links measured phase fraction and texture with stress state sensitive void nucleation, void growth, void shape evolution and a homogenized ferrite-martensite interface contribution. Across uniaxial tension, plane strain tension and simple shear, the simulations differentiated the expected effects of stress triaxiality and Lode parameter on damage accumulation and softening: plane strain tension promoted earlier damage development, whereas simple shear delayed volumetric damage growth under lower triaxiality.

Calibration against selected DP590 uniaxial tensile data from 0.001 to 100 s^{-1} provided a consistent representation of elastic-plastic response, post-peak softening, failure strain and temperature rise from plastic dissipation. Responses at additional strain rates retained the main experimental trends, indicating that the model captures important rate-dependent mechanisms without strain rate specific damage parameter fitting. Application to DP780 required only limited additional grade specific calibration, mainly through phase fraction, phase strength and effective initial damage descriptors. This supports, while not proving universally, the transferability of the damage model structure across the two DP grades examined.

The framework also reproduced the main differences between RD and TD responses and separated the damage trends under plane strain tension and simple shear. The predicted texture evolution under uniaxial, shear and plane strain loading captured the dominant qualitative changes in pole

figure symmetry, lobe movement and texture sharpening. These results indicate that the model represents the major links among slip system activity, anisotropic hardening, localization tendency and damage evolution, although phase specific texture evolution and local interface damage require more direct validation.

The idealized texture study showed that individual BCC texture components influence strength, plastic anisotropy and damage evolution in different ways. The {112}<110> component promoted high strength but rapid damage acceleration after initiation, whereas {223}<110> produced more gradual damage growth and larger elongation in the idealized aggregate. Gamma-fiber components primarily affected plastic anisotropy, while the rotated-cube {001}<110> component showed early softening. These findings indicate that a texture component favorable for strength or r-value is not necessarily the most favorable for damage resistance. Overall, the framework provides a microstructure informed structure property modeling tool for interpreting rate- and path-dependent damage in DP steels relevant to forming and crash loading.

7 Development of a Crystal Plasticity-Based Transformation Coupled Damage Evolution Model for Q&P Steels

In this chapter, a thermomechanically coupled crystal plasticity damage model is developed for quenching and partitioning steels. The formulation accounts for crystallographic slip, deformation induced martensitic transformation, temperature evolution, and phase-sensitive degradation within a modified Taylor homogenization framework. Damage is represented through an effective grain-level description that combines ferrite matrix damage, ferrite–martensite interface degradation, and austenite-containing interface degradation. This allows the model to capture the transition from transformation-assisted hardening to damage-driven softening without introducing a separate post-processing failure criterion.

The framework is applied to QP3Mn and QP980 steels to investigate the coupled effects of retained-austenite stability, strain rate, temperature, and phase-sensitive damage evolution. For QP3Mn, the model is evaluated under different strain rate and temperature conditions using tensile response and retained-austenite evolution data. For QP980, the model is used to capture the measured rate-dependent tensile response while incorporating retained-austenite evolution as physically informed input. The chapter also introduces a transition-strain analysis to distinguish the macroscopic onset of softening, rapid damage acceleration, and the internal shift from retained-austenite assisted stabilization to damage-dominated degradation.

This chapter presents a manuscript submitted to the International Journal of Plasticity.

International Journal of Plasticity, INTPLA-D-26-00833.

A Thermomechanically Coupled Crystal Plasticity Damage Model for Quenching and Partitioning Steels: Effects of Retained Austenite Stability, Strain Rates, and Temperatures

Sandipkumar Dayani[a], Waqas Muhammad[a], Abhijit Brahme[a], Fatemeh Hekmat[b], Trevor Sabiston[c], Kathy Wang[b], Kaan Inal[a]

[a] Department of Mechanical and Mechatronics Engineering, University of Waterloo, Waterloo, Ontario, N2L 3G1, Canada

[b] General Motors Technical Centre, General Motors, Warren, MI, 48092, United States

[c] Canadian Technical Centre, General Motors of Canada Limited, Oshawa, Ontario, L1J 0C5, Canada

Overview

Quenching and partitioning (Q&P) steels exhibit a deformation response governed by the coupled evolution of crystallographic slip, retained austenite transformation, temperature rise, and progressive damage. In this work, a thermo-mechanically coupled crystal plasticity damage model is developed for Q&P steels within a modified Taylor homogenization framework. The formulation is derived from the Helmholtz free energy and dissipation inequality, from which the driving forces for plastic slip, martensitic transformation, damage evolution, and temperature evolution are obtained in a thermodynamically consistent manner. The key constitutive extension is the introduction of a phase-sensitive effective damage model that incorporates ferrite matrix damage, ferrite-martensite interface decohesion, and austenite containing interface degradation within a unified grain level framework. The model is applied to QP3Mn and QP980 steels under different thermomechanical loading conditions. For QP3Mn, the framework reproduces the coupled evolution of tensile response including onset of softening and failure and retained-austenite depletion over multiple thermomechanical conditions. For QP980, the model captures the measured rate-dependent tensile response. A transition strain analysis is introduced to distinguish the macroscopic onset of softening, the rapid acceleration of damage, and the internal constitutive shift from retained austenite assisted stabilization to damage dominated degradation. The results show that retained austenite plays a dual mechanical role: it delays degradation at lower strain through transformation-assisted hardening, but at larger strain promotes instability through increased phase contrast and local incompatibility. The proposed framework provides a physically

interpretable constitutive basis for linking retained-austenite stability, thermomechanical loading, and phase sensitive damage evolution in Q&P steels.

Keywords: Crystal plasticity; Damage evolution; Thermo-mechanical modeling; Transformation-induced plasticity; Interface decohesion.

7.1 Introduction

Quenching and partitioning (Q&P) steels have become important third-generation advanced high strength steels for automotive applications because they provide an attractive combination of strength, ductility, formability, and energy absorption through a multiphase microstructure containing metastable retained austenite (RA) [267,268]. Their use in forming- and crash-relevant applications increasingly requires constitutive models that can predict not only the monotonic flow response, but also the coupled evolution of phase transformation, thermal response, damage accumulation, and softening. This requirement is particularly important for virtual material characterization and forming simulations, where the mechanical response of Q&P steels is governed by phase-dependent plasticity, transformation-induced plasticity (TRIP), and the progressive loss of load-carrying capacity [268,269].

The contribution of RA to the mechanical response of Q&P steels depends not only on its initial fraction, but also on its mechanical stability during deformation. RA stability during deformation is governed by carbon enrichment, morphology, phase ratio, and the surrounding microstructural constraint. As a result, retained austenite content may lead to different transformation responses [270–272]. The transformation response is further influenced by the applied deformation conditions. Experimental and modeling work has demonstrated that temperature, strain rate, and stress state alter the kinetics of the austenite to martensite transformation, while local neighborhood effects and strain partitioning further modify when and where retained austenite transforms during loading [273,274]. At higher strain rates, the influence of deformation induced heating becomes especially important because the resulting non-isothermal conditions can change the apparent stability of retained austenite and therefore the evolution of strain hardening and deformation localization [275,276]. These observations indicate that retained austenite evolution in Q&P steels must be treated as a coupled thermomechanical and microstructure sensitive process, rather than as a fixed or purely strain driven phase transformation.

Although deformation induced martensitic transformation contributes to the high work-hardening capacity of Q&P steels, softening and failure are controlled by competing damage mechanisms. In

multiphase steels, damage can develop through ferrite-martensite interface decohesion, martensite cracking, void nucleation in softer phases, and void growth or coalescence under increasing constraint [6,277,278]. In Q&P steels, these mechanisms are further complicated by the progressive transformation of RA into fresh martensite. Transformation may initially stabilize deformation by sustaining hardening and redistributing strain, but extensive transformation can also increase local strength mismatch, transformation strain incompatibility, and interface tractions. Recent in situ and micromechanical studies have shown that RA stability, phase neighborhood, microstrain partitioning, transformation kinetics, and damage evolution are closely coupled in Q&P steels [274,279–282]. Therefore, damage in Q&P steels should not be modeled independently from martensitic transformation.

The strain rate and temperature dependence of Q&P steels further complicates the prediction of softening. At elevated strain rates, deformation can become increasingly non-isothermal because a larger fraction of plastic work is converted into heat over a short time scale. The resulting temperature rise may reduce slip resistance, modify the thermodynamic stability of RA, and change the rate of martensitic transformation [23,273,276,283,284]. Since increasing temperature generally reduces the chemical driving force for martensitic transformation, high-rate deformation can simultaneously increase mechanical driving forces and suppress transformation through adiabatic heating. Recent work has also shown that the rate dependence of Q&P steels can be non-monotonic and may involve competing effects of thermal softening, transformation suppression, phase-level hardening, and solute-drag-related mechanisms [285]. Thus, the measured response under intermediate or dynamic loading reflects the coupled outcome of rate-dependent plasticity, thermal evolution, transformation kinetics, and evolving phase constraint.

Several crystal plasticity formulations have been developed to describe TRIP-assisted and Q&P steels. Foundational thermodynamic and crystal plasticity formulations established the basis for coupling crystallographic slip with martensitic transformation, including the micromechanical framework of Cherkaoui et al. [286,287], the thermomechanical treatment of Turteltaub & Suiker [22,288], the crystal plasticity finite element model of Lee et al. [289], crystal plasticity framework with martensitic transformation [52], and the deformation transformation coupling framework of Ma and Hartmaier [132]. More recent work has moved toward QP and related third-generation advanced high-strength steels, where phase-resolved constitutive identification has been performed for QP980 using synchrotron diffraction and crystal plasticity [133], and crystal

plasticity-based formulations have been developed to capture strain path dependence, variant selection, and stress state-sensitive retained austenite transformation in QP1180 and QP980 steels [24,25,134,275]. Thermomechanically coupled crystal plasticity models have also expanded the description of transformation behavior over wider ranges of strain rate and temperature in TRIP-assisted steels [23]. These studies have significantly improved the predictive treatment of RA transformation and phase partitioned plasticity, but the literature remains more developed for transformation kinetics and hardening than for the coupled prediction of RA evolution, damage accumulation, softening, and failure related degradation under varying thermomechanical conditions.

The closest prior efforts can be situated within two related lines of work. Connolly et al. [23] developed a thermomechanically coupled crystal plasticity formulation for QP3Mn that captured tensile response, RA depletion, and adiabatic heating over a comparable strain rate and temperature range. However, their model did not include constitutive damage, so post-peak softening and loss of load-carrying capacity were not represented as internal state evolution. Park et al. [25] advanced stress state-sensitive martensitic transformation modeling in QP980 using crystal plasticity with strain path effects and variant selection, but the formulation was essentially isothermal and did not include phase resolved degradation. Other recent crystal plasticity studies on Q&P steels have focused mainly on transformation kinetics and hardening [24,134,275] or on microstructure specific damage processes [280,281], but not on their coupled evolution within a single constitutive framework. Parallel crystal plasticity damage formulations have coupled crystallographic plasticity with micromechanics- or thermodynamics-based damage evolution [237,257], but these works do not address the simultaneous coupling of retained austenite transformation, thermomechanical response, phase-sensitive degradation, and post-peak softening in Q&P steels. The remaining scientific need is therefore not only to fit stress–strain curves, but to identify when the stabilizing effect of RA transformation is overtaken by damage mechanisms under different thermomechanical paths.

Accordingly, the present work develops a thermomechanically coupled crystal plasticity damage model for Q&P steels within a modified Taylor homogenization framework. The contribution is threefold. First, a thermodynamically consistent constitutive formulation is established in which crystallographic slip, deformation induced martensitic transformation, temperature evolution, and phase sensitive degradation are treated within a single coupled framework. Second, degradation is

represented through an effective grain level damage description combining ferrite matrix damage and interface-related damage associated with ferrite-martensite and austenite containing phase boundaries; this allows the transition from hardening to softening to arise from the internal constitutive response rather than from an external failure criterion. Third, the framework is used to interpret instability through measurable and predicted transition events: the stress peak, rapid damage acceleration, and the transformation-damage crossover. The QP980 temperature evolution result is included for this reason: it constrains the thermal path controlling retained austenite stability and interface degradation, thereby making the strain rate interpretation mechanistic rather than a curve fit to flow stress. The proposed framework is applied to QP3Mn and QP980 steels to examine how retained austenite stability, thermomechanical loading, and phase sensitive degradation interact in Q&P steels.

7.2 Modeling Approach

This section presents the coupled crystal plasticity framework used to describe deformation, martensitic transformation, damage evolution, and thermal effects in the multiphase steel. The formulation is developed at the grain scale within a Taylor-based homogenization scheme. Grain kinematics are first decomposed into elastic, thermal, plastic, and damage-induced contributions. The grain-level constitutive response is then obtained from a damage-degraded crystal elasticity law. A thermodynamic structure is introduced through the Helmholtz free energy and the dissipation inequality, from which the driving forces for slip, damage, and transformation are identified. Finally, kinetic relations are specified for dislocation mediated slip, deformation induced martensitic transformation, and matrix/interface damage.

7.2.1 Deformation Kinematics

The deformation of each grain g is described by the local velocity gradient

$$L^{(g)} = \dot{F}^{(g)} {F^{(g)}}^{-1} \tag{7-1}$$

which is decomposed into elastic, thermal, plastic, and damage-induced parts. In the present formulation, martensitic transformation is not introduced as an additional grain-level multiplicative kinematics contribution. Instead, its kinematic effect is incorporated at the polycrystal scale through a transformation velocity gradient introduce later. Accordingly, the local velocity gradient is written as

$$L^{(g)} = L_e^{(g)} + L_\theta^{(g)} + L_p^{(g)} + L_d^{(g)} \tag{7-2}$$

where $L_e^{(g)}$, $L_\theta^{(g)}$, $L_p^{(g)}$, and $L_d^{(g)}$ are the elastic, thermal, plastic slip, and damage-induced volumetric deformation velocity gradients. The thermal velocity gradient can be given by

$$L_\theta^{(g)} = A^{(g)} \boldsymbol{I} \dot{\theta} \tag{7-3}$$

where $A^{(g)}$ is the linear thermal expansion coefficient for grain g, $\boldsymbol{I}$ is the second order identity tensor and $\dot{\theta}$ is the rate of change of temperature.

Plastic flow occurs by crystallographic slip on the active systems of grain g. The plastic part of the velocity gradient is expressed as

$$L_p^{(g)} = \sum_{i=1}^{N_p^{(g)}} \dot{\gamma}^{(g,i)} \left[s_e^{(g,i)} \otimes m_e^{(g,i)} \right] \tag{7-4}$$

where $N_p^{(g)}$ is the number of slip system for grain g, $\dot{\gamma}^{(g,i)}$ is the slip rate for slip system i of grain g, and $s_e^{(g,i)}$ and $m_e^{(g,i)}$ are the current slip direction and slip plane normal, respectively.

Ductile damage is represented by a scalar variable $\phi_{eff}^{(g)} \in [0,1)$ assigned to each grain. It enters the kinematics only through volumetric contribution to the local velocity gradient

$$L_d^{(g)} = \frac{\dot{\phi}_{eff}^{(g)}}{3\left(1 - \phi_{eff}^{(g)}\right)} \boldsymbol{I} \tag{7-5}$$

This form ensures the volumetric expansion remains conjugate to the damage driving force and automatically reduces to zero when $\phi_{eff}^{(g)}$ is constant.

For austenite, ferrite, and pre-existing martensite, the evolution of the slip directions and slip plane normals is governed by

$$\dot{s}_e^{(g,i)} = \left[L_e^{(g)} + L_\theta^{(g)} + L_d^{(g)} \right] s_e^{(g,i)} \tag{7-6}$$

$$\dot{m}_e^{(g,i)} = -m_e^{(g,i)} \left[L_e^{(g)} + L_\theta^{(g)} + L_d^{(g)} \right] \tag{7-7}$$

where $s_e^{(g,i)}$ and $m_e^{(g,i)}$ are the reference slip directions and slip plane normals associated with slip system i in grain grain g.

When martensitic transformation occurs within a grain, the slip systems in the newly formed martensite do not, in general, coincide with those in the previously transformed martensitic regions, because the new martensitic orientation is inherited from the parent austenite lattice. The instantaneous slip direction in a partially transformed grain is taken as a volume-weighted average

of the newly formed martensite orientation and the updated orientation of the pre-existing transformed material. After a transformation increment Δt, the slip direction is updated as

$$s_e^{(g,i)}(t+\Delta t) = \frac{\Delta\xi^{(g)}\hat{s}_e^{(g,i)} + \xi^{(g)}(t)\left(I + \left[L_e^{(g)}(t) + L_\theta^{(g)}(t) + L_d^{(g)}(t)\right]\Delta t\right)s_e^{(g,i)}(t)}{\Delta\xi^{(g)} + \xi^{(g)}(t)} \qquad 7\text{-}8$$

where $\hat{s}_e^{(g,i)}$ denotes the slip direction in the newly transformed material and $\xi^{(g)}$ is the volume fraction associated with grain g. The corresponding rate form is

$$\dot{s}_e^{(g,i)} = \frac{\dot{\xi}^{(g)}}{\xi^{(g)}}\left[\hat{s}_e^{(g,i)} - s_e^{(g,i)}\right] + \left[L_e^{(g)} + L_\theta^{(g)} + L_d^{(g)}\right]s_e^{(g,i)} \qquad 7\text{-}9$$

A similar construction gives the evolution for slip plane normal,

$$\dot{m}_e^{(g,i)} = \frac{\dot{\xi}^{(g)}}{\xi^{(g)}}\left[\hat{m}_e^{(g,i)} - m_e^{(g,i)}\right] - m_e^{(g,i)}\left[L_e^{(g)} + L_\theta^{(g)} + L_d^{(g)}\right] \qquad 7\text{-}10$$

where $\hat{m}_e^{(g,i)}$ are the slip normals in the newly transformed material. The reference slip system families and the construction of the newly transformed martensite slip directions and slip plane normals are summarized in Appendix E.

Plastic slip also produces dislocation accumulation within each grain. The initial dislocation density is given by $\rho_{d,0}^{(g)}$ and its evolution is assumed to follow

$$\dot{\rho}_d^{(g)} = \sum_{i=1}^{N_p^{(g)}}\left[\frac{1}{b^{(g)}k_1^{(g)}}\sqrt{\rho_d^{(g)}} - k_2^{(g)}\rho_d^{(g)}\right]\left|\dot{\gamma}^{(g,i)}\right| \qquad 7\text{-}11$$

where $b^{(g)}$ is the Burger's vector of grain g and $k_1^{(g)}$ and $k_2^{(g)}$ are material parameters governing dislocation generation and dynamic recovery.

At the polycrystal scale, transformation-induced deformation is introduced through a macroscopic velocity gradient L_{tr}, constructed from the rate of formation of martensite variants. The macroscopic velocity gradient is defined as

$$\langle L\rangle = \sum_{g=1}^{N_g}\xi^{(g)}L^{(g)} + L_{tr} \qquad 7\text{-}12$$

where L_{tr} represents the transformation-induced kinematic contribution associated with the formation of martensite plates at austenite–martensite interfaces. Within the Taylor-type constraint, each grain satisfies

$$L^{(g)} = \langle L \rangle - L_{tr} \quad \forall g \tag{7-13}$$

so that compatibility is enforced between the grain-scale kinematics and the macroscopic deformation. In the present formulation, damage affects only $L^{(g)}$ and therefore influences macroscopic response only indirectly through grain averaging. The transformation velocity gradient is written as

$$\boldsymbol{L}_{tr} = \sum_{a=1}^{N_a} \sum_{\beta=1}^{24} \dot{\xi}^{(a,\beta)} \left[\hat{\gamma}_{tr} \boldsymbol{b}_e^{(a,\beta)} \otimes \boldsymbol{d}_e^{(a,\beta)} \right] \tag{7-14}$$

where $\dot{\xi}^{(a,\beta)}$ is the transformation rate of martensite plate orientation β from austenite grain a, $\hat{\gamma}_{tr}$ is the transformation shear magnitude, and $\boldsymbol{b}_e^{(a,\beta)}$ and $\boldsymbol{d}_e^{(a,\beta)}$ are the transformation direction and habit plane normal, respectively.

7.2.2 Governing Equations for Stress

The stress evolution in each grain is described by a rate form of crystal elasticity for phases not undergoing transformation. The Jaumann objective rate is adopted,

$$\hat{\sigma}^{(g)} = \dot{\sigma}^{(g)} + \sigma^{(g)}\Omega^{(g)} - \Omega^{(g)}\sigma^{(g)} \tag{7-15}$$

where the spin tensor is $\Omega^{(g)} = \frac{1}{2}\left(L^{(g)} - L^{(g)^T}\right)$.

Damage is introduced into the constitutive model through a degradation of the elastic stiffness and through an additional relaxation produced by the dilatational term $L_d^{(g)}$. The effective crystal stiffness is

$$\mathbb{C}_{eff}^{(g)} = \left(1 - \phi_{eff}^{(g)}\right) \mathbb{C}_e^{(g)} \tag{7-16}$$

where $\mathbb{C}_e^{(g)}$ is the crystal elastic tensor at the current time and it can be defined as

$$\mathbb{C}_{e(ijkl)}^{(g)} = F_{e(ia)}^{(g)} F_{e(jb)}^{(g)} F_{e(kc)}^{(g)} F_{e(ld)}^{(g)} \mathbb{C}_{abcd}^{(g)} \tag{7-17}$$

where $F_e^{(g)}$ is an elastic deformation gradient given by $F_e^{(g)} = \int_0^t L_e^{(g)} F_e^{(g)} dt$ with the initial condition, $F_e^{(g)}(t = 0) = I$. $\mathbb{C}^{(g)}$ is the initial crystal elasticity tensor for grain g and the initial crystal elasticity tensor as a function of the elasticity coefficients $c_{11}^{(g)}$, $c_{12}^{(g)}$, and $c_{44}^{(g)}$ as in Dayani et al. [257].

The resulting stress-rate equation is

$$\hat{\sigma}^{(g)} = \mathbb{C}_{eff}^{(g)} : \boldsymbol{D}^{(g)} - \sum_{i=1}^{N_p^{(g)}} \dot{\gamma}^{(g,i)} \boldsymbol{R}^{(g,i)} - A^{(g)} \dot{\theta} \left[\mathbb{C}_{eff}^{(g)} : I\right] - \frac{\dot{\phi}_{eff}^{(g)}}{3\left(1 - \phi_{eff}^{(g)}\right)} \left[\mathbb{C}_{eff}^{(g)} : I\right] \quad 7\text{-}18$$

where

$$\boldsymbol{R}^{(g,i)} = \mathbb{C}_{eff}^{(g)} : \boldsymbol{P}^{(g,i)} + \boldsymbol{W}^{(g,i)} \sigma - \sigma \boldsymbol{W}^{(g,i)} \quad 7\text{-}19$$

where $\boldsymbol{P}^{(g,i)}$ and $\boldsymbol{W}^{(g,i)}$ are the symmetric and skew-symmetric parts of the slip system $s_e^{(g,i)} \otimes m_e^{(g,i)}$, respectively.

The macroscopic stress is obtained by volume averaging over all grains,

$$\langle \sigma \rangle = \sum_{g=1}^{N_g} \xi^{(g)} \sigma^{(g)} \quad 7\text{-}20$$

and the corresponding macroscopic stress rate is

$$\langle \dot{\sigma} \rangle = \sum_{g=1}^{N_g} \xi^{(g)} \dot{\sigma}^{(g)} + \sum_{a=1}^{N_a} \sum_{\beta=1}^{24} \dot{\xi}^{(a,\beta)} \left[\sum_{i=1}^{2} \lambda^{\left(\zeta_i^{\beta}\right)} \sigma^{\left(a,\zeta_i^{\beta}\right)} - \sigma^{(a)} \right] \quad 7\text{-}21$$

where $\sigma^{(g)}$ and $\dot{\sigma}^{(g)}$ are the grain averaged Cauchy stress and Cauchy stress rate of the grain g, $\sigma^{\left(a,\zeta_i^{\beta}\right)}$ is the average Cauchy stress in martensite variant i of plate β transforming from austenite grain a, and $\sigma^{(a)}$ is the average Cauchy stress in the parent austenite grain a.

7.2.3 Thermodynamic Equations with Damage

7.2.3.1 Energy Balance and Entropy Decomposition

The first law of thermodynamics is enforced using the energy balance

$$\rho \langle \dot{e} \rangle + \boldsymbol{\nabla} \cdot \boldsymbol{q} - \rho \langle r \rangle - \langle \sigma : \boldsymbol{D} \rangle = 0 \quad 7\text{-}22$$

where ρ is the current material density, $\langle \dot{e} \rangle$ is the current rate of change of internal energy, $\boldsymbol{\nabla} \cdot \boldsymbol{q}$ is the divergence of the current heat flux, $\langle r \rangle$ is the energy source per unit mass, $\langle \sigma : \boldsymbol{D} \rangle$ is the volume averaged external work applied and $\boldsymbol{D}$ is the symmetric part of the velocity gradient $\boldsymbol{L}$. The second law of thermodynamics is written in the form

$$\mathcal{D} = -\rho \langle \dot{e} \rangle + \rho \theta \langle \dot{\eta} \rangle + \langle \sigma : \boldsymbol{D} \rangle - \frac{\boldsymbol{\nabla} \theta \cdot \boldsymbol{q}}{\theta} \quad 7\text{-}23$$

where $\mathcal{D}$ is the energy dissipation rate which must be greater than 0 and $\langle \dot{\eta} \rangle$ is the macroscopic internal entropy generation rate. The macroscopic entropy is the volume average of the grain entropies

$$\langle \eta \rangle = \sum_{g=1}^{N_g} \xi^{(g)} \eta^{(g)} \tag{7-24}$$

with $\eta^{(g)}$ the entropy of grain g. The volume averaged entropy can further decompose as

$$\langle \eta \rangle = \langle \eta_I \rangle + \langle \eta_e \rangle + \langle \eta_m \rangle + \langle \eta_p \rangle + \langle \eta_d \rangle \tag{7-25}$$

Similarly, the local grain entropy is written as

$$\eta^{(g)} = \eta_I^{(g)} + \eta_e^{(g)} + \eta_m^{(g)} + \eta_p^{(g)} + \eta_d^{(g)} \tag{7-26}$$

where $\langle \eta_I \rangle$ and $\eta_I^{(g)}$ are the averaged and local grain g entropy associated with the undeformed crystal at reference temperature θ_T, $\langle \eta_e \rangle$ and $\eta_e^{(g)}$ are the averaged and local grain g reversible entropy due to temperature change from θ_T, $\langle \eta_m \rangle$ and $\eta_m^{(g)}$ are the averaged and local grain g reversible entropy due to thermo-elastic coupling, $\langle \eta_p \rangle$ and $\eta_p^{(g)}$ are the averaged and local grain g reversible entropy generated during plastic slip, and $\langle \eta_d \rangle$ and $\eta_d^{(g)}$ are the averaged and local grain g reversible entropy related to void mechanisms. The reference temperature θ_T is chosen to be the temperature at which transformation will occur spontaneously without any applied stress or transformation energy barriers.

The volume average and local entropies are related

$$\langle \eta_X \rangle = \sum_{g=1}^{N_g} \xi^{(g)} \eta_X^{(g)}, \qquad X \in \{I, e, m, p, d\} \tag{7-27}$$

where $X = I, e, m, p, d$ shows the reference, thermal, thermomechanical, plastic slip, and damage-related entropy contributions, respectively.

A volume averaged Helmholtz free energy $\langle \Psi \rangle$, defined by $\langle \Psi \rangle = \langle e \rangle - \theta \langle \eta_e \rangle$, the dissipation rate given by Eq. (7-23) can be rewritten as

$$\mathcal{D} = -\rho \langle \dot{\Psi} \rangle - \rho \dot{\theta} \langle \eta_e \rangle + \rho \theta \langle \dot{\eta}_m \rangle + \rho \theta \langle \dot{\eta}_p \rangle + \rho \theta \langle \dot{\eta}_d \rangle + \rho \theta \langle \dot{\eta}_I \rangle + \langle \sigma : \boldsymbol{D} \rangle - \frac{\boldsymbol{\nabla} \theta \cdot \boldsymbol{q}}{\theta} \geq 0 \tag{7-28}$$

where $\langle \dot{\eta}_m \rangle$, $\langle \dot{\eta}_p \rangle$, $\langle \dot{\eta}_d \rangle$, and $\langle \dot{\eta}_I \rangle$ are the volume averaged rates of change of the thermomechanical coupling part of the reversible entropy density, the plastic slip entropy density, the damage induced entropy density, and the initial undeformed crystal entropy density.

The local thermal contribution to the reversible entropy is taken as

$$\eta_e^{(g)} = h^{(g)} ln \left(\frac{\theta}{\theta_T} \right) \tag{7-29}$$

where $h^{(g)}$ is the specific heat capacity of the grain g.

The rates of change of the macroscopic thermomechanical, plastic, and damage entropy contribution are given by

$$\langle \dot{\eta}_X \rangle = \sum_{g}^{N} \dot{\xi}^{(g)} \eta_X^{(g)} + \xi^{(g)} \dot{\eta}_X^{(g)}, \quad X \in \{m, p, d\} \tag{7-30}$$

where the local thermomechanical coupling part of the reversible entropy density for grain g is assumed to take the form $\eta_m^{(g)} = \eta_m^{(g)}(E_e, \eta_e)$. Using $\dot{E}_e^{(g)} = \left(F_e^{(g)}\right)^T D_e^{(g)} F_e^{(g)}$, the rate of change of local thermomechanical coupling part of the reversible entropy density can be written as

$$\dot{\eta}_m^{(g)} = F_e^{(g)} \frac{\partial \eta_m^{(g)}}{\partial E_e^{(g)}} \left(F_e^{(g)}\right)^T : D_e^{(g)} + \frac{\partial \eta_m^{(g)}}{\partial \eta_e^{(g)}} \frac{\partial \eta_e^{(g)}}{\partial \theta} \dot{\theta} \tag{7-31}$$

The rate of the macroscopic reference entropy contributions is written as

$$\langle \dot{\eta}_I \rangle = \sum_{a=1}^{N_a} \sum_{\beta=1}^{24} \dot{\xi}^{(a,\beta)} \frac{\lambda_T}{\theta_T} \tag{7-32}$$

The local plastic and damage entropy rates are taken as

$$\dot{\eta}_p^{(g)} = \sum_{i=1}^{N_p^{(g)}} \left| \dot{\gamma}^{(g,i)} \right| \varphi^{(g,i)} \tag{7-33}$$

$$\dot{\eta}_d^{(g)} = S_d^{(g)} \dot{\phi}_{eff}^{(g)} \tag{7-34}$$

where $\varphi^{(g,i)}$ is the rate of entropy generation per unit slip strain in slip system i of grain g and $S_d^{(g)}$ is damage entropy scalar of grain g.

7.2.3.2 Grain-Level Free Energy

The volume averaged Helmholtz free energy and the rate of change of Helmholtz free energy are related to the internal variables in grain g through

$$\langle \Psi \rangle = \sum_{g=1}^{N_g} \xi^{(g)} \Psi^{(g)} \tag{7-35}$$

$$\langle \dot{\Psi} \rangle = \sum_{g=1}^{N_g} \dot{\xi}^{(g)} \Psi^{(g)} + \xi^{(g)} \dot{\Psi}^{(g)} \tag{7-36}$$

where $\Psi^{(g)}$ and $\dot{\Psi}^{(g)}$ are the local Helmholtz free energy and rate of the Helmholtz free energy for grain g. The local Helmholtz free energy is assumed to depend on elastic green strain, temperature, dislocation density, and damage,

$$\Psi^{(g)} = \Psi^{(g)}\left(E_e^{(g)}, \theta, \rho_d^{(g)}, \phi_{eff}^{(g)}\right) \tag{7-37}$$

The rate of change of Helmholtz free energy can be

$$\dot{\Psi}^{(g)} = \frac{\partial \Psi^{(g)}}{\partial E_e^{(g)}} : \dot{E}_e^{(g)} + \frac{\partial \Psi^{(g)}}{\partial \theta}\dot{\theta} + \frac{\partial \Psi^{(g)}}{\partial \rho_d^{(g)}}\dot{\rho}_d^{(g)} + \frac{\partial \Psi^{(g)}}{\partial \phi_{eff}^{(g)}}\dot{\phi}_{eff}^{(g)} \tag{7-38}$$

The dislocation density rate is also written in the form

$$\dot{\rho}_d^{(g)} = \sum_{i=1}^{N_p^{(g)}} w_p^{(g,i)} \dot{\gamma}^{(g,i)} \tag{7-39}$$

where

$$w_p^{(g,i)} = \left[\frac{1}{b^{(g)} k_1^{(g)}}\sqrt{\rho_d^{(g)}} - k_2^{(g)}\rho_d^{(g)}\right] sign\left(\dot{\gamma}^{(g,i)}\right) \tag{7-40}$$

Using Eq. (7-39) and $\dot{E}_e^{(g)} = \left(F_e^{(g)}\right)^T D_e^{(g)} F_e^{(g)}$, where $D_e = sym(L_e)$ is the symmetric part of the elastic velocity gradient, then Eq. (7-38) can be rewritten as

$$\dot{\Psi}^{(g)} = F_e^{(g)} \frac{\partial \Psi^{(g)}}{\partial E_e^{(g)}} \left(F_e^{(g)}\right)^T : D_e^{(g)} + \frac{\partial \Psi^{(g)}}{\partial \theta}\dot{\theta} + \frac{\partial \Psi^{(g)}}{\partial \rho_d^{(g)}} \sum_{i=1}^{N_p^{(g)}} w_p^{(g,i)} \dot{\gamma}^{(g,i)} + \frac{\partial \Psi^{(g)}}{\partial \phi_{eff}^{(g)}}\dot{\phi}_{eff}^{(g)} \tag{7-41}$$

By using decomposition of dissipation (see Appendix F) and adopting the same structure as Dayani et al. [257] for elastic, thermal, dislocation contributions, and damage the Helmholtz free energy for grain g as

$$\begin{aligned}\Psi^{(g)} = {} & \left(1 - \phi^{(g)}\right)\frac{1}{2\rho}\mathbb{C}^{(g)} : \left[E_e^{(g)} \otimes E_e^{(g)}\right] + \theta\eta_m - \eta_e^{(g)}\theta + h^{(g)}\theta \\ & + \frac{1}{2}\omega^{(g)}\mu^{(g)}\left(b^{(g)}\right)^2\rho_d^{(g)} + \frac{\kappa^{(g)}}{2\rho}\left(\phi_{eff}^{(g)}\right)^2 + \Psi_1^{(g)}\end{aligned} \tag{7-42}$$

where the change in surface energy due to transformation is neglected, $\omega^{(g)}$ is the coefficient representing the impact of dislocation density on energy for grain g, $\mu^{(g)}$ is the shear modulus for grain g, κ is coefficient associate with damage hardening grain g, and $\Psi_1^{(g)}$ is a constant

representing the Helmholtz free energy of grain g with no elastic strain or dislocation density and at the reference temperature $\theta = \theta_T$. $\mu^{(g)}$ is assumed to $c_{44}^{(g)}$.

7.2.3.3 Driving Forces

The plastic, damage, and transformation dissipation terms are written as the product of thermodynamic driving forces and their conjugate fluxes,

$$\mathcal{D}_p^{(g)} = \sum_{i=1}^{N_p^{(g)}} f_p^{(g,i)} \dot{\gamma}^{(g,i)} \tag{7-43}$$

$$\mathcal{D}_d^{(g)} = f_d^{(g)} \dot{\phi}_{eff}^{(g)} \tag{7-44}$$

$$\mathcal{D}_{tr}^{(a,\beta)} = f_{tr}^{(a,\beta)} \dot{\xi}^{(a,\beta)} \tag{7-45}$$

where $f_p^{(g,i)}$ is the driving force of the slip rate $\dot{\gamma}^{(g,i)}$ of slip system i of grain g, $f_d^{(g)}$ is the driving force of the damage rate $\dot{\phi}_{eff}^{(g)}$ of grain g, and $f_{tr}^{(a,\beta)}$ is the driving force of martensitic transformation $\dot{\xi}^{(a,\beta)}$ of martensite plate β transformed from austenite grain a. Note that the volume fraction rates $\dot{\xi}^{(a,\beta)}$ must be used instead of the rates $\dot{\xi}^{\left(a,\zeta_i^{\beta}\right)}$ since the rates $\dot{\xi}^{\left(a,\zeta_1^{\beta}\right)}$ and $\dot{\xi}^{\left(a,\zeta_2^{\beta}\right)}$ are not independent. The slip driving force is decomposed as

$$f_p^{(g,i)} = f_{p,1}^{(g,i)} + f_{p,2}^{(g,i)} - f_{p,3}^{(g,i)} + f_{p,4}^{(g,i)} \tag{7-46}$$

where $f_{p,1}^{(g,i)}$ is resolved stress, $f_{p,2}^{(g,i)}$ is dynamic recovery, $f_{p,3}^{(g,i)}$ is dislocation generation, and $f_{p,4}^{(g,i)}$ is entropy generation slip system i of grain g. In this work, it has been assumed that $sign\left(\dot{\gamma}^{(g,i)}\right) = f_{p,1}^{(g,i)}$ such that the driving force components are given by

$$f_{p,1}^{(g,i)} = \sigma^{(g)} : P^{(g,i)} \tag{7-47}$$

$$f_{p,2}^{(g,i)} = \frac{1}{2}\omega^{(g)}\mu^{(g)}\left(b^{(g)}\right)^2 \rho_d^{(g)} sign\left(f_{p,1}^{(g,i)}\right) \tag{7-48}$$

$$f_{p,3}^{(g,i)} = \frac{\omega^{(g)}\mu^{(g)}b^{(g)}}{2k_1^{(g)}} \sqrt{\rho_d^{(g)}}\, sign\left(f_{p,1}^{(g,i)}\right) \tag{7-49}$$

$$f_{p,4}^{(g,i)} = \rho\theta\varphi^{(g,i)} sign\left(f_{p,1}^{(g,i)}\right) \tag{7-50}$$

The damage driving force is decomposed into mechanical, energetic, and entropic contributions as

$$f_d^{(g)} = f_{d,1}^{(g)} - f_{d,2}^{(g)} + f_{d,3}^{(g)} \tag{7-51}$$

$$f_{d,1}^{(g)} = \frac{1}{3\left(1-\phi_{eff}^{(g)}\right)}\left[\sigma^{(g)}: I\right] \quad 7\text{-}52$$

$$f_{d,2}^{(g)} = \kappa^{(g)}\phi_{eff}^{(g)} \quad 7\text{-}53$$

$$f_{d,1}^{(g)} = \rho\theta S_{\phi}^{(g)} \quad 7\text{-}54$$

The transformation driving force is written as

$$f_{tr}^{(a,\beta)} = f_{tr,1}^{(a,\beta)} + f_{tr,2}^{(a,\beta)} + f_{tr,3}^{(a,\beta)} + f_{tr,4}^{(a,\beta)} - f_{tr,5}^{(a,\beta)} - f_{tr,6}^{(a,\beta)} - f_{tr,7}^{(a,\beta)} - f_{tr,8}^{(a,\beta)} \quad 7\text{-}55$$

where $f_{tr,1}^{(a,\beta)}$ is resolved stress, $f_{tr,2}^{(a,\beta)}$ is latent heating, $f_{tr,3}^{(a,\beta)}$ is plastic entropy jump, $f_{tr,4}^{(a,\beta)}$ is void entropy jump, $f_{tr,5}^{(a,\beta)}$ is elastic distortion energy jump, $f_{tr,6}^{(a,\beta)}$ is dislocation energy jump, $f_{tr,7}^{(a,\beta)}$ os damage energy jump, and $f_{tr,8}^{(a,\beta)}$ is internal thermal energy jump between austenite and martensite plate orientation β transformed from austenite grain a. These terms are defined as

$$f_{tr,1}^{(a,\beta)} = \frac{1}{2}\left[\sum_{i=1}^{2}\lambda^{\left(\zeta_i^{\beta}\right)}\sigma^{\left(a,\zeta_i^{\beta}\right)} + \sigma^{(a)}\right]: P_{tr}^{(a,\beta)} \quad 7\text{-}56$$

$$f_{tr,2}^{(a,\beta)} = \rho(\theta-\theta_T)\left[\frac{\lambda_T}{\theta_T}\right] \quad 7\text{-}57$$

$$f_{tr,3}^{(a,\beta)} = \rho\theta\left[\sum_{i=1}^{2}\lambda^{\left(\zeta_i^{\beta}\right)}\eta_p^{\left(a,\zeta_i^{\beta}\right)} - \eta_p^{(a)}\right] \quad 7\text{-}58$$

$$f_{tr,4}^{(a,\beta)} = \rho\theta\left[\sum_{i=1}^{2}\lambda^{\left(\zeta_i^{\beta}\right)}\eta_d^{\left(a,\zeta_i^{\beta}\right)} - \eta_d^{(a)}\right] \quad 7\text{-}59$$

$$f_{tr,5}^{(a,\beta)} = \sum_{i=1}^{2}\lambda^{\left(\zeta_i^{\beta}\right)}\mathbb{C}^{\left(a,\zeta_i^{\beta}\right)}: \left[E_e^{\left(a,\zeta_i^{\beta}\right)} \otimes E_e^{\left(a,\zeta_i^{\beta}\right)}\right] - \frac{1}{2}\mathbb{C}^{(a)}: \left[E_e^{(a)} \otimes E_e^{(a)}\right] \quad 7\text{-}60$$

$$f_{tr,6}^{(a,\beta)} = \sum_{i=1}^{2}\lambda^{\left(\zeta_i^{\beta}\right)}\omega^{\left(a,\zeta_i^{\beta}\right)}\mu^{\left(a,\zeta_i^{\beta}\right)}\left(b^{\left(a,\zeta_i^{\beta}\right)}\right)^2\rho_d^{\left(a,\zeta_i^{\beta}\right)} - \frac{1}{2}\omega^{(a)}\mu^{(a)}\left(b^{(a)}\right)^2\rho_d^{(a)} \quad 7\text{-}61$$

$$f_{tr,7}^{(a,\beta)} = \sum_{i=1}^{2}\lambda^{\left(\zeta_i^{\beta}\right)}\kappa^{\left(a,\zeta_i^{\beta}\right)}\left(\phi_{eff}^{\left(a,\zeta_i^{\beta}\right)}\right)^2 - \frac{1}{2}\kappa^{(a)}\left(\phi_{eff}^{(a)}\right)^2 \quad 7\text{-}62$$

$$f_{tr,8}^{(a,\beta)} = \rho\left[\sum_{i=1}^{2}\lambda^{\left(\zeta_i^{\beta}\right)}h^{\left(a,\zeta_i^{\beta}\right)} - h^{(a)}\right]\left[\theta - \theta_T - ln\left(\frac{\theta}{\theta_T}\right)\theta\right] \quad 7\text{-}63$$

Finally, the temperature evolution equation is written as

$$\rho\left[\sum_{g=1}^{N_g}\xi^{(g)}\mathrm{h}^{(g)}\right]\dot{\theta}$$

$$= \sum_{g=1}^{N_g}\xi^{(g)}M_e^{(g)}:D_e^{(g)} + \sum_{g=1}^{N_g}\sum_{i=1}^{N_p^{(g)}}\xi^{(g)}M_p^{(g,i)}\dot{\gamma}^{(g,i)} + \sum_{g=1}^{N_g}\xi^{(g)}M_d^{(g)}\dot{\phi}_{eff}^{(g)} \qquad 7\text{-}64$$

$$+ \sum_{a=1}^{N_a}\sum_{\beta=1}^{24}M_{tr}^{(a,\beta)}\dot{\xi}^{(a,\beta)} - \nabla\cdot q$$

where $M_e^{(g)}$, $M_p^{(g,i)}$, and $M_d^{(g)}$ represent the change in internal energy due to elastic stretching, plastic slip, and damage in grain g and $M_{tr}^{(a,\beta)}$ represents the energy dissipated during transformation of martensite plate β from austenite grain a. These terms are given by

$$M_e^{(g)} = 4\theta A^{(g)}\sigma^{(g)} + \theta A^{(g)}F_e^{(g)}\left[I:\mathbb{C}^{(g)}\right]\left(F_e^{(g)}\right)^T \qquad 7\text{-}65$$

$$M_p^{(g,i)} = f_{p,1}^{(g,i)} + f_{p,2}^{(g,i)} - f_{p,3}^{(g,i)} \qquad 7\text{-}66$$

$$M_d^{(g)} = f_{d,1}^{(g)} - f_{d,2}^{(g)} \qquad 7\text{-}67$$

$$M_{tr}^{(a,\beta)} = f_{tr,1}^{(a,\beta)} - f_{tr,5}^{(a,\beta)} - f_{tr,6}^{(a,\beta)} - f_{tr,7}^{(a,\beta)}$$

$$- \sum_{i=1}^{2}\theta\lambda^{\left(\zeta_i^\beta\right)}A^{\left(a,\zeta_i^\beta\right)}\left[\sigma^{\left(a,\zeta_i^\beta\right)}:I\right] + \theta A^{(a)}\left[\sigma^{(a)}:I\right] \qquad 7\text{-}68$$

$$- \rho\left[\sum_{i=1}^{2}\lambda^{\left(\zeta_i^\beta\right)}h^{\left(a,\zeta_i^\beta\right)} - h^{(a)}\right][\theta - \theta_T]$$

7.2.4 Kinetics Relations

7.2.4.1 Damage Kinetics

Damage evolution in the present framework is governed by three physically distinct but kinematically coupled mechanisms: damage growth within ferrite grains, decohesion at ferrite–martensite interfaces, and transformation-assisted decohesion at austenite-containing interfaces. The formulation is implemented within the Taylor-type crystal plasticity model through a set of bounded internal variables whose evolution remains consistent with the volumetric damage kinematics introduced in Section 2.2. Additionally, interfaces are not treated as separate geometric entities. Instead, their mechanical effect is incorporated through internal damage variables that

modify the constitutive response of the grains that are mechanically constrained by those interfaces.

To represent these effects consistently, two classes of damage variables are introduced. The first corresponds to matrix damage within ferrite grains, while the second represents interface-driven degradation associated with phase boundaries. Rather than introducing separate damage variables directly into the stress update, these contributions are combined into an effective grain-level damage variable that governs the loss of load-carrying capacity of each crystal.

For each grain g, the effective damage variable is written as

$$\phi_{eff}^{(g)} = 1 - \left(1 - \phi_{mat}^{(g)}\right)\left(1 - \phi_{int}^{(g)}\right) \quad 7\text{-}69$$

where $\phi_{mat}^{(g)}$ represents matrix damage within ferrite and $\phi_{int}^{(g)}$ represents the combined contribution of interface-driven degradation mechanisms. This multiplicative form ensures bounded evolution and preserves the physical constrain $0 \leq \phi_{eff}^{(g)} \leq 1$. The effective damage variable enters the constitutive update through the volumetric damage relaxation term described in Section 2.2. Consequently, both matrix cavitation and interface decohesion influence the grain stress response before the Taylor averaging operation is performed.

7.2.4.1.1 Ferrite Grain Damage Evolution

Soft phase ferrite is the only phase carrying grain-scale matrix damage in this implementation. For each ferrite grain g, the matrix damage variable evolves according to a first-order kinetic law

$$\dot{\phi}_{mat}^{(g)} = \lambda_F^{(g)}\left[1 - \phi_{mat}^{(g)}\right] \quad 7\text{-}70$$

where $\lambda_F^{(g)}$ is the local ferrite damage intensity. The multiplicative factor enforces bounded evolution and ensures that the damage variable asymptotically approaches unity without exceeding the physically admissible range.

The governing equation admits an exact solution over a time increment Δt if the intensity is assumed constant during the step. The discrete update used in the numerical implementation is therefore

$$\left(\phi_{(n+1)}^{(g)}\right)_{mat} = 1 - \left(1 - \left(\phi_{(n)}^{(g)}\right)_{mat}\right) exp\left(-\lambda_F^{(g)}\Delta t\right) \quad 7\text{-}71$$

This exponential integration preserves the constraint $0 \leq \phi_{mat}^{(g)} \leq 1$. It is particularly advantageous in the softening regime because it preserves boundedness and prevents nonphysical overshoot even when the damage rate becomes large.

The ferrite damage intensity represents nucleation and growth of voids within the ferrite matrix under tensile stress states. For each grain, the local stress tensor is used to compute an equivalent stress $S_{eq}^{(F)}$ and the associated stress triaxiality T_F. Mechanical damage activates only when plastic deformation occurs, and the local stress exceeds a critical threshold.

The corresponding damage intensity is written as

$$\lambda_F^{(g)} = C_{0,F}\left(\frac{S_{eq}^{(F)} - \sigma_{0,F}}{\sigma_{ref}}\right)^{p} exp(\beta_T T_F) \quad 7\text{-}72$$

where $C_{0,F}$ is a kinetic coefficient controlling the rate of void growth, $\sigma_{0,F}$ is a critical stress threshold for damage activation, p governs stress sensitivity of the growth process, and β_T control the influence of stress triaxiality. The exponential dependence on stress triaxiality reflects the well-known promotion of void growth under hydrostatic tension. In the implemented formulation, no explicit multiplicative power-law term in plastic strain rate is used in this expression. Instead, strain rate and temperature effects enter primarily through the calibrated reference stress $\sigma_{ref}(\dot{\varepsilon}, \theta)$, which is identified from the rate- and temperature-dependent calibration procedure described later. This strategy allows the model to capture strain rate and temperature sensitivity while maintaining a compact kinetic form.

7.2.4.1.2 Ferrite-Martensite Interface Damage

Ferrite–martensite interfaces are preferential locations for damage initiation due to the strong mechanical incompatibility between the softer ferrite matrix and the harder martensitic phase. This mechanism is represented by an interface damage variable ϕ_{FM}, which evolves independently from the ferrite grain variable. The amount of ferrite–martensite interface available for decohesion is represented by the dimensionless measure

$$I_{FM} = v_F^{2/3} v_M \quad 7\text{-}73$$

where v_F and v_M denote the volume fractions of ferrite and martensite, respectively. This expression provides a simple proxy for interface area density based on surface-to-volume scaling. The driving traction for interface degradation is obtained from the mismatch between ferrite grain stresses and the phase-averaged martensite stress. A scalar traction quantity is extracted from this stress difference and compared with a thermally activated threshold,

$$\sigma_{thr} = \sigma_0^{th}\left[1 - \frac{k_B\theta}{\Delta V} ln\left(\frac{\dot{\varepsilon}_p^{(g)}}{\dot{\varepsilon}_{p0}^{th}}\right)\right]\left[1 + \beta_T\left(T_F - T_{ref}\right)\right] \quad 7\text{-}74$$

where k_B is Boltzmann's constant, ΔV is an activation volume, and $\dot{\varepsilon}_{p0}^{th}$ is a reference plastic strain rate. The threshold therefore decreases with increasing thermal activation and depends on the local stress state through the triaxiality-dependent correction.

The corresponding traction kernel is defined as

$$\mathcal{G}_{FM} = \left(\frac{\sigma_{FM} - \sigma_{thr}}{\sigma_{ref}}\right)^{r_\sigma} exp\big(\alpha_T(\theta - \theta_0)\big) \quad 7\text{-}75$$

where σ_{FM} is the mismatch stress between ferrite and martensite, r_σ is traction exponent which controls the sharpness of activation, and the thermal sensitivity α_T capture the reduction in interface strength with increasing temperature.

The evolution of the FM interface damage variable follows

$$\dot{\phi}_{FM} = \lambda_{FM}(1 - \phi_{FM}) \quad 7\text{-}76$$

with $\lambda_{FM} = I_{FM}\mathcal{G}_{FM}$.

7.2.4.1.3 Austenite-Martensite Interface Damage

A second class of interface mechanisms arises from the presence of retained austenite and its transformation during deformation. This contribution is represented by a single interface damage variable ϕ_{AM}, but its kinetics include two distinct physical channels. The first channel corresponds to decohesion along retained-austenite / pre-existing-martensite boundaries. The second channel represents mismatch between retained austenite and martensite that forms dynamically during deformation. Transformation-induced shear and dilatational strains intensify local stress concentrations, making this mechanism particularly important in QP steels.

The interfacial area measures entering these contributions are constructed from the relevant phase fractions. The corresponding interfacial area measures are approximated as

$$I_{AM} = v_A^{2/3} v_M;\ I_{AT} = v_A^{2/3} v_T \quad 7\text{-}77$$

where v_A and v_T is the retained austenite and transformed martensite volume fraction, respectively. Using the traction kernels $\mathcal{G}_{AM}$ and $\mathcal{G}_{AT}$, the austenite-related interface damage intensity becomes

$$\lambda_{AM} = C_{0,AM}\, I_{AM}\mathcal{G}_{AM} + C_{0,AT}\, I_{AT}\mathcal{G}_{AT} \quad 7\text{-}78$$

The evolution equation for the austenite-related interface variable is therefore

$$\dot{\phi}_{AM} = \lambda_{AM}(1 - \phi_{AM}) \quad 7\text{-}79$$

7.2.4.1.4 Effective Damage

In the present Taylor-type crystal plasticity formulation, interfaces are not homogenized as separate phases. Instead, interface degradation alters the constitutive response of the neighboring grains through the effective grain damage variable introduced earlier. The interface contribution to grain damage is therefore written as

$$\phi_{int}^{(g)} = \phi_{FM} + \phi_{AM} \tag{7-80}$$

The rate of effective damage entering the volumetric damage kinematics $\dot{\phi}_{eff}^{(g)}$ is used in the constitutive update. It is important to note that the present Taylor-type crystal plasticity framework does not explicitly resolve geometric phase boundaries. Consequently, phase interfaces are not treated as independent constituents in the homogenization procedure. Instead, interface degradation modifies the constitutive response of the grains that are mechanically constrained by those interfaces through the effective grain damage variable $\phi_{eff}^{(g)}$. The stress in each grain is therefore updated using the local effective damage state, which already incorporates both matrix cavitation and interface-driven degradation. The macroscopic response of the polycrystal is subsequently obtained through the standard Taylor volume averaging of the damaged grain stresses. In this manner, interface damage influences the macroscopic behavior indirectly through modified grain constitutive responses rather than through a separate interface homogenization rule.

7.2.4.2 Dislocation Kinetics

For plastic slip, the rate of plastic shearing is related to the plasticity driving force through,

$$\dot{\gamma}^{(g,i)} = \begin{cases} a^{(g)} sign\left(f_{p,1}^{(g,i)}\right) \left| \dfrac{f_p^{(g,i)}}{g_p^{(g)}} \right|^{1/m^{(g)}} & f_{p,1}^{(g,i)} + f_{p,2}^{(g,i)} + f_{p,4}^{(g,i)} > f_{p,3}^{(g,i)} \\ 0 & f_{p,1}^{(g,i)} + f_{p,2}^{(g,i)} + f_{p,4}^{(g,i)} < f_{p,3}^{(g,i)} \end{cases} \tag{7-81}$$

where $a^{(g)}$ is reference rate for grain g, $m^{(g)}$ is rate coefficient for grain g, and $g_p^{(g)}$ represent critical plastic slip driving force for grain g. The critical plastic slip driving force can be related to the dislocation density in grain g through

$$g_p^{(g)} = g_{p,0}^{(g)} + c^{(g)} \mu^{(g)} b^{(g)} \sqrt{\rho_d^{(g)}} \tag{7-82}$$

where $g_{p,0}^{(g)}$ is the initial critical driving force for grain g and $c^{(g)}$ is the interaction coefficient between dislocation in grain g.

7.2.4.3 Transformation Kinetics

The deformation induced austenite to martensite transformation is modeled using the statistical framework originally proposed by Olson and Cohen [290] and later extended by Stringfellow et al. [291] to account for nucleation at shear band intersections. In this approach, martensitic transformation is assumed to occur through the formation of martensite plates within individual austenite grains. The rate of transformation depends on the density of available nucleation sites, the probability of transformation at those sites, and the thermodynamic driving force for the phase change.

The rate of change of martensite volume fraction associated with transformation system β in austenite grain a is expressed as

$$\dot{\xi}^{(a,\beta)} = \xi^{(a)} v_T \dot{N}_t^{(a,\beta)} \tag{7-83}$$

where v_T is the average volume of a newly transformed martensite and $\dot{N}_t^{(a,\beta)}$ represents the rate of formation of martensitic units with orientation β. The evolution of transformed units includes contributions from newly created strain-induced nucleation sites, existing strain-induced sites that become activated due to an increase in driving force, and nucleation sites that were already present in the initial microstructure. Accordingly,

$$\dot{N}_t^{(a,\beta)} = P_n^{(a,\beta)} \dot{N}_n^{(a)} + R\left(\dot{P}_n^{(a,\beta)}\right) N_n^{(a)} + R\left(\dot{P}_o^{(a,\beta)}\right) N_o \tag{7-84}$$

where $P_n^{(a,\beta)}$ is the probability that a strain-induced nucleation site transforms into martensite plate orientation β, $N_n^{(a)}$ is the density of strain-induced nucleation sites within the austenite grain, and N_o denotes the density of nucleation sites already present in the original microstructure. The function $R(\cdot) = max(0,\cdot)$ ensures that only positive increments in transformation probability contribute to the evolution of martensite.

The density of strain-induced nucleation sites is assumed to be proportional to the volume fraction of shear-band intersections within the austenite grain,

$$N_n^{(a)} = \frac{f_I^{(a)}}{v_I} \tag{7-85}$$

where $f_I^{(a)}$ is the volume fraction of shear-band intersections and v_I represents the characteristic volume associated with an interface site. Following previous formulations, the intersection density is related to the volume fraction of shear bands $f_{sb}^{(a)}$ through a power-law relation,

$$f_I^{(a)} = \kappa_I \left(f_{sb}^{(a)} \right)^{n_I} \tag{7-86}$$

where κ_I and n_I are material parameters that control the density of intersection sites.

The evolution of the shear-band volume fraction is driven by plastic deformation and is expressed as

$$\dot{f}_{sb}^{(a)} = \left(1 - f_{sb}^{(a)}\right) a_{sb}^{(a)} \dot{\gamma}_{sb}^{(a)} \tag{7-87}$$

where $\dot{\gamma}_{sb}^{(a)}$ is the accumulated shear rate projected onto the shear-band systems and $a_{sb}^{(a)}$ control the rate of shear-band formation. In order to capture the dependence of shear-band formation on temperature and strain rate, this coefficient is modeled as

$$a_{sb}^{(a)} = (a_1 + a_2\theta + a_3\theta^2) \left[1 - a_4 \left(\frac{\dot{\gamma}_{sb}^{(a)}}{\dot{\gamma}_0^{(a)}} \right)^{a_5} \right] \tag{7-88}$$

where a_1 – a_5 are calibration constants, θ is the temperature, and $\dot{\gamma}_0^{(a)}$ denotes the reference shear rate.

The total shear rate acting on the shear-band system is obtained by projecting the slip activity of the crystallographic slip systems onto the shear-band planes,

$$\dot{\gamma}_{sb}^{(a)} = \sum_{i=1}^{N_{sb}} \sum_{j=1}^{N_p} H(i,j) \left| \dot{\gamma}^{(a,j)} \right| \tag{7-89}$$

where N_{sb} is the number of shear-band systems, N_p is the number of slip systems, $H(i,j)$ represents the projection tensor linking slip system j to shear-band system i, and $\dot{\gamma}^{(a,j)}$ is the slip rate on slip system j.

Combining the preceding relations yields the final expression governing the evolution of martensite transformation during deformation. The probability that a nucleation site transform is assumed to depends on the thermodynamic driving force for transformation. Following the statistical treatment proposed by Olson and Cohen [290], the resistance to transformation is represented by a Gaussian distribution of critical driving forces. The probability of transformation at strain-induced nucleation sites therefore takes the form

$$P_n^{(a,\beta)} = \frac{1}{2} \left[1 + erf \left(\frac{f_{tr}^{(a,\beta)} - g_{tr,n}}{\sqrt{2}\sigma_{tr,n}} \right) \right] \tag{7-90}$$

where $f_{tr}^{(a,\beta)}$ is transformation driving force associated with system β, and $g_{tr,n}$ and $\sigma_{tr,n}$ represent the mean and standard deviation of the critical driving force for transformation at strain-induced

nucleation sites. The evolution of the transformation probability is obtained by differentiating the above expression with respect to the driving force, yielding the rate $\dot{P}_n^{(a,\beta)}$. An analogous formulation is adopted for nucleation sites present in the original microstructure, characterized by parameters $g_{tr,o}$ and $\sigma_{tr,o}$.

7.3 Experimental Characterization

This section summarizes the material basis and experimental procedures used to characterize the Q&P steels considered in the present study. Two quenching and partitioning steels, denoted QP3Mn and QP980, are considered in the present study to investigate the coupled influence of initial microstructure, deformation induced transformation, strain rate, and temperature on the mechanical response and damage evolution. The QP3Mn material corresponds to an experimental 0.28C–2.56Mn–1.56Si–0.049Al (wt. %) Q&P sheet steel that is cold rolled to a thickness of 1.1 mm prior to the quenching and partitioning treatment reported by Poling [292]. The QP3Mn dataset adopted from that work includes tensile behavior over a broad range of strain rate and temperature conditions together with retained austenite measurements during deformation. By contrast, the QP980 material considered here is a commercial cold-rolled sheet with a thickness of 1.3 mm, for which the initial microstructural characterization and strain rate-dependent tensile response are measured in the present work, while the retained austenite evolution used later in the constitutive analysis is taken from Poling [292]. This combined experimental basis is used to define the starting microstructure, constrain the transformation response, and assess the rate- and temperature-dependent mechanical behavior of the two steels.

7.3.1 Experimental Procedure for QP980

Since the initial microstructure, strain rate-dependent tensile response, and surface temperature evolution of QP980 are measured in the present work, the corresponding experimental procedures are summarized in this section. By contrast, the retained austenite evolution used for QP980 is not measured directly in the present study and is introduced below as literature-based input for the transformation kinetics.

7.3.1.1 Microstructural Characterization Procedure

The initial microstructure and crystallographic texture of QP980 are characterized using a field-emission ThermoScientific Quattro Environmental scanning electron microscope equipped with a Lumis electron backscatter diffraction (EBSD) detector. EBSD scans are performed on the rolling

direction-transverse direction (RD-TD) plane with a step size of 0.1 μm. The acquired orientation data are processed using TSL OIM™ software. During post-processing, a neighbor confidence index threshold of 0.2 is applied for data cleaning. Phase segmentation is performed to distinguish ferrite, tempered martensite, and retained austenite, and the corresponding phase fractions are quantified from the processed EBSD maps. The resulting inverse pole figure maps and phase distribution maps are used to characterize the initial phase constitution and texture of QP980.

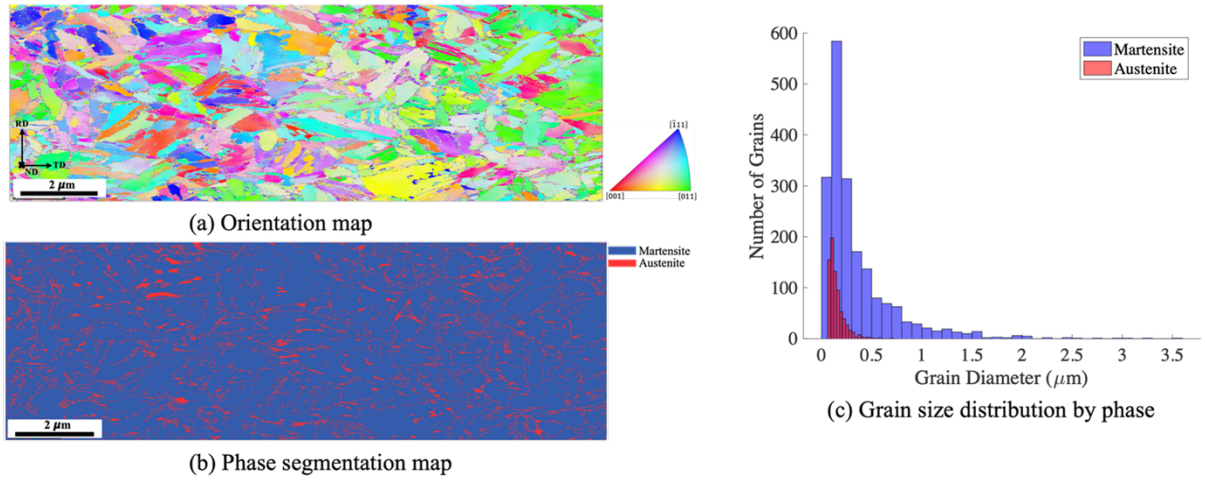
7.3.1.2 Uniaxial Tensile Testing

Uniaxial tensile tests on QP980 are conducted along the rolling direction at room temperature over a range of applied strain rates. The experiments are performed using an MTS Criterion 45 servo-hydraulic tensile testing system for the lower strain rate regime and a hydraulic intermediate strain rate apparatus for the higher strain rate regime. The nominal strain rates considered in the present study are 0.001, 0.1, 1, 10, and 100 s^{-1}. The tensile response is recorded in terms of load and displacement, from which the corresponding engineering stress–strain curves are obtained for each loading condition. High-resolution strain fields are measured using a stereoscopic GRAS-50S5M-C camera system paired with Tamron AF Micro 180 mm lenses. The specimen surfaces are prepared using a random speckle pattern generated with Rust-Oleum spray paint following the recommendations of Correlated Solutions. The images are subsequently analyzed using VIC software to extract the local strain evolution during deformation. The surface temperature evolution of the specimen is measured using a high-speed infrared radiation camera with a mid-wavelength range of 3-5 μm from the Telops IRC-TS series. More details on the experimental procedure, specimen geometry, DIC, and infrared camera parameters can be found in Dayani et el. [257].

7.3.2 Initial Microstructural Characterization

The initial microstructure of QP3Mn and QP980 are shown in Figure 7-1 and Figure 7-2, through inverse pole figure (IPF) maps, phase segmentation maps, and phase resolved grain size distributions. These microstructural datasets are used not only to quantify phase fractions, but also to identify the characteristic morphology and grain size scale of each phase. QP3Mn exhibits a fine, lath-dominated martensitic microstructure containing retained austenite in both film-like and blocky forms, whereas QP980 exhibits a coarser and more heterogeneous multiphase structure composed of ferrite, tempered martensite, and retained austenite. These differences indicate that the two materials differ not only in constituent fraction, but also in the spatial scale and

morphological arrangement through which transformation and damage develop during deformation.

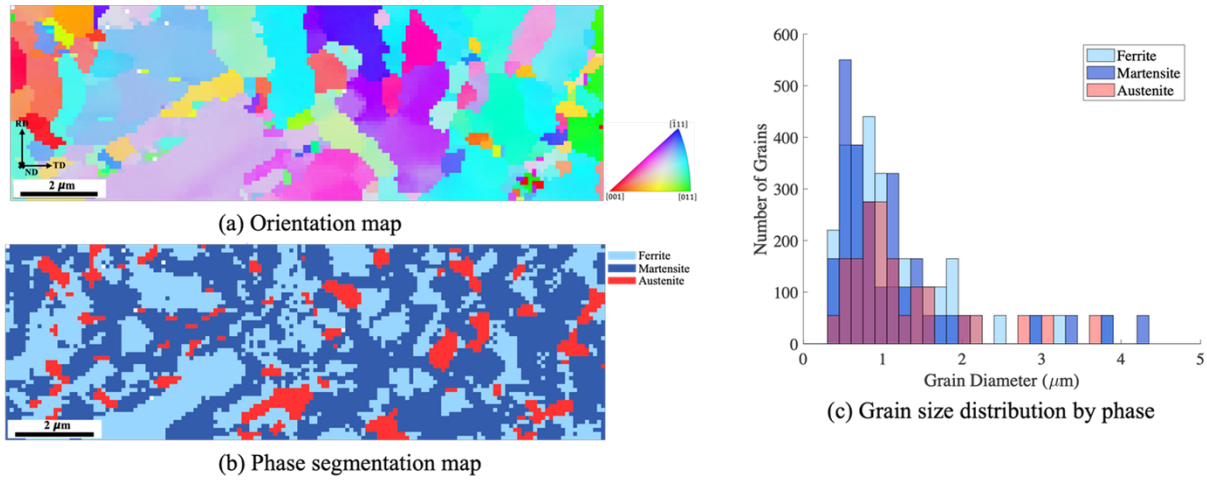


(a) Orientation map

(b) Phase segmentation map

(c) Grain size distribution by phase

Figure 7-1: Microstructure of QP3Mn from [292].



(a) Orientation map

(b) Phase segmentation map

(c) Grain size distribution by phase

Figure 7-2: Microstructure of QP980.

For QP3Mn, the initial microstructure is predominantly tempered martensite, with retained austenite distributed throughout the matrix. The IPF map indicates a fine microstructural scale with elongated and irregular martensitic features spanning a broad range of crystallographic orientations rather than being concentrated within a narrow texture component. The phase map further shows that the retained austenite is present in two characteristic morphologies: thin film-like regions embedded within the martensitic matrix and a smaller population of fine blocky grains. Quantitative phase analysis indicates approximately 14.5% retained austenite and 85.5% tempered martensite. The phase resolved grain size distributions are strongly concentrated at small equivalent diameters, consistent with the fine lath-martensitic scale of the microstructure. In

particular, the retained austenite distribution is centered in the finer size regime but exhibits a broader tail associated with the blocky austenite population. The average grain sizes of martensite and retained austenite are 0.35 μm and 0.14 μm, respectively. Pole figures reconstructed from the reported EBSD data for the retained austenite and tempered martensite phases are shown in Figure 7-3 and indicate anisotropic phase textures.

For QP980, the phase map shown in Figure 7-2 indicates a multiphase microstructure composed of ferrite, tempered martensite, and retained austenite, with a distinctly coarser and more heterogeneous morphology than that of QP3Mn. The IPF map shows relatively large, blocky grains distributed over a broad range of crystallographic orientations, while the phase segmentation map indicates that ferrite forms a continuous soft matrix within which tempered martensite and retained austenite are dispersed as discrete harder constituents. In contrast to the fine lath-dominated morphology of QP3Mn, the characteristic phase arrangement in QP980 is more equiaxed and spatially heterogeneous. The phase resolved grain size distributions are also broader and shifted toward larger equivalent diameters, consistent with the coarser structural scale of this steel. The average grain diameters of ferrite, tempered martensite, and retained austenite are 0.79 μm, 1.08 μm, and 1.24 μm, respectively. The corresponding pole figures for retained austenite, ferrite, and tempered martensite are shown in Figure 7-4. These pole figures indicate phase-dependent texture distributions, which are used as the crystallographic basis.

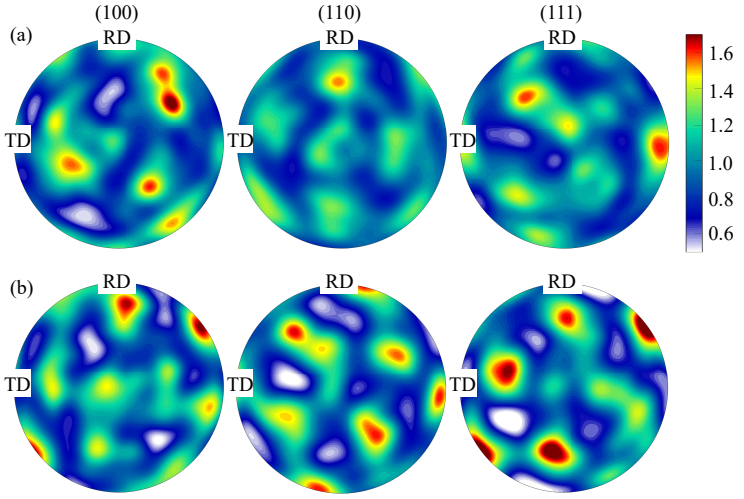


Figure 7-3: QP3Mn (a) RA and (b) tempered martensite texture.

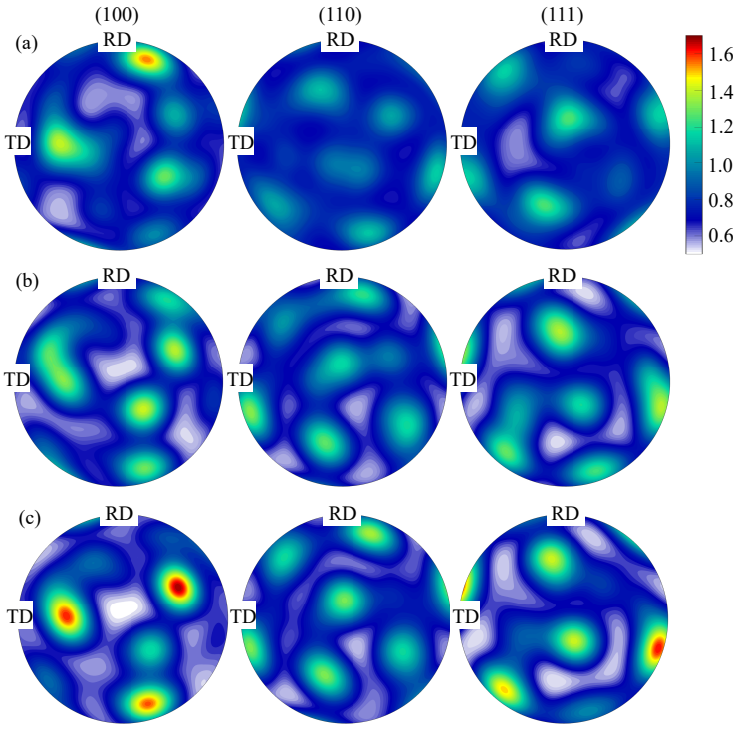
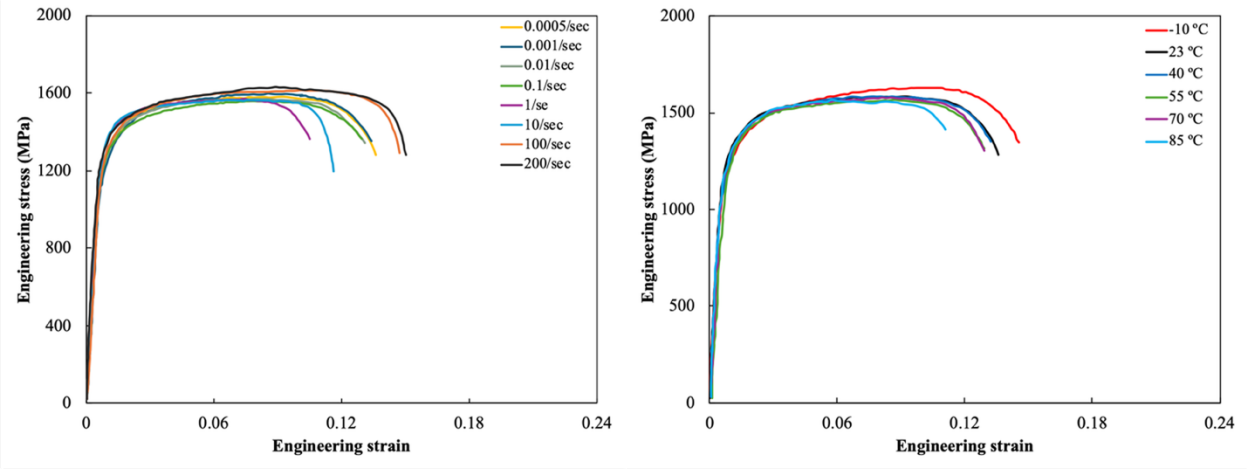


Figure 7-4: QP980 (a) RA, (b) ferrite, and (c) tempered martensite texture.

7.3.3 Tensile Response

The engineering stress–strain responses shown in Figure 7-5 indicate that both steels are sensitive to loading rate, while QP3Mn also shows a distinct temperature dependence. For the present work, the more relevant observation is that the onset of softening and the strain interval sustained after peak stress vary with both material and loading condition. In QP3Mn, changes in strain rate and temperature modify not only the stress level, but also the point at which the tensile response departs from hardening and enters the post-peak regime. In QP980, the stress level remains lower than that of QP3Mn, but the material sustains deformation over a wider strain interval before final loss of load-carrying capacity. The tensile data therefore provide the macroscopic basis for evaluating whether the proposed constitutive damage framework can represent the transition from stable deformation to degradation.



(a) Varying strain rate for QP3Mn

(b) Varying temperature for QP3Mn

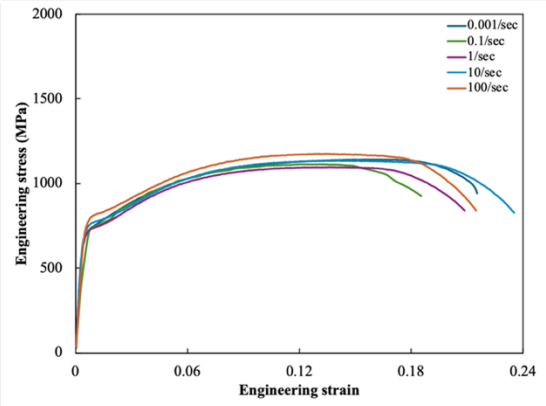
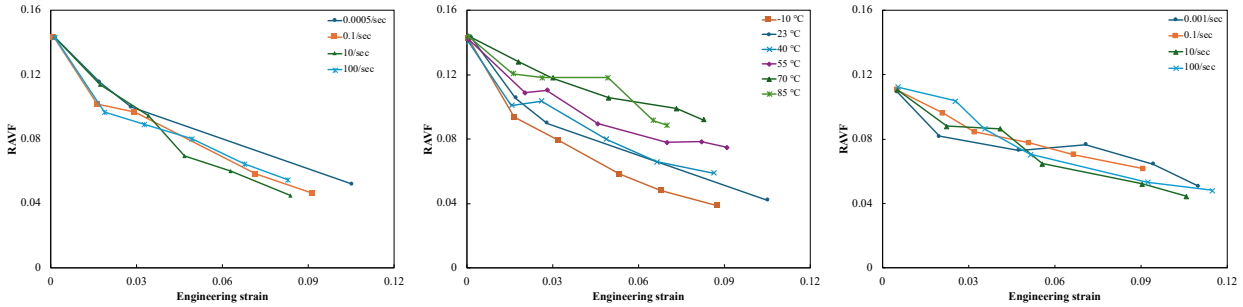


Figure 7-5: Engineering stress–strain responses of QP3Mn and QP980 steels.

7.3.4 Evolution of RA

The evolution of retained austenite volume fraction (RAVF) during tensile deformation is shown in Figure 7-6. For QP3Mn, the retained austenite fraction is reported as a function of strain under different strain rate and temperature conditions, whereas for QP980 the corresponding retained austenite evolution is introduced as literature-based input for the transformation kinetics. The QP980 temperature histories measured in the present work are used separately to evaluate the thermomechanical path under strain rate-dependent loading. In both steels, the retained austenite fraction decreases progressively with increasing strain, indicating continued deformation induced transformation during loading. The important observation is that the rate at which retained austenite is depleted depends on the test condition and differs between the two steels. In QP3Mn, variations in strain rate and temperature modify the transformation trajectory, with lower temperatures associated with more rapid depletion and higher temperatures preserving a larger retained austenite fraction over a comparable strain range. The QP980 data provide a constrained

transformation path for interpreting how deformation induced heating modifies retained austenite stability during rate-dependent loading. Taken together, the retained austenite and temperature measurements provide the experimental basis for evaluating whether the proposed framework can reproduce the coupling between deformation, transformation, thermal state, softening, and failure.



(a) Varying strain rate for QP3Mn (b) Varying temperature for QP3Mn (c) Varying strain rate for QP980

Figure 7-6: Evolution of retained austenite volume fraction during tensile deformation.

In QP3Mn, variations in strain rate and temperature modify the transformation trajectory, with lower temperatures associated with more rapid depletion and higher temperatures preserving a larger retained austenite fraction over a comparable strain range. It should be noted, however, that the strain rate-dependent transformation behavior observed under non-isothermal loading conditions reflects the combined influence of loading rate and deformation induced heating. The experimentally observed trends therefore represent the net response of the coupled thermomechanical system rather than an isolated constitutive strain rate effect on transformation.

7.4 Result and Discussion

7.4.1 Computational Framework and Thermomechanical Loading Conditions

The constitutive framework described in Section 7.2 is implemented into a single material point under coupled thermomechanical loading. For each steel, a representative modified Taylor-based polycrystal is constructed using the measured phase fractions and phase specific crystallographic textures. For each constituent phase, 300 grain orientations are sampled from the corresponding orientation distribution, and the phase fractions are imposed through the volume weighting used in the homogenization. As a result, QP3Mn is represented as a two-phase aggregate consisting of retained austenite and tempered martensite, whereas QP980 is represented as a three-phase aggregate composed of ferrite, tempered martensite, and retained austenite. This construction preserves the phase specific texture information without assigning equal physical volume to phases with different measured fractions.

During deformation, retained austenite grains may transform into martensite according to the orientation relationship introduced in Appendix D. The transformation kinetics, slip evolution, and damage evolution are integrated simultaneously within each increment, so that mechanical response, phase transformation, heat generation, and stiffness degradation remain fully coupled throughout the simulation.

At the crystal level, plastic slip is integrated using the rate-tangent procedure. Because the present framework is based on Taylor homogenization, the macroscopic response is obtained from the volume average of the grain-level responses after updating the local slip, transformation, temperature, and effective damage variables.

For thermal loading, two different assumptions are adopted depending on the experimental condition. For tests performed under externally controlled isothermal conditions, the specimen temperature is prescribed as constant. For room temperature tests without active thermal control, the temperature is allowed to evolve due to internal heat generation associated with elastic deformation, plastic dissipation, damage evolution, and deformation induced transformation. Under the single material point approximation, the gauge section is treated as a lumped thermal control volume with spatially uniform temperature. This assumption does not resolve temperature gradients, but it provides the thermal state entering the transformation and damage kinetics.

$$\rho V C_{eff} \dot{\theta} = Q_{gen} - Q_{bound} \tag{7-91}$$

where C_{eff} is the effective heat capacity of the aggregate, Q_{gen} is the total internally generated heat, and Q_{bound} is the heat exchanged with the surroundings. For tests performed under externally controlled isothermal conditions, θ is prescribed and the above equation is not solved. This treatment is consistent with the thermodynamic structure introduced in Section 7.2, where the temperature evolution follows from the balance of internal energy changes and dissipative contributions at the grain scale.

The internal source term is decomposed as

$$Q_{gen} = Q_e + Q_p + Q_d + Q_{tr} \tag{7-92}$$

where Q_e is the thermoelastic contribution, Q_p is the contribution associated with crystallographic slip, Q_d is the contribution associated with damage evolution, and Q_{tr} is the contribution associated with martensitic transformation. These terms are computed from the grain level constitutive update as

$$Q_e = -V \sum_{g=1}^{N_g} \xi^{(g)} M_e^{(g)} : D_e^{(g)} \quad 7\text{-}93$$

$$Q_p = V \sum_{g=1}^{N_g} \sum_{i=1}^{N_p^{(g)}} \xi^{(g)} M_p^{(g,i)} \dot{\gamma}^{(g,i)} \quad 7\text{-}94$$

$$Q_d = V \sum_{g=1}^{N_g} \xi^{(g)} M_d^{(g)} \dot{\phi}_{eff}^{(g)} \quad 7\text{-}95$$

$$Q_{tr} = V \sum_{a=1}^{N_a} \sum_{\beta=1}^{24} M_{tr}^{(a,\beta)} \dot{\xi}^{(a,\beta)} \quad 7\text{-}96$$

Heat exchange with the surroundings is modeled using an effective boundary transfer law,

$$Q_{bound} = A_{tot} h_{eff} (\theta - \theta_\infty) \quad 7\text{-}97$$

where is the exposed surface area of the thermal control volume, is the ambient boundary temperature, and is an effective heat transfer coefficient. This effective coefficient accounts, in an averaged sense, for both convective losses to the surrounding air and conductive heat extraction through the specimen and grips. Since these contributions are difficult to determine independently within the present reduced order framework, the coefficient is identified during calibration rather than prescribed a priori.

7.4.2 Model Calibration and Validation

7.4.2.1 Calibration Strategy and Identified Parameter Groups

The experimental dataset is partitioned into calibration and validation subsets, as summarized in Table 7-1. This partition is selected to span the dominant loading sensitivities of each steel while preserving independent conditions for model assessment. For QP3Mn, calibration is performed using room temperature tensile responses at multiple strain rates together with temperature-dependent tensile responses at a fixed low strain rate. For QP980, mechanical calibration is carried out using the lowest and highest room temperature strain rate conditions, whereas the intermediate strain rate responses are reserved for validation. The QP980 thermal response is calibrated using the 100 s^{-1} temperature history and then predicted for the remaining strain rates. This partition tests whether a single parameter set can reproduce the calibrated conditions and predict the intermediate mechanical and thermal loading cases not used during parameter identification.

Table 7-1: Calibration and validation experimental data set.

Material	Temperature	Strain rate	
QP3Mn	23°C	0.005, 1, 100	Calibration
	-10°C	0.005	Calibration
	70°C	0.005	Calibration
	Other available conditions	Remaining conditions	Prediction
QP980	23°C	0.001, 100	Calibration
	23°C	0.1, 1, 10	Prediction

A further distinction must be made between directly measured inputs, literature-based constrained inputs, and independent validation quantities. The initial phase fractions and phase specific textures are fixed from microstructural characterization or from literature, depending on the steel and dataset availability. For QP3Mn, the tensile response and retained austenite evolution are adopted from Poling[292] and are used in calibration and assessment of the coupled transformation degradation response. For QP980, the tensile response, initial microstructure, and surface temperature evolution are measured in the present work, whereas the retained austenite evolution is not measured directly and is taken from Poling [292]. The validation of the QP980 model should therefore be interpreted primarily in terms of the measured tensile response and temperature evolution under the strain rate conditions not used for the corresponding calibration step.

The calibration procedure is staged in order to reduce parameter compensation and preserve physical interpretability. Parameters fixed from Connolly et al. [149] are not adjusted and listed in Table 7-2. The remaining unknown coefficients are identified in three steps. First, phase specific plasticity parameters are calibrated to reproduce the initial yield level and the pre-peak hardening response. Second, transformation parameters are identified using the retained-austenite evolution together with its strain rate and temperature dependence for the conditions where such information is available. Third, damage parameters are calibrated using the onset of softening, the magnitude of post-peak stress degradation, and the strain interval sustained prior to final loss of load-carrying capacity. In this manner, the calibrated parameter groups are associated with distinct physical aspects of the response rather than determined through a single undifferentiated fitting procedure. The agreement between simulation and experiment is quantified using a normalized objective function of the form

$$MSE = \sum_{i=1}^{N_\sigma}\left(\frac{\sigma_i^{Sim}-\sigma_i^{Exp}}{\sigma_i^{Exp}}\right)^2 + \sum_{i=1}^{N_\theta}\left(\frac{\theta_i^{Sim}-\theta_i^{Exp}}{\theta_i^{Exp}}\right)^2 + \sum_{i=1}^{N_\xi}\left(\frac{\xi_i^{Sim}-\xi_i^{Exp}}{\xi_i^{Exp}}\right)^2 + \sum_{i=1}^{N_{\varepsilon_f}}\left(\frac{\left(\varepsilon_f\right)_i^{Sim}-\left(\varepsilon_f\right)_i^{Exp}}{\left(\varepsilon_f\right)_i^{Exp}}\right)^2 \quad 7\text{-}98$$

where N_σ, N_θ, N_ξ, and N_{ε_f} denotes the number of data points used for stress, temperature, RAVF evolution, and failure strain respectively, σ_i^{Sim}, θ_i^{Sim}, ξ_i^{Sim}, and $\left(\varepsilon_f\right)_i^{Sim}$ are the simulated values, σ_i^{Exp}, θ_i^{Exp}, ξ_i^{Sim}, and $\left(\varepsilon_f\right)_i^{Exp}$ are the corresponding experimental values.

Table 7-2: Literature coefficients.

Steel grades	QP980		QP3Mn	Both	
Phases	Ferrite	Tempered martensite	Tempered martensite	Retained austenite	Transformed martensite
Elastic moduli (GPa)	$c_{11} = 233.5$ $c_{12} = 135.5$ $c_{44} = 118.0$	$c_{11} = 372.4$ $c_{12} = 345.0$ $c_{44} = 191.1$	$c_{11} = 372.4$ $c_{12} = 345.0$ $c_{44} = 191.1$	$c_{11} = 286.8$ $c_{12} = 166.4$ $c_{44} = 145$	$c_{11} = 372.4$ $c_{12} = 345.0$ $c_{44} = 191.1$
Hardening law (GPa)	$\mu = 118.0$ $h = 519\frac{\mathrm{J}}{\mathrm{kgK}}$	$\mu = 191.1$ $h = 519\frac{\mathrm{J}}{\mathrm{kgK}}$	$\mu = 191.1$ $h = 519\frac{\mathrm{J}}{\mathrm{kgK}}$	$\mu = 145$ $h = 519\frac{\mathrm{J}}{\mathrm{kgK}}$	$\mu = 191.1$ $h = 519\frac{\mathrm{J}}{\mathrm{kgK}}$
Thermal parameters	$A = 17 \cdot 10^{-6}\mathrm{K}^{-1}$ $\rho = 7.8 \cdot 10^3\frac{\mathrm{kg}}{\mathrm{m}^3}$	$A = 17 \cdot 10^{-6}\mathrm{K}^{-1}$ $\rho = 7.8 \cdot 10^3\frac{\mathrm{kg}}{\mathrm{m}^3}$	$A = 17 \cdot 10^{-6}\mathrm{K}^{-1}$ $\rho = 7.8 \cdot 10^3\frac{\mathrm{kg}}{\mathrm{m}^3}$	$A = 17 \cdot 10^{-6}\mathrm{K}^{-1}$ $\rho = 7.8 \cdot 10^3\frac{\mathrm{kg}}{\mathrm{m}^3}$	$A = 17 \cdot 10^{-6}\mathrm{K}^{-1}$ $\rho = 7.8 \cdot 10^3\frac{\mathrm{kg}}{\mathrm{m}^3}$
Transformation parameters				$\lambda_T = -50500\frac{\mathrm{J}}{\mathrm{kg}}$	

The calibrated plasticity, transformation, thermal, and damage parameters are listed in Table 7-3 and Table 7-4. For the damage formulation, calibration is required not only to capture the post-peak stress drop, but also to reproduce the experimentally observed shift in softening onset with strain rate and temperature. The purpose of the calibration is therefore not merely to match flow curves, but to identify a constitutive parameter set capable of reproducing the transition from stable deformation to degradation under varying thermomechanical conditions.

Table 7-3: Calibrated plasticity and damage coefficients.

Steel grades	QP980		QP3Mn	Both	
Phases	Ferrite	Tempered martensite	Tempered martensite	Retained austenite	Transformed martensite
Hardening	$g_{p,0} = 130\ MPa$	$g_{p,0} = 310\ MPa$	$g_{p,0} = 466\ MPa$	$g_{p,0} = 662\ MPa$	$g_{p,0} = 815\ MPa$

Driving force	$c = 1.18$ $k_1 = 35$ $k_2 = 10.6$ $\rho_{d,0} = 10m^{-2}$ $\omega = 20.0$ $\varphi = 0$ $S_\phi = 0$ $\kappa = 50.0$	$c = 0.659$ $k_1 = 35.8$ $k_2 = 8.7$ $\rho_{d,0} = 10m^{-2}$ $\omega = 40$ $\varphi = 0$	$c = 0.659$ $k_1 = 38.8$ $k_2 = 9.7$ $\rho_{d,0} = 10m^{-2}$ $\omega = 40.0$ $\varphi = 0$	$c = 0.304$ $k_1 = 54.6$ $k_2 = 38.5$ $\rho_{d,0} = 10m^{-2}$ $\omega = 55.0$ $\varphi = 0$	$c = 0.221$ $k_1 = 33.6$ $k_2 = 49.5$ $\rho_{d,0} = 10m^{-2}$ $\omega = 58.2$ $\varphi = 0$
Kinetics	$a = 1 \cdot 10^{-3}s^{-1}$ $m = 1 \cdot 10^{-3}$	$a = 1 \cdot 10^{-3}s^{-1}$ $m = 1 \cdot 10^{-3}$	$a = 1 \cdot 10^{-3}s^{-1}$ $m = 1 \cdot 10^{-3}$	$a = 1 \cdot 10^{-3}s^{-1}$ $m = 1 \cdot 10^{-3}$	$a = 1 \cdot 10^{-3}s^{-1}$ $m = 1 \cdot 10^{-3}$
Damage	$\sigma_{0,F} = 140\ MPa$ $\sigma_{ref} = 1650\ MPa$ $p = 50$ $\dot{\varepsilon}_{p0}^{th} = 0.01$ $\beta_T = 0.45$ $\alpha_T = 0.002$ $\sigma_{0,F} = 1.0$	$\sigma_0^{th} = 1.4\ MPa$ $\sigma_{ref} = 338\ MPa$ $r_\sigma = 50$ $\dot{\varepsilon}_{p0}^{th} = 0.01$ $\beta_T = 0.3$ $\alpha_T = 0.002$ $C_{0,AM} = 1.0$ $C_{0,AT} = 1.0$	$\sigma_0^{th} = 1.4\ MPa$ $\sigma_{ref} = 271\ MPa$ $r_\sigma = 50$ $\dot{\varepsilon}_{p0}^{th} = 0.01$ $\beta_T = 0.3$ $\alpha_T = 0.002$ $C_{0,AM} = 1.0$ $C_{0,AT} = 1.0$		

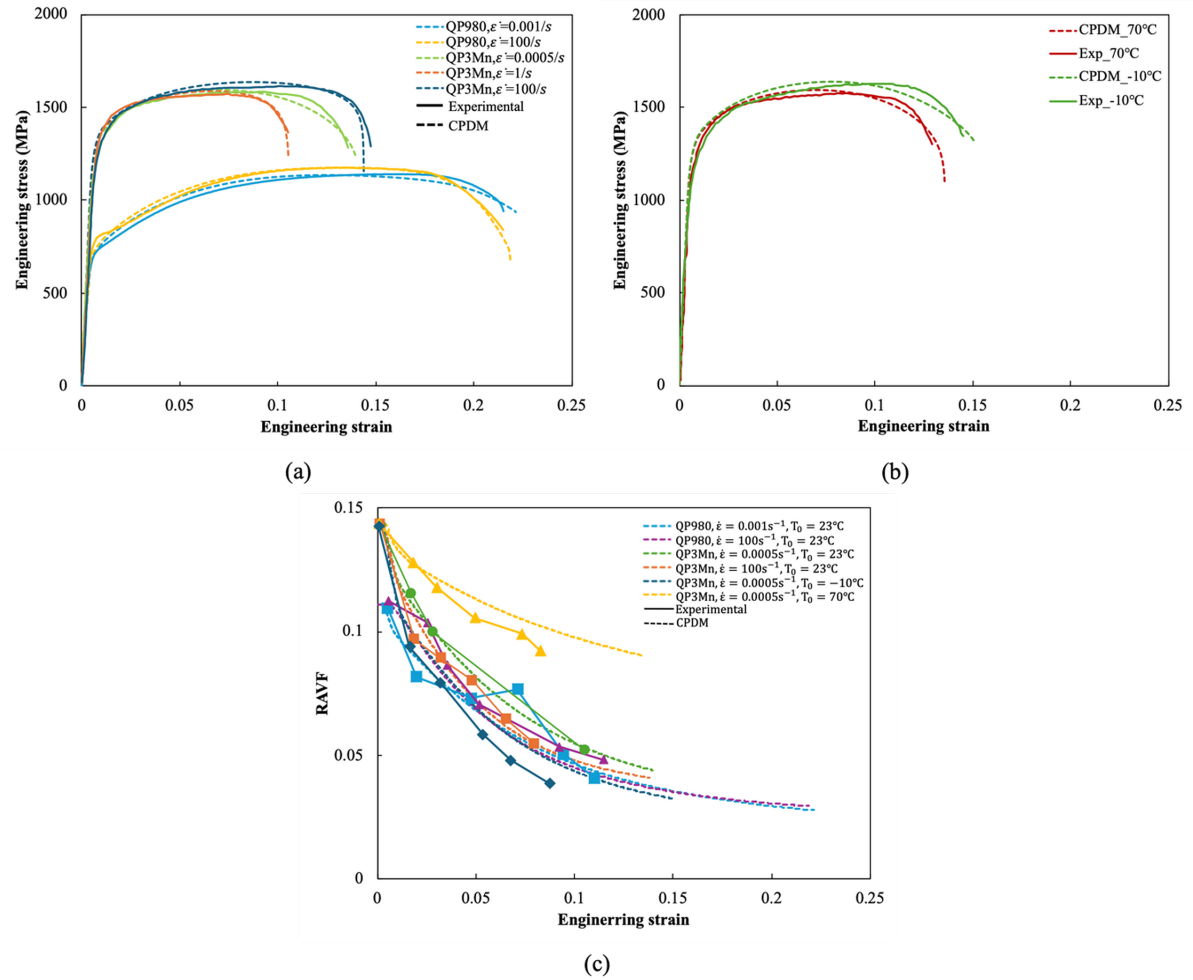


Figure 7-7: Comparison of experimental and CPDM predicted response for the calibration data set (a) Eng. stress–strain response at various strain rate for QP3Mn and QP980, (b) Eng. stress–strain response for at various temperature at 0.005 s^{-1} strain rate for QP3Mn, and (c) evolution of RAVF at various conditions.

Table 7-4: Calibrated transformation coefficients.

$\theta_T = 650\ K$	$\kappa = 0.103$	$n_I = 1.39$	$a_1 = -8.29$	$a_2 = 7.79 \cdot 10^{-2}$
$a_3 = -1.49 \cdot 10^{-4}$	$a_4 = -0.15$	$a_5 = 0.100$	$g_{tr,n} = 0\ MPa$	$\sigma_{tr,n} = 515MPa$
		$f_o = 0.075$	$\sigma_{tr,o} = 40.4MPa$	$g_{tr,o} = 371MPa$

Figure 7-7 confirms that the selected parameter set reproduces the calibration targets in a physically consistent manner. More importantly, the agreement is obtained simultaneously for the macroscopic tensile response and the retained austenite evolution, indicating that the calibrated parameters do not merely fit the flow curves, but preserve the coupling among plastic flow, deformation induced martensitic transformation, thermal effects, and damage. This point is

important for Q&P steels, because their tensile performance is governed not only by slip resistance, but also by the stability of metastable retained austenite and the extent to which transformation remains active during the strain interval preceding degradation. The contrast between QP3Mn and QP980 is already evident at the calibration stage: QP3Mn maintains a higher stress level, whereas QP980 sustains deformation over a broader strain interval. The calibrated framework therefore captures not only the strength difference between the two steels, but also the distinct balance between transformation-assisted stabilization and damage-controlled degradation.

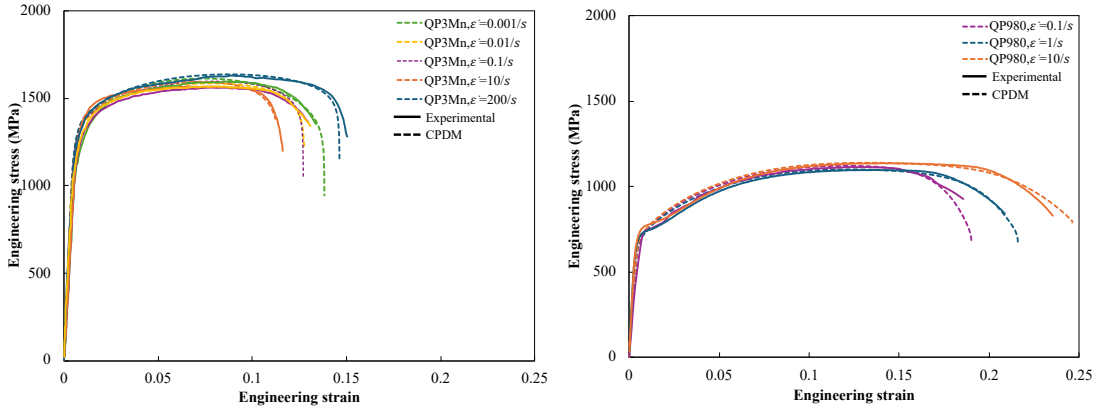
7.4.2.2 Strain Rate Dependence Of Damage Evolution

Figure 7-8 illustrates that the strain rate dependence of the tensile response is expressed not only through changes in stress level, but more importantly through the strain interval over which transformation-assisted hardening can delay degradation. This distinction is significant in Q&P steels, where macroscopic ductility depends on the evolving balance among retained austenite transformation, deformation induced heating, and damage accumulation rather than on rate-sensitive slip alone. The stress–strain curves therefore identify the macroscopic consequence of rate dependence, but they do not by themselves reveal whether the change originates from plastic flow, thermal evolution, retained austenite stability, or damage activation.

For QP3Mn, the strain rate effect is most evident near the onset and progression of softening rather than in the early part of the flow curve. This indicates that the dominant role of loading rate is not simply to shift the flow stress, but to modify the competition between transformation-assisted stabilization and degradation. In a microstructure dominated by tempered martensite and retained austenite, continued transformation increases local stiffness contrast and transformation strain mismatch, so the influence of loading rate becomes more visible in the terminal deformation regime than in the initial plastic regime. Such an interpretation is consistent with earlier studies showing that retained austenite stability, together with the character of the surrounding matrix, governs how long the TRIP effect can sustain hardening before the evolving microstructure begins to promote damage initiation [293,294].

The response of QP980 is qualitatively different from QP3Mn. Although the overall stress level is lower, QP980 sustains deformation over a broader strain interval and exhibits a more gradual post-peak decline. This behavior is consistent with the presence of ferrite, which provides a more compliant deformation path and reduces the severity of local incompatibility relative to the martensite dominant QP3Mn microstructure. The important point is that this apparent ductility

cannot be interpreted from the stress–strain response alone. In QP980, loading rate changes the thermal path, the retained austenite transformation trajectory, and the timing of damage activation. The rate dependence should therefore be interpreted as a coupled change in thermomechanical state, RA stability, and degradation pathway rather than as a simple change in peak stress.



(a) (b)

Figure 7-8: Experimental and CPDM-predicted engineering stress–strain response at different strain rates for (a) QP3Mn and (b) QP980.

Figure 7-9 provides the internal variable explanation for the QP980 rate effect. The agreement between measured and predicted temperature rise shows that the thermal path entering the constitutive update is anchored to experiment. This matters because the same thermal path enters the RA transformation kinetics and the temperature sensitive interface damage terms. As the strain rate increases, deformation induced heating alters retained austenite stability and therefore changes the rate at which retained austenite is consumed, while also shifting the strain interval over which damage grows rapidly. Thus, the rate-dependent response of QP980 does not arise only from viscoplastic hardening; its macroscopic ductility reflects the timing among heat generation, RA depletion, and damage activation.

This distinction is important for the rest of the analysis. Similar stress–strain agreement can be obtained from different combinations of hardening, transformation, and degradation, but Figure 7-9 reduces that ambiguity by showing the internal thermal and microstructural paths. The delayed growth of the normalized damage variable at some strain rates, despite continued RA depletion, indicates that the onset of degradation is controlled by a competition between transformation-assisted stabilization, ferrite mediated strain accommodation, deformation induced heating, and interface degradation.

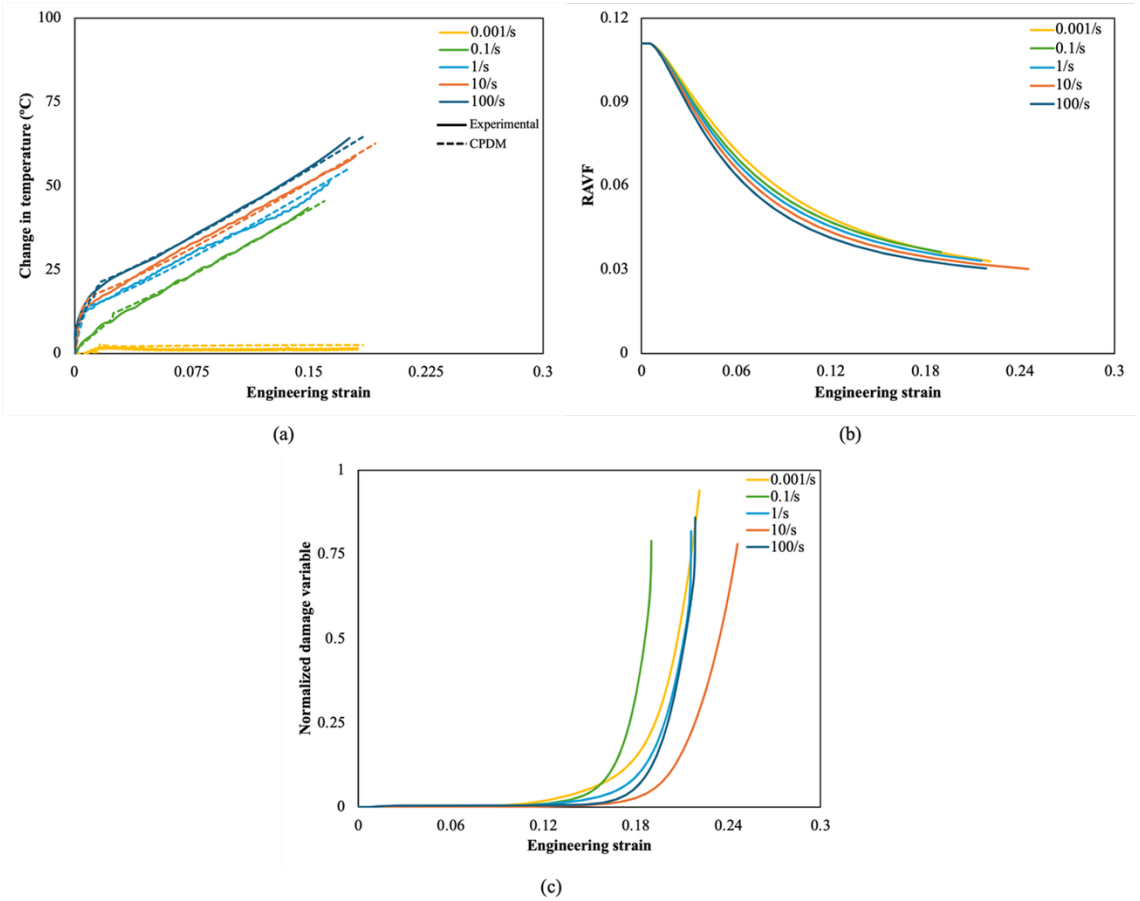


Figure 7-9: Thermomechanical response and internal variable evolution of QP980 at different strain rates: (a) experimental and CPDM predicted temperature rise, (b) predicted retained austenite volume fraction, and (c) predicted normalized damage variable.

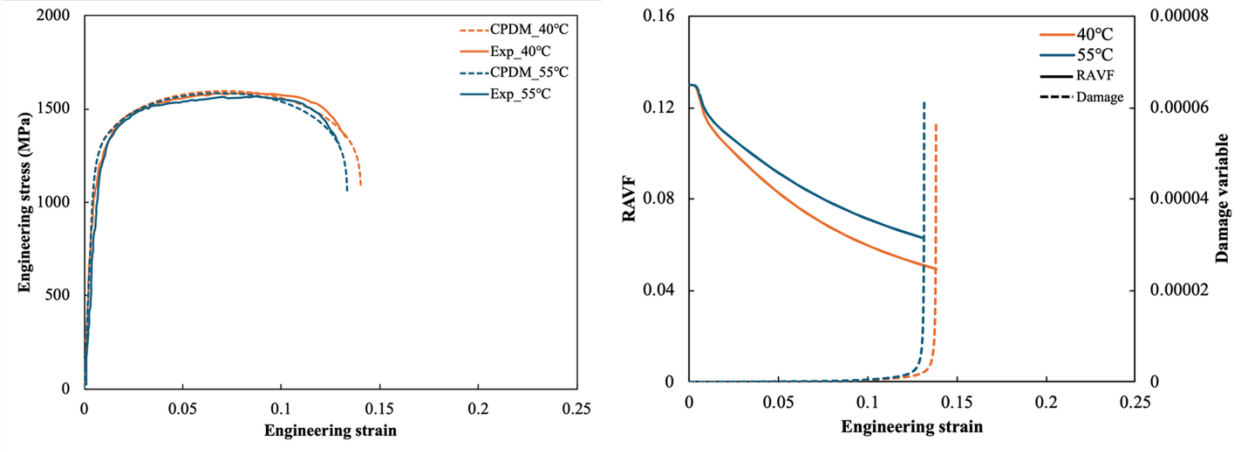
7.4.2.3 Temperature controlled response of QP3Mn

Figure 7-10 shows that the effect of imposed temperature in QP3Mn is expressed more strongly through the evolution of RA stability and the onset of degradation than through a major change in the overall stress level. In Figure 7-10(a), the engineering stress–strain curves at 40 and 55 °C remain nearly indistinguishable up to the peak stress of approximately 1600 MPa, and separate only in the post-peak regime, where failure occurs at $\varepsilon \approx 0.140$ at 40 °C and at $\varepsilon \approx 0.135$ at 55 °C. The corresponding internal variable evolution in Figure 7-10(b) reveals a markedly different temperature sensitivity: the retained austenite volume fraction depletes faster at 40 °C, reaching approximately 0.05 at failure compared with approximately 0.06 at 55 °C. The damage variable remains negligible throughout most of the deformation history and rises abruptly only in the terminal stage, with the activation occurring at slightly lower strain at 55 °C than at 40 °C. This

combination of observations indicates that the macroscopic stress–strain response can mask a stronger temperature sensitivity in the underlying transformation state. This is consistent with prior observations that RA stability, rather than fraction alone, governs the balance between sustained hardening and loss of ductility in TRIP and Q&P steels .

The mechanistic origin of this behavior follows from the structure of the present damage framework. In QP3Mn, the absence of ferrite eliminates the matrix damage channel, so the dominant degradation pathway is the austenite related interface channel, which captures decohesion at retained austenite/martensite boundaries and mismatch at interfaces with transformed martensite. Temperature acts on this channel in two competing ways: it raises retained austenite stability and slows transformation, while simultaneously lowering the thermally activated threshold governing interface decohesion. At 55 °C, the slower transformation reduces the rate of transformation-assisted hardening during the strain interval in which localization would otherwise develop, and within the present constitutive framework, the reduced interface threshold promotes earlier activation of austenite interface degradation. Both effects act in the same direction, advancing the transition to the degradation dominated regime even though more retained austenite remains in the microstructure.

The implication for the present QP3Mn system is that residual RA content alone is a poor predictor of remaining ductility within this temperature window. The benefit of retained austenite arises from the progression of its transformation rather than from the magnitude of its remaining fraction, since only transformation concurrent with the strain interval of incipient localization contributes effectively to stabilization. Once the transformation rate falls below the level required to offset the accelerating interface degradation, the constitutive balance shifts to a degradation dominated regime regardless of how much retained austenite remains. The 40–55 °C range therefore emerges as a sensitive stability window in which a modest change in temperature produces a disproportionate change in transformation kinetics and in the activation of austenite interface damage, while leaving the macroscopic flow response nearly unchanged.



(a) (b)

Figure 7-10: (a) Experimental and CPDM predicted engineering stress–strain response (b) Predicted evolution of RAVF and damage variable for QP3Mn at 40 and 55 °C at a strain rate of 0.0005 s^{-1}.

7.4.2.4 Effect of retained austenite fraction on degradation

The role of RA in Q&P steels is often discussed in terms of its amount, based on the expectation that a larger RA reservoir will prolong the TRIP contribution during deformation. The present results show that this interpretation is incomplete. As shown in Figure 7-11(a), increasing the initial retained austenite volume fraction from 12 to 16% leads to a monotonic reduction in both peak strength and failure strain in QP3Mn. The case with 12% RA reaches the highest peak stress and sustains deformation to approximately $\varepsilon \approx 0.155$, whereas the 16% case gives the lowest peak stress and fails at approximately $\varepsilon \approx 0.135$. The tensile curves remain close during the early hardening regime and separate progressively only near the peak and in the post-peak regime. This behavior indicates that the influence of RA is expressed primarily through the timing of the stabilization to degradation transition rather than through a large change in the initial flow response.

The internal variable evolution in Figure 7-11(b) explains the origin of this trend. Within the present constitutive framework, higher initial retained austenite volume fraction is associated with faster RA depletion and earlier activation of the damage variable. The key point is therefore that the mechanical role of retained austenite is governed not by its initial fraction alone, but by the strain interval over which it transforms. When the initial RA reservoir is increased without a corresponding increase in its mechanical stability, the transformation contribution becomes concentrated too early in the deformation history. In that case, the transformation-assisted

hardening is exhausted before it can continue to stabilize the response in the strain range where localization and degradation begin to accelerate. The result is an earlier shift to damage dominated behavior, despite the larger initial RA content.

This interpretation provides the kinetic complement to the temperature effect discussed in the previous subsection. There, imposed temperature increases RA stability and slows transformation to the point that the stabilizing contribution becomes insufficient over the relevant strain interval. Here, by contrast, increasing the initial RA fraction accelerates depletion within the present calibrated conditions, so that the transformation contribution is consumed too early. In both cases, the conclusion is the same: RA contributes beneficially only when its transformation kinetics are matched to the strain interval over which instability develops. This is consistent with the broader view that the mechanical role of retained austenite in multiphase steels depends on its stability, morphology, and surrounding phase constraint rather than on phase fraction alone [294–296].

The present results therefore suggest a clearer microstructural design implication for Q&P steels. Increasing RA content is beneficial only when accompanied by sufficient stability to sustain progressive transformation over the deformation history. Without such stability, the added RA promotes earlier formation of transformed martensite, stronger phase contrast, and earlier activation of austenite related interface damage rather than prolonged stabilization [6]. The relevant design variable is thus the combined effect of RA fraction and RA stability, since these together determine the strain interval over which transformation can continue to contribute mechanically before degradation becomes dominant.

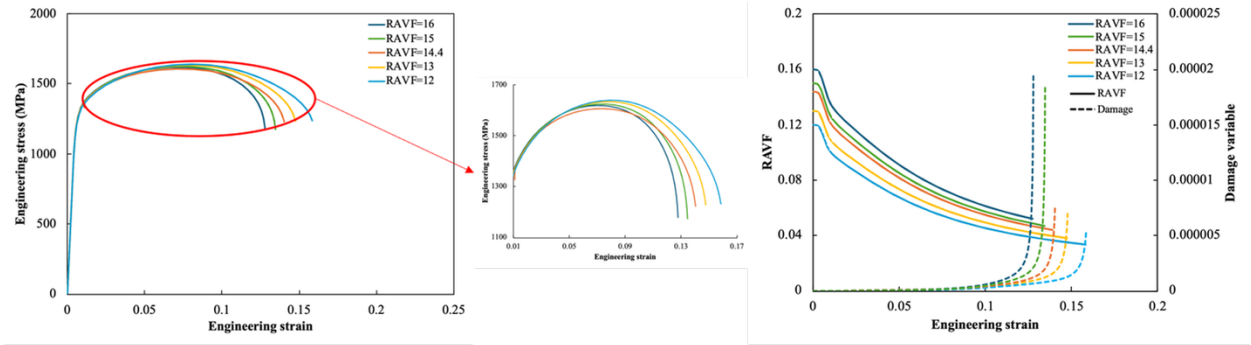


Figure 7-11: Influence of initial RAVF on the tensile response: (a) engineering stress–strain behavior and (b) predicted evolution of RAVF and damage variable.

7.4.2.5 Characteristic transition strains controlling softening and failure

The preceding sections examined how temperature, initial retained austenite volume fraction, and strain rate affect stress response, RA transformation, temperature evolution, and damage growth. The deformation response is therefore further analyzed using three characteristic transition strains, summarized in Table 7-5. These measures distinguish the onset of macroscopic softening, the onset of rapid damage acceleration, and the transformation-damage crossover where the stabilizing contribution of RA transformation becomes outweighed by damage accumulation associated with phase incompatibility and progressive loss of load-carrying capacity. The transition strains show that softening, damage acceleration, and transformation-damage crossover are related but not identical events.

Table 7-5: Characteristic strain measures extracted from the simulated response.

Condition	ε_{soft}	ε_D	ε_{tr}
40 °C	0.09025	0.1357	0.1362
55 °C	0.08694	0.1252	0.1296
RAVF = 12%	0.09657	0.0841	0.1371
RAVF = 16%	0.08440	0.1148	0.1239
0.001 s^{-1}	0.09391	0.0928	0.1278
1 s^{-1}	0.07559	0.0820	0.1019
200 s^{-1}	0.10852	0.1364	0.1435

The temperature-dependent cases show that increasing the deformation temperature shifts the transition sequence to lower strain. When the temperature is increased from 40 °C to 55 °C, ε_{soft} decreases from 0.0902 to 0.0869, while ε_D decreases from 0.1357 to 0.1252 and ε_{tr} decreases from 0.1362 to 0.1296. This indicates that elevated temperature promotes an earlier transition from transformation-assisted deformation to damage dominated softening. Although RA transformation continues to contribute to the mechanical response, the beneficial hardening contribution is exhausted over a shorter strain interval, allowing damage to become dominant at lower deformation levels.

A stronger shift is observed when the initial retained austenite volume fraction is increased from 12% to 16%. For the RAVF = 12% condition, the onset of softening occurs at $\varepsilon_{soft} = 0.0965$, while rapid damage acceleration and transformation–damage crossover occur at $\varepsilon_D = 0.1548$ and $\varepsilon_{tr} = 0.1591$, respectively. In contrast, for the RAVF = 16% condition, these transition strains decrease to $\varepsilon_{soft} = 0.08440$, $\varepsilon_D = 0.1211$, and $\varepsilon_{tr} = 0.12390$. Therefore, a higher initial RA content does not necessarily delay softening or improve ductility. Instead, the larger transformable

phase fraction promotes earlier transformation-induced phase mismatch and accelerates the transition toward damage-controlled deformation. This result emphasizes that the mechanical role of RA is governed not only by its initial volume fraction, but also by the strain range over which transformation remains mechanically stabilizing.

The strain rate-dependent cases exhibit a non-monotonic transition sequence. Under quasi-static loading, the onset of rapid damage acceleration occurs close to the onset of macroscopic softening, indicating that damage acceleration and loss of load-carrying capacity develop almost simultaneously. At an intermediate strain rate, the transition strains shift to lower values, indicating earlier softening and earlier transformation-damage crossover. At the highest simulated strain rate, the transition strains increase again. The non-monotonic sequence therefore reflects competing thermal, transformation, and damage mechanisms rather than a single monotonic rate effect.

Conditions with a larger separation between the onset of macroscopic softening and rapid damage acceleration sustain deformation over a broader post-peak strain interval, whereas conditions in which these events occur close together undergo a more abrupt transition from softening to rapid loss of load-carrying capacity. A delayed transformation-damage crossover further indicates that retained austenite transformation continues to provide mechanical stabilization over a wider strain range before degradation becomes dominant. Taken together, the transition-strain analysis shows that temperature, strain rate, and initial retained austenite content influence ductility primarily by shifting the relative timing of macroscopic softening, rapid damage growth, and the transition from transformation-assisted stabilization to damage dominated response.

7.5 Chapter Conclusion

This work presented a thermomechanically coupled crystal plasticity damage framework for quenching and partitioning steels within a modified Taylor homogenization model. The constitutive formulation combined crystallographic slip, deformation induced martensitic transformation, temperature evolution, and phase sensitive degradation in a thermodynamically consistent manner. A damage variable was introduced through an effective grain level description that incorporates ferrite matrix damage together with interface-related damage associated with ferrite-martensite and austenite containing phase boundaries. In this manner, the transition from hardening to softening was treated as an internal constitutive evolution rather than through an external post-processing failure criterion.

The proposed framework was calibrated and assessed using tensile response, retained austenite, and temperature evolution data for QP3Mn and QP980 steels under varying loading conditions. For QP3Mn, the model captured the coupled evolution of stress response, retained austenite fraction, and softening trends over different strain rates and temperatures. For QP980, the model reproduced the tensile response under various strain rates and captured the measured temperature evolution, with the 100 s^{-1} thermal response used for calibration and the remaining strain rates predicted. The key outcome is not simply agreement with experiments, but the mechanistic separation of stress response, thermal path, retained austenite depletion, and damage activation. On this basis, the following conclusions are drawn:

- The proposed crystal plasticity damage model reproduced the tensile response of Q&P steels across calibrated and validation conditions, including the onset of softening and post-peak degradation. This indicates that the coupled transformation damage formulation can describe constitutive instability development within the limits of Taylor homogenization framework.
- Retained austenite plays a dual mechanical role in the present Q&P steels. At lower strain, transformation contributes to deformation stabilization through sustained hardening. At larger strain, continued transformation increases phase contrast and local incompatibility, thereby promoting damage accumulation and the transition to degradation dominated response.
- The transition-strain analysis distinguishes the macroscopic onset of softening, the acceleration of damage, and the internal shift from retained austenite-assisted stabilization to damage dominated degradation. This analysis shows that instability in Q&P steels is better interpreted as a sequence of constitutive transitions than as the stress peak alone.
- Within the present calibrated conditions, increasing temperature and increasing the initial retained austenite fraction both shift the stabilization to degradation transition to lower strain, although the damage acceleration indicator does not necessarily evolve identically in each case.
- The QP980 temperature evolution analysis provides the thermomechanical link between strain rate and internal variable evolution. After calibration at 100 s^{-1}, the model predicts the temperature histories at the remaining strain rates, supporting the interpretation that QP980 rate dependence is governed by coupled plastic flow, deformation induced heating, retained austenite transformation, and damage activation rather than by a simple monotonic shift in strength or ductility.

8 Conclusions and Future Work

8.1 Key Conclusions

This thesis examined how the constitutive description of damage evolution must change as the microstructural complexity of advanced high-strength steels increases from HSLA to DP to Q&P steels. The main conclusion is that predictive modeling of damage-driven softening and failure cannot be achieved by recalibrating a single damage law across different steel grades. Instead, the framework must be enriched according to the dominant microstructural mechanism governing damage accumulation.

The progression from HSLA to DP to Q&P steels revealed a clear hierarchy of required constitutive components. In ferrite-dominated HSLA steels, a rate- and temperature-sensitive crystal plasticity damage formulation is sufficient to describe void-driven degradation. In DP steels, the fixed mechanical contrast between ferrite and martensite requires additional phase specific plasticity, stress-state-dependent void evolution, and interface-sensitive degradation. In Q&P steels, the evolving phase constitution requires retained-austenite transformation to be coupled directly with thermomechanical deformation and damage evolution. This hierarchy establishes the main contribution: the crystal plasticity damage framework must be expanded according to the dominant mechanism governing damage accumulation and loss of load-carrying capacity, progressing from void driven degradation to phase interaction driven degradation, to transformation coupled degradation.

The key conclusions from the work presented in this thesis are as follows.

8.1.1 Development of Thermodynamically Consistent Crystal Plasticity Damage Model for HSLA Steels

- A thermodynamically consistent, rate-dependent crystal plasticity damage model was developed to capture the stress–strain response, temperature evolution, and damage-driven softening of HR340 and HR550 steels over quasi-static and intermediate strain rates.
- The model successfully coupled crystallographic slip, dislocation evolution, void nucleation, void growth, and internal temperature evolution within a single constitutive framework.

- The inclusion of internal temperature evolution was necessary to capture the strain rate hardening and thermal softening. Simulations without temperature coupling overpredicted flow stress and dislocation density at higher strain rates.
- The model captured the experimentally observed increase in temperature rise with strain rate, demonstrating that plastic-work heating becomes important even at intermediate deformation rates.
- Damage accumulation was shown to be strongly influenced by strain rate and temperature. Higher strain rates delayed the onset of damage evolution and contributed to improved post-necking deformation in the investigated HSLA steels.
- The predicted texture evolution showed good agreement with EBSD measurements, demonstrating that the Taylor-type crystal plasticity framework can capture the main orientation changes during large plastic deformation.

8.1.2 Development of a Phase and Interface Driven Damage Model Coupled with Crystal Plasticity for Dual Phase Steels

- The baseline crystal plasticity damage framework was extended to dual phase steels by incorporating ferrite and martensite phase specific plasticity, microstructure-sensitive void kinetics, and homogenized ferrite–martensite interface degradation.
- The model captured the elastic–plastic response, post-necking softening, failure strain, and temperature rise of DP590 over a range of strain rates. Predictions at intermediate strain rates retained consistency, indicating that the formulation captured underlying rate-dependent mechanisms rather than relying only on strain rate specific fitting.
- Application of the framework to DP780 required only limited additional calibration, primarily through changes in phase fraction and void-related microstructural descriptors. This demonstrated the ability of the framework to transfer between DP steel grades while retaining a mechanistic basis.
- Plane strain tension and simple shear simulations showed that damage evolution is strongly dependent on stress state. Plane strain tension promoted earlier damage accumulation and stronger softening, while simple shear delayed damage evolution under lower-triaxiality conditions.

- Directional anisotropy between rolling and transverse directions was reproduced for both DP grades, showing that crystallographic texture and slip-system activity influence strain localization and damage evolution.
- Orientation resolved simulations showed that high Taylor factor orientations promoted higher strength but accelerated localization and damage, whereas orientations associated with more homogeneous slip delayed damage accumulation and improved post-necking deformation.

8.1.3 Development of a Crystal Plasticity-Based Transformation Coupled Damage Evolution Model for Q&P Steels

- The crystal plasticity damage framework was extended to Q&P steels by coupling crystallographic slip, retained-austenite transformation, internal temperature evolution, and phase-sensitive damage evolution.
- The model reproduced the coupled evolution of tensile response, retained-austenite depletion, damage accumulation, and stress–strain softening for QP3Mn under different strain rate and temperature conditions.
- The framework also captured the rate-dependent tensile response of QP980, demonstrating its applicability to retained-austenite-containing AHSS with different compositions and microstructural states.
- Retained austenite was shown to play a dual mechanical role. At lower strains, transformation-assisted hardening delayed degradation and improved deformation stability. At larger strains, continued transformation increased phase contrast and local incompatibility, contributing to accelerated damage accumulation.
- A transition strain analysis was introduced to distinguish the macroscopic onset of softening, rapid damage acceleration, and the internal transition from retained-austenite-assisted stabilization to damage-dominated degradation.
- The results demonstrated that transformation-coupled damage modeling is required to interpret Q&P steel response beyond hardening behavior alone, particularly when the objective is to capture the transition from stable deformation to damage-driven softening.

8.2 Limitations of the Proposed Work

The proposed framework is subject to limitations that follow from its material-point formulation and homogenization assumptions. As such, explicit crack propagation, fracture-surface formation, and geometry dependent failure paths are not considered. The predicted failure response is interpreted as damage-driven softening and progressive loss of load-carrying capacity. Void nucleation, growth, and shape evolution are included through internal damage variables, while void coalescence is not explicitly resolved as a separate geometric process. Propagative instabilities such as PLC bands, dynamic strain ageing, and explicit shear-band propagation are also outside the scope of the present formulation. Since the framework is based on Taylor-type homogenization, it does not predict the spatial extent, orientation, or morphology of a localization band. The model therefore captures the constitutive onset and progression of damage-driven softening, but not the specimen-scale development of a localized failure path.

The Taylor-type homogenization framework assumes that all grains experience the imposed macroscopic deformation. As a result, local strain gradients, grain-neighborhood effects, spatially resolved strain partitioning, and explicit grain-boundary damage are not captured. Ferrite–martensite and austenite containing interfaces are not represented as explicit geometric boundaries. Instead, their effects are introduced through homogenized phase-interaction and interface-sensitive damage variables. The model therefore cannot predict the local morphology of interface separation or the spatial path of damage development. The temperature evolution is also treated as a material point quantity, and spatial variations in temperature within the specimen are not resolved. In addition, grains belonging to the same phase are assumed to have the same chemistry and phase properties. No distinction is made between film-like and blocky retained austenite, local carbon-enrichment variations, martensite substructure, or carbide distributions.

The framework is expected to apply to HSLA, DP, and Q&P steels within the range of strain rates, temperatures, and loading conditions for which experimental data are available. The HSLA model is restricted to uniaxial tensile deformation over the measured quasi-static and intermediate strain rate range. The DP steel model is restricted to the tested uniaxial tension, plane strain tension, and simple shear loading paths. The Q&P steel model is restricted to the available tensile data and retained austenite evolution measurements. Therefore, the proposed framework should be interpreted as a constitutive description of damage evolution, stress–strain softening, and failure

response in advanced high-strength steels, rather than as a fully resolved simulation of specimen-scale cracking or local fracture morphology.

8.3 Future Work

The constitutive framework developed in this thesis provides a basis for predicting damage evolution and stress–strain softening in AHSS. However, several extensions would improve the physical fidelity, transferability, and applicability of the model:

- Incorporate a more advanced homogenization scheme, such as viscoplastic self-consistent or full-field crystal plasticity, to better capture strain partitioning between grains and phases while retaining the current damage and transformation framework.
- Develop a spatially resolved implementation of the proposed damage framework to examine localization-band formation, interface damage paths, and specimen-scale instability under forming-relevant loading conditions.
- Explicitly resolve ferrite–martensite and austenite containing interfaces in selected representative volume elements to calibrate and validate the homogenized interface-damage variables used in the current framework.
- Extend the void evolution model to include a more detailed treatment of void coalescence and void interaction, while maintaining the distinction between material-point damage evolution and explicit crack path prediction.
- Incorporate spatially resolved heat conduction and a variable Taylor–Quinney coefficient to improve temperature predictions during localized deformation and high strain rate loading.
- Incorporate phase specific local chemistry and retained-austenite morphology, particularly for Q&P steels, where carbon enrichment, austenite size, film-like or blocky morphology, martensite substructure, and surrounding phases can influence retained-austenite stability and damage evolution.

References

[1] Bharodiya V, Sisodia D, Singh P. Structural design and simulation of battery enclosure for an electric vehicle against mechanical abuse test, 2023. https://doi.org/10.4271/2023-28-1345.

[2] Pan Y, Xiong Y, Wu L, Diao K, Guo W. Lightweight design of an automotive battery-pack enclosure via advanced high-strength steels and size optimization. International Journal of Automotive Technology 2021;22:1279–90. https://doi.org/10.1007/s12239-021-0112-5.

[3] Kuziak R, Kawalla R, Waengler S. Advanced high strength steels for automotive industry. Archives of Civil and Mechanical Engineering 2008;8:103–17. https://doi.org/10.1016/S1644-9665(12)60197-6.

[4] Zhang W, Xu J. Advanced lightweight materials for Automobiles: A review. Mater Des 2022;221:110994. https://doi.org/10.1016/j.matdes.2022.110994.

[5] Garcia CI. High strength low alloyed (HSLA) steels. Automotive Steels, Elsevier; 2017, p. 145–67. https://doi.org/10.1016/B978-0-08-100638-2.00006-7.

[6] Tasan C, Hoefnagels J, Diehl M, Yan D, Roters F, Raabe D. Strain localization and damage in dual phase steels investigated by coupled in-situ deformation experiments and crystal plasticity simulations. Int J Plast 2014;63:198–210. https://doi.org/10.1016/j.ijplas.2014.06.004.

[7] Calcagnotto M, Adachi Y, Ponge D, Raabe D. Deformation and fracture mechanisms in fine- and ultrafine-grained ferrite/martensite dual-phase steels and the effect of aging. Acta Mater 2011;59:658–70. https://doi.org/10.1016/j.actamat.2010.10.002.

[8] Speer J, Matlock K, De Cooman C, Schroth G. Carbon partitioning into austenite after martensite transformation. Acta Mater 2003;51:2611–22. https://doi.org/10.1016/S1359-6454(03)00059-4.

[9] Santofimia MJ, Zhao L, Petrov R, Sietsma J. Characterization of the microstructure obtained by the quenching and partitioning process in a low-carbon steel. Mater Charact 2008;59:1758–64. https://doi.org/10.1016/j.matchar.2008.04.004.

[10] Rice JR, Tracey DM. On the ductile enlargement of voids in triaxial stress fields. J Mech Phys Solids 1969;17:201–17. https://doi.org/10.1016/0022-5096(69)90033-7.

[11] Gurson AL. Continuum Theory of Ductile Rupture by Void Nucleation and Growth: Part I—Yield Criteria and Flow Rules for Porous Ductile Media. J Eng Mater Technol 1977;99:2–15. https://doi.org/10.1115/1.3443401.

[12] McClintock FA. A Criterion for Ductile Fracture by the Growth of Holes. J Appl Mech 1968;35:363–71. https://doi.org/10.1115/1.3601204.

[13] Tvergaard V, Needleman A. Analysis of the cup-cone fracture in a round tensile bar. Acta Metallurgica 1984;32:157–69. https://doi.org/10.1016/0001-6160(84)90213-X.

[14] Bai Y, Wierzbicki T. A new model of metal plasticity and fracture with pressure and Lode dependence. Int J Plast 2008;24:1071–96. https://doi.org/10.1016/j.ijplas.2007.09.004.

[15] Asaro RJ, Needleman A. Texture development and strain hardening in rate dependent polycrystals. Acta Metallurgica 1985;33:923–53. https://doi.org/10.1016/0001-6160(85)90188-9.
[16] Roters F, Eisenlohr P, Hantcherli L, Tjahjanto DD, Bieler TR, Raabe D. Overview of constitutive laws, kinematics, homogenization and multiscale methods in crystal plasticity finite-element modeling: Theory, experiments, applications. Acta Mater 2010;58:1152–211. https://doi.org/10.1016/j.actamat.2009.10.058.
[17] Potirniche GP, Horstemeyer MF, Ling XW. An internal state variable damage model in crystal plasticity. Mechanics of Materials 2007;39:941–52. https://doi.org/10.1016/j.mechmat.2007.04.004.
[18] Kadkhodapour J, Butz A, Ziaei-Rad S, Schmauder S. A micro mechanical study on failure initiation of dual phase steels under tension using single crystal plasticity model. Int J Plast 2011;27:1103–25. https://doi.org/10.1016/j.ijplas.2010.12.001.
[19] Qin S, Lu Y, Sinnott SB, Beese AM. Influence of phase and interface properties on the stress state dependent fracture initiation behavior in DP steels through computational modeling. Materials Science and Engineering: A 2020;776:138981. https://doi.org/10.1016/j.msea.2020.138981.
[20] Vermeij T, Mornout CJA, Rezazadeh V, Hoefnagels JPM. Martensite plasticity and damage competition in dual-phase steel: A micromechanical experimental–numerical study. Acta Mater 2023;254:119020. https://doi.org/10.1016/j.actamat.2023.119020.
[21] Aydiner IU, Tatli B, Yalçinkaya T. Investigation of failure mechanisms in dual-phase steels through cohesive zone modeling and crystal plasticity frameworks. Int J Plast 2024;174:103898. https://doi.org/10.1016/j.ijplas.2024.103898.
[22] Turteltaub S, Suiker A. Transformation-induced plasticity in ferrous alloys. J Mech Phys Solids 2005;53:1747–88. https://doi.org/10.1016/j.jmps.2005.03.004.
[23] Connolly DS, Kohar CP, Inal K. A novel crystal plasticity model incorporating transformation induced plasticity for a wide range of strain rates and temperatures. Int J Plast 2022;152:103188. https://doi.org/10.1016/j.ijplas.2021.103188.
[24] Yang H, Zhou G, Wang H, Wu P, Lee M-G, Li D. Experimental and numerical study on strain path and crystal orientation dependences of phase transformation behaviors of QP1180 steel. Int J Plast 2023;160:103499. https://doi.org/10.1016/j.ijplas.2022.103499.
[25] Park J, Hou Y, Min J, Hou Z, Han HN, He B, et al. Understanding plasticity in multiphase quenching partitioning steels: Insights from crystal plasticity with stress state-dependent martensitic transformation. Int J Plast 2024;180:104075. https://doi.org/10.1016/j.ijplas.2024.104075.
[26] Schmitt J-H, Iung T. New developments of advanced high-strength steels for automotive applications. C R Phys 2018;19:641–56. https://doi.org/10.1016/j.crhy.2018.11.004.
[27] David M, John S, Emmanuel M, Paul G. Recent developments in advanced high strength sheet steels for automotive applications: An overview. Jestech 2012;15:1–12.

[28] Wang L, Speer JG. Quenching and Partitioning Steel Heat Treatment. Metallography, Microstructure, and Analysis 2013;2:268–81. https://doi.org/10.1007/s13632-013-0082-8.
[29] Singh R. Classification of steels. Applied Welding Engineering, Elsevier; 2020, p. 53–60. https://doi.org/10.1016/B978-0-12-821348-3.00014-8.
[30] Marder AR, Goodwin FE. Zn-coated high-strength steel. The Metallurgy of Zinc Coated Steels, Elsevier; 2023, p. 457–505. https://doi.org/10.1016/B978-0-323-99984-7.00016-6.
[31] Zhang Y, Wang M, Yong Q, Jose MR-I, Leonardo S. Solution and Precipitation Behavior of Nb and Its Role in Medium Carbon Long Product Steels. Journal of Mechanics Engineering and Automation 2022;12. https://doi.org/10.17265/2159-5275/2022.01.001.
[32] Wang L, Wang S. Study on Austenite Transformation and Growth Evolution of HSLA Steel. Materials 2023;16:3578. https://doi.org/10.3390/ma16093578.
[33] Rashid MS. Dual Phase Steels. Annual Review of Materials Science 1981;11:245–66. https://doi.org/10.1146/annurev.ms.11.080181.001333.
[34] Tasan CC, Diehl M, Yan D, Bechtold M, Roters F, Schemmann L, et al. An Overview of Dual-Phase Steels: Advances in Microstructure-Oriented Processing and Micromechanically Guided Design. Annu Rev Mater Res 2015;45:391–431. https://doi.org/10.1146/annurev-matsci-070214-021103.
[35] Rana AK, Paul SK, Dey PP. Effect of martensite volume fraction on cyclic plastic deformation behavior of dual phase steel: micromechanics simulation study. Journal of Materials Research and Technology 2019;8:3705–12. https://doi.org/10.1016/j.jmrt.2019.06.022.
[36] Badkoobeh F, Mostaan H, Rafiei M, Bakhsheshi-Rad HR, Berto F. Microstructural Characteristics and Strengthening Mechanisms of Ferritic–Martensitic Dual-Phase Steels: A Review. Metals (Basel) 2022;12:101. https://doi.org/10.3390/met12010101.
[37] De Moor E. Advanced high-strength sheet steels for automotive applications. High-Performance Ferrous Alloys, Cham: Springer International Publishing; 2021, p. 113–51. https://doi.org/10.1007/978-3-030-53825-5_4.
[38] Grajcar A, Kuziak R, Zalecki W. Third generation of AHSS with increased fraction of retained austenite for the automotive industry. Archives of Civil and Mechanical Engineering 2012;12:334–41. https://doi.org/10.1016/j.acme.2012.06.011.
[39] De Moor E, Speer JG. Bainitic and quenching and partitioning steels. Automotive Steels, Elsevier; 2017, p. 289–316. https://doi.org/10.1016/B978-0-08-100638-2.00010-9.
[40] Edmonds DV, He K, Rizzo FC, De Cooman BC, Matlock DK, Speer JG. Quenching and partitioning martensite—A novel steel heat treatment. Materials Science and Engineering: A 2006;438–440:25–34. https://doi.org/10.1016/j.msea.2006.02.133.
[41] Seo EJ, Cho L, Estrin Y, De Cooman BC. Microstructure-mechanical properties relationships for quenching and partitioning (Q&P) processed steel. Acta Mater 2016;113:124–39. https://doi.org/10.1016/j.actamat.2016.04.048.

[42] Kumar S. Quenching and partitioning (Q&P) process: A critical review of the competing reactions. Materials Science and Technology 2022;38:663–75. https://doi.org/10.1080/02670836.2022.2062646.
[43] Dong XX, Shen YF, Jia N, Zhu YT. Improving mechanical properties and retained-austenite stability of a medium carbon Q&P steel by adjusting phase ratio. Materials Science and Engineering: A 2022;833:142580. https://doi.org/10.1016/j.msea.2021.142580.
[44] Santofimia MJ, Zhao L, Sietsma J. Microstructural evolution of a low-carbon steel during application of quenching and partitioning heat treatments after partial austenitization. Metallurgical and Materials Transactions A 2009;40:46–57. https://doi.org/10.1007/s11661-008-9701-4.
[45] Speer J, Matlock DK, De Cooman BC, Schroth JG. Carbon partitioning into austenite after martensite transformation. Acta Mater 2003;51:2611–22. https://doi.org/10.1016/S1359-6454(03)00059-4.
[46] Li Y, Chen S, Wang C, Martín DS, Xu W. Modeling retained austenite in Q&P steels accounting for the bainitic transformation and correction of its mismatch on optimal conditions. Acta Mater 2020;188:528–38. https://doi.org/10.1016/j.actamat.2020.02.033.
[47] Toji Y, Miyamoto G, Raabe D. Carbon partitioning during quenching and partitioning heat treatment accompanied by carbide precipitation. Acta Mater 2015;86:137–47. https://doi.org/10.1016/j.actamat.2014.11.049.
[48] Ebner S, Suppan C, Stark A, Schnitzer R, Hofer C. Austenite decomposition and carbon partitioning during quenching and partitioning heat treatments studied via in-situ X-ray diffraction. Mater Des 2019;178:107862. https://doi.org/10.1016/j.matdes.2019.107862.
[49] HajyAkbary F, Sietsma J, Miyamoto G, Furuhara T, Santofimia MJ. Interaction of carbon partitioning, carbide precipitation and bainite formation during the Q&P process in a low C steel. Acta Mater 2016;104:72–83. https://doi.org/10.1016/j.actamat.2015.11.032.
[50] Miettunen I, Ghosh S, Somani MC, Pallaspuro S, Kömi J. Competitive mechanisms occurring during quenching and partitioning of three silicon variants of 0.4 wt.% carbon steels. Journal of Materials Research and Technology 2021;11:1045–60. https://doi.org/10.1016/j.jmrt.2021.01.085.
[51] Carpio M, Calvo J, García O, Pedraza JP, Cabrera JM. Heat Treatment Design for a QP Steel: Effect of Partitioning Temperature. Metals (Basel) 2021;11:1136. https://doi.org/10.3390/met11071136.
[52] Park T, Hector LG, Hu X, Abu-Farha F, Fellinger MR, Kim H, et al. Crystal plasticity modeling of 3rd generation multi-phase AHSS with martensitic transformation. Int J Plast 2019;120:1–46. https://doi.org/10.1016/j.ijplas.2019.03.010.
[53] Kohne T, Fahlkrans J, Stormvinter A, Maawad E, Winkelmann A, Hedström P, et al. Evolution of Martensite Tetragonality in High-Carbon Steels Revealed by In Situ High-Energy X-Ray Diffraction. Metallurgical and Materials Transactions A 2023;54:1083–100. https://doi.org/10.1007/s11661-022-06948-z.

[54] D. Hull, D.J. Bacon. Introduction to Dislocations. Fifth. Elsevier; 2011. https://doi.org/10.1016/C2009-0-64358-0.
[55] Joanna Moneta. Mechanisms of strain relaxation in InGaN films grown on (0001)-oriented GaN substrates. Institute of High Pressure Physics of the Polish Academy of Sciences, 2022.
[56] Du C, Maresca F, Geers MGD, Hoefnagels JPM. Ferrite slip system activation investigated by uniaxial micro-tensile tests and simulations. Acta Mater 2018;146:314–27. https://doi.org/10.1016/j.actamat.2017.12.054.
[57] Chaussidon J, Fivel M, Rodney D. The glide of screw dislocations in bcc Fe: Atomistic static and dynamic simulations☆. Acta Mater 2006;54:3407–16. https://doi.org/10.1016/j.actamat.2006.03.044.
[58] Gröger R, Vitek V. Impact of non-Schmid stress components present in the yield criterion for bcc metals on the activity of {110}<111> slip systems. Comput Mater Sci 2019;159:297–305. https://doi.org/10.1016/j.commatsci.2018.12.021.
[59] Influence of the lattice structure on ductility. Https://WwwTec-ScienceCom/ 2023.
[60] Kraych A, Clouet E, Dezerald L, Ventelon L, Willaime F, Rodney D. Non-glide effects and dislocation core fields in BCC metals. NPJ Comput Mater 2019;5:109. https://doi.org/10.1038/s41524-019-0247-3.
[61] Han Q, Kang Y, Hodgson PD, Stanford N. Quantitative measurement of strain partitioning and slip systems in a dual-phase steel. Scr Mater 2013;69:13–6. https://doi.org/10.1016/j.scriptamat.2013.03.021.
[62] Kestens LAI, Pirgazi H. Texture formation in metal alloys with cubic crystal structures. Materials Science and Technology 2016;32:1303–15. https://doi.org/10.1080/02670836.2016.1231746.
[63] F.J. Humphreys, M. Hatherly. Recrystallization and Related Annealing Phenomena. second. Elsevier; 2004. https://doi.org/10.1016/B978-0-08-044164-1.X5000-2.
[64] Ruer D, Baro R. A New Method for yhe Determination of the Texture of Materials of Cubic Structure From Incomplete Reflection Pole Figures. Advances in X-Ray Analysis 1976;20:187–200. https://doi.org/10.1154/S0376030800011812.
[65] Engler O, Randle V. Introduction to Texture Analysis. CRC Press; 2009. https://doi.org/10.1201/9781420063660.
[66] Hölscher M, Raabe D, Lücke K. Rolling and recrystallization textures of bcc steels. Steel Research 1991;62:567–75. https://doi.org/10.1002/srin.199100451.
[67] Liu W. Microstructure modeling guided design of high-strength steels. RWTH Aachen University, 2022.
[68] Zhang J, Di H, Deng Y, Misra RDK. Effect of martensite morphology and volume fraction on strain hardening and fracture behavior of martensite–ferrite dual phase steel. Materials Science and Engineering: A 2015;627:230–40. https://doi.org/10.1016/j.msea.2015.01.006.
[69] Dastur P, Slater C, Moore T, Davis C. Martensite size and morphology influence on strain distribution and micro-damage evolution in dual-phase steels; comparing segregation-

neutralised and banded grades. Mater Des 2024;246:113340. https://doi.org/10.1016/j.matdes.2024.113340.

[70] Garrison WM, Moody NR. Ductile fracture. Journal of Physics and Chemistry of Solids 1987;48:1035–74. https://doi.org/10.1016/0022-3697(87)90118-1.

[71] Avramovic-Cingara G, Ososkov Y, Jain MK, Wilkinson DS. Effect of martensite distribution on damage behaviour in DP600 dual phase steels. Materials Science and Engineering: A 2009;516:7–16. https://doi.org/10.1016/j.msea.2009.03.055.

[72] He XJ, Terao N, Berghezan A. Influence of martensite morphology and its dispersion on mechanical properties and fracture mechanisms of Fe-Mn-C dual phase steels. Metal Science 2013;18:367–73. https://doi.org/10.1179/030634584790419953.

[73] Maire E, Bouaziz O, Di Michiel M, Verdu C. Initiation and growth of damage in a dual-phase steel observed by X-ray microtomography. Acta Mater 2008;56:4954–64. https://doi.org/10.1016/j.actamat.2008.06.015.

[74] Landron C, Maire E, Bouaziz O, Adrien J, Lecarme L, Bareggi A. Validation of void growth models using X-ray microtomography characterization of damage in dual phase steels. Acta Mater 2011;59:7564–73. https://doi.org/10.1016/j.actamat.2011.08.046.

[75] Chen J, Magdysyuk O V., Li X, Withers PJ, Yan K. Investigation of ductile damage in dual phase steel during tensile deformation by in situ X-ray computed tomography. Eng Fract Mech 2023;293:109711. https://doi.org/10.1016/j.engfracmech.2023.109711.

[76] Benzerga AA, Leblond J-B. Ductile Fracture by Void Growth to Coalescence, 2010, p. 169–305. https://doi.org/10.1016/S0065-2156(10)44003-X.

[77] Pathak N, Butcher C, Worswick M, Bellhouse E, Gao J. Damage Evolution in Complex-Phase and Dual-Phase Steels during Edge Stretching. Materials 2017;10:346. https://doi.org/10.3390/ma10040346.

[78] Toda H, Takijiri A, Azuma M, Yabu S, Hayashi K, Seo D, et al. Damage micromechanisms in dual-phase steel investigated with combined phase- and absorption-contrast tomography. Acta Mater 2017;126:401–12. https://doi.org/10.1016/j.actamat.2017.01.010.

[79] Bao Y, Wierzbicki T. On fracture locus in the equivalent strain and stress triaxiality space. Int J Mech Sci 2004;46:81–98. https://doi.org/10.1016/j.ijmecsci.2004.02.006.

[80] Barsoum I, Faleskog J. Micromechanical analysis on the influence of the Lode parameter on void growth and coalescence. Int J Solids Struct 2011;48:925–38. https://doi.org/10.1016/j.ijsolstr.2010.11.028.

[81] Liu W, Lian J, Münstermann S. Damage mechanism analysis of a high-strength dual-phase steel sheet with optimized fracture samples for various stress states and loading rates. Eng Fail Anal 2019;106:104138. https://doi.org/10.1016/j.engfailanal.2019.08.004.

[82] Lai Q, Bouaziz O, Gouné M, Brassart L, Verdier M, Parry G, et al. Damage and fracture of dual-phase steels: Influence of martensite volume fraction. Materials Science and Engineering: A 2015;646:322–31. https://doi.org/10.1016/j.msea.2015.08.073.

[83] Saeidi N, Ashrafizadeh F, Niroumand B, Forouzan MR, Barlat F. Damage mechanism and modeling of void nucleation process in a ferrite–martensite dual phase steel. Eng Fract Mech 2014;127:97–103. https://doi.org/10.1016/j.engfracmech.2014.05.017.

[84] Narayanasamy R, Parthasarathi NL, Sathiya Narayanan C. Effect of microstructure on void nucleation and coalescence during forming of three different HSLA steel sheets under different stress conditions. Mater Des 2009;30:1310–24. https://doi.org/10.1016/j.matdes.2008.06.043.

[85] Liu L, Maresca F, Hoefnagels JPM, Vermeij T, Geers MGD, Kouznetsova VG. Revisiting the martensite/ferrite interface damage initiation mechanism: The key role of substructure boundary sliding. Acta Mater 2021;205:116533. https://doi.org/10.1016/j.actamat.2020.116533.

[86] de Diego-Calderón I, Sabirov I, Molina-Aldareguia JM, Föjer C, Thiessen R, Petrov RH. Microstructural design in quenched and partitioned (Q&P) steels to improve their fracture properties. Materials Science and Engineering: A 2016;657:136–46. https://doi.org/10.1016/j.msea.2016.01.011.

[87] Wu R, Li J, Li W, Wu X, Jin X, Zhou S, et al. Effect of metastable austenite on fracture resistance of quenched and partitioned (Q&P) sheet steels. Materials Science and Engineering: A 2016;657:57–63. https://doi.org/10.1016/j.msea.2016.01.051.

[88] Hidalgo J, Celada-Casero C, Santofimia MJ. Fracture mechanisms and microstructure in a medium Mn quenching and partitioning steel exhibiting macrosegregation. Materials Science and Engineering: A 2019;754:766–77. https://doi.org/10.1016/j.msea.2019.03.055.

[89] Wang Y, Li A, Hu C, Guo X, Li X, Bi W, et al. Microstructure, Texture, and Anisotropic Properties of High-Strength Low-Alloy Steel. Coatings 2023;13:1442. https://doi.org/10.3390/coatings13081442.

[90] Pan B. Digital image correlation for surface deformation measurement: historical developments, recent advances and future goals. Meas Sci Technol 2018;29:082001. https://doi.org/10.1088/1361-6501/aac55b.

[91] Chu TC, Ranson WF, Sutton MA. Applications of digital-image-correlation techniques to experimental mechanics. Exp Mech 1985;25:232–44. https://doi.org/10.1007/BF02325092.

[92] Rahmaan T, Abedini A, Butcher C, Pathak N, Worswick MJ. Investigation into the shear stress, localization and fracture behaviour of DP600 and AA5182-O sheet metal alloys under elevated strain rates. Int J Impact Eng 2017;108:303–21. https://doi.org/10.1016/j.ijimpeng.2017.04.006.

[93] Wang Y, Gao Y, Liu Y, Gao Z, Su Y, Zhang Q. Optimal Aperture and Digital Speckle Optimization in Digital Image Correlation. Exp Mech 2021;61:677–84. https://doi.org/10.1007/s11340-021-00694-w.

[94] Schreier H, Orteu J-J, Sutton MA. Image Correlation for Shape, Motion and Deformation Measurements. Boston, MA: Springer US; 2009. https://doi.org/10.1007/978-0-387-78747-3.

[95] LaVision. Digital Image Correlation 2025. https://www.lavision.de/en/techniques/dic-dvc/ (accessed June 8, 2025).
[96] Chrysochoos A, Maisonneuve O, Martin G, Caumon H, Chezeaux JC. Plastic and dissipated work and stored energy. Nuclear Engineering and Design 1989;114:323–33. https://doi.org/10.1016/0029-5493(89)90110-6.
[97] Taylor GI, Quinney H. The latent energy remaining in a metal after cold working. Proceedings of the Royal Society of London Series A, Containing Papers of a Mathematical and Physical Character 1997;143:307–26. https://doi.org/10.1098/rspa.1934.0004.
[98] Rosakis P, Rosakis AJ, Ravichandran G, Hodowany J. A thermodynamic internal variable model for the partition of plastic work into heat and stored energy in metals. J Mech Phys Solids 2000;48:581–607. https://doi.org/10.1016/S0022-5096(99)00048-4.
[99] Hodowany J, Ravichandran G, Rosakis AJ, Rosakis P. Partition of plastic work into heat and stored energy in metals. Exp Mech 2000;40:113–23. https://doi.org/10.1007/BF02325036.
[100] Mason JJ, Rosakis AJ, Ravichandran G. On the strain and strain rate dependence of the fraction of plastic work converted to heat: an experimental study using high speed infrared detectors and the Kolsky bar. Mechanics of Materials 1994;17:135–45. https://doi.org/10.1016/0167-6636(94)90054-X.
[101] Soares GC, Vázquez-Fernández NI, Hokka M. Thermomechanical Behavior of Steels in Tension Studied with Synchronized Full-Field Deformation and Temperature Measurements. Exp Tech 2021;45:627–43. https://doi.org/10.1007/s40799-020-00436-y.
[102] Brahme AP, Inal K, Mishra RK, Saimoto S. A new strain hardening model for rate-dependent crystal plasticity. Comput Mater Sci 2011;50:2898–908. https://doi.org/10.1016/j.commatsci.2011.05.006.
[103] Rossiter J, Brahme A, Simha MH, Inal K, Mishra R. A new crystal plasticity scheme for explicit time integration codes to simulate deformation in 3D microstructures: Effects of strain path, strain rate and thermal softening on localized deformation in the aluminum alloy 5754 during simple shear. Int J Plast 2010;26:1702–25. https://doi.org/10.1016/j.ijplas.2010.02.007.
[104] Sachs G. Zur ableitung einer fliessbedingung. Mitteilungen Dtsch Mater 1929:94–7.
[105] Taylor GI, Elam CF. Bakerian Lecture: The distortion of an aluminium crystal during a tensile test. Proceedings of the Royal Society of London Series A, Containing Papers of a Mathematical and Physical Character 1923;102:643–67. https://doi.org/10.1098/rspa.1923.0023.
[106] Kröner E. Zur plastischen verformung des vielkristalls. Acta Metallurgica 1961;9:155–61. https://doi.org/10.1016/0001-6160(61)90060-8.
[107] Hill R. Continuum micro-mechanics of elastoplastic polycrystals. J Mech Phys Solids 1965;13:89–101. https://doi.org/10.1016/0022-5096(65)90023-2.

[108] Hutchinson JW. Elastic-plastic behaviour of polycrystalline metals and composites. Proceedings of the Royal Society of London A Mathematical and Physical Sciences 1970;319:247–72. https://doi.org/10.1098/rspa.1970.0177.
[109] Molinari A, Canova GR, Ahzi S. A self consistent approach of the large deformation polycrystal viscoplasticity. Acta Metallurgica 1987;35:2983–94. https://doi.org/10.1016/0001-6160(87)90297-5.
[110] Lebensohn RA, Tomé CN. A self-consistent anisotropic approach for the simulation of plastic deformation and texture development of polycrystals: Application to zirconium alloys. Acta Metallurgica et Materialia 1993;41:2611–24. https://doi.org/10.1016/0956-7151(93)90130-K.
[111] Wang H, Wu PD, Tomé CN, Huang Y. A finite strain elastic–viscoplastic self-consistent model for polycrystalline materials. J Mech Phys Solids 2010;58:594–612. https://doi.org/10.1016/j.jmps.2010.01.004.
[112] Lebensohn RA, Rollett AD. Spectral methods for full-field micromechanical modelling of polycrystalline materials. Comput Mater Sci 2020;173:109336. https://doi.org/10.1016/j.commatsci.2019.109336.
[113] Li J, Romero I, Segurado J. Development of a thermo-mechanically coupled crystal plasticity modeling framework: Application to polycrystalline homogenization. Int J Plast 2019;119:313–30. https://doi.org/10.1016/j.ijplas.2019.04.008.
[114] Rusinek A, Klepaczko JR. Experiments on heat generated during plastic deformation and stored energy for TRIP steels. Mater Des 2009;30:35–48. https://doi.org/10.1016/j.matdes.2008.04.048.
[115] McClintock FA. Local criteria for ductile fracture. International Journal of Fracture Mechanics 1968;4:101–30. https://doi.org/10.1007/BF00188939.
[116] Johnson GR, Cook WH. Fracture characteristics of three metals subjected to various strains, strain rates, temperatures and pressures. Eng Fract Mech 1985;21:31–48. https://doi.org/10.1016/0013-7944(85)90052-9.
[117] Lou Y, Huh H, Lim S, Pack K. New ductile fracture criterion for prediction of fracture forming limit diagrams of sheet metals. Int J Solids Struct 2012;49:3605–15. https://doi.org/10.1016/j.ijsolstr.2012.02.016.
[118] Lou Y, Huh H. Extension of a shear-controlled ductile fracture model considering the stress triaxiality and the Lode parameter. Int J Solids Struct 2013;50:447–55. https://doi.org/10.1016/j.ijsolstr.2012.10.007.
[119] Lemaitre J. A continuous damage mechanics model for ductile fracture. J Eng Mater Technol 1985;107:83–9. https://doi.org/10.1115/1.3225775.
[120] Tvergaard V. Material Failure by Void Growth to Coalescence, 1989, p. 83–151. https://doi.org/10.1016/S0065-2156(08)70195-9.
[121] Tvergaard V, Needleman A. Analysis of the cup-cone fracture in a round tensile bar. Acta Metallurgica 1984;32:157–69. https://doi.org/10.1016/0001-6160(84)90213-X.

[122] Chu C, Needleman A. Void Nucleation Effects in Biaxially Stretched Sheets. J Eng Mater Technol 1980;102:249–56. https://doi.org/10.1115/1.3224807.
[123] Nahshon K, Hutchinson JW. Modification of the Gurson Model for shear failure. European Journal of Mechanics - A/Solids 2008;27:1–17. https://doi.org/10.1016/j.euromechsol.2007.08.002.
[124] Gologanu M, Leblond J-B, Devaux J. Approximate models for ductile metals containing non-spherical voids—Case of axisymmetric prolate ellipsoidal cavities. J Mech Phys Solids 1993;41:1723–54. https://doi.org/10.1016/0022-5096(93)90029-F.
[125] Pardoen T, Hutchinson JW. An extended model for void growth and coalescence. J Mech Phys Solids 2000;48:2467–512. https://doi.org/10.1016/S0022-5096(00)00019-3.
[126] Pineau A, Benzerga AA, Pardoen T. Failure of metals I: Brittle and ductile fracture. Acta Mater 2016;107:424–83. https://doi.org/10.1016/j.actamat.2015.12.034.
[127] Bammann DJ, Aifantis EC. A damage model for ductile metals. Nuclear Engineering and Design 1989;116:355–62. https://doi.org/10.1016/0029-5493(89)90095-2.
[128] Potirniche GP, Hearndon JL, Horstemeyer MF, Ling XW. Lattice orientation effects on void growth and coalescence in fcc single crystals. Int J Plast 2006;22:921–42. https://doi.org/10.1016/j.ijplas.2005.06.003.
[129] Yerra SK, Tekog˘lu C, Scheyvaerts F, Delannay L, Van Houtte P, Pardoen T. Void growth and coalescence in single crystals. Int J Solids Struct 2010;47:1016–29. https://doi.org/10.1016/j.ijsolstr.2009.12.019.
[130] Ha S, Kim K. Void growth and coalescence in f.c.c. single crystals. Int J Mech Sci 2010;52:863–73. https://doi.org/10.1016/j.ijmecsci.2010.03.001.
[131] Fehlemann NC, Biermann I, Münstermann S. Exploring structure–property relations in dual phase steels using crystal plasticity and variance based global sensitivity analysis. Mater Des 2025;259:114794. https://doi.org/10.1016/j.matdes.2025.114794.
[132] Ma A, Hartmaier A. A study of deformation and phase transformation coupling for TRIP-assisted steels. Int J Plast 2015;64:40–55. https://doi.org/10.1016/j.ijplas.2014.07.008.
[133] Hu XH, Sun X, Hector LG, Ren Y. Individual phase constitutive properties of a TRIP-assisted QP980 steel from a combined synchrotron X-ray diffraction and crystal plasticity approach. Acta Mater 2017;132:230–44. https://doi.org/10.1016/j.actamat.2017.04.028.
[134] Cheng J, Lin BK, Pottore NS, Sadagopan S, Zhu H, Hu X. A mesoscale crystal plasticity model to predict room-temperature deformation and martensitic transformation of high-strength Quenching and Partitioning (Q&P) Steels and validation with synchrotron X-ray diffraction. Int J Plast 2024;172:103833. https://doi.org/10.1016/j.ijplas.2023.103833.
[135] Tvergaard V. On localization in ductile materials containing spherical voids. Int J Fract 1982;18:237–52. https://doi.org/10.1007/BF00015686.
[136] Liu W, Li X, Liu M, Cui H, Huang J, Pang Y, et al. Virtual laboratory enabled constitutive modelling of dual phase steels. Int J Plast 2024;175:103930. https://doi.org/10.1016/j.ijplas.2024.103930.

[137] Needleman A. A Continuum Model for Void Nucleation by Inclusion Debonding. J Appl Mech 1987;54:525–31. https://doi.org/10.1115/1.3173064.
[138] Horstemeyer MF, Gokhale AM. A void–crack nucleation model for ductile metals. Int J Solids Struct 1999;36:5029–55. https://doi.org/10.1016/S0020-7683(98)00239-X.
[139] Seaman L, Curran DR, Shockey DA. Computational models for ductile and brittle fracture. J Appl Phys 2008;47:4814–26. https://doi.org/10.1063/1.322523.
[140] Tvergaard V. Ductile fracture by cavity nucleation between larger voids. J Mech Phys Solids 1982;30:265–86. https://doi.org/10.1016/0022-5096(82)90033-3.
[141] Cocks ACF, Ashby MF. Intergranular fracture during power-law creep under multiaxial stresses. Metal Science 1980;14:395–402. https://doi.org/10.1179/030634580790441187.
[142] Horstemeyer MF, Ramaswamy S. On Factors Affecting Localization and Void Growth in Ductile Metals: A Parametric Study. International Journal of Damage Mechanics 2000;9:5–28. https://doi.org/10.1177/105678950000900102.
[143] Pathak N, Adrien J, Butcher C, Maire E, Worswick M. Experimental stress state-dependent void nucleation behavior for advanced high strength steels. Int J Mech Sci 2020;179:105661. https://doi.org/10.1016/j.ijmecsci.2020.105661.
[144] Guo Y, Paramatmuni C, Avcu E. Void Nucleation and Growth from Heterophases and the Exploitation of New Toughening Mechanisms in Metals. Crystals (Basel) 2023;13:860. https://doi.org/10.3390/cryst13060860.
[145] Yang X, Zeng X, Wang J, Wang J, Wang F, Ding J. Atomic-scale modeling of the void nucleation, growth, and coalescence in Al at high strain rates. Mechanics of Materials 2019;135:98–113. https://doi.org/10.1016/j.mechmat.2019.05.005.
[146] Rawat S, Raole PM. Molecular dynamics investigation of void evolution dynamics in single crystal iron at extreme strain rates. Comput Mater Sci 2018;154:393–404. https://doi.org/10.1016/j.commatsci.2018.08.010.
[147] Guery A, Hild F, Latourte F, Roux S. Slip activities in polycrystals determined by coupling DIC measurements with crystal plasticity calculations. Int J Plast 2016;81:249–66. https://doi.org/10.1016/j.ijplas.2016.01.008.
[148] Yalçinkaya T, Güngör GÖ, Çakmak SO, Tekoğlu C. A Micromechanics Based Numerical Investigation of Dual Phase Steels. Procedia Structural Integrity 2019;21:61–72. https://doi.org/10.1016/j.prostr.2019.12.087.
[149] Connolly DS, Kohar CP, Muhammad W, Hector LG, Mishra RK, Inal K. A coupled thermomechanical crystal plasticity model applied to Quenched and Partitioned steel. Int J Plast 2020;133:102757. https://doi.org/10.1016/j.ijplas.2020.102757.
[150] Joudivand Sarand MH, Misirlioglu IB. A physics-based plasticity study of the mechanism of inhomogeneous strain evolution in dual phase 600 steel. Int J Plast 2024;174:103918. https://doi.org/10.1016/j.ijplas.2024.103918.
[151] Abed FH, Al-Tamimi AK, Al-Himairee RM. Characterization and Modeling of Ductile Damage in Structural Steel at Low and Intermediate Strain Rates. J Eng Mech 2012;138:1186–94. https://doi.org/10.1061/(ASCE)EM.1943-7889.0000415.

[152] Hu P, Liu Y, Zhu Y, Ying L. Crystal plasticity extended models based on thermal mechanism and damage functions: Application to multiscale modeling of aluminum alloy tensile behavior. Int J Plast 2016;86:1–25. https://doi.org/10.1016/j.ijplas.2016.07.001.
[153] Shang X, Zhang H, Cui Z, Fu MW, Shao J. A multiscale investigation into the effect of grain size on void evolution and ductile fracture: Experiments and crystal plasticity modeling. Int J Plast 2020;125:133–49. https://doi.org/10.1016/j.ijplas.2019.09.009.
[154] Meade ED, Sun F, Tiernan P, O'Dowd NP. A multiscale experimentally-based finite element model to predict microstructure and damage evolution in martensitic steels. Int J Plast 2021;139:102966. https://doi.org/10.1016/j.ijplas.2021.102966.
[155] Frodal BH, Thomesen S, Børvik T, Hopperstad OS. On the coupling of damage and single crystal plasticity for ductile polycrystalline materials. Int J Plast 2021;142:102996. https://doi.org/10.1016/j.ijplas.2021.102996.
[156] Liu J, Huang M, Li Z, Zhao L, Zhu Y. Microvoid growth mechanism in FCC polycrystals and a statistical damage model. Int J Plast 2021;137:102888. https://doi.org/10.1016/j.ijplas.2020.102888.
[157] Zhu J, Liu J, Huang M, Li Z, Zhao L. Investigation on intragranular and intergranular void growth and their competition in polycrystalline materials. Int J Plast 2022;159:103472. https://doi.org/10.1016/j.ijplas.2022.103472.
[158] Salvini M, Grilli N, Demir E, He S, Martin T, Flewitt P, et al. Effect of grain boundary misorientation and carbide precipitation on damage initiation: A coupled crystal plasticity and phase field damage study. Int J Plast 2024;172:103854. https://doi.org/10.1016/j.ijplas.2023.103854.
[159] Nabil Bassim M, Panic N. High strain rate effects on the strain of alloy steels. J Mater Process Technol 1999;92–93:481–5. https://doi.org/10.1016/S0924-0136(99)00248-4.
[160] Lin M-R, Wagoner RH. An experimental investigation of deformationinduced heating during tensile testing. Metallurgical Transactions A 1987;18:1035–42. https://doi.org/10.1007/BF02668552.
[161] Gao Y, Wagoner RH. A simplified model of heat generation during the uniaxial tensile test. Metallurgical Transactions A 1987;18:1001–9. https://doi.org/10.1007/BF02668548.
[162] Farren WS, Taylor GI. The heat developed during plastic extension of metals. Proceedings of the Royal Society of London Series A, Containing Papers of a Mathematical and Physical Character 1997;107:422–51. https://doi.org/10.1098/rspa.1925.0034.
[163] Andrade-Campos A, Teixeira-Dias F, Krupp U, Barlat F, Rauch EF, Grácio JJ. Effect of Strain Rate, Adiabatic Heating and Phase Transformation Phenomena on the Mechanical Behaviour of Stainless Steel. Strain 2010;46:283–97. https://doi.org/10.1111/j.1475-1305.2008.00572.x.
[164] Dumoulin S, Louche H, Hopperstad OS, Børvik T. Heat sources, energy storage and dissipation in high-strength steels: Experiments and modelling. European Journal of Mechanics - A/Solids 2010;29:461–74. https://doi.org/10.1016/j.euromechsol.2009.11.005.

[165] Sung JH, Kim JH, Wagoner RH. A plastic constitutive equation incorporating strain, strain-rate, and temperature. Int J Plast 2010;26:1746–71. https://doi.org/10.1016/j.ijplas.2010.02.005.
[166] Mareau C, Cuillerier D, Morel F. Experimental and numerical study of the evolution of stored and dissipated energies in a medium carbon steel under cyclic loading. Mechanics of Materials 2013;60:93–106. https://doi.org/10.1016/j.mechmat.2013.01.011.
[167] Subhash G, Pletka BJ, Ravichandran G. Plastic deformation of hafnium under uniaxial compression. Metallurgical and Materials Transactions A 1997;28:1479–87. https://doi.org/10.1007/s11661-997-0210-7.
[168] Galiev E, Winter S, Reuther F, Psyk V, Tulke M, Brosius A, et al. Local temperature development in the fracture zone during uniaxial tensile testing at high strain rate: Experimental and numerical investigations. Applied Sciences 2022;12. https://doi.org/10.3390/app12052299.
[169] Khan AS, Liu H. Variable strain rate sensitivity in an aluminum alloy: Response and constitutive modeling. Int J Plast 2012;36:1–14. https://doi.org/10.1016/j.ijplas.2012.02.001.
[170] Sung JH, Kim JH, Wagoner RH. A plastic constitutive equation incorporating strain, strain-rate, and temperature. Int J Plast 2010;26:1746–71. https://doi.org/10.1016/j.ijplas.2010.02.005.
[171] Geng H, Sun X, Guo X, Zhao Y, Yin X, Du Z. Achieving 1.7 GPa Considerable Ductility High-Strength Low-Alloy Steel Using Hot-Rolling and Tempering Processes. Materials 2024;17:4495. https://doi.org/10.3390/ma17184495.
[172] Dolzhenko A, Pydrin A, Gaidar S, Kaibyshev R, Belyakov A. Microstructure and Strengthening Mechanisms in an HSLA Steel Subjected to Tempforming. Metals (Basel) 2021;12:48. https://doi.org/10.3390/met12010048.
[173] Yadav SD, Vijayanand VD, Nandgopal M, Prasad Reddy G V. On the tensile flow stress response of 304 HCu stainless steel employing a dislocation density based model and electron backscatter diffraction measurements. Philosophical Magazine 2020;100:312–36. https://doi.org/10.1080/14786435.2019.1680887.
[174] Zhu J, Barber G, Sun X. Effects of Isothermal Temperature on Dislocation Density in Bainite Transformation of 4140 Steel. Materials 2022;15:6066. https://doi.org/10.3390/ma15176066.
[175] Cortese L, Nalli F, Rossi M. A nonlinear model for ductile damage accumulation under multiaxial non-proportional loading conditions. Int J Plast 2016;85:77–92. https://doi.org/10.1016/j.ijplas.2016.07.003.
[176] Wu H, Zhang Y, Zou T, Wang Q, Zhang H, Wang T, et al. Crystal plasticity analysis of tensile plastic behavior and damage mechanisms of additive manufactured TiAl alloy under elevated temperatures. Journal of Materials Research and Technology 2024;32:2188–99. https://doi.org/10.1016/j.jmrt.2024.08.047.

[177] Li A, Hu W, Li H, Zhan Z, Meng Q. A crystal plasticity-based microdamage model and its application on the tensile failure process analysis of 7075 aluminum alloy. Materials Science and Engineering: A 2023;884:145541. https://doi.org/10.1016/j.msea.2023.145541.
[178] Aydiner IU, Tatli B, Yalçinkaya T. Investigation of failure mechanisms in dual-phase steels through cohesive zone modeling and crystal plasticity frameworks. Int J Plast 2024;174:103898. https://doi.org/10.1016/j.ijplas.2024.103898.
[179] Finfrock CB, Thrun MM, Bhattacharya D, Ballard TJ, Clarke AJ, Clarke KD. Strain Rate Dependent Ductility and Strain Hardening in Q&P Steels. Metallurgical and Materials Transactions A 2021;52:928–42. https://doi.org/10.1007/s11661-020-06127-y.
[180] Bardelcik A. High Strain Rate Behaviour of Hot Formed Boron Steel with Tailored Properties. University of Waterloo, 2013.
[181] Smerd R, Winkler S, Salisbury C, Worswick M, Lloyd D, Finn M. High strain rate tensile testing of automotive aluminum alloy sheet. Int J Impact Eng 2005;32:541–60. https://doi.org/10.1016/j.ijimpeng.2005.04.013.
[182] Anya CC, Baker TN. The effect of silicon on the grain size and the tensile properties of low carbon steels. Materials Science and Engineering: A 1989;118:197–206. https://doi.org/10.1016/0921-5093(89)90071-3.
[183] Furmanski J, Cady CM, Brown EN. Time–temperature equivalence and adiabatic heating at large strains in high density polyethylene and ultrahigh molecular weight polyethylene. Polymer (Guildf) 2013;54:381–90. https://doi.org/10.1016/j.polymer.2012.11.010.
[184] Gao Y, Wagoner RH. A simplified model of heat generation during the uniaxial tensile test. Metallurgical Transactions A 1991;18:1001–9. https://doi.org/10.1007/BF03325709.
[185] Stevens AL, Davison L, Warren WE. Spall fracture in aluminum monocrystals: a dislocation-dynamics approach. J Appl Phys 2003;43:4922–7. https://doi.org/10.1063/1.1661046.
[186] Horstemeyer MF, Lathrop J, Gokhale AM, Dighe M. Modeling stress state dependent damage evolution in a cast Al–Si–Mg aluminum alloy. Theoretical and Applied Fracture Mechanics 2000;33:31–47. https://doi.org/10.1016/S0167-8442(99)00049-X.
[187] Turteltaub S, Suiker ASJ. A multiscale thermomechanical model for cubic to tetragonal martensitic phase transformations. Int J Solids Struct 2006;43:4509–45. https://doi.org/10.1016/j.ijsolstr.2005.06.065.
[188] Coleman BD, Noll W. The thermodynamics of elastic materials with heat conduction and viscosity. Arch Ration Mech Anal 1963;13:167–78. https://doi.org/10.1007/BF01262690.
[189] Lemaitre J. A Course on Damage Mechanics. 2nd ed. Springer/Sci-Tech/Trade; 1996.
[190] Kitayama K, Tomé CN, Rauch EF, Gracio JJ, Barlat F. A crystallographic dislocation model for describing hardening of polycrystals during strain path changes. Application to low carbon steels. Int J Plast 2013;46:54–69. https://doi.org/10.1016/j.ijplas.2012.09.004.
[191] Gurland J, Plateau J. The mechanism of ductile rupture of metals containing inclusions. 1963.

[192] Rosenfield AR. Criteria for ductile fracture of two-phase alloys. Metallurgical Reviews 1968;13:29–40. https://doi.org/10.1179/mtlr.1968.13.1.29.
[193] Argon AS, Im J, Safoglu R. Cavity formation from inclusions in ductile fracture. Metallurgical Transactions A 1975;6:825–37. https://doi.org/10.1007/BF02672306.
[194] Chandler MQ, Bammann DJ, Horstemeyer MF. A continuum model for hydrogen-assisted void nucleation in ductile materials. Model Simul Mat Sci Eng 2013;21:055028. https://doi.org/10.1088/0965-0393/21/5/055028.
[195] Dighe MD, Gokhale AM, Horstemeyer MF. Effect of loading condition and stress state on damage evolution of silicon particles in an Al-Si-Mg-Base cast alloy. Metallurgical and Materials Transactions A 2002;33:555–65. https://doi.org/10.1007/s11661-002-0117-2.
[196] Peirce D, Shih CF, Needleman A. A tangent modulus method for rate dependent solids. Comput Struct 1984;18:875–87. https://doi.org/10.1016/0045-7949(84)90033-6.
[197] Peirce D, Asaro RJ, Needleman A. An analysis of nonuniform and localized deformation in ductile single crystals. Acta Metallurgica 1982;30:1087–119. https://doi.org/10.1016/0001-6160(82)90005-0.
[198] Uenishi A, Teodosiu C, Nesterova EV. Microstructural evolution at high strain rates in solution-hardened interstitial free steels. Materials Science and Engineering: A 2005;400–401:499–503. https://doi.org/10.1016/j.msea.2005.02.066.
[199] Galindo-Nava EI, Sietsma J, Rivera-Díaz-del-Castillo PEJ. Dislocation annihilation in plastic deformation: II. Kocks–Mecking Analysis. Acta Mater 2012;60:2615–24. https://doi.org/10.1016/j.actamat.2012.01.028.
[200] Sadeghi A, Kozeschnik E. Modeling the Evolution of the Dislocation Density and Yield Stress of Al over a Wide Range of Temperatures and Strain Rates. Metallurgical and Materials Transactions A 2024;55:1643–53. https://doi.org/10.1007/s11661-024-07358-z.
[201] Semple JK, Bechetti DH, Zhang W, Fisher CR. Temperature-Dependent Material Property Databases for Marine Steels—Part 3: HSLA-80. Integr Mater Manuf Innov 2022;11:648–74. https://doi.org/10.1007/s40192-022-00288-x.
[202] Park M, Fujimura Y, Shibata A, Tsuji N. Effect of martensite hardness on mechanical properties and stress/strain-partitioning behavior in ferrite + martensite dual-phase steels. Materials Science and Engineering: A 2024;916:147301. https://doi.org/10.1016/j.msea.2024.147301.
[203] Gao B, Liu Y, Chen X, Sui Y, Sun W, Xiao L, et al. Heterogeneous plastic deformation and HDI strengthening of the heterostructured dual-phase steels investigated by in-situ SEM-DIC. Materials Science and Engineering: A 2024;893:146149. https://doi.org/10.1016/j.msea.2024.146149.
[204] Zhang Z, Wang N, Li J, Chen Y, Wu G, Chen X, et al. Investigation on strain localization and hardening of dual-phase steel by hetero-deformation induced stress. Journal of Materials Research and Technology 2023;25:1832–43. https://doi.org/10.1016/j.jmrt.2023.06.057.

[205] Tang A, Liu H, Chen R, Liu G, Lai Q, Zhong Y, et al. Mesoscopic origin of damage nucleation in dual-phase steels. Int J Plast 2021;137:102920. https://doi.org/10.1016/j.ijplas.2020.102920.
[206] Jafari M, Ziaei-Rad S, Saeidi N, Jamshidian M. Micromechanical analysis of martensite distribution on strain localization in dual phase steels by scanning electron microscopy and crystal plasticity simulation. Materials Science and Engineering: A 2016;670:57–67. https://doi.org/10.1016/j.msea.2016.05.094.
[207] Niehüser A, Mosler J. Microscale modeling of damage mechanisms in dual-phase steel DP800. PAMM 2024;24. https://doi.org/10.1002/pamm.202400012.
[208] Park K, Nishiyama M, Nakada N, Tsuchiyama T, Takaki S. Effect of the martensite distribution on the strain hardening and ductile fracture behaviors in dual-phase steel. Materials Science and Engineering: A 2014;604:135–41. https://doi.org/10.1016/j.msea.2014.02.058.
[209] Saeidi N, Ashrafizadeh F, Niroumand B. Development of a new ultrafine grained dual phase steel and examination of the effect of grain size on tensile deformation behavior. Materials Science and Engineering: A 2014;599:145–9. https://doi.org/10.1016/j.msea.2014.01.053.
[210] Calcagnotto M, Ponge D, Demir E, Raabe D. Orientation gradients and geometrically necessary dislocations in ultrafine grained dual-phase steels studied by 2D and 3D EBSD. Materials Science and Engineering: A 2010;527:2738–46. https://doi.org/10.1016/j.msea.2010.01.004.
[211] Ramazani A, Schwedt A, Aretz A, Prahl U, Bleck W. Characterization and modelling of failure initiation in DP steel. Comput Mater Sci 2013;75:35–44. https://doi.org/10.1016/j.commatsci.2013.04.001.
[212] Ghadbeigi H, Pinna C, Celotto S. Failure mechanisms in DP600 steel: Initiation, evolution and fracture. Materials Science and Engineering: A 2013;588:420–31. https://doi.org/10.1016/j.msea.2013.09.048.
[213] Kadkhodapour J, Butz A, Ziaei Rad S. Mechanisms of void formation during tensile testing in a commercial, dual-phase steel. Acta Mater 2011;59:2575–88. https://doi.org/10.1016/j.actamat.2010.12.039.
[214] Ramazani A, Kazemiabnavi S, Larson R. Quantification of ferrite-martensite interface in dual phase steels: A first-principles study. Acta Mater 2016;116:231–7. https://doi.org/10.1016/j.actamat.2016.06.047.
[215] Alsharif A, Moinuddin SQ, Dowding R, Pinna C. In-Situ microstructure characterization and micromechanical modelling of damage initiation and propagation in DP1000 dual phase steel. Mater Des 2025;258:114684. https://doi.org/10.1016/j.matdes.2025.114684.
[216] Kadkhodapour J, Schmauder S, Raabe D, Ziaei-Rad S, Weber U, Calcagnotto M. Experimental and numerical study on geometrically necessary dislocations and non-homogeneous mechanical properties of the ferrite phase in dual phase steels. Acta Mater 2011;59:4387–94. https://doi.org/10.1016/j.actamat.2011.03.062.

[217] Matsuno T, Yoshioka T, Watanabe I, Alves L. Three-dimensional finite element analysis of representative volume elements for characterizing the effects of martensite elongation and banding on tensile strength of ferrite-martensite dual-phase steels. Int J Mech Sci 2019;163:105133. https://doi.org/10.1016/j.ijmecsci.2019.105133.
[218] Gu GH, Kwon J, Moon J, Kwon H, Lee J, Kim Y, et al. Determination of damage model parameters using nano- and bulk-scale digital image correlation and the finite element method. Journal of Materials Research and Technology 2022;17:392–403. https://doi.org/10.1016/j.jmrt.2022.01.012.
[219] Pan B, Zhu L, Shen F, Münstermann S. Dual-scale investigation of temperature-dependent plasticity and damage of DP780. Int J Mech Sci 2025;302:110565. https://doi.org/10.1016/j.ijmecsci.2025.110565.
[220] Liu L, Maresca F, Vermeij T, Hoefnagels JPM, Geers MGD, Kouznetsova VG. An integrated experimental-numerical study of martensite/ferrite interface damage initiation in dual-phase steels. Scr Mater 2024;239:115798. https://doi.org/10.1016/j.scriptamat.2023.115798.
[221] Ayatollahi MR, Darabi ACh, Chamani HR, Kadkhodapour J. 3D Micromechanical Modeling of Failure and Damage Evolution in Dual Phase Steel Based on a Real 2D Microstructure. Acta Mechanica Solida Sinica 2016;29:95–110. https://doi.org/10.1016/S0894-9166(16)60009-5.
[222] West O, Lian J, Münstermann S, Bleck W. Numerical Determination of the Damage Parameters of a Dual-phase Sheet Steel. ISIJ International 2012;52:743–52. https://doi.org/10.2355/isijinternational.52.743.
[223] Al-Abbasi FM, Nemes JA. Micromechanical modeling of dual phase steels. Int J Mech Sci 2003;45:1449–65. https://doi.org/10.1016/j.ijmecsci.2003.10.007.
[224] Xue L. Damage accumulation and fracture initiation in uncracked ductile solids subject to triaxial loading. Int J Solids Struct 2007;44:5163–81. https://doi.org/10.1016/j.ijsolstr.2006.12.026.
[225] Zhou J, Gao X, Sobotka JC, Webler BA, Cockeram B V. On the extension of the Gurson-type porous plasticity models for prediction of ductile fracture under shear-dominated conditions. Int J Solids Struct 2014;51:3273–91. https://doi.org/10.1016/j.ijsolstr.2014.05.028.
[226] Park K, Paulino GH, Roesler JR. A unified potential-based cohesive model of mixed-mode fracture. J Mech Phys Solids 2009;57:891–908. https://doi.org/10.1016/j.jmps.2008.10.003.
[227] Tandogan IT, Yalcinkaya T. Development and implementation of a micromechanically motivated cohesive zone model for ductile fracture. Int J Plast 2022;158:103427. https://doi.org/10.1016/j.ijplas.2022.103427.
[228] Hosseini-Toudeshky H, Parandavar P, Anbarlooie B. Stress–strain prediction of dual phase steels using 3D RVEs considering both interphase hardness variation and interface debonding at grain boundaries. Archive of Applied Mechanics 2022;92:255–70. https://doi.org/10.1007/s00419-021-02054-5.

[229] Hosseini-Toudeshky H, Jamalian M. Simulation of micromechanical damage to obtain mechanical properties of bimodal Al using XFEM. Mechanics of Materials 2015;89:229–40. https://doi.org/10.1016/j.mechmat.2015.06.015.
[230] Vajragupta N, Uthaisangsuk V, Schmaling B, Münstermann S, Hartmaier A, Bleck W. A micromechanical damage simulation of dual phase steels using XFEM. Comput Mater Sci 2012;54:271–9. https://doi.org/10.1016/j.commatsci.2011.10.035.
[231] Wen L-F, Tian R, Wang L-X, Feng C. Improved XFEM for multiple crack analysis: Accurate and efficient implementations for stress intensity factors. Comput Methods Appl Mech Eng 2023;411:116045. https://doi.org/10.1016/j.cma.2023.116045.
[232] Linke M, Lammering R. On the calibration of the cohesive strength for cohesive zone models in finite element analyses. Theoretical and Applied Fracture Mechanics 2023;124:103733. https://doi.org/10.1016/j.tafmec.2022.103733.
[233] Foulk JW. An examination of stability in cohesive zone modeling. Comput Methods Appl Mech Eng 2010;199:465–70. https://doi.org/10.1016/j.cma.2009.08.025.
[234] Ahmadikia B, Shadle D, Stinville J-C, Nygren KE, Kumar MA, Pollock TM, et al. Role of microstructure on the development of local orientation gradients in polycrystals. Journal of Materials Research and Technology 2024;33:168–79. https://doi.org/10.1016/j.jmrt.2024.08.195.
[235] Aragon NK, Rezwan AA, de Oca Zapiain DM, Lim H. Investigating the orientation dependence of local fields around spherical defects using crystal plasticity simulations. Journal of Materials Research and Technology 2024;33:235–43. https://doi.org/10.1016/j.jmrt.2024.09.029.
[236] Boubaker HB, Mareau C, Ayed Y, Germain G, Tidu A. A crystal plasticity-based constitutive model for near- β titanium alloys under extreme loading conditions: Application to the Ti17 alloy. Mechanics of Materials 2022;166:104198. https://doi.org/10.1016/j.mechmat.2021.104198.
[237] Cheng Z, Zhang C, Meng Z, Wang K, Chen L, Ji Z, et al. Coupled crystal plasticity and micromechanics damage model based on viscoplastic self-consistent theory and X-ray computed tomography. Int J Plast 2023;160:103511. https://doi.org/10.1016/j.ijplas.2022.103511.
[238] Sedighiani K, Traka K, Roters F, Sietsma J, Raabe D, Diehl M. Crystal plasticity simulation of in-grain microstructural evolution during large deformation of IF-steel. Acta Mater 2022;237:118167. https://doi.org/10.1016/j.actamat.2022.118167.
[239] Li Q, Zhang H, Chen F, Xu D, Sui D, Cui Z. Study on the plastic anisotropy of advanced high strength steel sheet: Experiments and microstructure-based crystal plasticity modeling. Int J Mech Sci 2020;176:105569. https://doi.org/10.1016/j.ijmecsci.2020.105569.
[240] Woo W, Em VT, Kim E-Y, Han SH, Han YS, Choi S-H. Stress–strain relationship between ferrite and martensite in a dual-phase steel studied by in situ neutron diffraction and crystal plasticity theories. Acta Mater 2012;60:6972–81. https://doi.org/10.1016/j.actamat.2012.08.054.

[241] Tran MT, Nguyen XM, Kim H, Chae H, Woo W, Lee HW, et al. Correlation between individual phase constitutive properties and plastic heterogeneities in advanced-high strength dual-phase steels. Mater Charact 2024;217:114356. https://doi.org/10.1016/j.matchar.2024.114356.
[242] Dou W, Xu Z, Han Y, Huang F. A ductile fracture model incorporating stress state effect. Int J Mech Sci 2023;241:107965. https://doi.org/10.1016/j.ijmecsci.2022.107965.
[243] Xue L, Wierzbicki T. Ductile fracture initiation and propagation modeling using damage plasticity theory. Eng Fract Mech 2008;75:3276–93. https://doi.org/10.1016/j.engfracmech.2007.08.012.
[244] Tsuchida N, Izaki Y, Tanaka T, Fukaura K. Effects of temperature and strain rate on stress-strain curves for dual-phase steels and their calculations by using the Kocks-Mecking model. ISIJ International 2012;52:729–34. https://doi.org/10.2355/isijinternational.52.729.
[245] Gao Y, Xu C, He Z, He Y, Li L. Response characteristics and adiabatic heating during high strain rate for TRIP steel and DP steel. Journal of Iron and Steel Research International 2015;22:48–54. https://doi.org/10.1016/S1006-706X(15)60008-5.
[246] Ramalingam K, Motaman SAH, Haase C, Krupp U. Thermo-micro-mechanical modeling of plasticity and damage in single-phase S700 steel. Int J Mech Sci 2025;286:109909. https://doi.org/10.1016/j.ijmecsci.2024.109909.
[247] Thompson A. High Strain Rate Characterization of Advanced High Strength Steels. University of waterloo, 2006.
[248] Cantara AM, Zecevic M, Eghtesad A, Poulin CM, Knezevic M. Predicting elastic anisotropy of dual-phase steels based on crystal mechanics and microstructure. Int J Mech Sci 2019;151:639–49. https://doi.org/10.1016/j.ijmecsci.2018.12.021.
[249] Ashrafi H, Aghili SE. Study on the Micro-Texture and Anisotropy of a Cold-Rolled and Intercritically Annealed DP800 Steel. Physics of Metals and Metallography 2023;124:1426–32. https://doi.org/10.1134/S0031918X22601081.
[250] Unnikrishnan R, Kumar A, Khatirkar RK, Shekhawat SK, Sapate SG. Structural developments in un-stabilized ultra low carbon steel during warm deformation and annealing. Mater Chem Phys 2016;183:339–48. https://doi.org/10.1016/j.matchemphys.2016.08.037.
[251] Zou X, Liu Q, Qiu S. A study on the formation of fiber texture in the subsurface layer of hot-rolled plate of 3.2%Si grain-oriented steel. Metals (Basel) 2023;13:1597. https://doi.org/10.3390/met13091597.
[252] Oh G-J, Lee K-M, Huh M-Y, Park JE, Park SH, Engler O. Effect of r-value and texture on plastic deformation and necking behavior in interstitial-free steel sheets. Metals and Materials International 2017;23:26–34. https://doi.org/10.1007/s12540-017-6375-8.
[253] Xie CL, Nakamachi E. Investigations of the formability of BCC steel sheets by using crystalline plasticity finite element analysis. Mater Des 2002;23:59–68. https://doi.org/10.1016/S0261-3069(01)00043-7.

[254] Liu W, Lian J, Aravas N, Münstermann S. A strategy for synthetic microstructure generation and crystal plasticity parameter calibration of fine-grain-structured dual-phase steel. Int J Plast 2020;126:102614. https://doi.org/10.1016/j.ijplas.2019.10.002.
[255] Liu W, Lian J. Microstructure Effects on the Plastic Anisotropy of a Fine-Structured Dual-Phase Steel. Procedia Manuf 2020;47:1552–60. https://doi.org/10.1016/j.promfg.2020.04.349.
[256] Jung J, Lee H, Cho W, Jeong B-S, Ko YS, Kim S-I, et al. Sequential dual-scale approach for microstructure-informed ductile fracture prediction. Int J Mech Sci 2024;284:109719. https://doi.org/10.1016/j.ijmecsci.2024.109719.
[257] Dayani S, Muhammad W, Brahme A, Hekmat F, Sabiston T, Inal K. Thermodynamically consistent damage evolution model coupled with rate-dependent crystal plasticity: Application to high-strength low alloy steel at various strain rates. Int J Plast 2025;186:104255. https://doi.org/10.1016/j.ijplas.2025.104255.
[258] Huang Y. Accurate Dilatation Rates for Spherical Voids in Triaxial Stress Fields. J Appl Mech 1991;58:1084–6. https://doi.org/10.1115/1.2897686.
[259] Søvik OP. Experimental and Numerical Investigation of Void Nucleation in an AlMgSi Alloy. Le Journal de Physique IV 1996;06:C6-155-C6-164. https://doi.org/10.1051/jp4:1996615.
[260] Zhuang X, Xu C, Zhao Z. Experimental and numerical investigation of failure mode in geometrically imperfect DP590 steel. Sci China Technol Sci 2015;58:476–84. https://doi.org/10.1007/s11431-015-5772-9.
[261] Wang W, Qi H, Da Z, Li W, Wan Y, Guo C, et al. Evolution of Microstructure and Mechanical Properties of DP590 Structural Steel of Vehicle in Heat-Treatment Post-Fire Simulation. J Mater Eng Perform 2025;34:4081–92. https://doi.org/10.1007/s11665-024-09376-9.
[262] Li S, Zhang L, Zhao H, Qi L, Kang Y. Mechanical behavior of DP780 dual phase steel at a wide range of strain rates. Mater Res Express 2018;5:096519. https://doi.org/10.1088/2053-1591/aad7ea.
[263] Karantza KD, Manolakos DE. Numerical Study on the Development of Adiabatic Shear Bands During High Strain-Rate Compression of AISI 1045 Steel: A Comparative Analysis Between Plane-Strain and Axisymmetric Problems. Materials 2024;17:5286. https://doi.org/10.3390/ma17215286.
[264] Kamarulzaman MF, Mohd Nor MK, Abdul Samad MS. Microstructural analysis of strain rate dependence for commercial dual phase steel DP590 undergoing finite strain deformation. International Journal of Integrated Engineering 2021;13:226–34.
[265] Benzerga AA, Leblond J-B, Needleman A, Tvergaard V. Ductile failure modeling. Int J Fract 2016;201:29–80. https://doi.org/10.1007/s10704-016-0142-6.
[266] Nakamachi E, Xie CL, Harimoto M. Drawability assessment of BCC steel sheet by using elastic/crystalline viscoplastic finite element analyses. Int J Mech Sci 2001;43:631–52. https://doi.org/10.1016/S0020-7403(00)00048-5.

[267] Kumar S, Singh SB. Microstructure-property relationship in the quenching and partitioning (Q&P) steel. Mater Charact 2023;196:112561. https://doi.org/10.1016/j.matchar.2022.112561.
[268] Pereira R, Peixinho N, Costa SL. A Review of Sheet Metal Forming Evaluation of Advanced High-Strength Steels (AHSS). Metals (Basel) 2024;14:394. https://doi.org/10.3390/met14040394.
[269] Butuc MC, Vincze G, Santos R, Pereira A, Santos AD, Amaral RL, et al. Formability of third generation advanced high strength steel: experimental and theoretical approach. Int J Mech Sci 2024;281:109559. https://doi.org/10.1016/j.ijmecsci.2024.109559.
[270] Liu L, He BB, Cheng GJ, Yen HW, Huang MX. Optimum properties of quenching and partitioning steels achieved by balancing fraction and stability of retained austenite. Scr Mater 2018;150:1–6. https://doi.org/10.1016/j.scriptamat.2018.02.035.
[271] Dong XX, Shen YF, Jia N, Zhu YT. Improving mechanical properties and retained-austenite stability of a medium carbon Q&P steel by adjusting phase ratio. Materials Science and Engineering: A 2022;833:142580. https://doi.org/10.1016/j.msea.2021.142580.
[272] Thrun M, Euser V, Clarke A, Clarke K. Tuning austenite stability through prior microstructure control in a low-alloy Q&P steel. Materialia (Oxf) 2024;38:102261. https://doi.org/10.1016/j.mtla.2024.102261.
[273] Finfrock CB, Thrun MM, Bhattacharya D, Ballard TJ, Clarke AJ, Clarke KD. Strain rate dependent ductility and strain hardening in Q&P steels. Metallurgical and Materials Transactions A 2021;52:928–42. https://doi.org/10.1007/s11661-020-06127-y.
[274] Kang J, Pottore NS, Zhu H, Tasan CC. An in situ investigation of neighborhood effects in a ferrite-containing quenching and partitioning steel: Mechanical stability, strain partitioning, and damage. Acta Mater 2023;254:118985. https://doi.org/10.1016/j.actamat.2023.118985.
[275] Lv Z, Dai E, Guo N, Yuan P, Liu G, Tang B. Strain-Induced phase transformation modeling of QP980 steel and its application to complex loading paths. Metals (Basel) 2023;13:823. https://doi.org/10.3390/met13040823.
[276] Xiao B, Yu J, Yu Y, Hu B, Misra RDK, Liu S, et al. Uncovering the effect of retained austenite stability on the dynamic mechanical properties of TRIP-aided steel. Materials Science and Engineering: A 2025;942:148729. https://doi.org/10.1016/j.msea.2025.148729.
[277] Liu L, Maresca F, Hoefnagels JPM, Vermeij T, Geers MGD, Kouznetsova VG. Revisiting the martensite/ferrite interface damage initiation mechanism: The key role of substructure boundary sliding. Acta Mater 2021;205:116533. https://doi.org/10.1016/j.actamat.2020.116533.
[278] Tang A, Liu H, Chen R, Liu G, Lai Q, Zhong Y, et al. Mesoscopic origin of damage nucleation in dual-phase steels. Int J Plast 2021;137:102920. https://doi.org/10.1016/j.ijplas.2020.102920.

[279] Juan R, Lian J. Failure mechanisms in quenching and partitioning (Q&P) steel under varying stress states. J Mater Sci Technol 2026;263:175–88. https://doi.org/10.1016/j.jmst.2025.09.010.
[280] Kozłowska A, Kokot G, Matus K, Grajcar A. Monitoring the phase evolution and fracture behavior of advanced multiphase QP steel using EBSD technique and digital image correlation. Theoretical and Applied Fracture Mechanics 2024;133:104520. https://doi.org/10.1016/j.tafmec.2024.104520.
[281] Pelligra C, Samei J, Shalchi Amirkhiz B, Hector LG, Wilkinson DS. Microstrain partitioning, Transformation Induced Plasticity, and the evolution of damage during deformation of an austenitic-martensitic 1.5 GPa Quench and Partition steel. Materials Science and Engineering: A 2024;895:146181. https://doi.org/10.1016/j.msea.2024.146181.
[282] Wang M-M, Hell J-C, Tasan CC. Martensite size effects on damage in quenching and partitioning steels. Scr Mater 2017;138:1–5. https://doi.org/10.1016/j.scriptamat.2017.05.021.
[283] Finfrock CB, Ellyson B, Likith SRJ, Smith D, Rietema CJ, Saville AI, et al. Elucidating the temperature dependence of TRIP in Q&P steels using synchrotron X-Ray diffraction, constituent phase properties, and strain-based kinetics models. Acta Mater 2022;237:118126. https://doi.org/10.1016/j.actamat.2022.118126.
[284] Xia P, Vercruysse F, Petrov R, Sabirov I, Castillo-Rodríguez M, Verleysen P. High strain rate tensile behavior of a quenching and partitioning (Q&P) Fe-0.25C-1.5Si-3.0Mn steel. Materials Science and Engineering: A 2019;745:53–62. https://doi.org/10.1016/j.msea.2018.12.064.
[285] Zhang J, Huang C, Wang M, Huang M, Duan H. Unraveling negative strain-rate sensitivity of a quenching & partitioning steel by a crystal plasticity model coupling solute-drag effect. J Mech Phys Solids 2026;212:106588. https://doi.org/10.1016/j.jmps.2026.106588.
[286] Cherkaoui M, Berveiller M, Sabar H. Micromechanical modeling of martensitic transformation induced plasticity (TRIP) in austenitic single crystals. Int J Plast 1998;14:597–626. https://doi.org/10.1016/S0749-6419(99)80000-X.
[287] Cherkaoui M, Berveiller M, Lemoine X. Couplings between plasticity and martensitic phase transformation: overall behavior of polycrystalline TRIP steels. Int J Plast 2000;16:1215–41. https://doi.org/10.1016/S0749-6419(00)00008-5.
[288] Turteltaub S, Suiker ASJ. A multiscale thermomechanical model for cubic to tetragonal martensitic phase transformations. Int J Solids Struct 2006;43:4509–45. https://doi.org/10.1016/j.ijsolstr.2005.06.065.
[289] Lee M-G, Kim S-J, Han HN. Crystal plasticity finite element modeling of mechanically induced martensitic transformation (MIMT) in metastable austenite. Int J Plast 2010;26:688–710. https://doi.org/10.1016/j.ijplas.2009.10.001.

[290] Olson GB, Cohen M. A mechanism for the strain-induced nucleation of martensitic transformations. Journal of the Less Common Metals 1972;28:107–18. https://doi.org/10.1016/0022-5088(72)90173-7.
[291] Stringfellow RG, Parks DM, Olson GB. A constitutive model for transformation plasticity accompanying strain-induced martensitic transformations in metastable austenitic steels. Acta Metallurgica et Materialia 1992;40:1703–16. https://doi.org/10.1016/0956-7151(92)90114-T.
[292] Poling WA. Tensile Deformation of Third Generation Advanced High Strength Sheet Steels Under High Strain Rates. Colorado School of Mines, 2016.
[293] Jacques P. On the role of martensitic transformation on damage and cracking resistance in TRIP-assisted multiphase steels. Acta Mater 2001;49:139–52. https://doi.org/10.1016/S1359-6454(00)00215-9.
[294] Chiang J, Lawrence B, Boyd JD, Pilkey AK. Effect of microstructure on retained austenite stability and work hardening of TRIP steels. Materials Science and Engineering: A 2011;528:4516–21. https://doi.org/10.1016/j.msea.2011.02.032.
[295] Jacques PJ, Delannay F, Ladrière J. On the influence of interactions between phases on the mechanical stability of retained austenite in transformation-induced plasticity multiphase steels. Metallurgical and Materials Transactions A 2001;32:2759–68. https://doi.org/10.1007/s11661-001-1027-4.
[296] Speer JG, Assunção FCR, Matlock DK, Edmonds D V. The “quenching and partitioning” process: background and recent progress. Materials Research 2005;8:417–23. https://doi.org/10.1590/S1516-14392005000400010.
[297] Hane KF, Shield TW. Symmetry and microstructure in martensites. Philosophical Magazine A 1998;78:1215–52. https://doi.org/10.1080/01418619808239984.

Appendices

Appendix A. Experimental Setup and Analysis Parameters

This appendix summarizes supporting experimental details for mechanical and thermal measurements. Specimen geometries are provided first, followed by the digital image correlation (DIC) and infrared (IR) camera settings used to record deformation and temperature evolution. These details support reproducibility while keeping the main text focused on material response and model assessment.

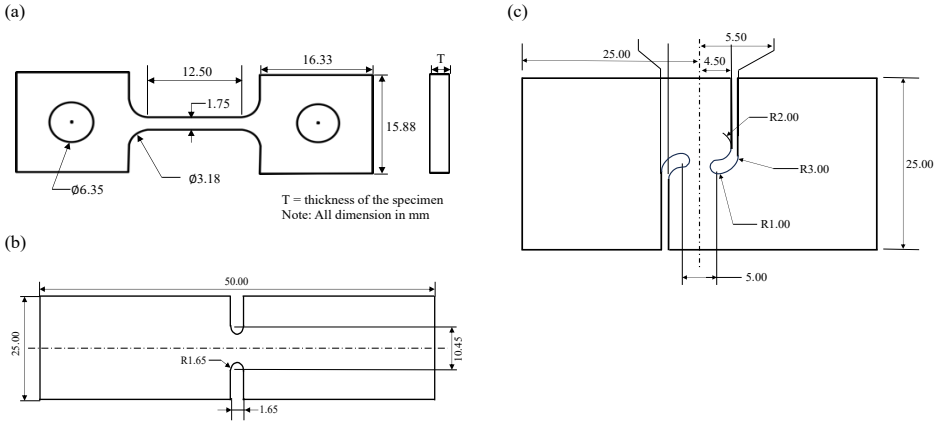


Figure A1: Specimen geometries used in the experiment: (a) uniaxial tension, (b) plane strain tension, and (c) simple shear. The dimensions shown define the geometries used in the corresponding mechanical tests reported in the main text.

Table A1: Summary of DIC hardware and analysis parameters used for deformation measurements at different strain rates.

Strain rate (s^{-1})	**0.001**	**0.1**	**1**	**10**	**100**
Camera manufacturer and model	Telops IRC TS-IR-2K				
IR software name and manufacturer	HypIR, Telops				
Lens manufacturer, model, focal length	Telops bayonet mounted lens, f/2.5, 50 mm		Telops bayonet mounted lens, f/2.5, 100 mm		
Frame rate (Hz)	2	100	2000	15000	21000
Image size (px)	320x256	320x256	64x112	64x96	64x80

Table A2: Summary of infrared camera system parameters used to record temperature evolution during tensile deformation at different strain rates.

Strain rate (s^{-1})	**0.001**	**0.1**	**1**	**10**	**100**
Camera manufacturer and model	Telops IRC TS-IR-2K				
IR software name and manufacturer	HypIR, Telops				
Lens manufacturer, model, focal length	Telops bayonet mounted lens, f/2.5, 50 mm		Telops bayonet mounted lens, f/2.5, 100 mm		
Frame rate (Hz)	2	100	2000	15000	21000
Image size (px)	320x256	320x256	64x112	64x96	64x80

Appendix B. Invariants

This appendix summarizes the stress invariants used throughout the constitutive and damage formulation. Crystal plasticity outputs and invariants for each crystal orientation:

Hydrostatic stress and effective stress can be expressed as

$$S^{(p)} = \sigma^{(p)} - \frac{1}{3} tr\left(\sigma^{(p)}\right) I,\ \sigma_e^{(p)} = \sqrt{\frac{3}{2} S^{(p)} : S^{(p)}} \tag{B.1}$$

Stress triaxiality is defined as

$$T^{(p)} = \frac{tr\left(\sigma^{(p)}\right)}{3\sigma_e^{(p)}} \tag{B.2}$$

The Lode angle uses the stress invariants and is given by

$$\begin{gathered} J_2^{(p)} = \frac{1}{2} S^{(p)} : S^{(p)},\ J_3^{(p)} = det\left(S^{(p)}\right) \\ J_3^{(p)} = det\left(S^{(p)}\right),\ \theta_L^{(p)} = \frac{1}{3} arccos\left(\frac{3\sqrt{3}}{2} \frac{J_3^{(p)}}{\left(J_2^{(p)}\right)^{3/2}}\right),\ L^{(p)} = 1 - \frac{2}{\pi} \theta_L^{(p)} \in [-1,1] \end{gathered} \tag{B.3}$$

Appendix C. Boundary Conditions

This appendix summarizes the macroscopic boundary conditions used in the Taylor-homogenized simulations for uniaxial tension, plane-strain tension and simple shear. These expressions prescribe the deformation gradient used to impose the corresponding nominal stress states in the constitutive calculations.

In the case of uniaxial tension, a continuous axial strain rate aligned with the L_{11} direction is applied, while shear strain and transverse/normal stresses are constrained to zero:

$$\begin{aligned} &\langle L_{11} \rangle = \dot{\varepsilon}_{app} \\ &\langle L_{12} \rangle = \langle L_{21} \rangle = \langle L_{13} \rangle = \langle L_{31} \rangle = \langle L_{23} \rangle = \langle L_{32} \rangle = 0 \end{aligned} \tag{C.1}$$

For plane strain tension, deformation is applied along L_{11} with the transverse strain (L_{22}) and shear strain (L_{23}) constrained to zero. The axial stress in the loading direction is traction free:

$$\begin{aligned} &\langle L_{11} \rangle = \dot{\varepsilon}_{app} \\ &\langle L_{22} \rangle = \langle L_{23} \rangle = 0 \end{aligned} \tag{C.2}$$

For simple shear, shear deformation is applied via L_{12} while all normal components are held fixed at zero.

$$\begin{aligned} &\langle L_{12} \rangle = \dot{\gamma}_{app} \\ &\langle L_{11} \rangle = \langle L_{22} \rangle = \langle L_{33} \rangle = 0 \end{aligned} \tag{C.3}$$

These boundary conditions provide a controlled framework for comparing damage evolution under higher-triaxiality plane-strain tension and lower-triaxiality simple shear at 0.001 s^{-1}.

Appendix D. Transformation Kinematic Properties

The deformation induced transformation of retained austenite to fresh martensite is represented using the phenomenological theory of martensitic transformation. In the present work, a common FCC to BCT transformation kinematic set is adopted for both QP3Mn and QP980. This assumption defines the crystallographic shape strain associated with the formation of martensite plates and does not imply identical retained austenite stability in the two steels. Differences between QP3Mn and QP980 are instead represented through their measured phase fractions, phase specific textures, transformation kinetics, thermomechanical loading conditions, and damage evolution parameters. For a martensite variant ζ_i^β formed from a parent austenite grain a, the transformation stretch tensor is written in the austenite basis as

$$\mathbf{U}^{(a,\zeta_i^\beta)} = \left(\frac{\sqrt{2}a_M}{a_A}\right)\mathbf{I} + \left(\frac{c_M}{a_A} - \frac{\sqrt{2}a_M}{a_A}\right) e_{\zeta_i^\beta}^{(a)} \otimes e_{\zeta_i^\beta}^{(a)} \tag{D.1}$$

where a_A is the lattice parameter of retained austenite, and a_M and c_M are the lattice parameters of BCT martensite. The lattice parameters are evaluated from the retained austenite carbon content following Turteltaub & Suiker [22],

$$c_M = 2.861 + 0.116p_c \tag{D.2}$$

$$a_M = 2.861 - 0.0136p_c \tag{D.3}$$

$$a_A = 3.548 + 0.044p_c \tag{D.4}$$

where p_c is the retained austenite carbon concentration in wt. %. Following Connolly et al. [23], p_c=1.12 wt. % is used for the transformation kinematic calculation, giving

$$c_M = 2.99092\ \text{Å}, \qquad a_M = 2.84644\ \text{Å}, \qquad c_M = 3.59728\ \text{Å} \tag{D.5}$$

Using these lattice parameters, the analytic solution of Hane and Shied [297] gives 24 martensite plate systems for each parent austenite grain, with two internally twinned martensite variants associated with each plate. The corresponding transformation shear magnitude is

$$\hat{\gamma}_{tr} = 0.1886 \tag{D.6}$$

For martensite plate orientation β, the transformation direction $\boldsymbol{b}^{(a,\beta)}$ and habit plane $\boldsymbol{d}^{(a,\beta)}$ are defined in the parent austenite basis as

$$\boldsymbol{b}^{(a,\beta)} = b_i^{(\beta)} \boldsymbol{e}_i^{(a)} \tag{D.7}$$

$$\boldsymbol{d}^{(a,\beta)} = d_i^{(\beta)} \boldsymbol{e}_i^{(a)} \tag{D.8}$$

where $b_i^{(\beta)}$ and $d_i^{(\beta)}$ are the transformation system components associated with plate system β. The transformation deformation across the austenite-martensite interface is then expressed as

$$\left[[\boldsymbol{F}]\right]^{(a,\beta)} = \hat{\gamma}_{tr}\boldsymbol{b}^{(a,\beta)}\otimes\boldsymbol{d}^{(a,\beta)} \tag{D.9}$$

The transformation systems $\left(\boldsymbol{b}^{(a,\beta)}\otimes\boldsymbol{d}^{(a,\beta)}\right)$, the internal martensite twin volume fractions $\lambda^{\left(\zeta_i^{\beta}\right)}$, the relative twin rotations, and the martensite plate rotations are adopted from the PTMC solution reported by Connolly et al. [23]. The adopted set consists of 24 martensite plate orientations and 48 possible variants for each parent austenite grain. These quantities provide the fixed crystallographic inputs used in the transformation velocity gradient defined in Eq. (7-14). They are not recalibrated for QP3Mn and QP980. Therefore, alloy dependent differences in transformation response are represented through the retained austenite stability, phase distribution, texture, temperature, strain rate, and damage evolution, rather than through separate transformation kinematic tables.

Appendix E. Slip System Definitions

The slip system families used in the present crystal plasticity formulation are summarized here. Retained austenite is treated as an FCC phase deforming by the $\{111\}\langle 110\rangle$ slip family, whereas ferrite, tempered martensite, and transformed martensite are treated as BCC phases deforming by the $\{110\}\langle 111\rangle$ and $\{112\}\langle 111\rangle$ slip families. Although the transformation kinematics are based on an FCC to BCT lattice correspondence, transformed martensite is approximated as BCC for elastic and plastic slip deformation, following the common treatment adopted in crystal plasticity models.

For a grain g, the reference slip direction and slip plane normal of slip system i are expressed in the crystal basis as

$$\boldsymbol{s}^{(g,i)} = s_j^{(i)} \boldsymbol{e}_j^{(g)} \tag{E.1}$$

$$\boldsymbol{m}^{(g,i)} = m_j^{(i)} \boldsymbol{e}_j^{(g)} \tag{E.2}$$

where $\boldsymbol{e}_j^{(g)}$ are the basis vectors of grain g, and $\boldsymbol{s}^{(g,i)}$ and $\boldsymbol{m}^{(g,i)}$ are the normalized components of the slip direction and slip plane normal, respectively.

For austenite, ferrite, and pre-existing martensite, the current slip directions and slip-plane normals evolve according to Eqs. (7-9) and (7-10). For newly transformed martensite, however, the reference orientation of the slip systems is inherited from the parent austenite grain and the selected martensite variant. Therefore, the slip direction and slip-plane normal in the newly transformed martensite are obtained as

$$\hat{\boldsymbol{s}}^{(g,i)} = \hat{\boldsymbol{s}}^{(\left(a,\zeta_i^{\beta}\right),i)} = s_j^{(i)} \widehat{\boldsymbol{Q}}^{(\zeta_i^{\beta})} \boldsymbol{e}_j^{(a)} \tag{E.3}$$

$$\widehat{\boldsymbol{m}}^{(g,i)} = \widehat{\boldsymbol{m}}^{(\left(a,\zeta_i^{\beta}\right),i)} = m_j^{(i)} \widehat{\boldsymbol{Q}}^{(\zeta_i^{\beta})} \boldsymbol{e}_j^{(a)} \tag{E.4}$$

where a denotes the parent austenite grain, ζ_i^{β} denotes martensite variant associated with martensite plate orientation β, and $\widehat{\boldsymbol{Q}}^{(\zeta_i^{\beta})}$ is the rotation tensor that maps the parent austenite basis to the corresponding martensite variant basis. This construction ensures that the plastic slip systems in newly formed martensite are consistent with the crystallographic orientation generated by the transformation kinematics summarized in Appendix D.

The Burgers vector magnitude is evaluated from the corresponding lattice geometry. For retained austenite, the FCC Burgers vector is

$$b_A = \frac{a_A}{2}\sqrt{1^2 + 1^2 + 0^2} \tag{E.6}$$

where a_A is the retained-austenite lattice parameter. For BCC ferrite and tempered martensite, the Burgers vector is

$$b_{BCC} = \frac{a_M}{2}\sqrt{1^2 + 1^2 + 1^2} \tag{E.7}$$

where a_M is the BCC lattice parameter. For transformed martensite, the Burgers vector is evaluated from the tetragonal lattice parameters as

$$b_{TM} = \frac{1}{2}\sqrt{(a_M)^2 + (a_M)^2 + (c_M)^2} \tag{E.8}$$

where a_M and c_M are the transformed-martensite lattice parameters.

Appendix F. Decomposition of Dissipation

The total dissipation is decomposed into elastic, thermal, plastic, damage, transformation, and heat-conduction contribution as

$$\mathcal{D} = \sum_{g=1}^{N_g} \xi^{(g)} \left(\mathcal{D}_e^{(g)} + \mathcal{D}_\theta^{(g)} + \mathcal{D}_p^{(g)} + \mathcal{D}_d^{(g)} \right) + \sum_{a=1}^{N_a} \sum_{\beta=1}^{24} \mathcal{D}_{tr}^{(a,\beta)} + \mathcal{D}_\theta \geq 0 \tag{F.1}$$

where $\mathcal{D}_e^{(g)}$, $\mathcal{D}_\theta^{(g)}$, $\mathcal{D}_p^{(g)}$, and $\mathcal{D}_d^{(g)}$ are the grain-level elastic, thermal, plastic, and damage dissipation terms, $\mathcal{D}_{tr}^{(a,\beta)}$ is the dissipation associated with transformation into martensite plate orientation β from austenite grain a, and $\mathcal{D}_\theta$ is heat conduction dissipation. These contributions are written as

$$\mathcal{D}_e^{(g)} = \left[\sigma^{(g)} - \rho F_e^{(g)} \frac{\partial \Psi^{(g)}}{\partial E_e^{(g)}} \left(F_e^{(g)} \right)^T + \rho \theta F_e^{(g)} \frac{\partial \eta_m^{(g)}}{\partial E_e^{(g)}} \left(F_e^{(g)} \right)^T \right] : \boldsymbol{D}_e^{(g)} \tag{F.2}$$

$$\mathcal{D}_\theta^{(g)} = \left[A^{(g)} \left[\sigma^{(g)} : I \right] - \rho \frac{\partial \Psi^{(g)}}{\partial \theta} - \rho h^{(g)} ln \left(\frac{\theta}{\theta_T} \right) + \rho \theta \frac{\partial \eta_m^{(g)}}{\partial \eta_e^{(g)}} \frac{\partial \eta_e^{(g)}}{\partial \theta} \right] \dot{\theta} \tag{F.3}$$

$$\mathcal{D}_p^{(g)} = \sum_{i=1}^{N_p^{(g)}} \left[\sigma^{(g)} : P^{(g,i)} - \rho \frac{\partial \Psi^{(g)}}{\partial \rho_d^{(g)}} w_p^{(g,i)} + \rho \theta \varphi^{(g,i)} sign\left(\dot{\gamma}^{(g,i)} \right) \right] \dot{\gamma}^{(g,i)} \tag{F.4}$$

$$\mathcal{D}_d^{(g)} = \left[\frac{1}{3\left(1 - \phi_{eff}^{(g)} \right)} \left[\sigma^{(g)} : I \right] - \rho \frac{\partial \Psi^{(g)}}{\partial \phi_{eff}^{(g)}} + \rho \theta \right] \dot{\phi}_{eff}^{(g)} \tag{F.5}$$

$$\mathcal{D}_{tr}^{(a,\beta)} = \rho\theta\left[\sum_{i=1}^{2}\lambda^{\left(\zeta_i^{\beta}\right)}\eta_m^{\left(a,\zeta_i^{\beta}\right)} - \eta_m^{(a)}\right]\dot{\xi}^{(a,\beta)} - \rho\left[\sum_{i=1}^{2}\lambda^{\left(\zeta_i^{\beta}\right)}\Psi^{\left(a,\zeta_i^{\beta}\right)} - \Psi^{(a)}\right]\dot{\xi}^{(a,\beta)}$$
$$- \rho\left[\sum_{i=1}^{2}\lambda^{\left(\zeta_i^{\beta}\right)}\xi^{\left(a,\zeta_i^{\beta}\right)}\frac{\partial\Psi^{\left(a,\zeta_i^{\beta}\right)}}{\partial\xi^{\left(a,\zeta_i^{\beta}\right)}} - \xi^{(a)}\frac{\partial\Psi^{\left(a,\zeta_i^{\beta}\right)}}{\partial\xi^{\left(a,\zeta_i^{\beta}\right)}}\right]\dot{\xi}^{(a,\beta)} + \rho\theta\left[\frac{\lambda_T}{\theta_T}\right]\dot{\xi}^{(a,\beta)}$$
$$+ \rho\theta\left[\sum_{i=1}^{2}\lambda^{\left(\zeta_i^{\beta}\right)}\eta_p^{\left(a,\zeta_i^{\beta}\right)} - \eta_p^{(a)}\right]\dot{\xi}^{(a,\beta)} \tag{F.6}$$
$$+ \rho\theta\left[\sum_{i=1}^{2}\lambda^{\left(\zeta_i^{\beta}\right)}\eta_d^{\left(a,\zeta_i^{\beta}\right)} - \eta_d^{(a)}\right]\dot{\xi}^{(a,\beta)}$$
$$+ \frac{1}{2}\left[\sum_{i=1}^{2}\lambda^{\left(\zeta_i^{\beta}\right)}\sigma^{\left(a,\zeta_i^{\beta}\right)} + \sigma^{(a)}\right] : P_{tr}^{(a,\beta)}\dot{\xi}^{(a,\beta)}$$

$$\mathcal{D}_{\theta} = -\frac{\boldsymbol{\nabla}\theta\cdot\boldsymbol{q}}{\theta} \tag{F.7}$$

In the present constitutive framework, each dissipative contribution is independently required to be non-negative,

$$\mathcal{D}_e^{(g)} \geq 0 \qquad \mathcal{D}_{\theta}^{(g)} \geq 0 \qquad \mathcal{D}_p^{(g)} \geq 0 \qquad \mathcal{D}_d^{(g)} \geq 0 \qquad \mathcal{D}_{tr}^{(g)} \geq 0 \qquad \mathcal{D}_{\theta} \geq 0 \tag{F.8}$$